Order Number 9321849

Predicting the crystal structure of organic molecular materials

Chaka, Anne Marie, Ph.D.

Case Western Reserve University, 1993

U·M·I
300 N. Zeeb Rd.
Ann Arbor, MI 48106

PREDICTING THE CRYSTAL STRUCTURE OF ORGANIC MOLECULAR MATERIALS

by

ANNE MARIE CHAKA

Submitted in partial fulfillment of the requirements

for the Degree of Doctor of Philosophy

Thesis Advisors:

Professor Gilles Klopman

Professor Wiley Youngs

Department of Chemistry

Case Western Reserve University

January, 1992

CASE WESTERN RESERVE UNIVERSITY

GRADUATE STUDIES

We hereby approve the thesis of

ANNE MARIE CHAKA

candidate for the Ph. D.

degree.*

Signed: _____ (Chairman)

_____

_____

_____

Date 11/20/91

*We also certify that written approval has been obtained for any proprietary material contained therein.

PREDICTING THE CRYSTAL STRUCTURE OF ORGANIC MOLECULAR MATERIALS

Abstract

by

ANNE MARIE CHAKA

Considerable interest has developed in organic molecular materials since the discovery of a wide range of properties previously thought to be the exclusive domain of inorganic materials and metals. Many of these properties of organic materials, such as conductivity, nonlinear optical susceptibility, and ferromagnetism, are dependent upon the relative orientation of the constituent molecules within the material. Hence, to be able to predict crystal packing has long been recognized as being of great importance, but was believed to be too complicated or to involve too many long calculations to be feasible. We have developed a novel method which employs a series of successive approximations to focus on structures of high probability without resorting to a brute force search and energy minimization of all possible structures. The problem of multiple local minima was overcome by assuming that the crystal structure is closest packed, thereby eliminating 217 of the 230 possible space groups. Structures within the 13 remaining space groups were searched in rotational increments of 15°. Initial energy minimzation was performed using Lennard-Jones pair potentials to produce a set

of closest-packed structures. These structures were then refined with the introduction of a Coulombic potential calculated using molecular multipole moments. This method has successfully predicted the crystal structure of several saturated and unsaturated hydrocarbons with no *a priori* information provided. For large polycyclic aromatic hydrocarbons, additional refinements of the energy calculations are required to distinguish the experimental structure from a small number of closest-packed structures. All calculations were performed on the Ohio Supercomputer Center's Cray Y-MP.

Dedication

This work is dedicated to my husband, Brian Good, whose humor, patience, and help made the entire experience quite tolerable, if not pleasant.

Acknowledgement

I wish to thank the following people for their assistance: Dr. Brian Good, Dr. Mario Dimayuga, Dr. Ruben Venegas, Prof. Wiley Youngs, Prof. Claire Tessier, Prof. Gilles Klopman, Joseph Talafous, Shaomeng Wang, Dr. Sanjay Srivastava, Dr. Robert Henderson, Dmitri Ptchelinsev, Prof. Robert Brown, Prof. Philip Taylor, Prof. Rolfe Petshek, Dr. Mary Ann Meador, and Dr. Michael Meador.

I also wish to acknowledge the support of the Ohio Supercomputer Center, Cray Research, Inc., and the NASA Graduate Researchers Fellowship Program.

Table of Contents

List of Figures

List of Tables

"Every attempt to employ mathematical methods in the study of chemical questions must be considered profoundly irrational and contrary to the spirit of chemistry. If mathematical analysis should ever hold a prominent place in chemistry, an aberration which is happily almost impossible, it would occasion a rapid and widespread degeneration of that science."

Auguste Comte
Philosophic Positive (1830)

Chapter 1 Introduction

Considerable interest in molecular materials, thin films, and monolayers [1,2] has developed in recent years due to the discovery of their wide range of electronic [3], magnetic [4], and optical properties [5,6]. Organic materials have an advantage over more traditional materials in that their properties can be tailored to a specific application by changing the structure of the constituent molecules. Subtle differences in the magnitudes of various properties can be achieved by modification of the functional groups on a given molecule. In addition, organic materials can be designed which exhibit these properties anisotropically.

Most of these properties are dependent upon the relative orientation of the molecules within the material, i.e. how the molecules are packed within the crystal [3,4,5,6]. For example, materials with a centrosymmetric crystal structure will not exhibit second-order nonlinear optical effects, even if the individual molecules have a high second-order susceptibility coefficient [6]. While inorganic materials are usually easily made, the synthesis of organic molecules is often quite difficult and time consuming. Up to now there has not been a method to predict *a priori* whether the material to be synthesized will crystallize in a certain space group and hence be more likely to express the desired properties macroscopically in the bulk

phase. At the present time development of these conducting and optical systems is on a trial-and-error basis due to the lack of a working predictive model for the solid state structure of organic materials. Hence, there is a need to improve our understanding of how these materials crystallize in order to provide some direction to the synthetic chemist.

To be able to predict crystal packing has long been recognized as being of great importance, but was believed to be too complicated or to involve too many long calculations to be feasible. The observed structure will be, of course, the minimum free energy configuration. Due to the problem of multiple minima in a very large search space and the notoriously slow convergence of $1/r$ terms in the electrostatic energy over many unit cells, prediction techniques based on lattice energy minimization alone are not practical for molecular solids. We have developed a novel approach to predicting the crystal structures of organic molecular materials which circumvents the above difficulties by using a series of successive approximations to focus on crystal structures of high probability without performing a search by brute force of the nearly infinite number of possibilities. Our approach still requires a supercomputer, but the program, ICE9, is highly vectorized and enables us to predict the crystal structures of various hydrocarbons in less than four hours cpu time on a Cray Y-MP.

Chapter 2 Background and Statement of Problem

2.1. Properties of Organic Molecular Materials

A molecular material is defined as a substance in which groups of atoms can be found for which the interatomic distances within that group are significantly smaller than those between groups. For example, spacings between hydrogen atoms which are in different molecules are at least 2.4 Å apart in hydrocarbon crystals, whereas distances between these atoms and the carbon atoms to which they are bound are on the order of 1 Å. There are no actual bonds between molecules in these solids, and the dominant cohesive force of the lattice is due to weak Van der Waals interactions. This type of lattice is in contrast to solids which are primarily ionic, such as sodium chloride, covalent, such as graphite or silicon, or metallic. To illustrate the importance of predicting crystal structures, this section will describe two types of molecular materials and discuss in detail how their crystal packing relates to their macroscopic properties.

Intense interest in nonlinear optics has developed during the last ten years as demands for speed in computing and information transfer have increased. Since the discovery of second harmonic generation (SHG) in 1961 when Franken, Hill, Peters, and Weinrich [7] directed a ruby laser at a quartz crystal and generated radiation at twice the input frequency, most initial work in the area of nonlinear optics has been done on inorganic materials such as potassium dihydrogen phosphate, GaAs, and $LiNbO_3$. Although these inorganic materials are readily available, cheap, and easy to make, they are plagued by poor optical transparency, low thresholds for laser damage, high dielectric constants, and relatively slow response times when compared to the optical properties of organic materials. In addition,

recent excitement in the field of optics has been generated by the discovery of even higher nonlinear responses for organic crystals than for $LiNb0_3$, one of the most active inorganic nonlinear materials known [5]. The high conversion efficiency which is possible in organic single crystals will allow the use of much lower power lasers, which are cheaper to operate and cause less molecular damage.

The molecular basis of nonlinear optics is well understood. Electomagnetic radiation propagating through a medium, or application of an external electric field, induces polarization of the molecules in the medium. The molecular dipoles oscillate in turn, emitting electromagnetic radiation. In some cases, this emitted frequency can be twice (Second Harmonic Generation - 2ω), or even three times the incident frequency ω (Third Harmonic Generation - 3ω). The nonlinear polarization resulting from an applied static or optical electric field can be expanded in a power series of the electric field. For a single molecule, the induced dipole moment is given by the expression:

$$\mu_i = \sum_j \alpha_{ij} E_j + \sum_{jk} \beta_{ijk} E_j E_k + \sum_{jkl} \gamma_{ijkl} E_j E_k E_l + \ldots \qquad \text{[Eq. 2.1]}$$

where i is the molecular axis, E_j is the jth component of the electric field, α is the linear polarizability, β is the quadratic hyperpolarizability, and γ is the cubic hyperpolarizability. α, β and γ are second, third and fourth-rank tensors, respectively.

The coefficients for the bulk nonlinear susceptibility of a material can be determined from the molecular susceptibilities:

$$\chi^{(1\omega)} = N f_{\omega 1} f_{\omega 2} \langle \alpha_{ij} \rangle$$

$$\chi^{(2\omega)} = N f_{\omega 1} f_{\omega 2} f_{\omega 3} \langle \beta_{ijk} \rangle$$

$$\chi^{(3\omega)} = N f_{\omega 1} f_{\omega 2} f_{\omega 3} f_{\omega 4} \langle \gamma_{ijkl} \rangle \qquad \text{[Eqs. 2.2]}$$

where N is the number of molecules per unit volume, $f_{\omega 1}$ is the local electric field correction, and the brackets $\langle\,\rangle$ imply angular averaging over the irradiated area. Therefore the bulk nonlinear polarizability of a material can be expressed as:

$$P_i = \sum_j \chi_{ij}^{(1\omega)} E_j + \sum_{jk} \chi_{ijk}^{(2\omega)} E_j E_k + \sum_{jkl} \chi_{ijkl}^{(3\omega)} E_j E_k E_l + \ldots \qquad \text{[Eq. 2.3]}$$

Hence, materials with high bulk nonlinear optical susceptibilities can be designed from molecules with high nonlinear activity. These molecules which have a large nonlinear susceptibility coefficient β are characterized by extensive conjugated π systems, planarity, and substituents with strong electron donating and inductive effects at opposite ends of the molecular dipole which can yield low-lying charge-transfer resonance states [5]. Typical examples of molecules with high nonlinear activity are shown in Figure 2.1.

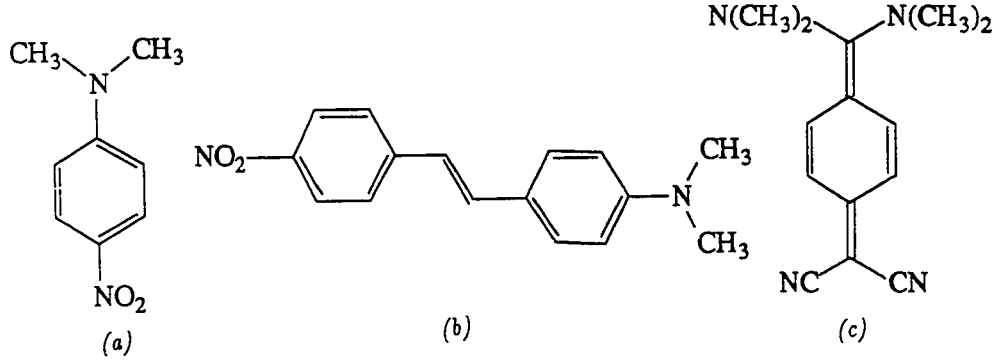

Fig. 2.1 (a). *N,N*-dimethyl-*p*-Nitroaniline, (b). Quinodimethane derivative, (c). *trans*-4'-Dimethyl-amino-1-nitrostilbene (DANS).

A material with the maximum nonlinear response will have all the individual molecular components arranged with their susceptibility tensor maxima aligned in the same direction, thus maintaining a polar orientation throughout the crystal. In a centrosymmetric environment, however, β vanishes altogether. This can be readily seen by the following argument. If a field $+E$ is applied to the medium, the polarization induced by the first nonlinear term is $+\beta E^2$. If a field $-E$ is applied, the symmetry requirement should result in a polarization of $-\beta E^2$, yet it is still predicted to be $+\beta E^2$. This contradiction can only be resolved if β equals zero in a centrosymmetric medium. In addition to being noncentrosymmetric, for maximum second order nonlinear response the crystal must be of a certain dimension to achieve phase matching between the fundamental and the harmonics, because their relative intensities are determined solely by the phase relationship at the boundary.

In 1982 Ouder and Zyss [8] analyzed the various space group symmetries for phase matching and optimized orientation of molecular susceptibilities in the crystal. They determined that polar molecules that crystallize in the space groups having 1, 2, m, and $mm2$ point groups have the largest potential nonlinear coefficients, given the proper orientation of the molecules within these groups. Oudar and Zyss's results are presented in Table 2.1 as the maximum fractional value of $\chi^{(2\omega)}$ within each space group as compared to that obtained in an ideal rigid lattice-oriented gas, [9] i.e. with all molecules pointing in the same direction and fixed in space.

Table 2.1 Polar point groups as maximum fractional value of the rigid oriented gas χ (2ω) for a phase-matched interaction and for optimum molecular orientation in the unit cell [5].

Point Group	$\chi(2\omega)(max)$
1,2,*m*,*mm2*	0.38
62M,6,3,3M,32	0.25
222,*6mm*,*6*,*4mm*,42M,23,43M	0.19
4	No possible phase interaction

Comparative statistics on materials reveal that organic molecules tend to crystallize in noncentrosymmetric space groups more frequently than do inorganic molecules [10]. Even so, only 27.6% of organics crystallize in this mannner. In addition, point symmetry is important in determining second harmonic generation and can further limit the number of possibilities. For example, the isotropic optical nature of cubic systems excludes the cubic acentric groups from the list of SHG candidates [5]. Other acentric groups are excluded for similar reasons.

In the last few years, not much use has been made of these known characteristics of the space groups outside of trial and error attempts to modify molecules in the hope of achieving the desired crystal structure [5]. Currently, investigators at IBM are attempting to circumvent this problem by using the Cambridge Crystallographic Database to predict which materials may be SHG active compounds. The IBM method is, of course, limited to compounds which have previously been synthesized and structurally characterized. Given the potential nonlinear optical properties of organic single crystals, a program which could predict the crystal structure of these molecular materials would be of great utility, and crucial for rapid advancement in this field. By predicting the space group in which a molecule will crystallize, one can optimize the structure for second order nonlinear

properties (noncentrosymmetric polar space group) or even third order properties (centrosymmetric space group).

In organic conducting systems, the arrangement of the molecules in the crystal is crucial. For example, most organic molecules form insulators when they crystallize [11]. Yet there are specific orientations in organic molecular solids which allow for dramatic increases in conductivity in certain directions. Materials such as phthallocyanines [12], nickel tribenzocyclyne [13], and $(TMTSF)_2PF_6$ [14] can form semiconductors, conductors, and even superconductors, respectively. The unique conduction properties of some organic materials have led to several new technologies for electrochemical cells, lightweight batteries, and photovoltaic devices.

Organic conductors and semiconductors are formed from charge-transfer compounds in a nonintegral oxidation state arranged in a particular segregated stacked geometry in the crystal lattice. Mixed stacks of alternating donor and acceptor molecules will be insulators. To design novel conducting systems one needs to predict the type of linear stacking and whether or not the stack is vertically eclipsed or skewed (Figure 2.2).

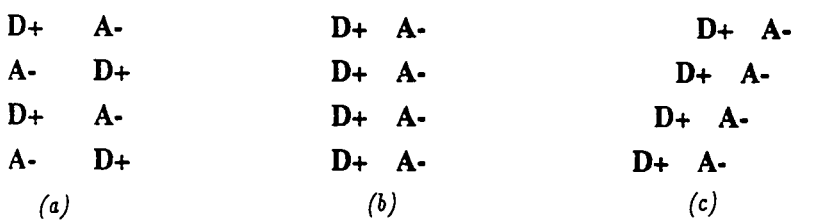

Fig. 2.2 Types of stacking observed in charge-transfer solids. (a). Mixed stacking in an insulator. (b). Segregated, eclipsed stacking. (c). Segregated, slipped stacking. Either structure in (b) or (c) can be conducting, depending upon the electronic states of the constituent species.

For organic conductors and semiconductors, the molecular interactions are no longer as simple as those between nonbonded neutral organic species. Whereas the constituent species in organic semiconductors are completely ionized, and those in organic conductors are partially ionized, the Madelung energy in these materials becomes the dominant term in the cohesive energy. In addition to posessing large Madelung forces, organic conductors also exhibit significant intermolecular π-overlap at Van der Waals distances, yielding a one dimensional band structure and metal-like conductivity, and in some cases, even superconductivity [3]. Due to the small charge-size ratio in these organic compounds, the Van der Waals and short-range repulsive energies still play a significant role in the the lattice energy and structure, unlike the typical inorganic ionic lattice where the non-Coulombic forces contribute less than 1-3% to the total energy [15].

Most investigative theoretical work on these charge-transfer conducting solids has been done using TTF and TCNQ dimers as models for the stacking calculations (Figure 2.3). The focus has been on a quantum mechanical treatment on the degree of the charge transfer[15] and π-overlap between two molecules using various self-consistent methods (Hartree-Fock, [16] CNDO/2, [17] and MNDO/3 [18,19,20] calculations. A discussion of these and other quantum mechanical methods is presented in Appendix B). Nonbonded interactions, such as the London dispersive forces, were not explicitly included in the calculation. Although excellent progress has been made in this area, more theoretical work, particularly in the inclusion of nonbonded forces in the cohesive energy, needs to be done to completely account for the observed lattice energies and structures in these conducting systems.

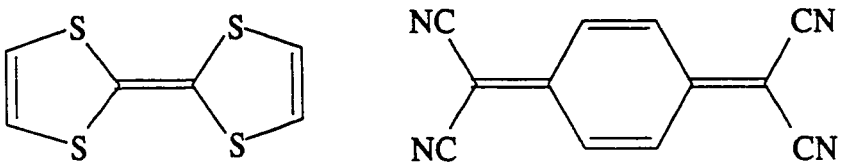

(a) *(b)*

Fig. 2.3 (a). Electron donor tetrathiofulvalene (TTF). (b). Electron acceptor tetracyanoquinodimethane (TCNQ).

2.2. Theory of Crystal Packing

Molecules with very similar structures can crystallize in very different orientations and have completely different properties. For example, benzene crystallizes in a herringbone configuration with 4 molecules per unit cell [21], hexachlorobenzene in a face-to-face stacked pancake arrangement with 2 molecules per cell [22], and hexafluorobenzene in a different herringbone configuration with 6 molecules per unit cell [23].

Before the first crystal structure was ever determined, Fedorov, Schoenflies, and Barlow [24] deduced independently from considerations of symmetry and packing alone that there are only 230 types of possible arrangements in space for crystalline materials [see Appendix A]. This was the first major theoretical advance in the understanding of the internal structure of crystals. Soon after this, in 1912, von Laue, Friedrich, and Knapping presented an elementary theory of diffraction of X-rays by a periodic array of atoms, along with results of actual diffraction experiments which Friedrich and Knapping had carried out, thus beginning the science of modern crystallography [25]. Since these pioneering experiments, the science of X-ray crystallography has advanced rapidly to very sophisticated levels. Today, with the help of computers and sophisticated equipment, average atomic

positions of small molecules in a crystal can be determined to within 0.001 Å. Though not routine, the determination of structures of biological macromolecules such as proteins and viruses can be done. Electron diffraction is capable of imaging the actual electron density between atoms, essentially visualizing the occupied molecular orbitals [26].

The theory of crystal packing, however, has not kept pace with the experimental developments. Historically most work on the energy characteristics of the solid state had been done on inorganic ionic and covalent lattices. Work by Madelung [27], Born [28], Oppenheimer [29], Lowdin [30], Goldschmidt [31], Pauling [32] and others has been fundamental in understanding the structure of the solid state. In the 1950's, Laves[33] described three general principles to describe metallic and non-metallic inorganic crystals. These principles maintain that within these crystals the most efficient use is made of space, the highest possible symmetry exists, and the highest number of connections form between components (highest coordination number). More recent theoretical work on bond type vs. crystal structure, such as that of Mooser and Pearson [34], and Philips and van Vechten [35], has been done on inorganic non-molecular materials and good predictions for these solids have been made.

Theoretical treatment of organic molecular solids, however, has lagged far behind that of inorganic materials for a variety of reasons, one of which is the inability to experimentally determine the positions of the hydrogen atoms by X-ray methods until the 1950's [36]. In addition, solid state physicists have largely ignored organic molecular solids, and chemists have only been interested in them as a prerequisite for determining the structure of individual molecules.

Another difficulty is that the weak nonbonded forces that cause molecular association and subsequent crystallization are not readily quantified. Fortunately, in organic molecular materials, the molecule maintains its integrity in the solid state, i.e. the structure the molecule exhibits in the gas phase is fairly well retained in the solid state, with distortions being minor, if present at all [36].

A molecule can be thought of as possessing a shape whose boundaries are delineated by the Van der Waals radii of the constituent atoms. In 1929-1930 B.P. Orelkin [37] pointed out that asymmetric molecules tend to stack so that the protrusions on one enter the hollows of another. The first rigorous theoretical treatment of molecular solids was published by the Russian crystallographer Kitaigorodsky in 1955, demonstrating that Laves' principles of crystals apply to organic molecular solids as well as metallic and non-metallic inorganic crystals [37]. Kitaigorodsky proposed a simple geometric model, using Orelkin's observation as a first approximation, which described a crystal as a close packing of solid molecules. "Connectivity" or "coordination", as mentioned by Laves, here implies only Van der Waals contact in a molecular crystal, and not a strong ionic or covalent bond.

Kitaigorodsky first examined packing in two dimensions, using the seventeen planar symmetry groups. If irregularly shaped figures are arranged in these groups, it is apparent that in the closest packed configuration, each figure is in contact with six other figures, i.e., each "molecule" has a coordination number of six. For example in Figure 2.4, (a) and (b) are closest packed with a coordination number of six, whereas (c) and (d) are not.

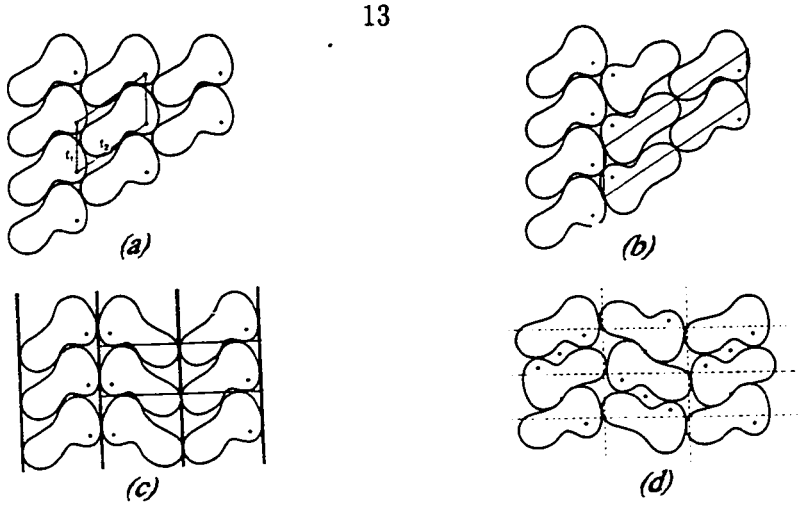

Fig. 2.4 Dense layers with symmetry (a) p1, and (b) p2. Open layers with symmetry (c) p*m* and (d) p*gg* [36].

If the molecule possesses some inherent symmetry, then the allowed set of closest packed space groups can be different, but the coordination number will still be six. To describe the structural density of a molecular solid, Kitaigorodsky developed an index called the packing coefficient. This packing coefficient is the ratio of the molecular Van der Waals volume to the volume per molecule in the crystal lattice. In an attempt to verify this closest packing hypothesis, Zorky and Poraj-Koshits [38] calculated all possible packings for several different planar molecules. A small number of closest-packed configurations were found. In all cases, the experimentally observed structures of these model compounds were found in this small set of closest-packed orientations. In fact, the true structure was found to be the one with the highest density to within an error of 0.01 in the packing coefficient.

In three dimensions, Kitaigorodsky postulated that the layers of molecules must also be closest packed. This packing can be achieved only through a monoclinic displacement of layers, inversion centers, glide planes, or screw axes. A mirror plane of symmetry between layers prevents closest packing, as can be seen by the large amount of empty space in Figure 2.5.

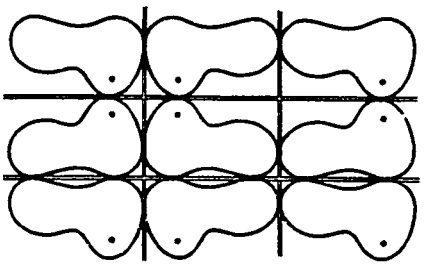

Fig. 2.5 Layer with symmetry p*mm*, containing two perpendicular mirror planes [36].

The optimum coordination number in three dimensions is 12. Experimentally this is usually the case, with only a small number of molecular symmetries crystallizing with a coordination number of 10 or 14. The requirement of closest packing reduces the possible number of space groups from 230 to 13 for the overwhelming majority of organic compounds. For totally asymmetric molecules, closest packing is possible only in the following groups: $P2_1$, $P2_1/c$, P*ca*, P*na*, and $P2_12_12_1$. For centrosymmetric molecules the number of possiblilities is even smaller : $P\bar{1}$, $P2_1/c$, and P*bca*. Table 2.2 summarizes the possible space groups for a given molecular symmetry in a crystal.

Table 2.2 Closest-Packed Space Groups and Space Groups of Maximum Density for Organic Molecular Crystals [36].

Molecular symmetry in crystal	1	2	*m*	$\bar{1}$	*mm*	2/*m*	222	*mmm*
Closest-packed space groups	$P\bar{1}$ $P2_1$ $P2_1/c$ P*ca* P*na* $P2_12_12_1$	none	none	$P\bar{1}$ $P2_1/c$ C2/*c* P*bca*	none	none	none	none
Space groups of Maximum density	none	C2/*c* $P2_12_12_1$ P*bcn*	P*mc* C*mc* P*nma*	none	F*mm* P*mma* P*mnn*	C2/*m* P*baa* C*mca*	C222 F222 I222 C*cca*	C*mmm* F*mmm* I*mmm*

In some cases the tendency to close pack is offset by an increase in symmetry. Crystals in which the high symmetry of a molecule is coincident with that of the crystal can be somewhat less than closest packed, but will still have a very high packing density. Occupation of a mirror symmetry plane in a crystal by a molecule may cause a decrease of only 0.02-0.03 in the packing coefficient.

Fitting structures with the closest-packed postulate provides an excellent first approximation to the true crystal structure. Kitaigorodsky reported that the overwhelming majority of organic crystals have a packing coefficient from 0.65 to 0.77, or approximately 23-35% free space in their lattices [36]. It is not strictly true, however, that molecular geometry alone determines the structure. Further refinement is possible by examining the internal energy of the solid. Geometric considerations often lead to a set of possible structures of roughly equal high density, one of which will also have the lowest internal energy, corresponding to the true structure.

2.3. Intermolecular Potential Models

Unlike strongly bonded covalent or ionic solids in typical inorganic lattices, dielectric molecular solids are held together by weak intermolecular Van der Waals forces. This attractive force between neutral atoms, irrespective of electrostatic dipole considerations, was first explained by F. London in 1930 [39] as a result of instantaneous multipole moments induced by the positions of primarily outer shell electrons. The average of these fluctuating multipole moments give rise to the overall attractive force. The magnitude of the dipole-dipole interaction energy between 2 atoms varies as the inverse 6th power of the distance between them.

$$U(r) = -\frac{A}{r^6} \qquad \text{[Eq. 2.4]}$$

London demonstrated that A can be calculated from second-order perturbation theory. A can also be approximated from atomic polarizability and ionization potentials [40,41]. Higher order terms can be included from dipole-quadrupole ($-A'/r^8$) and quadrupole-quadrupole ($-A''/r^{10}$) interactions, but with actual intermolecular distances being 3.5-4.0 Å, these interactions fall off too rapidly to be significant when compared with the dipole-dipole interactive forces. London demonstrated that the attractive force between molecules can be calculated by adding pairwise interactions of all the constituent atoms, i.e., the second order perturbation of force is additive. Axilrod and Teller[42] in 1943 examined third order perturbations to the internal energy for rigid inert gas lattices and found them to be nonadditive, but also of negligible consequence in lattice stability. Wojtala [43] found the nonadditive component to be significant for the artificial placement of H-atoms 1 Å or closer, and essentially zero for the realistic distances in liquids and solids of 2 Å or greater.

As atoms approach each other, overlap of occupied electron orbitals occurs and a strong repulsive force develops in accordance with the Pauli exclusion principle. In an effort to characterize the repulsive force, Lennard-Jones [44] found good agreement with experiment for gases with the following equation with m equal to 6 and n varying from 8 to 15:

$$U(r) = -\frac{A}{r^m} + \frac{B}{r^n} \qquad \text{[Eq. 2.5]}$$

Buckingham [45] developed a similar equation using an exponential:

$$U(repulsive) = 6e^{-ar} \qquad \text{[Eq. 2.6]}$$

The repulsive force has not yet been theoretically well-characterized sufficiently to be expressed with one definitive expression, and is usuallly approximated by either B/r^n or $\alpha e^{-r/\rho}$ with empirically determined constants. Hence, a formula for the total interaction potential between two nonbonded atoms can be represented as the sum of the attractive and the repulsive forces where $m = 6$:

$$U(r) = -\frac{A}{r^m} + 6e^{-Br} \quad \text{or} \quad U(r) = -\frac{A}{r^m} + \frac{B}{r^8} \qquad \text{[Eq. 2.7]}$$

These gas phase potential energy equations laid the foundation for theoretical treatment of the molecular solid. Early work was done on the solid state of inert gases and simple molecular crystals such as N_2, O_2, CH_4, and CO_2. Unfortunately, these early models treated the forces as spherically symmetric and radiating from a point at the center of mass of the entire molecule, an approximation which is not sufficiently accurate to describe organic molecular solids.

Theoretical modelling of the energetics of organic molecular solids was first done by treating the nonbonded forces as the sum of atomic potentials for simple hydrocarbons. In 1965 Williams calculated the lattice energy of hydrocarbons using experimentally derived coefficients to the Buckingham potentials and obtained good agreement with measured thermodynamic properties, such as heat of sublimation [46].

2.4. Electrostatic Interactions

These early studies of the lattice energy of organic molecular crystals did not involve dipole-dipole electrostatic interactions. Several investigators such as Kitaigorodsky [47], Craig, Mason, Pauling and Santry [48], and Williams [49], claimed in the sixties, that electrostatic dipoles or quadrupoles contribute very little to the lattice energy. For simple saturated hydrocarbons, this is indeed the case. Allinger's later work in molecular mechanics led to his development of a widely applicable force field derived from a potential energy surface based on internal molecular coordinates and dipole-dipole interactions [50]. He used this program to compare an extensive variety of optimized structures obtained with and without electrostatic dipole interactions to the actual structures. Van der Waals potentials were derived from crystal structures of graphite, diamond, n-hexane, and similar alkanes. Electrostatic dipoles were obtained from *ab initio* calculations. For simple alkanes there was no improvement in fitting the structures with the dipoles, despite the fact that the *ab initio* calculations showed a significant C-H dipole in alkanes.

Efforts to explain the crystal structures of aromatic compounds by Williams, Allinger, and others led to the inclusion of coulombic terms in the potential energy expression.

$$U(coulombic) = +\frac{q_i q_j}{r} \qquad \text{[Eq. 2.8]}$$

For benzene Williams demonstrated in 1974 [51] that it is not possible to explain nature's preference for the herringbone T-shaped crystal structure over the face-to-face stacked arrangement without the inclusion of these electrostatic interactions. Bates and Busing [52] studied hexachlorobenzene, which exhibits a stacked structure. They calculated a difference of 13° in the molecular rotation from the observed structure and a 4° difference in the lattice angle β when the electrostatic term was ignored and an agreement of within 2° for the rotation and 0.2° for β when it was included. In general, inclusion of the coulombic term can often account for 10-15% of the total lattice energy for dielectric molecular solids, resulting in small but significant changes in calculated structure. A difference in structure of this magnitude could have a significant effect on material properties such as conductivity and second order nonlinear optical susceptibility.

In an effort to standardize the hydrocarbon intermolecular potentials, Williams and Starr in 1976 [53] completed a thorough study of a data base consisting of 9 saturated and 9 aromatic hydrocarbons. Assuming spherically symmetric point charges and rigid molecules in which effects due to internal vibrations were ignored, Williams and Starr did not find a significant difference in the repulsive or the Van der Waals potentials between saturated and unsaturated compounds, but confirmed the importance of the coulombic interactions in the overall potential energy. In addition, with the electrostatic term included they

found that the geometric mean combining law holds for the coefficients of the Van der Waals and the repulsion energy terms, so that the overall interaction potential between nonbonded atoms i and j can be expressed as:

$$U(r) = -\frac{a_i a_j}{r_{ij}^6} + b_i b_j e^{-(c_i+c_j)r_{ij}} + \frac{q_i q_j}{r_{ij}} \qquad \text{[Eq. 2.9]}$$

Later Allinger also showed the importance of the coulombic term in the intermolecular potential for unsaturated compounds, justifying the additional parameters and computation time required, and has included this term in his 1988 MM3 force field calculation for unsaturated hydrocarbons [50]. Even though Allinger's 1977 molecular mechanics program, MM2, does not employ electrostatic charges in its energy calculations, it is still in widespread use and gives very good results in the conformational analysis of saturated molecules [54].

For more complex organic molecular solids, such as those containing halogens or heteroatoms, more complicated models have become necessary in order to account for the observed structures and energies. Williams, [55,56] as well as Profeta and Allinger, [57] have obtained reasonable structural fits for crystal lattices of oxygen and nitrogen heterocycles by modelling lone pairs as point charges. For fluorocarbons Williams has included an additional point charge in the carbon-fluorine bond in fluorobenzenes to reproduce experimentally determined structures and heats of sublimation [58].

In recent years other researchers have begun to explore intermolecular potential models other than simple point charges or dipoles. S.L. Price has begun to explore the use of an anisotropic potential model for energy calculations of organic solids [59]. In Price's approach a small molecular fragment is characterized by one anisotropic potential rather than an array of point charges. Methane, for instance would be represented as a single tetrahedral field centered on the carbon atom, instead of five separate point charges. Employing Wigand rotation matrices from angular momentum theory, Price has effectively modelled simple alkanes involving CH_2 and CH_3 fragments [60]. Price has also started pilot studies of the nonspherical potentials of Cl_2 and aromatic nitrogen and carbon in azabenzene [61]. More recent work has shown the role of quadrupolar potentials obtained by *ab initio* calculations in explaining the lattice structures of the diatomic molecules N_2, O_2, F_2, Cl_2, Br_2, and I_2, all of which have a non-spherical distribution of electrons [62]. This anisotropic potential approach does have the advantage of reducing the number of calculations required to characterize the intermolecular interaction vectors. For octane, Price claims her calculation runs 3-4 times faster than the point charge model. At the present time, however, for alkanes this method is no more accurate than electrostatic point charges or dipoles, and has not yet been applied to more complex molecules.

Several groups have obtained intermolecular potential surfaces from *ab initio* SCF calculations [63,64,65]. Potential surfaces between many geometrical configurations of dimers are calculated and then fit to various analytical functions between atoms or site charges in the molecules. For the water dimer, Clementi [63] and coworkers performed SCF-CI calculations on 68 different geometries, and

fit the results to the following expression:

$$\epsilon = q^2\left(\frac{1}{r_{13}}+\frac{1}{r_{14}}+\frac{1}{r_{23}}+\frac{1}{r_{24}}\right)+\frac{4q^2}{r_{78}}-2q^2\left(\frac{1}{r_{18}}+\frac{1}{r_{28}}+\frac{1}{r_{37}}+\frac{1}{r_{47}}\right)$$
$$+ a_1\exp(-b_1 r_{56}) + a_2[\exp(-b_2 r_{13})+\exp(-b_2 r_{14})+\exp(-b_2 r_{23})+\exp(-b_2 r_{24})]$$
$$+ a_3[\exp(-b_3 r_{16})+\exp(-b_3 r_{26})+\exp(-b_3 r_{35})+\exp(-b_3 r_{45})]$$
$$- a_4[\exp(-b_4 r_{16})+\exp(-b_4 r_{26})+\exp(-b_4 r_{35})+\exp(-b_4 r_{45})] \qquad \text{[Eq. 2.10]}$$

using the distances r_{ij} and point charges q defined in Figure 2.6.

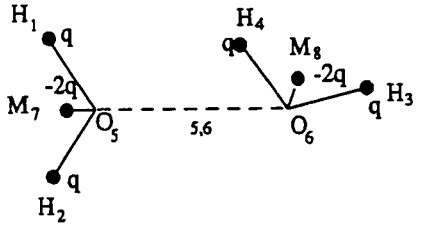

Fig. 2.6 Definition of the distances used by Clementi and coworkers in the water dimer calculation as shown in Equation 2.10.

For water dimers, benzene dimers, and water-benzene interactions, Karlström *et al.* used the expression below to describe the pair-wise interactions between atoms i and j in different molecules:

$$E = \sum_{ij}\left[\frac{A_{ij}}{r_{ij}}+\frac{B_{ij}}{r_{ij}^4}+\frac{C_{ij}}{r_{ij}^6}+\frac{D_{ij}}{r_{ij}^9}+\frac{E_{ij}}{r_{ij}^{12}}\right] \qquad \text{[Eq.2.11]}$$

Fraga proposed a similar model for benzene intermolecular interactions using a similar expression:

$$E = \sum_{ij}\left[\frac{A_{ij}}{r_{ij}}+\frac{B_{ij}}{r_{ij}^4}+\frac{C_{ij}}{r_{ij}^6}+\frac{D_{ij}}{r_{ij}^{12}}\right] \qquad \text{[Eq. 2.12]}$$

The *ab initio* calculations of nonbonded interactions require extensive basis sets, configuration interaction, and inclusion of correlation effects, and can therefore be performed on small molecules only. Semi-empirical methods are not adequate for these nonbonded interactions, as the errors due to correlation effects are often greater than the magnitude of the energy of the Van der Waals interaction [66].

One of the most successful models to date for Van der Waals interactions is Distributed Multipole Analysis (DMA) developed by A.J. Stone, [67] and applied to Van der Waals complexes by Buckingham and Fowler [68,69]. In DMA the attractive potential is due solely to electrostatic interactions arising between multipole expansions placed at atomic nuclei and in bonds. Closed shell repulsions are represented by hard-sphere constraints at the Van der Waals radii reported by Pauling [32]. The anisotropy of the molecular charge distribution can be adequately represented by the distribution of point monopoles, dipoles, and quadrupoles. A lone pair or a bonding pair of electrons can be represented by a dipole located at the atomic center. The two lone pairs on an oxygen atom in H_2O are represented by an atomic quadrupole. The π-electron distribution in a double bond can be approximated by a point quadrupole located at the bond center.

The distributed multipoles are calculated from *ab initio* wavefunctions. The best results have been obtained using very extensive gaussian basis sets, configuration interaction, and correlation effects at the second order Møller-Plesset level. The inclusion of correlation energy essentially describes the attractive force due to dispersion. All basis sets are at least double-zeta-plus polarization quality, and as such cannot be applied to very large systems. For example, for the HF $\cdots$ HF Van

der Waals complex contracted basis functions were necessary: 11s7p3d/6s2p→ 7s5p3d/4s2p [69]. The DMA point multipoles so obtained converge within the boundaries of the molecular charge distribution.

Buckingham and Fowler have obtained good qualitative, as well as quantitative agreement, with experimental geometries of gas phase Van der Waals complexes. DMA has not yet been applied to solids.

2.5. Predicting Crystal Structure - Progress in the Field to Date

Overall, considerable progress has been made in quantifying the weak non-bonded forces between organic molecules which determine the structure of the crystal solid. In recent years this progress, both in Van der Waals and electrostatic interactions, has begun to be applied towards the *a priori* prediction of crystal structure of organic molecular solids. At present, the Van der Waals radius hard-sphere model of intermolecular interactions is used primarily for conformational analysis of gas phase organic molecules. Small neutral organic molecules can be conformationally optimized by visual inspection using computer graphics, or by simple distance geometry calculations. In addition, the geometric approach has been applied to large biopolymers, such as proteins and nucleic acids, which can be manipulated into favorable conformations using complicated computer graphics routines for inspection and analysis of possible drug-receptor or enzyme-substrate docking sites [70].

Several programs are currently available for the calculation of molecular energies and structures by *ab initio* or semi-empirical methods such as Gaussian-90, [71] HONDO,[72] MOPAC, [73] CHARMm, [74] Sybil, [75] MM2, [54] and MM3 [50]. These programs are primarily used for gas phase structure determination, molecular modelling, and conformational analysis. Some of these programs, such as MM3, can also perform energy calculations on small gas phase clusters, such as dimers and trimers, when the user supplies the relative orientations of the molecules in space. These cluster calculations can be used to estimate the preference for one geometric orientation over another, i.e., the benzene dimer in a parallel or perpendicular configuration, but are not intended to model actual crystalline solids nor calculate lattice energies.

Some of the early lattice energy calculations on organic molecular solids were performed by Williams to aid in locating molecules in the unit cell from diffraction data and to check the plausibility of X-ray structural refinements [76]. Williams' program, PCK83, [77] optimizes the molecular orientation within an assumed space group by minimizing the lattice energy based on experimentally determined parameters. In order to perform a structure optimization via energy minimization, PCK83 requires the user to input the space group symmetry, the number of molecules per unit cell, the molecular coordinates and inital rotations and translations, the lattice constants, and atomic electrostatic charges. Given this information, PCK83 can then calculate a structure having a minimum energy. In the absence of experimental data, however, PCK83 provides no information as to whether the minimum obtained is a local one, or is the global minimum most likely corresponding to the true structure. The same problem with multiple minima arises if one uses PCK83 to perform cluster calculations with no assumed

symmetry. For crystal lattices, if the input deviates slightly from the actual values, the calculation can easily become trapped in a local minimum and give a misleading result. In addition, we determined that if the crystal structure is initially expanded to a point where the molecules are free to rotate, PCK83 is then unable to contract the lattice to find a stable minimum. If the material being studied is known and has an experimentally determined heat of sublimation, then the energy minimum obtained can be compared to the true lattice energy. To obtain a useful structure prediction using PCK83, one must already know, to within a high degree of certainty, what that structure already is, as in X-ray diffraction structural refinements.

Working towards the goal of *a priori* crystal structure prediction, Gavezzotti and Desiraju have investigated the relationship between the molecular geometry of fused-ring aromatic hydrocarbons and their crystal packing environment [78]. In their examination of experimental crystal structures, they found that planar aromatics with similar geometry exist in the same type of closest packed clusters within different crystalline polymorphs with their different space group symmetries. Athough the lattice energies were calculated using the Mirsky [79] nonbonded potentials instead of those of Williams, to be consistent with their previous statistical work, Gavezzotti and Desiraju maintain that their results on this class of hydrocarbons can withstand any reasonable change in nonbonded parameters.

Another approach to predicting the crystal structure of molecular solids is to model the process of crystallization using cluster calculations. Williams [80], van de Waal [81], and Oikawa *et al.* [82], have performed cluster calculations on benzene. Williams examined clusters ranging in size from 2 to 15 molecules using the exp-6-1 pair potentials which he developed for his work in crystal calculations. Clusters of size N were built up by adding two molecules to the previously optimized (N-2)-molecule cluster. The initial positions of the two additional molecules were determined by inspection. All molecular coordinates (positions and rotations) were allowed to vary about a center of inversion. Two stable configurations were found for the cluster of 13 molecules, which is, in effect, a central molecule surrounded by a complete coordination sphere. In all clusters, the preference of benzene to pack edge-to-face was apparent, but intermolecular distances and angles differed markedly from those observed in the solid state. Due to computational limitations, Williams was not able to evaluate larger clusters.

To investigate the effect of cluster size on the accuracy of structure predictions, van de Waal chose the initial configuration of a tridecamer cluster to be the actual positions of the molecules in the crystal lattice. Using Williams' pair potentials, van de Waal found considerable relaxation of the structure in the cluster, and concluded that for this type of cluster calculation to be effective, all molecules in the first coordination sphere should experience the same environment as the reference molecule, as is the case in the crystal.

Oikawa *et al.* performed calculations on larger benzene clusters of up to 42 molecules using the potential function R(1-4-6-12) proposed by Fraga [65]. Oikawa *et al.* constructed a monolayer of 42 molecules by performing a full optimization of 5(N-1) variables after the addition of each new molecule. Searching for different configurational possibilities was performed manually. The monolayers reproduced the herringbone edge-to-face configuration, although the orientation differed from that observed in the crystal (Fig. 2.7).

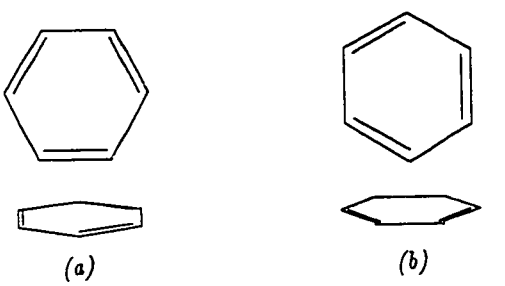

Fig. 2.7 (a) The orientation of benzene observed in the crystal. (b) Orientation obtained in the monolayer calculations of Oikawa *et al.*

The structure obtained in the central portion of the monolayer was then used to build up a three-dimensional model of a crystal. Structures consisting of three layers of up to 9, 16, and 9 molecules were subject to full optimization, and qualitative agreement with experiment was obtained. The orientation of the benzene molecules changed to the proper orientation shown in Figure 2.7.a. To obtain quantitative agreement with experimental crystal structure, however, Oikawa *et al.* maintain that cluster calculations of 168 molecules, arranged in layers of 16, 36, 64, 36, and 16 molecules, would be necessary. They were unable to perform these calcuations on larger clusters due to economic and computational limitations.

In general, cluster calculations are useful for obtaining qualitative information about the crystal packing of small, symmetric molecules such as benzene. Due to current computational limitations, however, these calculations would not be feasible for larger, asymmetric molecules. In addition to the fact that there are more atoms per molecule which necessitates smaller cluster size, larger asymmetric molecules are much more likely to become trapped in local minima, making it difficult to set up alternate configurations by inspection alone. Another difficulty arises in that the minimum energy configuration obtained in a cluster calculation may not exhibit the translational symmetry consistent with the crystal lattice.

Chapter 3 Methodology

3.1. Overview

Despite the recent advances in intermolecular potential models, there has not been until now a program which will produce a comprehensive list of the most probable crystal structures, for a given molecule. Calculating and minimizing energy over several unit cells or within a large cluster can be done quite readily for simple systems with only a few atoms. When one has dozens of atoms per molecule and several molecules per unit cell, however, the calculation rapidly becomes prohibitively expensive and time consuming. If significant coulombic forces are present the problem is compounded further, because the electrostatic energy between monopoles decreases only as $1/r$ and requires a long time to calculate, even with accelerated convergence methods. Even so, it is possible to perform energy minimizations on a few trial structures in a reasonable amount of time on the fastest computers that are available today. The main difficulty is that calculating a few trial structures is not sufficient to ensure that one has found the global minimum, and has not been caught in one of many local minima.

We have developed a novel approach to the prediction of crystal structures of organic molecular materials which circumvents the above difficulties by using a series of successive approximations to focus on structures of high probability without performing a search of a near infinite number of configurations by brute force. The principal assumptions are as follows:

- The molecular solid will be crystalline.
- The molecules will be closest-packed.
- Van der Waals pair potentials can be used to approximate the closest-packed configuration within a space group.

- The closest-packed structures form a good starting point for more sophisticated and complete energy calculations to determine the structure with the lowest energy and with the highest probability of being the observed structure.

The justifications for these assumptions will be presented in subsequent sections.

3.2. Assumption of Crystallinity

At first glance, it may appear that there must be an infinite number of ways molecules can be arranged to form a solid. For amorphous materials such as glasses, this is true. Amorphous materials may experience some very short range order, but any long range order is nonexistent and the molecular orientation is random. It is estimated that 70% [36] of organic materials, however, are not amorphous and do crystallize in one of the 230 space groups. Therefore, our first refinement in predicting a structure is to to assume that the material will be crystalline. During the energy minimization process, the molecules are constrained to move in accordance with specific symmetry operations, thus eliminating translational and rotational degrees of freedom for all but the reference molecule. The maximum number of variables in the energy minimization process is twelve: three rotational and three translation degrees of freedom for the reference molecule, as well as the magnitude and direction of each of the three lattice vectors. This maximum of twelve variables is in stark contrast to the 6(N-1) variables required in the cluster calculations of N molecules performed by Williams, van de Waal, Oikawa, and others.

3.3. Most Probable Space Groups

Imposing the condition of crystallinity on the structure of the molecular solid reduces the number of possible configurations from infinity to a finite number within the 230 space groups. Unfortunately, within each space group there are still many orientational degrees of freedom possible within a given set of symmetry constraints. Figure 3.1 shows two very different crystal structures, both of which are consistent with the symmetry of the 2-dimensional space group. We estimate that a reasonably fine search mesh for a large asymmetric molecule in a given space group consists of 10^6 orientations. Therefore, searching all 230 space groups would not be feasible.

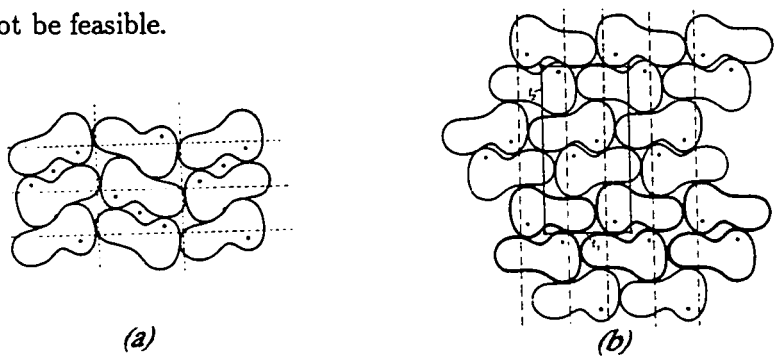

Fig. 3.1 Two different crystal structures possible in one space group. (a). Molecules lie simply along two perpendicular glide lines. (b). Molecules have been paired about an inversion center, and the pairs have been arranged according to the symmetry operations of the space group.

In most of the 230 possible space groups, however, it is not possible to arrange the molecules so that there are no large gaps or holes in the structure. Symmetry features, such as mirror planes, create these gaps in the crystal structure when filled with irregularly-shaped molecules (see Section 2.2). Large open spaces are not observed as periodic features in crystal structures in nature. Van der Waals forces are non-directional and the attractive energy is greatest when

the molecules are packed as closely as possible. Therefore, large gaps created by certain symmetry conditions are energetically unfavorable and will not occur.

According to the theory of Kitaigorodsky, which was presented in more detail in Section 2.2, molecules tend to pack so that the protrusions on one molecule fall into to hollows of another. Kitaigorodsky determined that this close-packing of organic molecules is possible in only 13 of the 230 possible space groups. Kitaigorodsky's theory is supported by experimental evidence. Of the 29,059 organic compounds whose crystal structures were determined prior to 1981, 75% crystallized in one of only five space groups.[83] These five groups, shown in Table 3.1, are the space groups which facilitate closest packing along all three lattice vectors. More than half of the 230 possible space groups were rarely observed (Table 3.2).

Table 3.1 Five most common space groups comprising 75% of all structures [83].

Space group	Frequency
$P2_1/c$	36.0%
$P\bar{1}$	13.7%
$P2_12_12_1$	11.6%
$P2_1$	6.7%
$C2/c$	6.6%

Table 3.2 Infrequently observed space groups[83].

Number of space groups	Occurences within space group
117	< 5
29	1
35	0

Reducing the number of possible space groups from 230 to the 13 listed in Table 2.2 is the next major step in the refinement process for predicting crystal structures. Hence, we not only limit our search by constraining molecules to move in a symmetrical manner during the energy minimization process, but we

only allow those symmetry elements which give us the best chance of obtaining a closest-packed structure.

3.4. Close-Packing the Structure

The 13 most probable space groups must be searched systematically for the lowest energy configurations. The search space is still too large to use the most sophisticated methods available to calculate the intermolecular interactions and minimize the energy, and the following assumptions are made to simplify the calculation at this stage of refinement:

- The crystal structure will be closest-packed.
- The molecules are assumed to be completely dielectric.
- Intermolecular electrostatic interactions are ignored.
- Thermal effects are ignored. The structures are considered to be at absolute zero.
- No many body effects are considered.
- The molecule is rigid and will exist in its optimized gas-phase conformation.

Several methods were evaluated to determine the most efficient way to close-pack the crystal structure. One approach was to use a hard-sphere model with the repulsive potential approximated by a step function (Fig. 3.2) in which the interaction potential between two nonbonded atoms is zero until the interatomic distance is less than a specific cutoff value r_c.

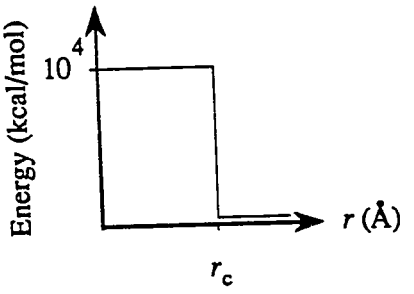

Fig. 3.2 The repulsive potential of the hard-sphere model. For values of r, the internuclear separation, less than the cutoff radius r_c, the potential is assigned an arbitrarily large number to represent an essentially infinite repulsion energy.

The attractive part of the potential could then be represented by a $-1/r^6$ term or simulated by minimizing the volume or maximizing the packing index. There are several difficulties with the hard-sphere model. One problem is that the IF/THEN search required of all nonbonded interatomic distances and the assignment of a potential value at an arbitrary cutoff point does not vectorize on the Cray Y-MP and is exceedingly slow. In addition, a step function is not well-behaved nor smoothly varying and does not lend itself to efficient minimization due to a discontinuity in the derivative at $\sigma = r_c$. The value of the total interaction function can vary wildly with very small shifts in molecular positions. Lastly, it does not allow for realistic situations in which a few atoms may be crowded if the total energy of the crystal is very favorable.

The other methods investigated for efficient close-packing were based on Van der Waals pair potential energy functions. As was discussed in Section 2.3, one of the two most common Van der Waals potential energy functions was proposed by Lennard-Jones, and can be expressed as:

$$E_{ij} = 4\epsilon_0 \left[\left(\frac{\sigma_{ij}}{r_{ij}} \right)^{12} - \left(\frac{\sigma_{ij}}{r_{ij}} \right)^{6} \right] \qquad \text{[Eq. 3.1]}$$

between two atoms i and j separated by distance r_{ij}, where ϵ_0 is the depth of the potential well, and σ_{ij} is the internuclear separation for which the interaction energy is zero. The other common Van der Waals pair potential function, proposed by Buckingham, is:

$$E_{ij} = \frac{A_{ij}}{r_{ij}^6} + B_{ij} \exp^{-\alpha_{ij} r_{ij}} \qquad \text{[Eq. 3.2]}$$

where A_{ij} is equivalent to $4\epsilon_0\sigma_{ij}^6$ above, and B_{ij} and α_{ij} are repulsion parameters. The Lennard-Jones and the Buckingham potential energy functions do not suffer from most of the difficulties encountered with the hard sphere model. Both functions are 'softer' than the repulsions in the hard-sphere model, and can accommodate a few crowded atoms. As can be seen by the plots of these potentials in Figures 3.3-5, they are also well-behaved and smoothly varying throughout their range, with the exception of a singularity at r equal to 0. Either function can reproduce the shape and the depth of the potential minimum (Fig. 3.5), but the Lennard-Jones function has the advantage of being an order of magnitude quicker to calculate. Calculating the Buckingham potential is slower because the value of the function goes to negative infinity at r equals 0 (Figure 3.6), and requires a cutoff radius r_c, below which the potential is assigned an arbitrarily high value. A typical cutoff radius for a C-C interaction, for example, would fall in the range 1 - 1.5 Å. In addition, calculating the repulsive term for the Buckingham potential requires calling both the square root and the exponential functions for every atom-atom pair, which are exceptionally time-consuming to calculate. Calculating the repulsive term for the Lennard-Jones potential, however, involves simply adding the square of the attractive term. Overall, we find that the Lennard-Jones pair potentials are approximately 95 times faster to calculate on the Cray Y-MP

than the Buckingham potentials, and hence are used to close-pack the molecules within the 13 most probable space groups.

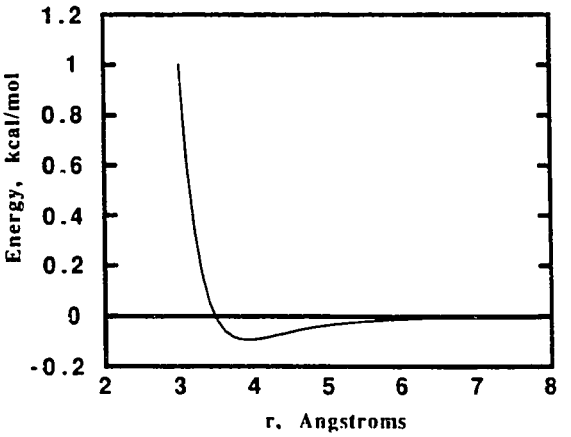

Fig. 3.3 Buckingham potential energy curve for the C-C Van der Waals interaction from Williams' program PCK83. $A = 583.12$ kcal/mol, $B = 88370.8$ kcal/mol, $\alpha = 3.6\mathring{A}^{-1}$.

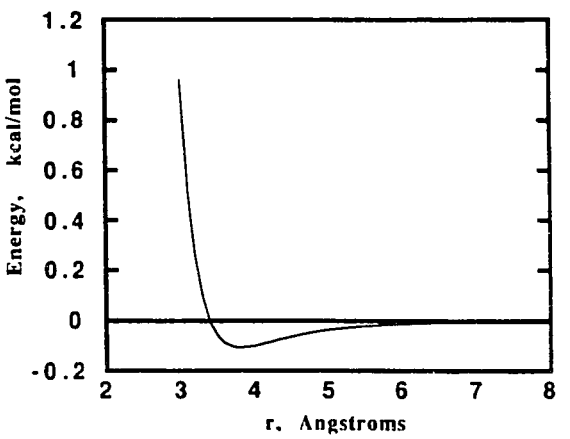

Fig. 3.4 Lennard-Jones potential energy curve for the C-C Van der Waals interaction (this work). $4\epsilon_0 = 0.4309$ kcal/mol, $\sigma = 3.388$ Å.

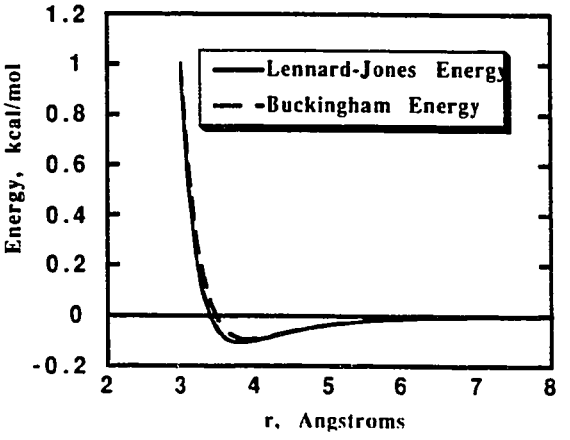

Fig. 3.5 Comparison of the Buckingham (dashed line) and Lennard-Jones potential energy curves shown in Figs. 3.3 and 3.4.

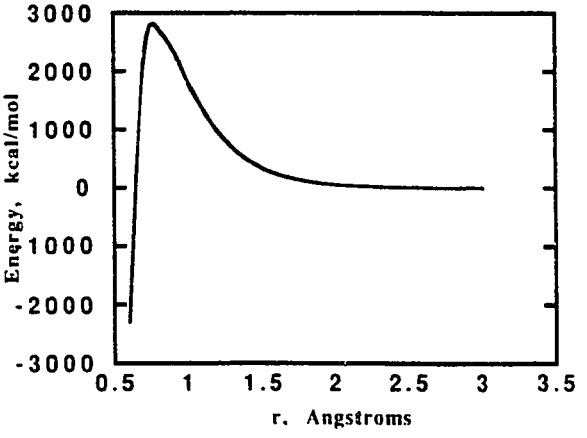

Fig. 3.6 The behavior of the Buckingham potential energy function, shown in Figure 3.1, as the internuclear separation goes to zero.

3.5. Parameterization

The desire among many researchers has been to find one set of universally transferable empirical pair potentials to describe intermolecular Van der Waals interactions. Many sets have been developed, and although they are fairly similar in many ways, there has not been general agreement on the values of these parameters. Table 3.4 shows the variety of Van der Waals radii proposed for unsaturated hydrocarbons. Perhaps most unusual are the parameters proposed by Momany, Vanderkooi and Scheraga [84], who studied benzene at three different temperatures, and claim that no potential minimum is necessary between unsaturated carbon atoms. If these potentials were applied to graphite, or a similar structure with parallel aromatic planes, the individual species or planes would fly apart to infinite separation.

Most of the recent work on parameterization has been done using the Buckingham expression (Eq. 3.2) for the Van der Waals potential energy. To obtain Lennard- Jones parameters for our work, we fit the σ and ϵ shown in Equation 3.1 to lowest temperature structures available for the aromatic hydrocarbons benzene, naphthalene and anthracene. The parameters were varied to obtain a least-squares fit to the lattice constants when used in ICE9. σ_{CH} is the sum of σ_H and σ_C and ϵ_{CH} is the geometric mean of ϵ_C and ϵ_H. These values are shown in Table 3.3.

Table 3.3 Lennard-Jones parameters used in ICE9. σ is the interaction radius and ϵ is the well-depth of the potential energy minimum.

Bond Type	σ	ϵ
C···C	3.388	0.1232
C···H	2.544	0.1208
H···H	2.966	0.1220

Table 3.4 Van der Waals Radii for Unsaturated Hydrocarbons

Source	H···H	H···C	C···C
Momany [84]	2.786 2.682 2.610	2.930 2.851 2.727	No minimum
Kitaigorodsky [36]	2.60	3.15	3.80
Mirsky [79]	2.80	3.30	3.80
This Work	2.85	3.32	3.79
MM2 [54]	3.00	3.44	3.88
Williams [53]	3.18	3.56	3.93
MM3 [50]	3.24	3.58	3.92

3.6. Multiple Minima

The main obstacle to finding an absolute minimum is the barrier of rotation. The various space groups have different numbers of parameters which can vary and hence have different likelihoods of multiple minima. For a given space group, the greater the number of variable lattice parameters, the higher the likelihood that a large number of multiple minima exists.

In 1969 Williams reported results concerning local minima using energy minimization for packing analysis of several aromatic compounds.[76] Williams employed starting rotations of $\pm 20°$ and $\pm 60°$ about each of the three axes to generate 12 trial models within the correct space group for each substance. Two of the compounds he studied, benzene and naphthalene, both crystallize in centric space groups and do not require initial translation for special positions. For benzene, all 12 models converged to the correct structure, and for naphthalene, 2 out of the 12 converged to the experimental structure. Phenanthrene, which

crystallizes in an acentric space group, required 2 molecular translations as well as 3 rotations and yielded a large number of false minima, yet convergence to the correct structure occurred in as many as four out of 12 trials for each initial translation. Price,[59] using the Modified Rosenbrock Search Method, as in *WMIN*,[85] optimized structures for diatomics in space groups *Cmca* starting with angular rotations of 15°, 30°, and 60° degrees and obtained the global minimum in at least one trial for each type of molecule. The number of rotations of trial starting positions required to generate a complete search space is dependent upon the molecular symmetry. Our work, as well as that of Williams and Price, indicates that for even the very worst case of an asymmetric molecule, sucessive runs with initial molecular positions rotated by 15° should suffice to ensure a complete search space. The higher the symmetry, or the fewer the protrusions, the fewer the number of rotation increments required.

3.7. Additional Refinements

Using Van der Waals pair potentials to close-pack the molecules is intended as a rough approximation with broad applications. The methodology presented up to this point is very general and can be applied to any organic molecular solid. For many systems, such as simple alkanes, this may even be sufficient for a good structure prediction. For most other systems, however, more complicated energy calculations are required and further refinement is necessary. Intermolecular electrostatic interactions in particular, which have been previously ignored, should be considered to determine which closest-packed configuration has the lowest energy. For example, without considering electrostatic interactions, benzene would be predicted to crystallize in the slipped-stack of pancakes configuration rather

than in the observed edge-to-face, herringbone structure. Various methods of calculating the electrostatic energy were evaluated to determine which, if any, were fast enough to be performed on every closest-packed structure before the final predictions are made. The details of these calculations are presented in the next chapter.

Chapter 4 Electrostatic Energy of the Lattice

The importance of the electrostatic contribution to the cohesive energy of organic molecular solids varies considerably with the type of molecule. For simple saturated alkanes, such as hexane, the electrostatic contribution is negligible. For neutral dielectric molecules with significant dipole or quadrupole moments, such as aniline or benzene, the electrostatic energy may account for 10 to 25% of the total lattice energy. In the case of the charge-transfer materials, such as TTF-TCNQ, the electrostatic energy becomes dominant and comprises 85% or more of the binding energy.

The electrostatic potential of a molecule is a rigorously defined property which can, in principle, be calculated exactly from the molecular wavefunctions Ψ_i. The molecular potential can be expressed as:

$$V(\vec{r}) = \sum_A \frac{Z_A}{|\vec{R}_A - \vec{r}|} \int \frac{\rho(\vec{r'})}{|\vec{r'} - \vec{r}|} d\vec{r'} \qquad \text{[Eq. 4.1]}$$

where Z_A is the nuclear charge of atom A located at $\vec{R}_A$, and $\rho(\vec{r'})$ is the electron density at point $\vec{r'}$. The electron density is calculated from the molecular orbitals as follows:

$$\rho(\vec{r'}) = \sum_i N_i \Psi_i^*(\vec{r'}) \Psi_i(\vec{r'}) \qquad \text{[Eq. 4.2]}$$

where N_i is the number of electrons in molecular orbital i . Realistically, it is not possible at the present time to calculate the electrostatic energy exactly from *ab initio* wavefunctions for a molecular solid, and therefore approximations must be used. There are four types of models used to approximate the molecular charge distribution. In one model, the charge distribution is considered as a group of discrete point charges usually, but not necessarily, located at the atomic nuclei. Another approach, very similar to the point charge method, is the bond or group dipole model in which the electron distribution is described by point dipoles located in bonds between the atoms in the molecule. Third, the charge distribution is described by multipole expansions about atomic centers. Lastly, the charge distribution of the molecule is expressed in a molecular multipole expansion. These methods of approximating the electrostatic interactions were examined to determine if any were fast enough to be performed on every closest-packed structure in order to refine the final sorting process. The merits of these approaches are discussed with respect to their accuracy and efficiency.

4.1. Background and Theory of Electrostatic Interactions

The potential of a point charge q located at the origin is given by:

$$\Phi = \frac{kq}{r} \qquad \text{[Eq. 4.3]}$$

where k is a proportionality constant which depends on the system of units used, and r is the distance from the origin. The electric field can then be expressed as:

$$\vec{E} = -\vec{\nabla}\Phi = -\hat{x}\frac{\partial\Phi}{\partial x} - \hat{y}\frac{\partial\Phi}{\partial y} - \hat{z}\frac{\partial\Phi}{\partial z} \qquad \text{[Eq. 4.4]}$$

where $\hat{x}, \hat{y}$, and $\hat{z}$ are the unit vectors in the x, y and z directions. Combining Eqs. 4.3 and 4.4 yields an expression for the cartesian components of the electric field:

$$\vec{E} = -\frac{kq}{r^2}[\hat{x}\frac{x}{r} + \hat{y}\frac{y}{r} + \hat{z}\frac{z}{r}] \qquad \text{[Eq. 4.5]}$$

If the point charge is not located at the origin, but is at $\vec{r'}$, then the potential at the observation point $\vec{r}$ due to the point charge is given by:

$$\Phi = \frac{kq}{|\vec{r} - \vec{r'}|} \qquad \text{[Eq. 4.6]}$$

For a system of charges the potential is given by:

$$\Phi_{Total} = k\sum_i \frac{q_i}{|\vec{r} - \vec{r_i'}|} \qquad \text{[Eq. 4.7]}$$

Similarly for a continuous charge distribution $\rho(\vec{r'})$ the potential seen at point $\vec{r}$ is:

$$\Phi_{Total} = k\int_{all\ space} \frac{\rho(\vec{r'})}{|\vec{r} - \vec{r'}|} d^3r' \qquad \text{[Eq. 4.8]}$$

The quantity $\frac{1}{|\vec{r}-\vec{r'}|}$ can be expanded in spherical coordinates in terms of the spherical harmonics $Y_{lm}(\theta, \phi)$.

$$\frac{1}{|\vec{r} - \vec{r'}|} = 4\pi\sum_{l=0}^{\infty}\sum_{m=-l}^{l} \frac{1}{2l+1}\frac{r_<^l}{r_>^{l+1}} Y_{lm}^*(\theta', \phi')Y_{lm}(\theta, \phi) \qquad \text{[Eq. 4.9]}$$

where $r_<$ is the smaller of $|\vec{r}|$, $|\vec{r'}|$, and $r_>$ is the larger of these. Combining these expressions yields

$$\Phi(\vec{r}) = \sum_{l=0}^{\infty}\sum_{m=-l}^{l} \left[Y_{lm}^*(\theta', \phi')r'^l\rho(\vec{r'})\right]\frac{Y_{lm}(\theta, \phi)}{r^{l+1}} \qquad \text{[Eq. 4.10]}$$

for the potential outside of the charge distirbution where $r_< \equiv r'$ and $r_> \equiv r$. The coefficients in the square brackets are called the multipole moments q_{lm}:

$$q_{lm} = \int Y^*_{lm}(\theta', \phi') r'^l \rho(\vec{r}') d^3 r' \qquad \text{[Eq. 4.11]}$$

The spherical harmonics $Y_{lm}(\theta, \phi)$ may be expressed in terms of the associated Legendre polynomials $P_l^m(\cos\theta)$:

$$Y_{lm}(\theta, \phi) = \sqrt{\frac{2l+1}{4\pi}\frac{(l-m)!}{(l+m)!}} P_l^m(cos\theta) e^{im\phi} \qquad \text{[Eq. 4.12]}$$

where

$$P_l^m(x) = \frac{(-1)^m}{2^l l!}(1-x^2)^{m/2}\frac{d^{l+m}}{dx^{l+m}}(x^2-1)^l \qquad \text{[Eq. 4.13]}$$

To calculate the energy between two charge distributions, a and b, it is convenient to express their orientations in a coordinate system in which their z-axes are coincident and the x- and y-axes are parallel (Fig. 4.1).

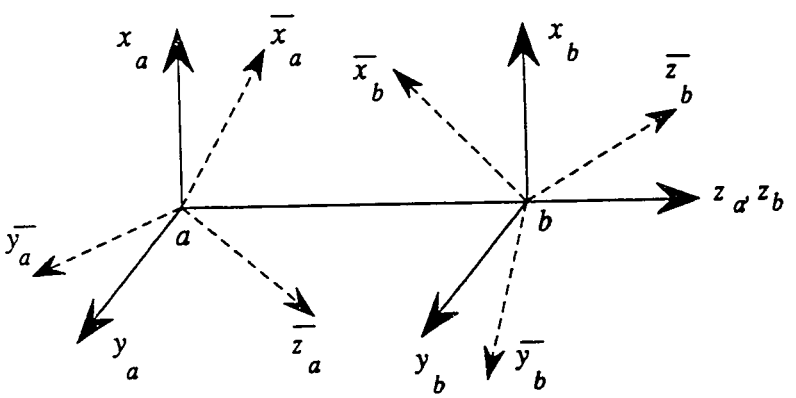

Fig. 4.1 Coordinate systems used to calculate multipole interactions between charge distributions a and b.

If these charge distributions do not overlap, the potential energy between them can be expressed as:

$$\phi_{ab} = \sum_{n_a=0}^{\infty} \sum_{n_b=0}^{\infty} \sum_{m=-n_<}^{+n_<} \frac{(-1)^{n_b+m}(n_a+n_b)!}{(n_a+|m|)!(n_b+|m|)!} \frac{1}{r_{ab}^{n_a+n_b+1}} Q_{n_a}^{m^*} Q_{n_b}^{m} \qquad \text{[Eq. 4.14]}$$

where n_a, n_b are the orders of the multipoles (0 = monopole, 1 = dipole, 2 = quadrupole, etc.), $n_<$ is the smaller of n_a, n_b, and $Q_{n_a}^m*$ and $Q_{n_b}^m$ are the multipole moments expressed as spherical harmonics. According to Hirschfelter [86], the quantities Q_n^m correspond to the tensor elements of the various multipole moments in cartesian coordinates as follows:

$$\begin{aligned}
C &= Q_0^0 \\
\mu_z &= Q_1^0 \\
\mu_x &= \tfrac{1}{2}[Q_1^1 + Q_1^{-1}] \\
\mu_y &= \tfrac{1}{2i}[Q_1^1 - Q_1^{-1}] \\
Q_{zz} &= 2Q_2^0 \\
Q_{xx} &= -Q_2^0 + \tfrac{1}{4}[Q_2^2 - Q_2^{-2}] \\
Q_{yy} &= -Q_2^0 - \tfrac{1}{4}[Q_2^2 - Q_2^{-2}] \\
Q_{xz} &= \tfrac{1}{2}[Q_2^1 + Q_2^{-1}] \\
Q_{yz} &= \tfrac{1}{2i}[Q_2^1 - Q_2^{-1}] \\
Q_{xy} &= \tfrac{1}{4i}[Q_1^2 - Q_1^{-2}]
\end{aligned} \qquad \text{[Eq. 4.15]}$$

The multipole moments in cartesian coordinates on the left-hand side of the equations above (μ_i or Q_{ij}) can be calculated as follows:

$$Q_{ij} = \int (\vec{x}_i \vec{x}_j - \tfrac{1}{3} r^2 \delta_{ij}) \rho(\vec{x}) d^3x \qquad \text{[Eq. 4.16]}$$

where $\vec{x}$ is the position vector of the charge, r is the distance from the origin, δ_{ij} is the Kronecker delta function, and $\rho(\vec{x})$ is the charge density at $\vec{x}$. The $\vec{x}_i\vec{x}_j$ terms can be obtained from the Gaussian 90 *ab initio* quantum chemistry program, and the Q_{ij} calculated by subtracting $\frac{1}{3}r^2\delta_{ij}$. Solving for the Q_n^m in terms of the μ_i or Q_{ii} yields:

$$
\begin{aligned}
Q_0^0 &= q \\
Q_1^1 &= -[\mu_x - i\mu_y] \\
Q_1^0 &= \mu_z \\
Q_1^{-1} &= \mu_x + i\mu_y \\
Q_2^0 &= \frac{1}{2}Q_{zz} \\
Q_2^1 &= -[Q_{xz} - iQ_{yz}] \\
Q_2^2 &= Q_{xx} - 2iQ_{xy} - Q_{yy}
\end{aligned}
\qquad \text{[Eq. 4.17]}
$$

The quadrupole tensors are symmetric, so that $Q_{ij} = Q_{ji}$. q is the total charge of the molecule or charge distribution.

4.2. Point Charge Model

Whereas the electrostatic potential of a molecule is a rigorously defined property, condensing the charge distribution, calculated from the molecular wavefunctions, into a relatively small number of point charges is not an exact procedure. Calculating the point charges depends heavily on the basis set used and how the electron density in the overlap matrix is proportioned between atoms of different atomic number. A wide variety of methods have been used to calculate the partial atomic point charges.[87-102] The most common method is Mulliken Population Analysis (MPA) [88], in which the electron density on an atom is determined

from the coefficients of the occupied atomic orbitals in the MO wavefunctions. The effect of the choice of basis set and SCF method [see Appendix B] on the partial charges from MPA can be seen in Table 4.1, where the charges on hydrogen in benzene range from 0.020 to 0.240 *e*.

Table 4.1 Partial charge on hydrogen in benzene from various Mulliken population analyses.

Method	δ (H)
CNDO	0.020*e*
MNDO	0.056
AM1	0.195
STO-3G	0.067
3-21G	0.240
6-311G	0.162
6-311G*	0.222
6-31G**	0.146
6-31+G	0.229

Attempts have been made to reduce the variability introduced through the use of different basis sets by linearly scaling the partial charges to be consistent with experimental dipole moments. Momany scaled the minimal basis sets STO-3G and 4-31G and obtained similar atomic partial charges for formamide, methanol, and formic acid for molecular mechanics application in biomacromolecules. This approach, however, assumes that the only difference between partial charges from different basis sets is a constant multiplicative factor, and does not account for differences in molecular polarization which could result from configuration interaction when using more extensive basis sets [100].

Point charges can be placed on sites other than at the nuclei. Rather than partitioning the overlap density between the atoms, a point charge can be placed within the bond itself [103,104]. In addition, lone pairs in heteroatoms can also be represented by point charges [87,88,105] A fluorine atom, therefore, can be represented by 5 point charges as Williams has done (Fig. 4.2) [105].

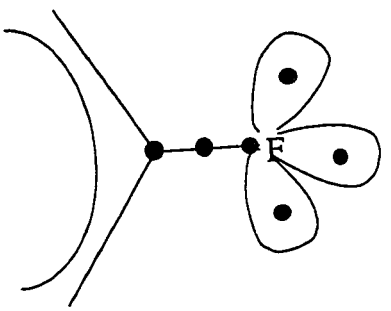

Fig. 4.2 Williams representation of the charge distribution of fluorine in fluorobenzene as 5 point charges.

4.3. Lattice calculations using point charges

If point charges are used and the electrostatic energy is calculated by direct summation, a cutoff radius of greater than 100 Å is required to achieve convergence of the $1/r$ term. To investigate the behavior of the $1/r$ term in a solid such as benzene, where the magnitude of the point charges is relatively small, the coordinates of all atoms in 13 × 13 × 13 unit cells were determined, and the electrostatic energy was calculated using successive cutoff radii from 3 Å to 40 Å about each atom in the central molecule. The results are shown in Fig. 4.3.

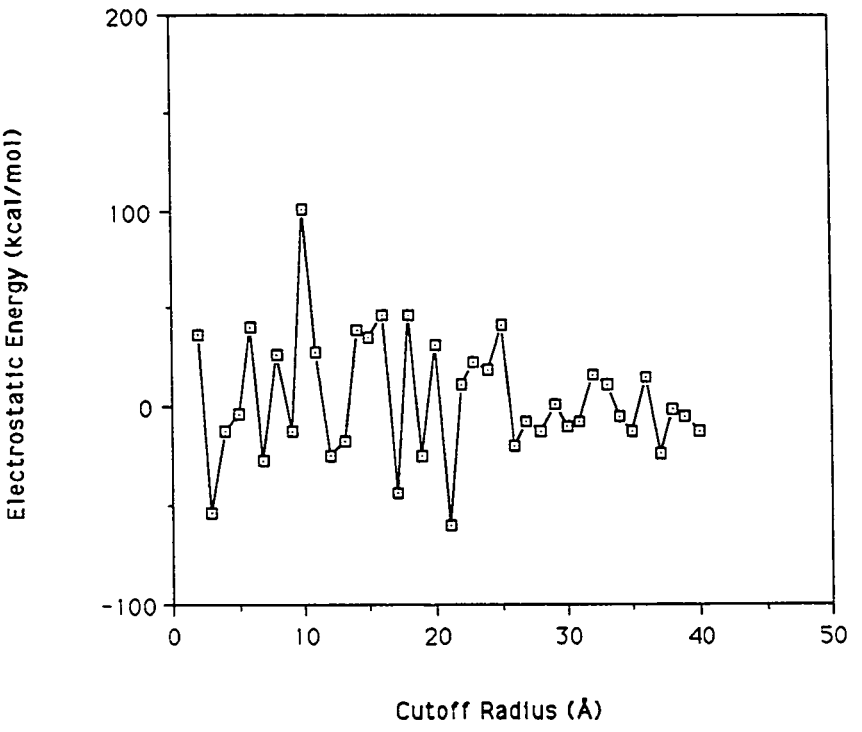

Fig. 4.3 Electrostatic energy as a function of cutoff radius for the observed crystal structure of benzene. Point charges used were +0.153 on hydrogen and -0.153 on carbon as recommended by Williams.

Although some indication of convergence is observed between 35 and 40 Å, the electrostatic energy still oscillates ± 20 kcal/mol about the expected value of approximately -2 kcal/mol (-2.57 kcal/mol according to Williams [77], and -1.22 kcal/mol per Evans and Watts [106]). Performing this calculation out to 40 Å required 0.1995 seconds on the Cray Y-MP, compared to 0.0082 seconds for calculating the Lennard-Jones 6-12 potentials to convergence at 10 Å.

Ewald [107] developed a method of performing lattice sums which converges more rapidly than direct summation. This method, in which a portion of the sum is evaluated in reciprocal space, was later expanded and generalized by Bertaut,[108] and Nijboer and de Wette.[109] More recently, other methods of performing lattice sums, such as representing the sums as Mellin transforms of complex Θ functions, have been developed (see review by Glasser and Zucker [110]). The general form of the lattice sum has been obtained for simple cubic and orthorhombic systems, such as the sodium chloride structure. The basis in these systems often involves only one or two point charges, and the coulombic energy for these systems can be readily calculated.

For organic molecular solids, however, the problem is more complex. These organic materials exhibit such a wide range of symmetry arrangements and ratios of lattice parameters, that obtaining a general form for the lattice sum is exceedingly difficult. The problem is further compounded by the large number of point charges associated with each lattice point, each of which requiries the calculation of a separate sublattice. Hence, even if general forms of lattice sums could be readily obtained for each space group, the number of calculations required for each sublattice of point charges in the unit cell exceeds present computer resources for any more than a few trial structures.

Williams has developed a modification of Ewald's method of accelerated convergence for performing lattice sums on organic molecular solids, which he applied to London dispersion forces, i.e. for when $n = 6$ in the following expression:

$$S_n = \frac{1}{2} \sum_{j \neq k} \frac{q_j q_k}{r_{jk}^n} \qquad \text{[Eq. 4.18]}$$

where j refers to point charges within one unit cell, and k refers to all points in the lattice. Williams' method is valid if the charges over the lattice cell sum to zero. The general form for $n = 6$ is as follows:

$$E = \frac{1}{2}\sum_{jkm}[B_{ab}\exp(-C_{\alpha\beta}r_{jkm})\frac{-A_{\alpha\beta}}{r_{jkm}^6}(1 + a_6^2 + \frac{1}{2}a_6^4)\exp(-a_6^2) + \frac{q_a q_b}{r_{jkm}}\mathrm{erfc}(a_1)]$$
$$- \frac{\pi^3 K_b^3}{6V}(\sum_\alpha A_{\alpha\alpha}^{1/2})^2 + \frac{\pi^3 K_b^6 Z}{12}(\sum_\alpha A_{\alpha\alpha}) - K_1 Z(\sum_\alpha q_\alpha^2) \qquad \text{[Eq. 4.19]}$$

where $a_i^2 = \pi K_i^2 r_{jkm}^2$, $\mathrm{erfc}(a_1) = \int_{a_1}^{\infty}\exp(-t^2)dt$, $A_{\alpha\beta} = (A_{\alpha\alpha}B_{\beta\beta})^{1/2}$, Z is the number of molecules in the unit cell, K_1 and K_b are convergence constants selected so as to make the reciprocal sum negligible, r_{jkm} is the nonbonded interatomic distance, $A_{\alpha\beta}$ is the coefficient of the London dispersion attraction term between atoms α and β, $B_{\alpha\beta}$ and $C_{\alpha\beta}$ are short range repulsion parameters, q_α is the electrostatic charge on atom α, and $\vec{t}$ is the translation vector in unit cell space [111].

Applying this expression to the calculation of the London dispersion energy for benzene crystals, Williams required calculation of 500 terms to obtain reasonable ($< 1\%$ error) convergence for $n = 6$, at a 6 Å summation limit. In later work, Williams applied his method for $n = 1$ for hydrocarbons [53]. A summation limit of 8 Å was used, but number of terms, time to calculate, % error, and degree of convergence were not reported. It is reasonable to assume that 8 Å was not adequate to obtain sufficient convergence for $n = 1$.

To summarize, the difficulties in calculating lattice sums of point charges are as follows:

- It is necessary to recalculate an expression for the lattice sum for each type of basis in each space group.

- The lattice sums of $1/r$ terms converge slowly - even using accelerated methods.
- A large summation limit is necessary.
- Very little of Equation 4.19 above can be vectorized.

In view of the above, it is apparent that calculating the electrostatic energy using point charges is not fast enough to be practical for every closest-packed structure.

Another method to calculate the electrostatic energy of a lattice of point charges is to sum over electrostatically neutral units, i.e. molecules, rather than using a strict cutoff radius. This calculation converges much faster than the direct lattice sum, and is easier to calculate than an Ewald sum. To determine the approximate distance at which the coulombic interaction between two neutral molecules becomes negligible, the electrostatic energy was calculated between two benzene molecules in six different relative orientations with their centers of mass at increasing distances apart. (Fig. 4.4)

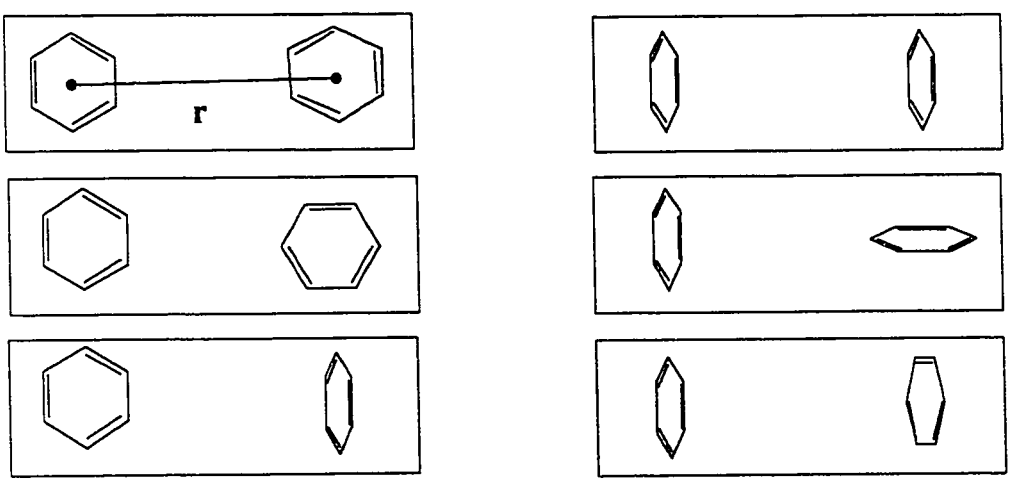

Fig. 4.4 The six possible alignments of the principal axes of two benzene molecules. r is the separation between their centers of mass.

As can be seen from the graph in Fig. 4.5, the electrostatic energy between two benzene molecules essentially goes to zero at a distance of 15 Å (-0.0044 kcal/mol). Multiplying this value by the number of molecules (22.6) expected to be at that distance (14.5 Å to 15.5 Å) in the solid, the contribution to the lattice energy at this distance is approximately -0.099 kcal/mol, or 0.8% of the total lattice energy. Hence, a 15 Å cutoff radius for a neighboring molecule's center of mass would be sufficient for this method. The results of these calculations are shown in Tables 4.2 and 4.3 and Fig. 4.5.

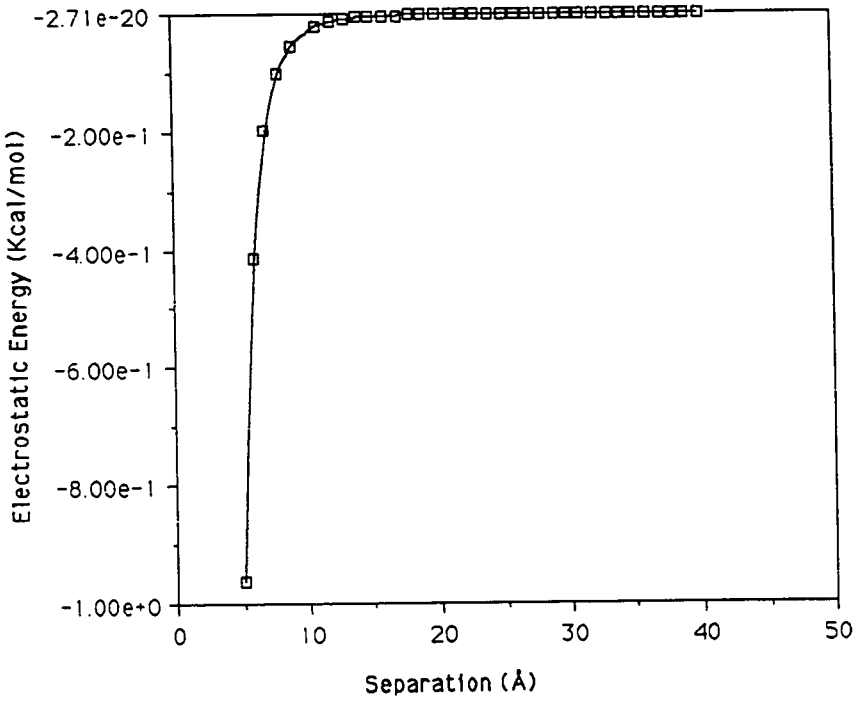

Fig. 4.5 Electrostatic energy between two benzene molecules as a function of separation of their centers of mass. The data shown is for the orientation in which the absolute value of the interaction energy is the greatest.

Table 4.2 Electrostatic energy between two benzene molecules separated by distance r (Å). Energy is given in units of kcal/mol.

r (Å)	E_{coul} from 1 molecule at r	# Molecules at distance r in solid.	# Molecules in solid between 5 and r Å	Increase in energy due to all molecules at distance r in solid	Total energy due to all molecules in solid between 5 and r Å
5	-0.9635	4.1920	4.1920	-4.039	-4.0391151
6	-0.4144	3.2604	7.4524	-1.351	-5.3902771
7	-0.1956	4.5503	12.0027	-0.8899	-6.2802184
8	-0.1009	6.0551	18.0578	-0.6112	-6.8914019
9	-0.5614E-01	7.7749	25.8327	-0.4365	-7.3279048
10	-0.3319E-01	9.7097	35.5424	-0.3223	-7.6502121
11	-0.2063E-01	11.8594	47.4018	-0.2447	-7.8949087
12	-0.1337E-01	14.2241	61.6259	-0.1901	-8.0850576
13	-0.8968E-02	16.8038	78.4297	-0.1507	-8.2357545
14	-0.6197E-02	19.5985	98.0282	-0.1215	-8.3572106
15	-0.4393E-02	22.6081	120.6363	-0.9932E-01	-8.4565329
16	-0.3184E-02	25.8327	146.4690	-0.8226E-01	-8.5387917
17	-0.2353E-02	29.2723	175.7413	-0.6889E-01	-8.6076836
18	-0.1770E-02	32.9269	208.6682	-0.5827E-01	-8.6659554
19	-0.1351E-02	36.7964	245.4646	-0.4973E-01	-8.7156824
20	-0.1046E-02	40.8809	286.3455	-0.4277E-01	-8.7584569
21	-0.8203E-03	45.1804	331.5259	-0.3706E-01	-8.7955165
22	-0.6503E-03	49.6948	381.2208	-0.3232E-01	-8.8278355
23	-0.5210E-03	54.4243	435.6450	-0.2835E-01	-8.8561890
24	-0.4213E-03	59.3687	495.0137	-0.2501E-01	-8.8811997
25	-0.3436E-03	64.5281	559.5418	-0.2217E-01	-8.9033731
26	-0.2825E-03	69.9024	629.4442	-0.1975E-01	-8.9231225
27	-0.2340E-03	75.4917	704.9360	-0.1767E-01	-8.9407885
28	-0.1952E-03	81.2960	786.2320	-0.1587E-01	-8.9566540
29	-0.1638E-03	87.3153	873.5473	-0.1430E-01	-8.9709557
30	-0.1383E-03	93.5496	967.0969	-0.1294E-01	-8.9838923
31	-0.1174E-03	99.9988	1067.0957	-0.1174E-01	-8.9956321
32	-0.1002E-03	106.6630	1173.7587	-0.1069E-01	-9.0063184
33	-0.8591E-04	113.5422	1287.3008	-0.9755E-02	-9.0160733
34	-0.7401E-04	120.6363	1407.9371	-0.8929E-02	-9.0250021
35	-0.6404E-04	127.9454	1535.8826	-0.8193E-02	-9.0331954
36	-0.5563E-04	135.4695	1671.3521	-0.7536E-02	-9.0407318
37	-0.4852E-04	143.2086	1814.5607	-0.6948E-02	-9.0476796
38	-0.4246E-04	151.1626	1965.7233	-0.6419E-02	-9.0540987
39	-0.3730E-04	159.3316	2125.0550	-0.5943E-02	-9.0600412
40	-0.3287E-04	167.7156	2292.7706	-0.5512E-02	-9.0655532

Table 4.3 Electrostatic energy estimated from the two benzene model at various summation radii as a percentage of the energy obtained at 40 Å. Energy is given in units of kcal/mol.

r (Å)	E_{coul}	% of total E_{coul} at 40Å
5	-4.039	44.55453
6	-5.390	59.45889
7	-6.280	69.27562
8	-6.891	76.01744
9	-7.328	80.83241
10	-7.650	84.38770
11	-7.895	87.08689
12	-8.085	89.18438
13	-8.236	90.84668
14	-8.357	92.18644
15	-8.457	93.28204
16	-8.539	94.18942
17	-8.608	94.94935
18	-8.666	95.59213
19	-8.716	96.14066
20	-8.758	96.61249
21	-8.796	97.02129
22	-8.828	97.37779
23	-8.856	97.69055
24	-8.881	97.96644
25	-8.903	98.21103
26	-8.923	98.42888
27	-8.941	98.62375
28	-8.957	98.79876
29	-8.971	98.95652
30	-8.984	99.09922
31	-8.996	99.22872
32	-9.006	99.34659
33	-9.016	99.45420
34	-9.025	99.55269
35	-9.033	99.64307
36	-9.041	99.72620
37	-9.048	99.80284
38	-9.054	99.87365
39	-9.060	99.93920
40	-9.066	100.00000

4.4. The Bond Dipole Model

Unlike partial atomic charges, bond dipole moments can be determined experimentally. [112] The potential energy between two point dipoles $\vec{\mu}_i$ and $\vec{\mu}_j$ is given by the expression

$$E_{ij} = \frac{1}{\epsilon}\left[\frac{\vec{\mu}_i \cdot \vec{\mu}_j}{r_{ij}^3} - \frac{3(\vec{\mu}_i \cdot \vec{r}_{ij})(\vec{\mu}_j \cdot \vec{r}_{ij})}{r_{ij}^5}\right] \qquad \text{[Eq. 4.20]}$$

where ϵ is the dielectric constant of the medium between the dipoles, and r_{ij} is the distance between them. The molecular charge distribution can be approximated fairly well by the bond dipole model, and this approximation has been used extensively in empirical molecular mechanics applications, such as MM3,[54] and for calculating the electrostatic lattice energy of polymers.[113]

General expressions for calculating the electric field for orthorhombic polar crystals with dipoles of finite size have been developed and applied to polymers [114]. The range of crystal structures for polymers is much less varied than for molecular solids, and obtaining general forms for lattice sums of bond dipoles for complex organic molecules suffers from the same difficulties as do point charges. Although dipole-dipole interactions converge much faster, as r^{-3}, the number of bond dipoles per molecule, and hence per unit cell, is large. Determining the positions, orientations, and interactions of all the bond dipoles results in a calculation which is too time consuming to perform on 10,000 closest-packed structures.

4.5. Atomic Multipoles

Approximating the molecular charge distribution by atomic monopoles, dipoles, and quadrupoles yields the most detailed representation of all the charge models. Stone, Buckingham, and Fowler have used Distributed Multipole Analysis, described in Section 2.4, to account for all nonbonded intermolecular interactions between molecules. Good results have been obtained for Van der Waals dimers, but this method has not yet been applied to solids due to computational limitations. Hirshfeld [116] has proposed a slightly different atomic multipole model in which the electrostatic component of the lattice energy is separated from the atom-atom Van der Waals potentials. Hirschfeld and Mirsky [115] have applied this model to calculating ethylene, carbon dioxide and cyanogen lattices, using summation radii of 15 Å. Although the atomic multipole model is the most accurate,[69] it is unfortunately the most computationally intensive, and is prohibitive for all but the simplest crystal structures.

4.6. Molecular Multipoles

Molecular multipoles represent the crudest approximation to molecular charge distribution. The model is most inappropriate for cases in which the charge distribution of one molecule significantly penetrates that of its nearest neighbor, but it does yield good results for the electrostatic energy when the charge distributions are separate.[115,86,117,118]

Electrostatic energy calculations employing molecular multipole-multipole interactions have several advantages over the various point-charge methods. One advantage is that the magnitude of the dipole and quadrupole moments can be verified experimentally. Secondly, higher-order multipole interactions fall off much more quickly than the $1/r$ dependence of point charge interactions, and can be calculated by a direct lattice summation. For example, dipole-dipole interactions exhibit an r^{-3} dependence, and will converge must faster than a $1/r$ series using even the most efficient Ewald summation techniques. From a sufficient distance, a point dipole will appear neutral, even if its magnitude is very large. Another advantage is the reduced number of interactions to be considered when using molecular multipoles. For example, each benzene molecule contains a point charge on each of the twelve atoms, but only one molecular quadrupole moment and no dipole or octapole moment.

Even thought the molecular multipole model offers the fastest means to approximate the electrostatic energy of a lattice, we had to determine whether the model offered sufficient accuracy to be useful, even as a quick screening technique. Most of the electrostatic calculations performed to date on molecular solids such as benzene have been done using point charges, and we used the calculations of Williams[77] as a basis for comparison.

One reported concern in using molecular multipoles is the lack of sensitivity to fine structural differences around the principal axes of symmetry, particularly for quadrupole moments, even when cylindrical symmetry is not assumed. For example, it is possible to distingush the eclipsed and antiparallel configurations

of aniline dimers (Fig 4.6) using only the quadrupole moments in expression 4.14, but not the eclipsed and staggered configurations of benzene (Fig. 4.7).

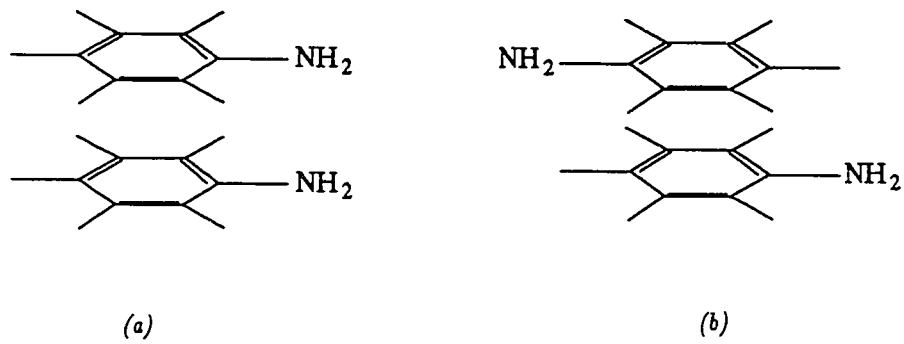

Fig. 4.6 Eclipsed (a) and Antiparallel (b) Configurations of Aniline Dimers

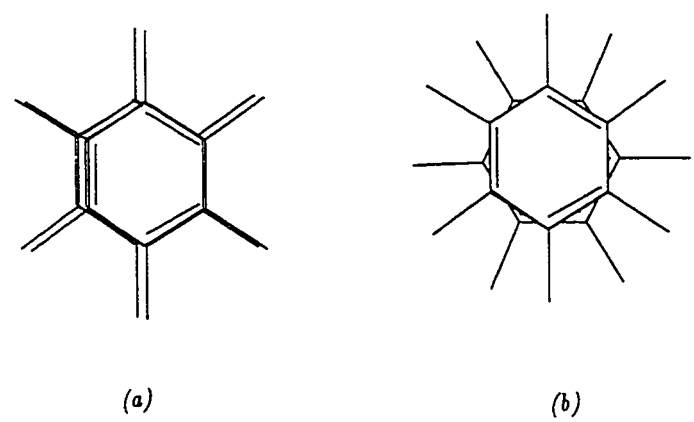

Fig. 4.7 Eclipsed (a) and Staggered (b) Configurations of Benzene

Two benzene molecules were placed in a face-to-face, parallel orientation, 3.55 Å apart. (Fig. 4.8) This separation is the distance observed in graphite. When we compared the benzene dimer calculations of the molecular multipole model with those using the point charge method, we were surprised to learn that the point charge model could not readily distinguish these configurations either. Using the point charge values of Williams ($\pm$ 0.153), the difference in the electrostatic energy was less than 0.5% between orientations in which the hydrogen atoms were either eclipsed or staggered. It is important to note that these calculations are based on the electrostatic contribution only, and do not include the dispersive nor closed-shell repulsive interactions, for which the difference in energy is considerable between the two configurations.

The molecular multipole and point charge models were compared for the 'slipped stack' configuration as well. Maintaining the benzene molecules in a parallel orientation, their planes 3.55 Å apart, one molecule was translated along the x-axis of the molecular plane, and the electrostatic energy was calculated. Results are shown in Table 4.4.

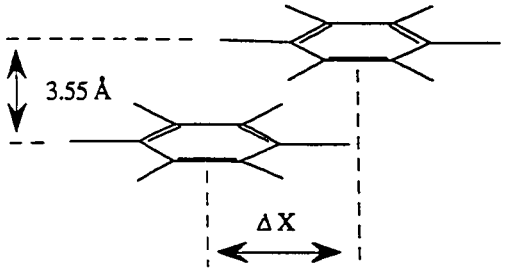

Fig. 4.8 Face-to-Face Parallel Configuration of Benzene Molecules Used to Compare Multipole and Point Charge Calculations of the Electrostatic Energy

Table 4.4 Electrostatic energy in kcal/mol between two benzene molecules in the parallel orientation illustrated in Figure 4.8, 3.55 Å apart. Δx is the lateral displacement of one of the benzene molecules. Molecular quadrupole moments are from experiment ($Q_{xx} = Q_{yy} = 2.8 = -\frac{1}{2}Q_{zz}$). Point charge values are ±0.153 as recommended by Williams. The asterisk (*) indicates position of minimum energy.

Δx	Molecular multipole model	E_{coul} from Point charge model, hydrogens eclipsed	Point charge model, hydrogens staggered	Point charge model, hydrogens staggered, by $y = 5.0$ Å
0.000	1.201	2.761	2.754	0.6884
0.250	1.157	2.725	2.719	0.6796
0.500	1.034	2.620	2.615	0.6538
0.750	0.8553	2.453	2.450	0.6125
1.000	0.6510	2.234	2.233	0.5582
1.250	0.4499	1.974	1.975	0.4937
1.500	0.2732	1.688	1.690	0.4224
1.750	0.1323	1.388	1.391	0.3477
2.000	0.2973E-01	1.089	1.092	0.2730
2.250	-0.3800E-01	0.8021	0.8042	0.2011
2.500	-0.7756E-01	0.5366	0.5380	0.1345
2.750	-0.9635E-01	0.3008	0.3011	0.7528E-01
3.000	-0.1011*	0.1003	0.9923E-01	0.2481E-01
3.250	-0.9707E-01	-0.6168E-01	-0.6457E-01	-0.1614E-01
3.500	-0.8832E-01	-0.1846	-0.1897	-0.4742E-01
3.750	-0.7747E-01	-0.2704	-0.2777	-0.6943E-01
4.000	-0.6623E-01	-0.3226	-0.3324	-0.8309E-01
4.250	-0.5555E-01	-0.3466	-0.3585	-0.8963E-01
4.500	-0.4594E-01	-0.3482*	-0.3619*	-0.9047E-01*
4.750	-0.3759E-01	-0.3336	-0.3483	-0.8707E-01
5.000	-0.3049E-01	-0.3082	-0.3232	-0.8080E-01
5.250	-0.2457E-01	-0.2766	-0.2913	-0.7282E-01
5.500	-0.1968E-01	-0.2426	-0.2564	-0.6410E-01
5.750	-0.1570E-01	-0.2087	-0.2213	-0.5532E-01
6.000	-0.1247E-01	-0.1768	-0.1879	-0.4697E-01
6.250	-0.9861E-02	-0.1477	-0.1573	-0.3932E-01
6.500	-0.7768E-02	-0.1221	-0.1302	-0.3254E-01
6.750	-0.6092E-02	-0.9995E-01	-0.1066	-0.2665E-01
7.000	-0.4753E-02	-0.8111E-01	-0.8654E-01	-0.2164E-01
7.250	-0.3686E-02	-0.6531E-01	-0.6968E-01	-0.1742E-01
7.500	-0.2837E-02	-0.5220E-01	-0.5569E-01	-0.1392E-01
7.750	-0.2163E-02	-0.4141E-01	-0.4417E-01	-0.1104E-01

Stable minima were revealed for both methods, occurring at Δx ~3.0 Å for the molecular quadrupoles, and at $\Delta x \sim 4.5$Å for the atomic point charge model. Hence, in an actual crystal, it should be possible to achieve a negative electrostatic lattice energy for the slipped-stack-of-pancakes structure using using either method. As can be seen from from Table 4.4, the depth of the potential minimum was much greater for Williams' point charge model, -.348 kcal/mol, as compared to -0.101 kcal/mol for the molecular quadrupole model.

The value for the energy obtained using the point charge values of Williams were approximately two and a half times larger in the eclipsed position ($\Delta x = 0$) than that using the experimental values for the molecular quadrupole. It should be noted that the partial charges of ± 0.153, which Williams assigns to the atoms in benzene, yield a Q_{zz} of -17.68 Debye-Å, compared to the experimental value of -5.6 Debye-Å. Unfortunately, there can be no experimental data on the gas-phase parallel orientation for the benzene dimer, so we cannot know which model yields a more accurate result in this case. Therefore energy calculations were compared using the experimental crystal structure of benzene. Using the molecular multipole model we obtained a value of -0.50 kcal/mol, compared to -2.57 kcal/mol from Williams' [105] point charge model, and to -1.22 kcal/mol from the six-bond point dipole model of Evans and Watts, [106]. These three values for the electrostatic energy are, in terms of the percent of total lattice energy, 4.1%, 20.5%, and 9.7%, repsectively. Craig, Mason, Pauling and Santry [48] have estimated, using molecular multipoles, that the maximum electrostatic energy for naphthalene, anthracene, and similar aromatic hydrocarbons, is on the order of 3% of the total binding energy. Hence, our molecular multipole method gives values within the wide range obtained by other workers.

The suitability of the molecular multipole model to sort closest packed structures was evaluated using benzene as a test case. When the molecular multipole model was applied to a series of closest-packed structures of benzene, the herringbone, edge-to-face configuration was shown to be more stable than the slipped stack of pancakes parallel structure, consistent with the experimental data. Without the electrostatic component, the slipped stack structure exhibited a lower energy. The details of this latter result are presented in Chapter 6.

Various basis sets were evaluated to calculate the multipole moments using Gaussian 90. With the exception of CNDO and STO-3G, the variability in multipole moments was not as great as that observed in calculating point charges (Table 4.1) The results are shown in Table 4.5.

Method	Q_{zz} (Debye-Å)
CNDO	-1.264
MNDO	N/A
AM1	-6.369
STO-3G	-2.449
3-21G	-6.264
6-311G	-5.747
6-31G	-5.518
6-31G**	-5.446
6-31+G(d)	-6.066

Table 4.5 Multipole moments for benzene calculated from Gaussian 90 using different basis sets. The experimental value for Q_{zz} is -5.6 Debye-Å.

The quadrupole moments obtained using the 6-31G basis sets exhibited the closest agreement with the experimental value of 5.6 Debye-Å. Unfortunately, 6-31G can be used only on the smallest molecules, due to memory limitations of the Cray Y-MP. Hence, the smaller basis sets 3-21G and STO-3G, as well as the semi-empirical method AM-1, were examined to determine which would give the best results for larger molecules. Calculations were performed on the aromatic hydrocarbon series naphthalene, anthracene, and tetracene, and the quadrupole moments were compared with those obtained using 6-31G (Table 4.6). The orientation with respect to the cartesian axes for the molecular multipole moment calculations is shown in Fig. 4.9.

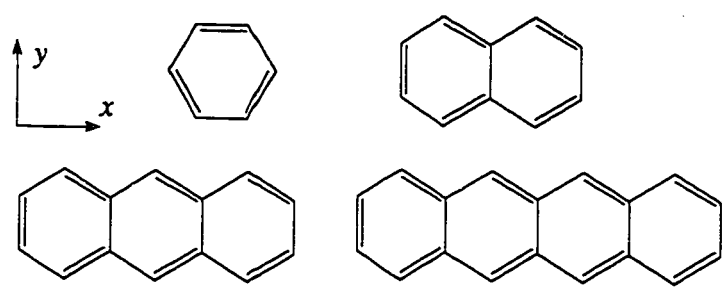

Fig. 4.9 Orientation of molecules in Table 4.6. For each molecule, the origin of the coordinate system is located at the center of mass. The z-direction is perpendicular to the page.

Table 4.6 Quadrupole tensor diagonal elements calculated with Gaussian 90 using various basis sets. Q'_{zz} is the value obtained with 6-31G for each molecule. Molecules are in the standard orientation shown in Figure 4.9.

Basis Set	Q_{xx}	Q_{yy}	Q_{zz}	Q_{zz}/Q'_{zz}
Benzene				
AM-1	3.184	3.184	-6.396	1.154
STO-3G	1.224	1.224	-2.449	0.444
3-21G	3.132	3.132	-6.264	1.135
6-31G	2.759	2.759	-5.518	1.000
Naphthalene				
AM-1	6.678	5.119	-11.797	1.269
STO-3G	1.878	2.131	-4.009	0.431
3-21G	5.381	5.372	-10.753	1.157
6-31G	4.593	4.704	-9.297	1.000
Anthracene				
AM-1	11.812	6.101	-17.912	1.389
STO-3G	2.571	2.948	-5.512	0.428
3-21G	7.713	7.407	-15.120	1.172
6-31G	6.422	6.476	-12.898	1.000
Tetracene				
AM-1	18.889	6.072	-24.962	1.543
STO-3G	3.007	3.862	-6.868	0.424
3-21G	9.687	9.531	-19.218	1.189
6-31G	7.818	8.362	-16.180	1.000

The ratio Q_{zz}/Q'_{zz} computed using AM1 showed more variability with the type of molecule than did the same ratio computed using any of the *ab initio* basis sets. The relative values of Q_{xx} and Q_{yy} were even more inconsistent, indicating that AM-1 would not be an acceptable method for calculating the multipole moments. The values of 3-21G were most consistent with 6-31G, and would be used when necessary, scaled down by an average factor of 1.165. For molecules in

which 3-21G is too large, STO-3G would be the next choice, scaled by a factor of 0.43.

Even though the electrostatic contribution to the lattice energy cannot be separated experimentally from the total binding energy of the solid for comparison with our results, the magnitude of the energy we obtained using the molecular multipole model was consistent with the results calculated by other methods, and the type of packing obtained agreed with experiment. The various models for the charge distributions may predict slightly different crystal structures if electrostatic energy was the sole criteria used, but as the electrostatic contribution to the lattice energy is only a minor part of the total, and is not used in the actual minimization process, it is hoped that any error is minimized. Therefore, at the present time the molecular multipole model appears adequate as an efficient screening tool.

Chapter 5 Details of the Program

The overall approach to predicting crystal structures rests on the assumptions that the structure will be closest packed and will have the lowest possible energy. According to Kitaigorodsky's theory, closest packing of organic molecules is possible in only 13 out of all 230 possible space groups (Table 2.1). All possible molecular orientations within each of the allowed space groups are searched for those which will yield the highest packing index, or fraction of space filled. The energy calculations are then performed on these closest packed structures to determine the most stable structure. The overall structure of the program is shown in Figure 5.1.

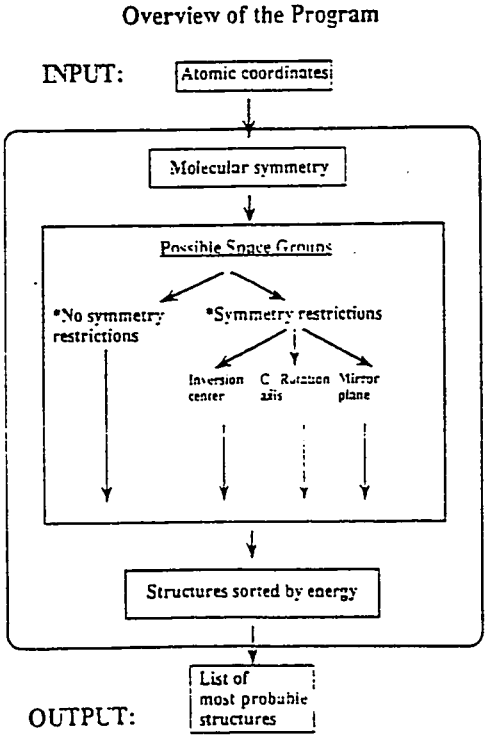

Figure 5.1 Overall program structure.

5.1. Input

For the section of the program which close-packs the molecules, one must input the atom types and positions, as well as the molecular Van der Waals volume. If electrostatic calculations are to be performed, then atomic charges and/or molecular multipole moments are required as well. Examples of input files used in this study are located in Appendix C.

The atomic coordinates and Van der Waals volume can be obtained from a number of standard quantum mechanics packages. In this work, optimized geometries were obtained from Gaussian 88 and Gaussian 90 using a 3-21G basis set where possible. For molecules which are too large to optimize the geometry with a 3-21G basis set, we either performed an optimization using MM2, or used the experimental coordinates. In all cases where optimization was performed, the geometries were found to be consistent with the experimental structures. The program does not perform any optimization or internal geometry modifications of the molecule or asymmetric unit provided in the input file. The Van der Waals volumes were obtained using CHEM-X [119].

5.2. Molecular Point Group

Upon reading the input file, atomic masses and default Lennard-Jones parameters, σ and ϵ, are assigned based on atom type. At present, only C and H are included in the default list, but this list can be easily expanded. The molecule is then positioned with its center of mass at the origin, and the principle axes of inertia are determined from the eigenvectors of the inertia tensor (Eq. 5.1).[121]

$$\begin{pmatrix} I_{xx} & I_{xy} & I_{xz} \\ I_{yx} & I_{yy} & I_{yz} \\ I_{zx} & I_{zy} & I_{zz} \end{pmatrix} \qquad \text{[Eq. 5.1]}$$

I_{xx}, I_{yy}, I_{zz} are called the 'moments of inertia' about the x, y, and z axes, respectively:

Moments of inertia:

$$I_{xx} = \sum_i m_i(y_i^2 + z_i^2)$$
$$I_{yy} = \sum_i m_i(x_i^2 + z_i^2)$$
$$I_{zz} = \sum_i m_i(x_i^2 + y_i^2) \qquad \text{[Eqs. 5.2]}$$

The I_{ij} are called the 'products of inertia', and are defined as follows:

Products of inertia:

$$I_{xy} = -\sum_i m_i x_i y_i = I_{yx}$$
$$I_{xz} = -\sum_i m_i x_i z_i = I_{zx}$$
$$I_{yz} = -\sum_i m_i y_i z_i = I_{zy} \qquad \text{[Eqs. 5.3]}$$

The rotational inertia about any principal axis must be zero, so that

$$(I_{xx} - I)x_i + I_{xy}y_i + I_{xz}z_i = 0$$
$$I_{yx}x_i + (I_{yy} - I)y_i + I_{yz}z_i = 0$$
$$I_{zx}x_i + I_{zy}y_i + (I_{zz} - I)z_i = 0 \qquad \text{[Eqs. 5.4]}$$

The program uses the *NAGLIB* library routine *F02BJF* to calculate the eigenvalues and eigenvectors of the inertia tensor. The molecular axes are then aligned with the coordinate axes with the following expression

$$X_{i'} = VX_i \qquad \text{[Eq. 5.5]}$$

where V is the 3×3 matrix of eigenvectors and X_i is the position vector of atom i. Any mirror planes, if they exist, will be perpendicular to the principle axes of inertia. Hence, once the axes are aligned, the atomic positions are easily examined to determine if any mirror planes are present in the molecule.

Rotation axes will be coincident with the principal axes of inertia. The order of each principal axis can be determined using De Moivre's Theorem:

$$(x + iy)^n = e^{in\phi} \qquad \text{[Eq. 5.6]}$$

where x and y are the components of the atomic coordinates in the plane perpendicular to the z-axis, n is an integer, and ϕ is the angle of rotation in the complex plane about the z-axis. The sum of $(x + iy)^n$ over all atoms will be zero when n equals the highest order of the z-axis.

5.3. Space Group Geometry

After the molecule has been properly positioned with its center of mass at the origin, the program begins to search the space groups consistent with the molecule's symmetry for the closest-packed orientations. In general, each minimization run begins with the molecule rotated a certain number of degrees about the $x-$, $y-$, or z-axes (Fig. 5.2). The default rotation increment is 15° to ensure a fairly complete search. The limits of the initial rotations are determined automatically by the molecular symmetry to eliminate redundant starting configurations for highly symmetric molecules. For a molecule such as benzene, approximately 2600 starting positions, distributed over thirteen space groups, are used. Successive rotations about each of the three axes, first about z, then y, then x, are

accomplished by multiplication of the coordinates by the following matrices:

$$\begin{pmatrix} 1 & 0 & 0 \\ 0 & \cos\phi_x & -\sin\phi_x \\ 0 & \sin\phi_x & \cos\phi_x \end{pmatrix} \begin{pmatrix} \cos\phi_y & 0 & -\sin\phi_y \\ 0 & 1 & 0 \\ \sin\phi_y & 0 & \cos\phi_y \end{pmatrix} \begin{pmatrix} \cos\phi_z & -\sin\phi_z & 0 \\ \sin\phi_z & \cos\phi_z & 0 \\ 0 & 0 & 1 \end{pmatrix} \quad \text{[Eq. 5.7]}$$

where ϕ_x, ϕ_y, and ϕ_z are the angles of rotation about the $x-, y-$, and z-axes, respectively.

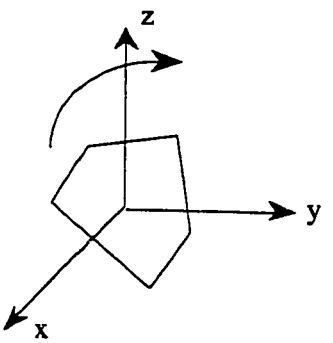

Figure 5.2. The molecule is initially positioned at the origin and then rotated by incremental amounts about the $x-, y-$, and z-axes.

Once the molecule is rotated about the origin, the reference unit cell is constructed around it (Fig 5.3a). The magnitudes of the lattice vectors a, b, and c are initially set to 2.5 times the maximum Van der Waals diameter of the molecule. For space groups in which it is assumed general positions are occupied, the molecule is first translated to a central general position at $(\frac{1}{4}a, \frac{1}{4}b, \frac{1}{4}c)$, as shown in Figure 5.3b. For a space group in which it is assumed special positions are occupied, the molecule is placed directly on the special position.

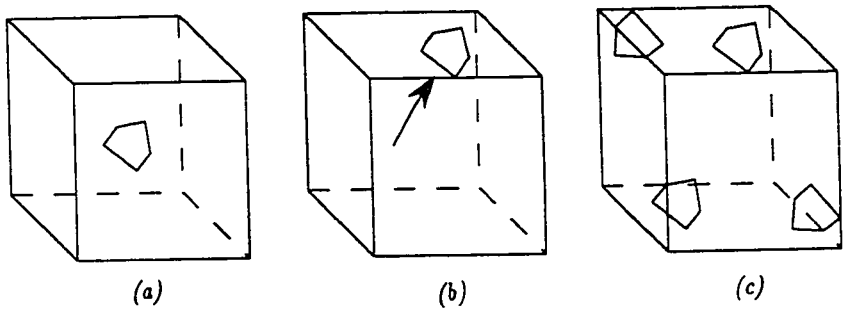

Figure 5.3. (a). The molecule is initially placed with its center of mass on the origin at the center of the unit cell. (b). The molecule is translated to a central general position at $(\frac{1}{4}a, \frac{1}{4}b, \frac{1}{4}c)$. (c). Molecules in the other symmetry positions are generated.

For example, in a space group such as *Pbca* containing an inversion center, the molecule would be centered on an inversion center at a corner of the unit cell at $(\frac{1}{2}a, \frac{1}{2}b, \frac{1}{2}c)$. The remainder of the molecules in the unit cell are then generated using the symmetry relations of the given space group (Fig. 5.3c). For example, in $P2_1/c$, if an atom in the first molecule is located at fractional coordinates (x, y, z), then the corresponding atom in the other three molecules in the unit cell are located at $(-x, -y, -z)$, $(x, \frac{1}{2}b - y, \frac{1}{2}c + z)$, and $(-x, \frac{1}{2}b + y, \frac{1}{2}c - z)$.

For energy calculations to be performed on the crystal structure, it is convenient to express the atomic positions in terms of a reference cartesian space rather than in fractions of lattice vectors. As shown in Appendix A, unit cell space can then be transformed into cartesian space by the operation $X' = DX$ where D is the transformation matrix shown in Fig. A.1. The x-coordinate of these atoms, for example, can be determined by the expression:

$$X_g = S^* X_i + a^* T_a \qquad \text{[Eq. 5.8]}$$

where X_g is the coordinate of an atom in a generated symmetry position, X_i is a coordinate in the first molecule, S is a matrix containing $\pm 1's$ corresponding to the sign of x in the symmetry operations, a is the lattice constant, and T_a is the extent of translation along the a axis.

5.4. Minimization Within a Space Group

The minimization process is the most time consuming calculation in the prediction of crystal structures, and must be performed as efficiently as possible. Hence this section of the program is intended to close-pack the structure using simplified interactions between nearest neighbor molecules only. More thorough energy calculations are then performed on the structure once it has been minimized; otherwise, 2,000 - 10,000 minimizations per molecule would be intractable, even on a Cray Y-MP.

Once the unit cell is constructed, it must be placed in the crystal environment. The most direct way is to construct 26 unit cells in a $3 \times 3 \times 3$ array around the reference unit cell. This is fairly time consuming, however, and several alternative methods were investigated and evaluated for their effectiveness and efficiency. One method is to exploit the periodic boundary conditions using a modulo function. Such a function can be used to map any atoms which fall outside of the reference unit cell back to their corresponding positions within the unit cell, as shown in Fig. 5.4. This method involves integer division, however, and was found to be at least a factor of three slower than creating and calculating the interactions with seven additional unit cells. In addition, the method using a modulo function did not always yield satisfactory information about interactions between molecules which were close to the unit cell border, but did not cross it.

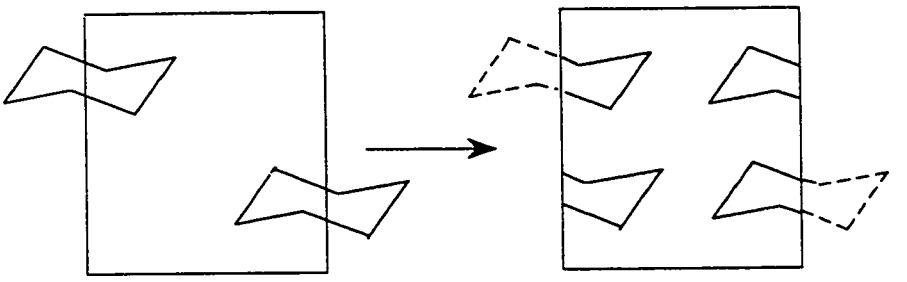

Figure 5.4. A modulo function will map atomic coordinates which fall outside of the unit cell boundaries back inside the unit cell.

An effective method for fairly compact molecules was found to be construction of a 2 × 2 × 2 arrangement of unit cells. This block of unit cells can simulate a 3×3×3 array of unit cells by simply shifting the reference unit cell (Fig. 5.5b). The seven additional unit cells are generated by translating all molecules one lattice vector in each of the [100], [010], [001], [110], [101], [011], and [111] directions (Fig. 5.5a).

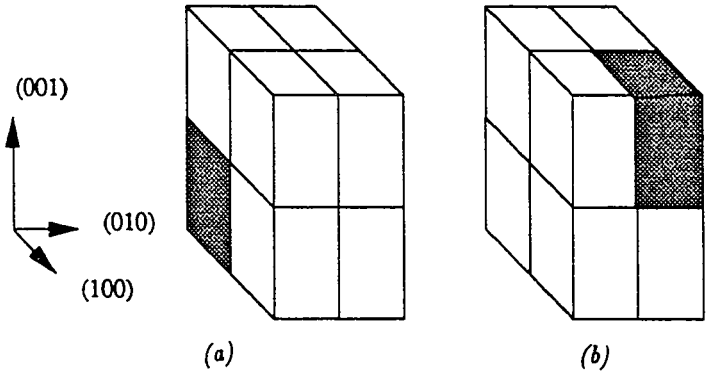

Figure 5.5. (a). Seven additional unit cells are generated by translating all molecules in the initial unit cell (shaded) in the [100], [010], [001], [110], [101], [011], and [111] directions. (b). The reference cell is shifted to the [111] unit cell.

This $2 \times 2 \times 2$ block of unit cells, however, was found to be inadequate for extended molecules such as pentacene. With pentacene and similar molecules, it is possible to construct crystal structures in which a molecule can overlap with other molecules in unit cells $2\vec{T}_i + \vec{T}_j$ translation vectors away (i not equal to j), and not overlap with molecules in adjacent unit cells, as is illustrated in Figure 5.6. This does not happen in nature, of course, but can occur when crystal structures are arbitrarily constructed. For benzene, this type of overlap occured with a frequency of less than 0.1%, but for pentacene it was observed in over 30% of the closest-packed structures.

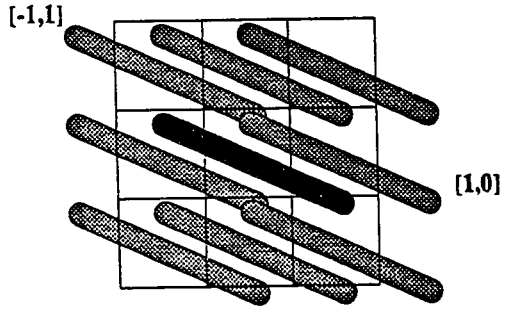

Figure 5.6. A 3×3 array of 2-dimensional unit cells. The dark central figure represents the reference molecule in the [00] unit cell, which does not overlap with any of the molecules in adjacent unit cells. Molecules in the $[\bar{1}1]$ and [10] unit cells, however, exhibit considerable overlap.

To avoid this overlap, the centers of mass of all the molecules in a $5 \times 5 \times 5$ array of unit cells are calculated. Atomic coordinates and interaction energies are calculated for those molecules whose centers of mass are separated from the reference molecule by less than the maximum molecular diameter plus minimum Van der Waals radius. In addition, the interaction energy between the reference

molecule and the molecules in the [11$\bar{1}$] unit cell are always calculated to facilitate the minimization process in the early stages when no molecules outside the reference unit cells may lie within the cutoff radius.

In a few cases, partial overlap was observed between molecules three unit cells apart. This generally occurred in the space group P$\bar{1}$ with 1 molecule per unit cell, and with long rod-like molecules such as octane, tetracene and pentacene. These occurrences, however were much rarer than those between molecules two unit cells apart, as was discussed above. For octane, for example, overlap between molecules three unit cells apart was observed only in space group P$\bar{1}$, and in only 3 of the 2240 calculated structures within this group. The list of the ten structures with the lowest energy in P$\bar{1}$, and their packing indices is shown in Table 5.1. In general, within in a space group, there are many structures which are fairly close in energy and packing index, and the relatively large increase in packing index observed in the four lowest-energy structures indicate that molecular overlap is occurring which had not been considered in the energy minimization process.

Table 5.1 Energy and packing indices of the ten lowest-energy structures in space group $P\bar{1}$ for octane, with 1 molecule per unit cell. The first four structures, which exhibit some overlap, have packing indices markedly higher than the other structures

E (kcal/mol)	Packing Index
-24.61	0.837350
-24.61	0.837350
-24.08	0.764690
-23.61	0.694996
-23.38	0.580684
-23.37	0.580348
-23.37	0.580272
-23.37	0.580042
-23.32	0.579678
-23.25	0.576929
-23.21	0.576569

For longer molecules such as tetracene and pentacene, the problem was even more apparent in that several packing indices greater than 1.0 were observed in space group $P\bar{1}$ with 1 molecule per unit cell. Table 5.2 shows the energies and packing indices of the top ten crystal structures for pentacene obtained in this space group when overlap between molecules 3 unit cells away was not considered. Table 5.3 shows the energies and packing indices of the ten best pentacene crystal structures obtained when interactions between molecules three unit cells away were considered. Although the packing indices were reduced significantly, there is still some overlap occuring between molecules four unit cells away.

Table 5.2 Pentacene, space group $P\bar{1}$, Z=1, with overlap three unit cells away

E (kcal/mol)	Packing Index
-45.33	1.471969
-48.40	1.322224
-45.48	1.283750
-47.50	1.251658
-46.05	1.227926
-46.58	1.207092
-44.90	1.048804
-44.55	0.889096
-44.71	0.886231
-44.87	0.886170

Table 5.3 The ten lowest energy structures obtained for pentacene in $P\bar{1}$when overlap between molecules 3 unit cells away was considered.

E (kcal/mol)	Packing Index
-43.65	0.8849
-38.61	0.7900
-37.97	0.6736
-37.95	0.6757
-37.56	0.6758
-36.07	0.6662
-35.91	0.6412
-35.52	0.6159
-34.90	0.6367
-34.71	0.6640

This phenomenon was not observed at all for molecules such as benzene, naphthalene, dimethyl fulvalene, etc. Even for the longer molecules such as pentacene, however, overlap of this type did not occur frequently enough (15 out of 2240) to justify the additional computation required to check every structure of these molecules. Therefore, the feature which checks molecules 3 unit cells away has been installed in the program as an option which can be used on various structures

when the problem is observed to occur. This feature uses the array of $5 \times 5 \times 5$ unit cells constructed above, but checks for molecular interactions between a reference molecule in the $[\bar{1}\bar{1}\bar{1}]$ unit cell and all molecules in unit cells with a $+2\vec{T}$ lattice translation vector, i.e. [200], [$\bar{1}$21], [221], etc. The occurence of overlap between molecules four unit cells away is so infrequent, however, that the option to check for it has not been included. Those cases in which it occurs can be detected by examination of the packing indices or by graphical inspection, and then discarded.

5.5. Optimization of Variables

Once the block of unit cells is constructed with the proper space group symmetry, the structure of the crystal is minimized with respect to all or part of the following variables:

Table 5.4 Ranges of variable used in structure minimization.

Variable	Description	Range
a, b, c	Lattice Dimensions	2.9Å $-$ 2.5* maximum molecular diameter
TX, TY, TZ	Fraction of unit cell dimension the first molecule is translated from the origin	0.0-0.5
RX, RY, RZ	Initial rotation around the x, y, and $z-$axes	$\pm 7.5°$
α, β, γ	Angles between the lattice vectors	$50° - 90°$

In the triclinic systems, space group $P\bar{1}$, all twelve variables are optimized. For orthorhombic systems with the molecules in general positions, α, β, and γ are fixed at 90°. For the groups with special positions occupied, all or part of the rotations and translations are fixed depending upon the symmetry of the space group.

Pairwise interactions are calculated between all atoms in molecules whose centers of mass are separated by less than the maximum Van der Waals diameter. The time required to minimize the energy of a triclinic crystal structure, with 12 variables, 2 benzene molecules per unit cell, and 2 atoms per molecule, requires approximately 490 milliseconds. An orthorhombic structure with six variables to optimize and 4 molecules per unit cell requires 110 milliseconds.

5.6 Effect of Machine Precision on Minimization

Minimization routines can rely on very small numeric differences in results to determine the derivative of a function with respect to a variable. If the evaluation of the function involves a large number of operations, on the order of several thousand or greater, the cumulative effect of small differences in each operation due to the precision level of the the computer can be significant enough to yield a different answer, and lead the minimization routine to a different local minimum. This problem became apparent when different local minima were obtained from otherwise-identical runs in which vectorization was enabled or disabled. The problem was traced to the following loop in which the Lennard-Jones energy between nearest neighbors, EPACK, is calculated:

Figure 5.7 FORTRAN loop where the Lennard-Jones Energy EPACK is calculated. BIG1 and BIG2 are the arrays of atomic coordinates, BIGSIG contains the σ values for the pairwise interactions, and BIGEPS holds the ϵ values. The calculation is broken down into many individual steps to take advantage of the Cray's multiple arithmetic functional units.

```
      DO 600 NA1=1,N1-1
        X2= (BIG1(NA1,1)-BIG2(NA1,1))**2
        XY2=(BIG1(NA1,2)-BIG2(NA1,2))**2+X2
        XYZ2=(BIG1(NA1,3)-BIG2(NA1,3))**2+XY2
        D6=(BIGSIG(NA1)/XYZ2)**3
        D12=(D6-1)*D6
        E612 =D12*BIGEPS(NA1)
        EPACK=EPACK + E612
600   CONTINUE
```

The loop control variable, N1, is the total number of all pairwise atomic interactions calculated and can easily reach 10^4 or 10^5. Different answers were obtained if the order of the steps were modified, as well as if the program was compiled with vectorization enabled or disabled for only this loop. Table 5.5 shows the results, and Table 5.6 shows selected intermediate values obtained when the above loop was vectorized, as well as when executed in scalar mode (vectorization disabled).

Table 5.5 The following results were obtained for 12 variables with vectorization enabled and with vectorization disabled for loop 600 above. The rest of the program was vectorized in both cases. Initial values and ranges were identical for both calculations.

Variable	Vectorization Disabled	Vectorization Enabled
A:	10.8404	5.7825
B:	9.9759	42.7647
C:	7.4670	6.2182
ALPHA:	73.65	90.00
BETA:	60.76	80.76
GAMMA:	60.00	60.00
ROTX:	7.50	22.50
ROTY:	-3.29	0.82
ROTZ:	7.50	7.50
TRANSX:	0.25	0.50
TRANSY:	0.50	0.04
TRANSZ:	0.00	0.00

Table 5.6 Intermediate values for the packing energy, EPACK, obtained when the above loop was executed with vectorization enabled and disabled.

	EPACK	
Iteration	Vectorization Disabled	Vectorization Enabled
1	-5.4101493903317E-5	-5.4101493903079E-5
2	-5.4100010497041E-5	-5.4100010496952E-5
3	-5.4102977348096E-5	-5.4102977348008E-5
4	-5.4099810610679E-5	-5.4099810610583E-5
5	-5.4103177251164E-5	-5.4103177251078E-5
6	-5.4099877413119E-5	-5.4099877413029E-5
7	-5.4103110442354E-5	-5.4103110442266E-5
8	-5.4101428670011E-5	-5.4101428669916E-5
9	-5.4101559136506E-5	-5.4101559136415E-5
10	-5.4101433989197E-5	-5.4101433989104E-5
...		
106	-8.44124919576	-8.442135384817
107	-8.44124919576	-8.442124462995
108	-8.44124919576	-8.442124462995
109	-8.44124919576	-8.442124462995
110	332105137.4145	-8.442124462995
111	-8.441249196363	314073581.2281
112	-8.441249196678	-8.44212446358
113	-8.441256300907	-8.442124463886
114	-8.442286800656	-8.442131318942
115	-8.450112195134	-8.443121042939
116	-8.451328578899	-8.450481053988
...		
430	-32.05549375401	-28.16078251094
431	-32.05605711931	-28.16083719133
432	-32.05601323661	-28.16079321902
433	-32.05613024967	-28.16078054556
434	-32.056003168	-28.16078262508
435	-32.05605174399	-28.16077749016
436	-32.05609634574	-28.16073438581
437	-32.05602447723	-28.16721956818

After studying this problem for several months, Cray Research determined that declaring EPACK as a double precision variable produces consistent solutions, irrespective of vectorization or summation order. Unfortunately, double precision on a Cray Computer is done in software and is considerably slower than single precision. Minimizations performed on various benzene structures required 8 times more cpu time when EPACK was declared double precision, than when single precision was used. In addition, double precision did not always yield local minima with lower energies, i.e. 'better' minima. Single and double precision results were compared for 351 starting positions for benzene crystal structures. The results are shown in Table 5.7. Double precision yielded a lower local minimum in 47.6% of the trial structures, single precision in 42.2%, and equal results were obtained in 10.2% of the cases. The average number of iterations to obtain a minimum was virtually identical in both cases (649).

Table 5.7 Comparison of results obtained for 351 structures with EPACK declared as a single or double precision variable. EPACK was the quantity minimized in both cases. ELJ is the Lennard-Jones energy obtained with a 10 Å cutoff radius on the minimized structures, and ECOUL is the coulombic energy determined by the molecular multipole model described previously. The number of iterations reported is the total number of iterations required to minimize all 351 structures.

Number of Minima (structures) with Lower Energy			
	SINGLE PRECISION	DOUBLE PRECISION	TIE
EPACK	148	167	36
ELJ	139	170	42
ECOUL	193	158	0
Total # of iterations.	227816	227818	

When single and double precision results were compared for benzene in all space groups, it was observed that the relative energy ranking between the space groups did not change with the level of precision. The minima obtained in either case were valid and reasonable, and the lowest energy structures obtained in each space group were found to be equivalent. In view of these similarities, and the factor of 8 difference in speed, the results in this study were obtained using single precision.

5.7. Sorting the Close-Packed Structures

The closest-packed structures obtained from the minimization process must be sorted to produce a list of the most probable structures. Several methods were investigated to determine which would be fast enough to perform on the two to ten thousand minimized structures, yet yield reasonable agreement with a more extensive energy calculation. The packing index, or fraction of space filled, was examined to determine if it was sufficient to form a reasonable basis for sorting the minimized structures. The packing index, although requiring negligible time to calculate, correlated only in a general way with the fully converged Lennard-Jones energy. Small though significant variations were observed, i.e., the structures with the highest packing index did not always exhibit the lowest energy, primarily due to the contribution of large repulsive energies from crowded atoms.

Examples of the relationship between packing index and fully converged Lennard-Jones energy between space groups (Table 5.8) and within a space group (Table 5.9) are shown below.

Table 5.8 Lennard-Jones energies (E_{lj}) and packing indices (PI) for the lowest-energy structures in each space group for naphthalene. The structures are listed in decreasing order with respect to the packing index

Space Group	Z	PI	E_{lj} (kcal/mol)
$P2_1$		20.6098	-16.69
$P2_1/c$		20.6056	-16.61
$Pnma$		40.6034	-16.11
$P2_1/a$		20.6031	-16.47
Pca		40.6004	-16.04
$P2_1/c$		40.6002	-16.65
Pna		40.5998	-16.00
$P2_12_12_1$		40.5970	-16.24
$P\bar{1}$		20.5932	-15.89
$P\bar{1}$		10.5931	-15.89
Cmc		40.5913	-15.14
$P2_1/a$		40.5850	-15.22
$C2/c$		40.5814	-15.12
$Pbca$		40.5699	-14.61
$Pbcn$		40.5650	-14.63
Pmc		20.5166	-13.27

Table 5.9 Comparison of packing indices and Lennard-Jones energies for 11 local minima within the same space group, $P2_1/a$, Z=2, for naphthalene.

PI	E_{lj} (kcal/mol)
0.584720	-15.36
0.563009	-14.20
0.555225	-14.17
0.554735	-14.12
0.554713	-14.14
0.554669	-13.89
0.553573	-14.06
0.541519	-13.07
0.539565	-13.20
0.509434	-11.92
0.493190	-12.07

5.7.1. Lennard-Jones Energy

To calculate the Lennard-Jones energy of the closest-packed structures to convergence, it is necessary to go beyond nearest neighbor interactions. The cutoff radius typically used for the Lennard-Jones potential in inert gases is $2.5\sigma_{ij}$ [121] where σ_{ij} is the interaction radius parameter in Equation 3.1. Following this rule of thumb for benzene, where the largest possible value of σ_{ij} is 3.388 Å for a carbon-carbon interaction, a sufficient cutoff radius would then be equal to 8.470 Å. To test this assumption, cutoff radii from 5 to 20 Å for Lennard-Jones interactions for benzene were evaluated in seven closest-packed structures from three different space groups. The results, expressed in percent of the energy obtained with a cutoff radius of 20 Å, are shown in Table 5.10. The origin of the cutoff radius is set at the atomic center. When the energy was plotted versus the cutoff radius (Figure 5.8), it was observed that the energy curves for the different structures did not cross. Therefore we selected 10 Å as the optimum cutoff radius, as it represents a balance between conversion of the Lennard-Jones energy (92-97%) and computational time. In the program, the number of additional unit cells which are generated are dependent upon the magnitude of the lattice constants, to ensure that the minimum number of additional cells are generated. The Lennard-Jones calculation using a 10 Å cutoff radius requires an additional 8.2 milliseconds of computer time per structure.

Table 5.10 Lennard-Jones energy for benzene in kcal/mol using various cutoff radii. Structure 1 in the monoclinic space group $P2_1$ with Z=4, Structure 2 is the triclinic space group $P\bar{1}$ with Z=2, and Structure 3 is the orthorhombic space group *Pbca* with Z=4. E_{20} is the Lennard-Jones energy obtained using a 20 Å cutoff radius.

Cutoff Radius, Å	Structure 1		Structure 2		Structure 3	
	E_{LJ}	$\%E_{20}$	E_{LJ}	$\%E_{20}$	E_{LJ}	$\%E_{20}$
5.00	-6.298	61.0171	-6.074	68.6986	-6.485	64.1055
6.00	-8.332	80.7209	-6.992	79.0902	-7.850	77.5962
7.00	-9.059	87.7662	-7.704	87.1420	-8.895	87.9205
8.00	-9.433	91.3889	-8.111	91.7483	-9.263	91.5593
9.00	-9.734	94.3109	-8.322	94.1329	-9.518	94.0785
10.00	-9.914	96.0534	-8.493	96.0663	-9.703	95.9062
11.00	-10.03	97.2044	-8.589	97.1529	-9.831	97.1801
12.00	-10.11	97.9423	-8.657	97.9199	-9.904	97.9002
14.00	-10.21	98.9273	-8.743	98.8874	-10.01	98.8991
16.00	-10.27	99.4559	-8.793	99.4547	-10.06	99.4523
18.00	-10.30	99.7891	-8.822	99.7860	-10.09	99.7763
20.00	-10.32	100.000	-8.841	100.000	-10.12	100.000

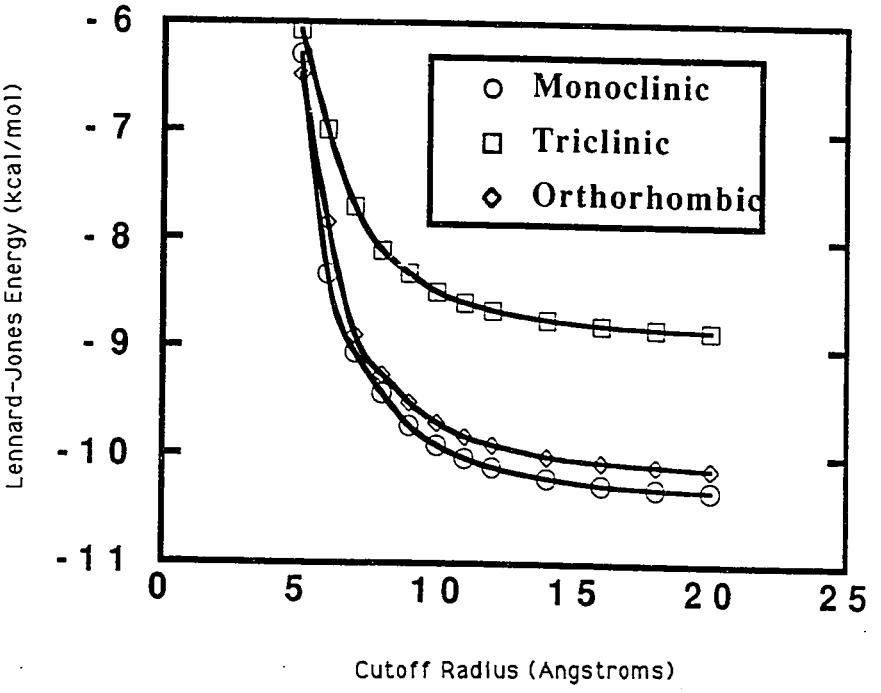

Figure 5.8 Lennard-Jones energy calculated using cutoff radii from 5 to 20 Å.

5.7.2 Electrostatic Interactions

The background, theory, accuracy and efficiency of the various models used to calculate the electrostatic energy in molecular solids have been discussed in Chapter 4. In our program, the electrostatic energy is calculated using molecular multipole interactions. These moments, up through hexadecapole, can be calculated using the Gaussian programs, although only dipole and quadrupole moments are used in this portion of the program. All moments are positioned at the molecular center of mass. Any rotations which are performed on the atomic position vectors are also performed on the multipole tensors according to equations 5.9 and 5.10:

$$\mu' = D\mu \qquad \text{[Eq. 5.9]}$$

$$Q' = DQD^{-1} \qquad \text{[Eq. 5.10]}$$

where D is a 3 × 3 matrix of direction cosines associated with a given rotation, μ is the 1 × 3 dipole moment tensor, and Q and Q' are the 3 × 3 quadrupole tensors. The rotations due to symmetry transformations involve changes of sign of the relevant components in the tensors. For example, the symmetry operation for a screw axis, $(x, y, z,) \rightarrow (x, \frac{1}{2} - y, -z)$, results in the following transformation of the quadrupole tensor:

$$\begin{pmatrix} xx & xy & xz \\ yx & yy & yz \\ zx & zy & zz \end{pmatrix} \longrightarrow \begin{pmatrix} xx & -xy & -xz \\ -yx & yy & yz \\ -zx & zy & zz \end{pmatrix} \qquad \text{[Eq. 5.11]}$$

The positions of all the tensors, *i.e.* the centers of mass of the molecules, in a 5 × 5 × 5 array of unit cells are determined and their distance to the reference molecule calculated. To calculate the energy between two charge distributions, it is convenient to represent their positions and orientations in a coordinate system in which their z-axes are coincident and the x- and y-axes are parallel. A new z-unit vector ($\hat{z}'$) is defined along the vector $\vec{r}_{ab}$ as follows:

$$\hat{z}'_x = \frac{\vec{x}_a - \vec{x}_b}{|\vec{r}_{ab}|} \qquad \text{[Eq. 5.12]}$$

where A is the reference molecule and B is another molecule in the lattice, and $\vec{x}_i$ is the position vector of A or B. The y- and z-components of the z'-unit vector are obtained similarly.

The x' and y' unit vectors perpendicular to the z'-unit vector in the new common-z right-handed coordinate system are determined as follows. For each molecule B, an arbitrary vector $\vec{w}$ is chosen which is not parallel to the z'-axis. The y'-unit vector in the new system is then obtained by taking the cross-product of $\vec{w}$ and $\hat{z}'$ and normalizing it as in Equation 5.12 above. Taking the cross-product between the z'- and y'-unit vectors yields the x'-unit vector. These three unit vectors comprise the rotation matrix D of direction cosines necessary to transform the multipole moment tensors to the common-z coordinate system as in Equations 5.9 and 5.10 above. These values for the moment tensor elements obtained in cartesian coordinates are then expressed in terms of their spherical harmonics (Equation 4.17), and the dipole-dipole, dipole-quadrupole, and quadrupole-quadrupole energies are calculated as follows:

$$\phi_{ab} = \sum_{n_a=0}^{\infty} \sum_{n_b=0}^{\infty} \sum_{m=-n_<}^{+n_<} \frac{(-1)^{n_b+m}(n_a+n_b)!}{(n_a+|m|)!(n_b+|m|)!} \frac{1}{r_{ab}^{n_a+n_b+1}} Q_{n_a}^{m^*} Q_{n_b}^{m} \qquad \text{[Eq. 5.13]}$$

where n_a, n_b are the orders of the multipoles (0=monopole, 1= dipole, 2=quadrupole, etc.), $n_<$ is the smaller of n_a, n_b, and $Q_{n_a}^{m}*$ and $Q_{n_b}^{m}$ are the multipole moments.

5.8. Output

As the energy of each closest packed structure is calculated, it is compared with the three best structures within its space group, and with the ten best strucutres overall. These results are then reported. An example of an output file is located in Appendix D.

5.9. Summary

To summarize this section, each structure is sorted on the basis of the energy obtained from the following expression:

$$E = \sum_{ij} 4\epsilon_{ij}\left[\left(\frac{\sigma_{ij}}{r_{ij}}\right)^{12} - \left(\frac{\sigma_{ij}}{r_{ij}}\right)^{6}\right] + E_{coul} \qquad \text{[Eq. 5.14]}$$

where i is summed over all atoms in the reference molecule and j over all other atoms within a 10 Å radius, and E_{coul} is calculated as in Eq. 5.13 above.

Chapter 6 Results

Fifteen molecules were selected for this study. The results are presented the following sections:

The conventions used in this chapter are as follows:

Molecular Structure: In the beginning of each section the molecular structure is shown and two of the three principal axes of inertia, **L** and **M**, are indicated. The third principal axis, **N**, is perpendicular to the plane of the page, intersecting the other axes at the center of mass of the molecule.

Experimental Data: The temperature, space group, lattice constants and angles of the experimental structure are given. If the molecules are located at special positions, then the angles are given that the principal molecular axes make with the a, b, and c' axes of the lattice, where c' is perpendicular to the ab plane. Experimental heats of sublimation are given, if available.

Input for the Calculation: States the method used to obtain the atomic coordinates and molecular multipole moments. Lists the Van der Waals volume.

Table of Results for Each Space Group: The lowest energy structures obtained in each of the space groups are listed in order of increasing total energy. The number of molecules in the unit cell (Z), the Lennard-Jones and electrostatic energies, and the packing index of each structure are also indicated.

Space groups in which different Z are possible, $P\bar{1}$ and $P2_1/c$ for example, can be treated as different space groups in this listing, as the structures in each case may be quite different. For space groups which have different settings, e.g. $P2_1/a$ is a nonstandard setting of $P2_1/c$, separate listings for these settings are given if different structures were obtained. This is discussed in greater detail in subsequent sections where different minima were obtained for $P2_1/a$ and $P2_1/c$.

Structural Data for Predicted Space Groups: The lattice constants and angles of the lowest energy structures from the three most probable space groups are given. The predicted structure closest to experiment is also given, if not previously included in the top three. This structure corresponding to the experimental structure was found by searching a list of all local minima, and using a least squares procedure to compare lattice dimensions and angles with experimental values. These structures would then be examined graphically to ensure that the calculated structure was indeed similar to the experimental structure.

Graphical Representations of the Crystal Structures: The graphics are included at the end of each section. For each molecule several projections of the experimental structure are shown, followed by the three lowest energy predicted structures. In general, hydrogen atoms are not shown in order to simplify the representation of the crystal structure. Following the crystal structures, the relative orientations of the molecules in different symmetry positions or unit cells in the crystal are shown with respect to a common reference molecule. Projections of each pair of molecules are shown along each of the three principal axes of the reference molecule. Where necessary the molecular plane is rotated 5°to show some structural detail, instead of a 1-dimensional edge. Hydrogen atoms are included except for experimental structures for which their positions were not reported.

6.1. Benzene

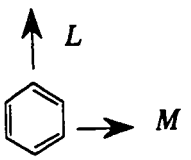

C_6H_6

6.1.1 Experimental Data

Heat of sublimation: 10.7 kcal/mol [122].

Experimental: [123]

Temperature:			138K
Space Group:			P*bca*
Molecules per cell:			4
a:	7.39	α:	90°
b:	9.42	β:	90°
c:	6.81	γ:	90°

6.1.2 Results

Input for calculations:

Coordinates:	Experiment
Multipole moments:	Gaussian 90, 6-31G basis set
Van der Waals Volume:	64.301 Å^3

Table 6.1 Lowest Energy Structures in Each Space Group for Benzene

Space Group	Z	Total Energy	E_{lj}	E_{coul}	Packing Index
$P2_12_12_1$	4	-11.98	-11.51	-0.47	0.5675
$P2_1$	2	-11.94	-11.44	-0.50	0.5646
$P2_1/c$	2	-11.91	-11.43	-0.44	0.5655
$P2_1/c$	4	-11.87	-11.43	-0.44	0.5655
Pna	4	-11.68	-11.21	-0.47	0.5597
$P\bar{1}$	2	-11.67	-11.26	-0.40	0.5652
$P\bar{1}$	1	-11.66	-11.31	-0.35	0.5616
Pca	4	-11.61	-11.11	-0.50	0.5450
$C2/c$	4	-11.49	-11.62	0.13	0.5709
$Pbca$	4	-11.46	-11.10	-0.36	0.5641
Cmc	4	-11.28	-10.90	-0.38	0.5443
$Pnma$	4	-10.84	-10.38	-0.46	0.5310
$C2/c$	4	-10.65	-10.51	-0.14	0.5582
$Pbcn$	4	-10.30	-10.53	0.23	0.5394
Pmc	2	-8.27	-7.81	-0.46	0.4419
Cmc	4	-6.88	-7.96	1.08	0.4399

Predicted Structure with Lowest Energy:

Space Group: $P2_12_12_1$
Molecules per cell: 4
Packing index: 0.5675

a:	14.2331	α:	90°	Energy:	-11.98
b:	5.6436	β:	90°	Lennard-Jones:	-11.51
c:	5.6420	γ:	90°	Coulombic:	-0.469

Structure With Lowest Energy in Second Most Probable Space Group:

Space Group: $P2_1$
Molecules per cell: 2
Packing index: 0.5645

a:	7.0254	α:	90°	Energy:	-11.94
b:	5.9442	β:	72.81°	Lennard-Jones:	-11.44
c:	5.7099	γ:	90°	Coulombic:	-0.4986

Structure With Lowest Energy in Third Most Probable Space Group:

Space Group: $P2_1/c$
Molecules per cell: 2
Packing index: 0.5647

a:	5.797	α:	90°	Energy:	-11.91
b:	5.791	β:	70.78°	Lennard-Jones:	-11.44
c:	7.183	γ:	90°	Coulombic:	-0.476

Predicted Structure Closest to Experiment:

Space Group: P*bca*
Molecules per cell: 4
Packing index: 0.5578

a:	6.804	α:	90°	Energy:	-11.36
b:	9.356	β:	90°	Lennard-Jones:	-10.87
c:	7.436	γ:	90°	Coulombic:	-0.484

6.1.3. Discussion of Benzene Results

Benzene crystallizes in a herringbone configuration in space group P*bca*, Z=4, in which the molecules are arranged in an edge-to-face manner at 87°angles (Fig.6.1.1 and Fig.6.1.5). The lowest energy structures predicted by ICE9 also exhibit the herringbone configuration. The three lowest in energy of these structures are shown in Fig. 6.1.2-6.1.4 and Fig. 6.1.6-6.1.9. The principal difference in structure between the experiment and the lowest energy predicted structure in $P2_12_12_1$ is that the principal axes of the molecules are inclined $\sim 53°$within layers in the predicted structure (Fig. 6.1.2 (d)), and $\sim 87°$in experiment.

A local minimum corresponding to the experimental structure was found which exhibited slightly higher electrostatic energy (-0.36 vs. -0.47 kcal/mol) as well as Lennard-Jones energy (-11.10 vs. -11.51 kcal/mol) than the global minimum in $P2_12_12_1$, for a total energy difference of 0.52 kcal.mol. The difference between the predicted and the observed lattice constants were small: 0.05 Å, -0.06 Å, -0.01Å. It should be noted that the experimental benzene structure was used in the parameterization.

Overall, ICE9 found ten structures in eight different space groups to be very close in energy, i.e. within 0.52 kcal/mol of the global minimum. All but two of these structures exhibited a herringbone configuration. The electrostatic energies of the ten lowest energy strucutres fell within the narrow range of -0.35 to -0.50 kcal/mol, with the exception of $C2/c$ with an electrostatic energy of +0.13 kcal/mol. The slipped-stack of pancakes configuration in $P\bar{1}$ possessed a negative electrostatic energy of -0.40 kcal/mol, as low as or lower than many of the herringbone structures.

The results obtained for benzene were compared with those calculated using Williams' program PCK83. PCK83 obtained good values for the lattice constants for the experimental structure, of course, the differences being 0.03 Å, -0.12 Å, and 0.18 Å. These results were obtained using the experimental structure as the starting point for the calculation. Calculations using PCK83 were also performed using several different starting positions distributed among several space groups, and the lowest energy results obtained for each group are shown in Table 6.1.2. Although the search of possible structures using PCK83 was hardly exhaustive, the results obtained were similar to those using ICE9 in that many structures in

different space groups were found to be close in energy to the global minimum. Surprisingly, Williams' method, which yields a much greater electrostatic contribution to the lattice energy, did not give a significantly different ordering of the space groups. The global minimum found by PCK83 was in the same space group, $P2_12_12_1$, as that predicted by ICE9. The energy of this global minimum found by PCK83 was 0.15 kcal/mol lower than that obtained by the same program for the experimental structure in P*bca*. In addition, local minima were found in space groups $P2_1$ and $P2_1/c$ with energies comparable to the experimental structure in P*bca*. In short, Williams program was not able to distinguish the experimental structure from a number of very close possibilities with any better success than ICE9.

Table 6.1.2 Energies calculated using PCK83 (kcal/mol)

Space Group	E_{Total}	E_{Coul}
$P2_12_12_1$	-12.6614	-2.1611
P*bca**	-12.5116	-2.3106
$P2_1/c$	-12.4545	-1.8308
$P2_1$	-12.4521	-1.2633
$P\bar{1}$	-11.6185	-1.7209
P*na*	-11.2614	-2.7698

*Experimental structure

One surprising result using PCK83 was the discovery of several slipped-stack of pancake structures in $P\bar{1}$with large negative electrostatic energies comparable to the experimental and other edge-to-face herringbone structures. As has been discussed previously in Section 2.4, Williams had justified the use of large partial charges on hydrogen and carbon as necessary to reproduce the herringbone configuration. This was demonstrated in the gas phase with benzene dimers, but

Williams did not examine parallel slipped-stack configurations in the solid for possible structures which could also have large negative electrostatic energies.

The electrostatic energies obtained by Williams program for these structures, using partial charges on the atoms of +0.153 *e* for hydrogen and -0.153 *e* for carbon, was four times greater than those using the molecular multipole moment model in ICE9. To compare the effect of larger electrostatic energies on the ordering of the space groups in ICE9, the above calculations on benzene were repeated with ICE9, but using molecular multipole moments which were double the experimental value of Qzz = -5.6 Debye-Å. The search performed by ICE9 was exhaustive, and the results obtained for the different space groups are shown in Table 6.1.3 in order of increasing energy. Doubling the molecular quadrupole moment gave electrostatic energies nearly as large as those obtained by Williams, and did not improve the ability of the program to distinguish the experimental structure from many close possibilities. Although the electrostatic energy obtained for the experimental structure was lower than that obtained for the best structures in all of the other space groups, the experimental structure had a higher Lennard-Jones energy than several others, and was not distinguished from other structures with very similar total energies. The experimental structure was 0.61 kcal/mol higher in energy than the global minimum in this case, compared to 0.52 kcal/mol higher using the observed values for the multipole moments.

Table 6.1.3 Lowest energy structures in each space group calculated using quadrupole moments of double the experimental value. Energy is given in kcal/mol.

Space Group	Z	Total Energy	E_{lj}	E_{coul}	Packing Index
$P2_1/c$	2	-13.21	-11.60	-1.614	0.5697
$P2_1/c$	4	-13.10	-11.44	-1.656	0.5654
$P2_1$	2	-13.03	-11.44	-1.590	0.5645
$P2_12_12_1$	4	-12.81	-11.30	-1.506	0.5608
$P\bar{1}$	2	-12.80	-11.14	-1.655	0.5603
Pna	4	-12.78	-11.23	-1.550	0.5560
Pca	4	-12.71	-11.11	-1.600	0.5561
$P\bar{1}$	1	-12.64	-11.18	-1.461	0.5599
Cmc	4	-12.53	-10.87	-1.652	0.5427
$Pbca$	4	-12.60	-10.92	-1.681	0.5446
$Pnma$	4	-11.90	-10.40	-1.494	0.5354
$C2/c$	4	-11.87	-10.93	-0.946	0.5492
$C2/c$	4	-10.57	-10.13	-0.438	0.5407
$Pbcn$	4	-9.752	-10.16	0.411	0.5268
Pmc	2	-9.242	-7.769	-1.473	0.4406
Cmc	4	-4.591	-8.028	3.437	0.4427

6.4.4. Graphical Representations of Benzene Crystal Structures

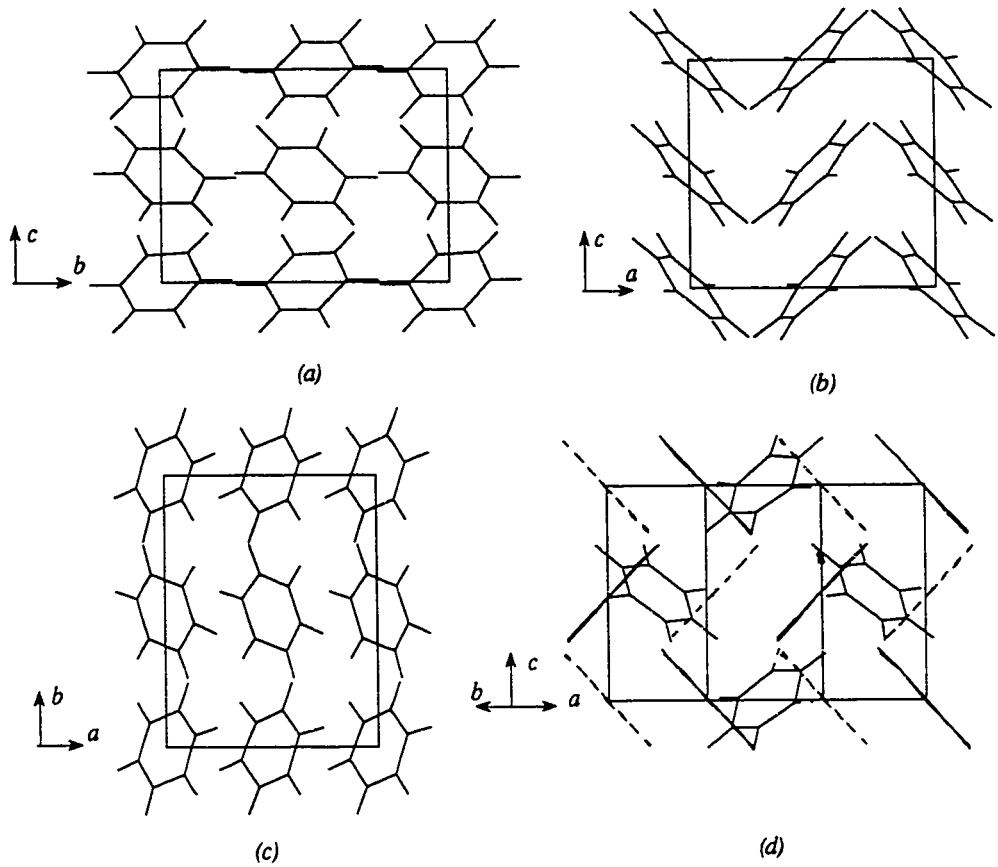

Figure 6.1.1. Experimental structure of benzene, space group P*bca*. (a). Projection along *a* axis. (b). Projection along *b* axis. (c). Projection along *c* axis. (d). Projection parallel to molecular plane of all layers. The second layer is indicated by dashed lines.

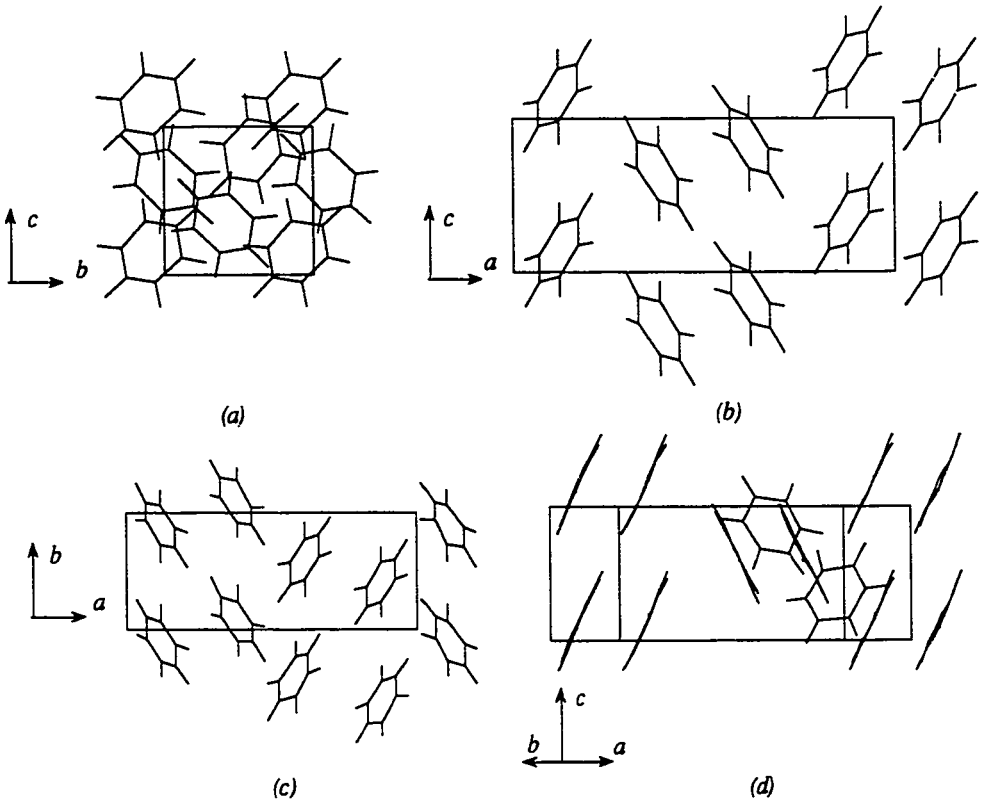

Figure 6.1.2. Most probable structure of benzene predicted by the program, space group $P2_12_12_1$. (a). Projection along *a* axis. (b). Projection along *b* axis. (c). Projection along *c* axis. (d). Projection of all layers along molecular plane.

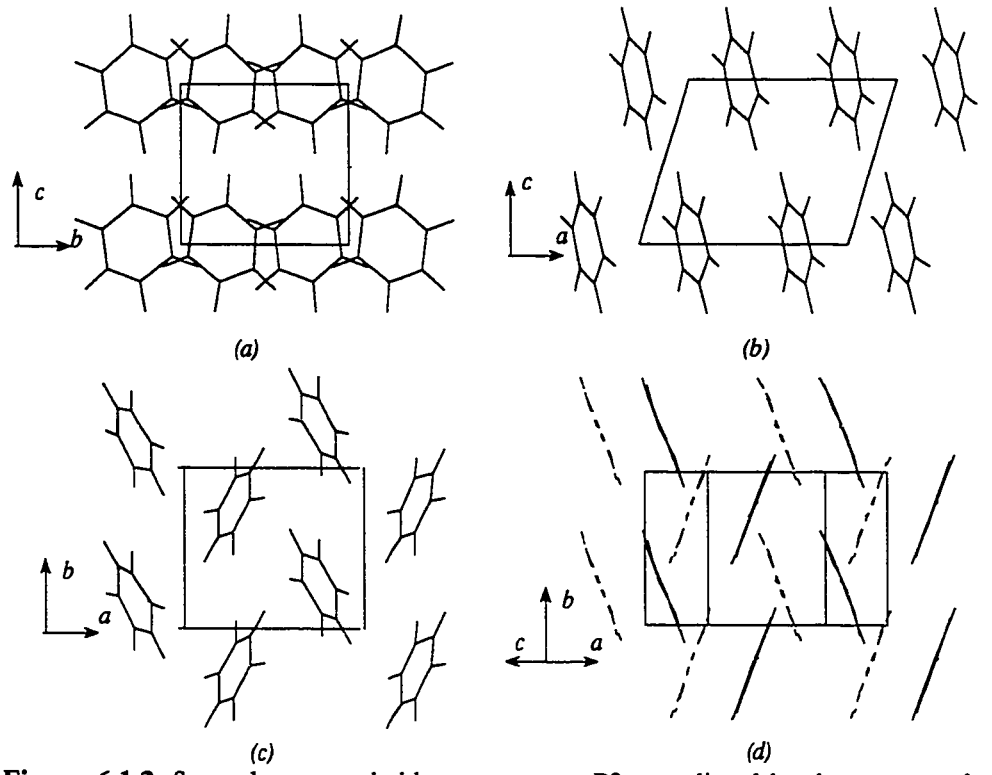

Figure 6.1.3. Second most probable space group $P2_1$, predicted by the program for benzene (a). Projection along *a* axis. (b). Projection along *b* axis. (c). Projection along *c* axis. (d). Projection along molecular plane of all layers. The second layer is indicated by dashed lines.

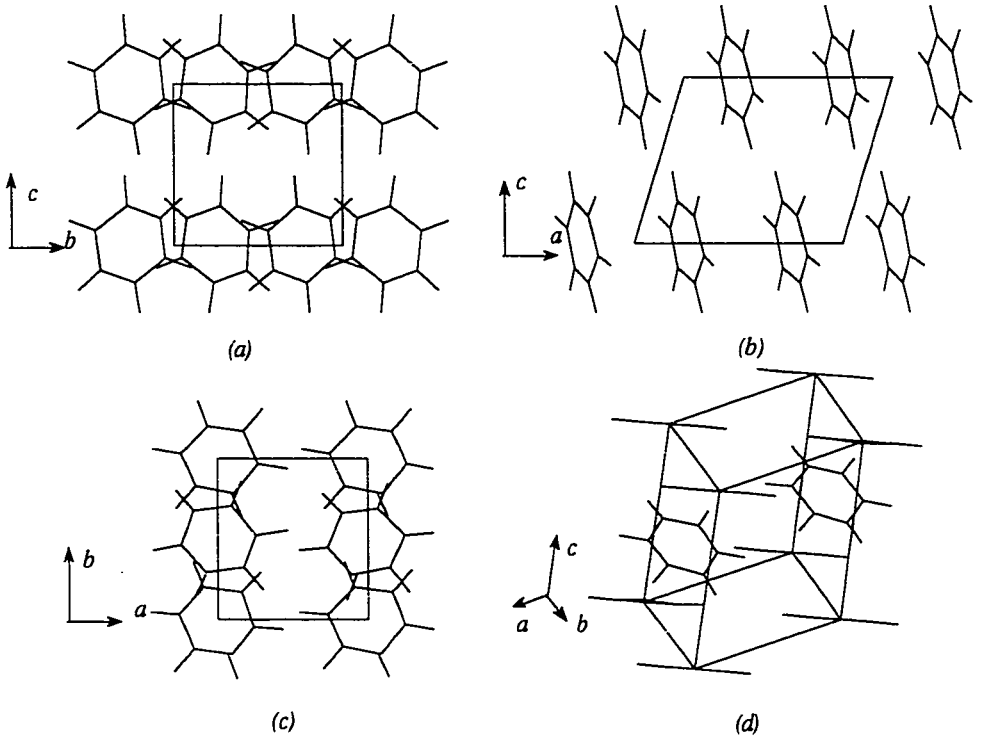

Figure 6.1.4. Third most probable space group $P2_1/c$, predicted by the program for benzene. (a). Projection along *a* axis. (b). Projection along *b* axis. (c). Projection along *c* axis. (d). General view.

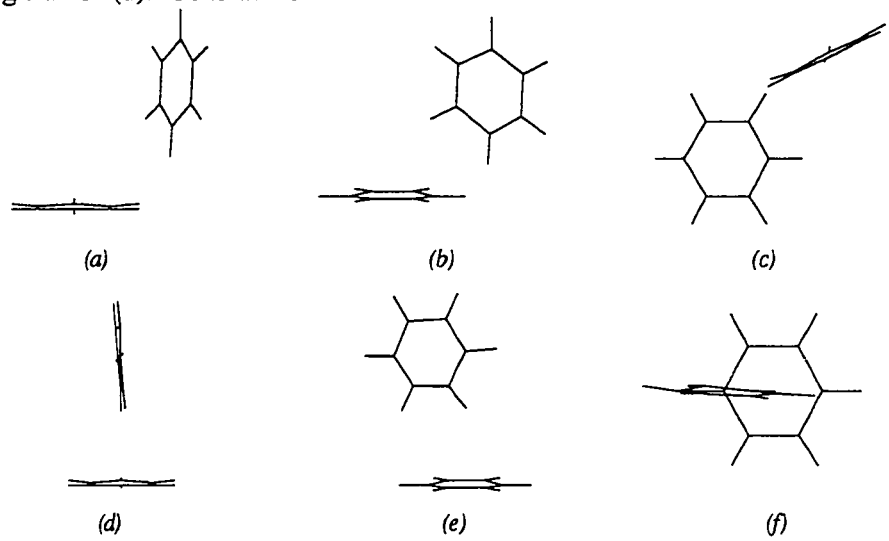

Figure 6.1.5. Two of the four symmetry positions in the unit cell in the experimental structure of benzene, as viewed along the principal axes of one of the molecules.

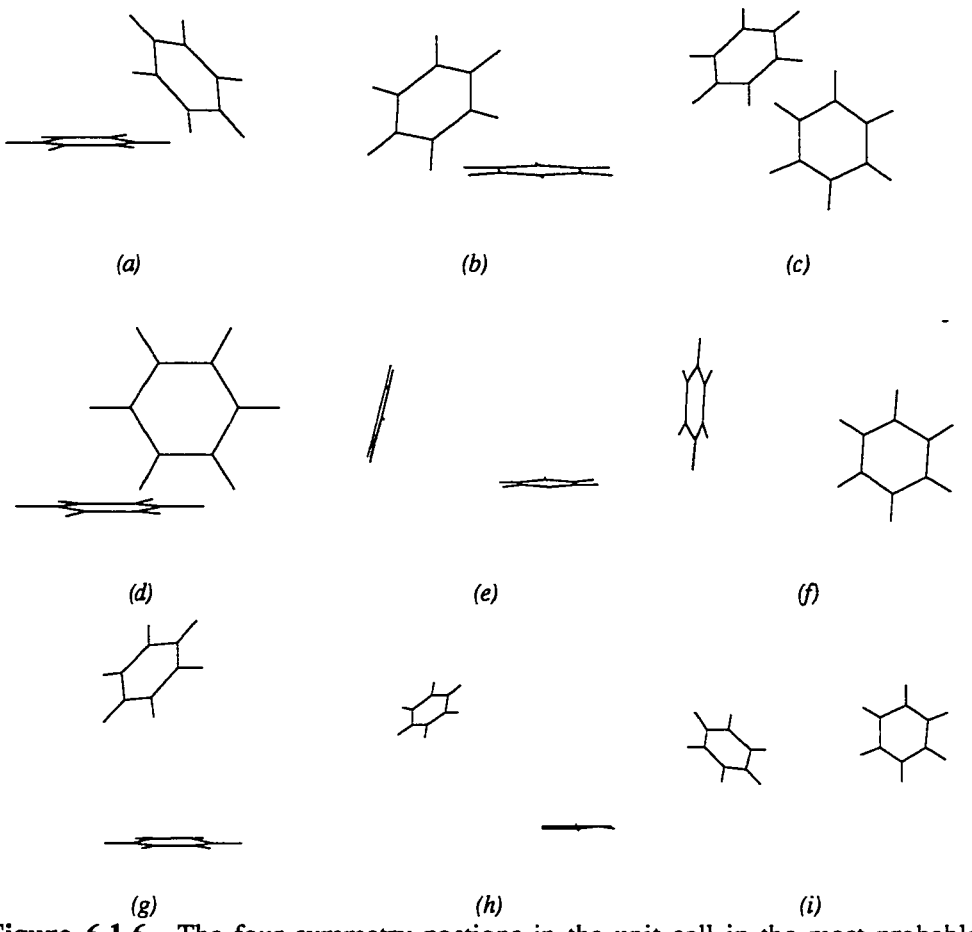

Figure 6.1.6. The four symmetry postions in the unit cell in the most probable structure of benzene, as viewed along the principal axes of one of the molecules.

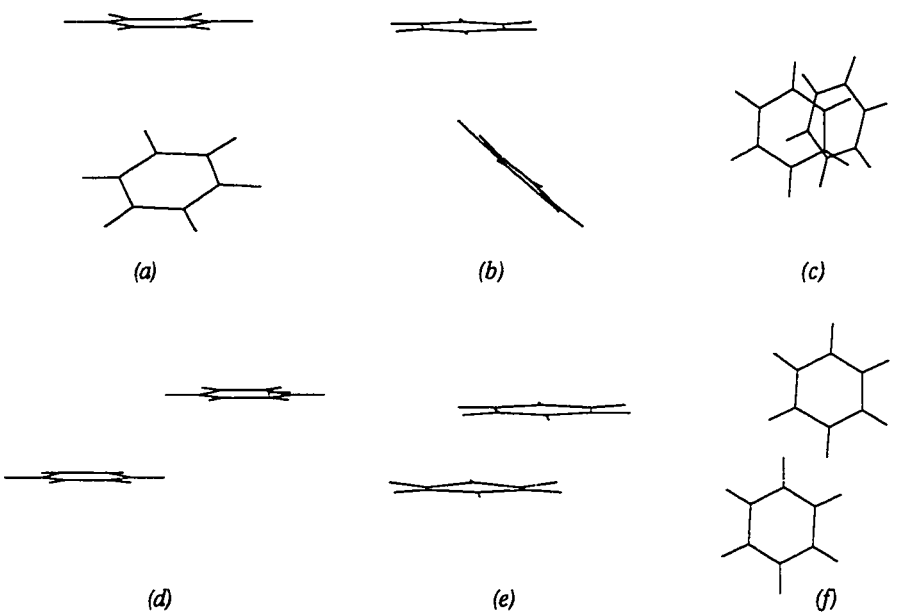

Figure 6.1.7. (a)-(c). The two molecules in the unit cell in the second most probable space group for benzene, as viewed along the principal axes of one of the molecules. (d)-(f). Nearest neighbor molecules in adjacent unit cells in the [001] direction.

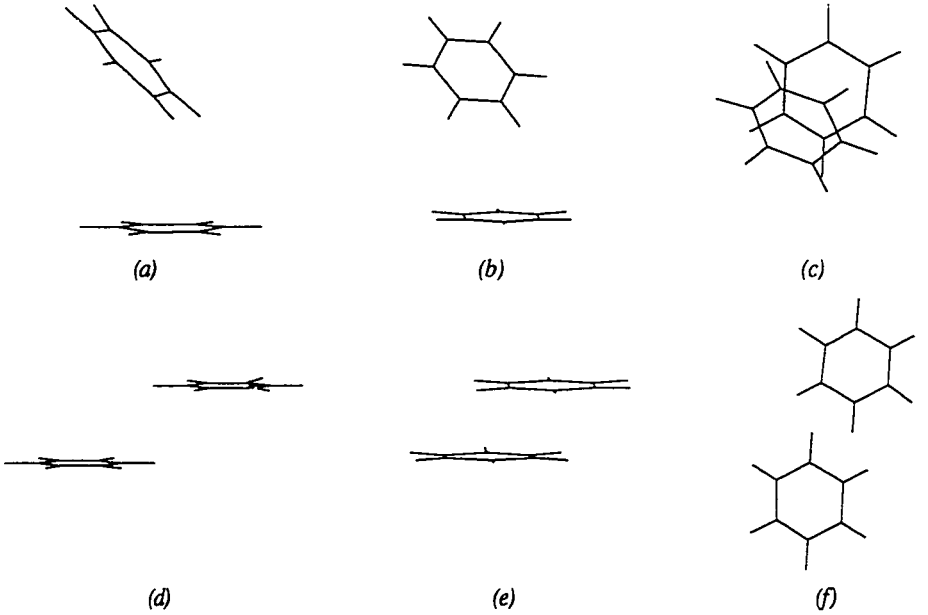

Figure 6.1.8. (a)-(c). The two molecules in the unit cell in the third most probable space group for benzene, as viewed along the principal axes of one of the molecules. (d)-(f). Nearest neighbors in adjacent unit cells in the [010] direction.

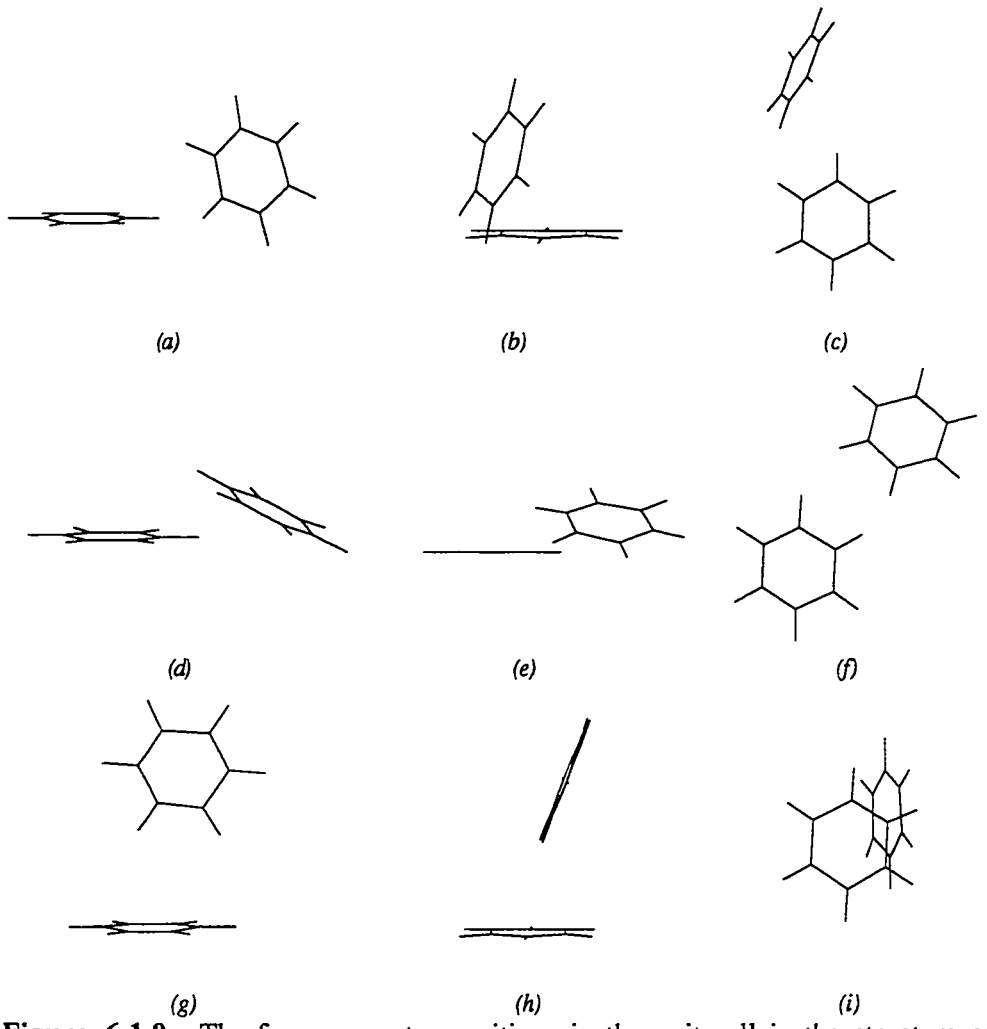

Figure 6.1.9. The four symmetry positions in the unit cell in the structure of benzene closest to the experimental structure.

6.2. Naphthalene

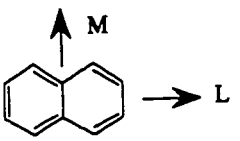

$C_{10}H_8$

6.2.1 Experimental Data

Heat of sublimation: 15.3-16.8 kcal/mol [124], 17.2 kcal/mol [125].

Experimental 1 [126]:

Temperature: 78K
Space Group: $P2_1/a$
Molecules per cell: 2

a:	8.124	α:	90°
b:	5.950	β:	124°40′
c:	8.636	γ:	90°

$LOa = 115.8°$ $MOa = 71.2°$ $NOa = 32.8°$
$LOb = 102.6°$ $MOb = 29.45°$ $NOb = 116.3°$
$LOc' = 29.0°$ $MOc' = 68.2°$ $NOc' = 71.9°$

Experimental 2 [127]:

Temperature: 293K
Space Group: $P2_1/a$
Molecules per cell: 2

a:	8.235	α:	90°
b:	6.002	β:	122°55′
c:	8.6575	γ:	90°

6.2.2 Results

Input for calculations:

Coordinates: Experiment
Multipole moments: Gaussian 90, 6-31G basis set
Van der Waals Volume: 104.321 Å^3

Table 6.2 Lowest Energy Structures in Each Space Group for Naphthalene

Space Group	Z	Total Energy	E_{lj}	E_{coul}	Packing Index
$P2_1/a$	2	-17.57	-17.07	-0.49	0.6174
$P2_1/c$	4	-17.40	-16.65	-0.75	0.6002
$P2_1$	2	-17.37	-16.69	-0.68	0.6098
$P2_1/c$	2	-17.36	-16.61	-0.74	0.6056
$P2_12_12_1$	4	-17.10	-16.24	-0.86	0.5970
Pca	4	-16.86	-16.04	-0.82	0.6004
$P2_1/a$	4	-16.79	-15.96	-0.83	0.5985
$P\bar{1}$	2	-16.78	-15.89	-0.89	0.5932
$P\bar{1}$	1	-16.75	-15.89	-0.86	0.5931
Pna	4	-16.67	-16.00	-0.67	0.5998
$Pnma$	4	-16.27	-16.11	-0.16	0.6034
$C2/c$	4	-15.84	-15.12	-0.72	0.5814
Cmc	4	-15.58	-15.14	-0.44	0.5913
$Pbca$	4	-15.15	-14.61	-0.54	0.5699
$C2/c$	4	-14.99	-14.85	-0.14	0.5701
$Pbcn$	4	-14.69	-14.63	-0.61	0.5650
Pmc	2	-14.54	-13.27	-1.27	0.5166
Cmc	4	-11.36	-11.29	-0.07	0.4727

Predicted Structure with Lowest Energy:

Space Group: $P2_1/a$
Molecules per cell: 2
Packing index: 0.6174

a:	10.265	α:	90°	Energy:	-17.57
b:	6.014	β:	71.96°	Lennard-Jones:	-17.07
c:	5.756	γ:	90°	Coulombic:	-0.493

Structure with lowest energy in second most probable space group:

Space Group: $P2_1/c$
Molecules per cell: 4
Packing index: 0.6078

a:	13.641	α:	90°	Energy:	-17.40
b:	4.610	β:	60.00°	Lennard-Jones:	-16.65
c:	12.606	γ:	90°	Coulombic:	-0.752

Structure with lowest energy in third most probable space group:

Space Group: $P2_1$
Molecules per cell: 2
Packing index: 0.6098

a:	6.743	α:	90°	Energy:	-17.37
b:	4.787	β:	90°	Lennard-Jones:	-16.69
c:	10.598	γ:	90°	Coulombic:	-0.68

Predicted Structure Closest to Experiment:

Space Group: $P2_1/a$
Molecules per cell: 2
Packing index: 0.5901

a:	8.071	α:	90°	Energy:	-16.68
b:	5.826	β:	60.31°	Lennard-Jones:	-15.83
c:	8.653	γ:	90°	Coulombic:	-0.8484

6.2.3. Discussion of Naphthalene Results

Naphthalene crystallizes in the edge-to-face configuration in $P2_1/a$ shown in Fig. 6.2.1. The program predicted the correct space group, $P2_1/a$ with Z=4 and the correct type of packing, although there are some differences with the experimental structure. The main difference between the predicted structures with the lowest energy and the observed experimental structure is that in the predicted structures, the molecules are positioned at very nearly 90°with respect to each other, whereas in the experimental structure the angle is $\sim$ 55° along

all three principal axes of the molecule. These differences can be clearly seen in Figures 6.2.5-6.2.8 with respect to the principal axes of inertia of a reference molecule in the structure. In the experimental structure the molecules are more nearly aligned along the c axis, as can be seen in Figs. 6.2.1(b) and (d). A local minimum corresponding to the experimental structure was observed (Fig. 6.2.4), with an energy of -17.26 kcal/mol, compared to the lowest energy of -17.57 kcal/mol. The electrostatic energy exhibited by this structure, -1.001, was twice that of the lowest energy structure overall, -0.49 kcal/mol, but the Lennard-Jones energy and packing index were smaller, -16.26 and 0.6007, as compared to -17.07 kcal/mol and 0.6174.

The top seven structures predicted by the program exhibited the herringbone configuration. The three best of these are shown in Figures 6.2.2 - 6.2.4 and 6.2.6 - 6.2.8. The slipped-stack of pancakes structure for naphthalene exhibited a lower electrostatic energy, -0.89 kcal/mol, than almost all of the lowest energy structures in each of the space groups examined in Table 6.3.

Separate listings are shown for $P2_1/a$ and $P2_1/c$ in Table 6.2, although they represent different settings of the same space group. The $P2_1/a$ setting was run in addition to the $P2_1/c$ orientation to facilitate the comparison with experimental results. The difference in the lowest energy local minima in these two orientations indicates that the search grid is not fine enough to obtain every local minimum. Decreasing the rotational increments in successive runs from 15° to 5° would be prohibitively time consuming to perform in all space groups, but can be done on an individual basis if desired.

6.2.4. Graphical Representations of Naphthalene Crystal Structures

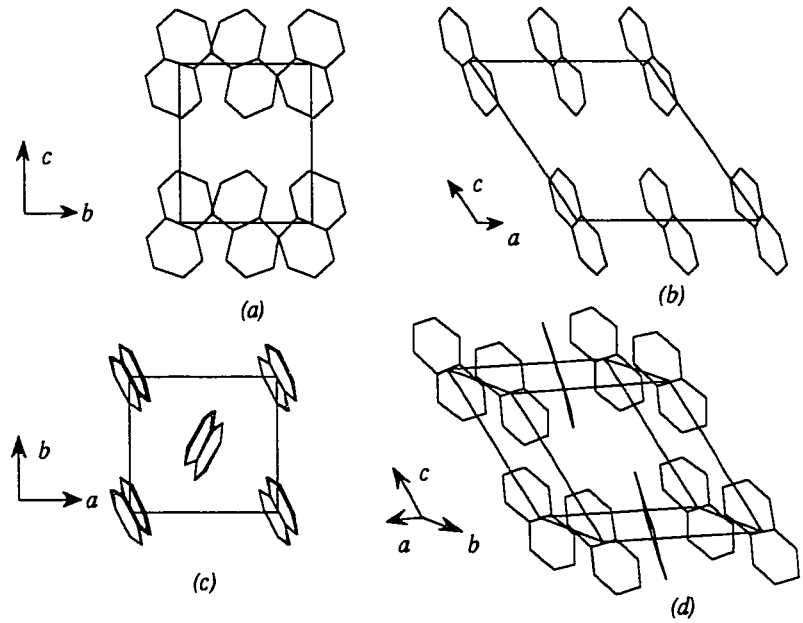

Figure 6.2.1. Experimental structure of naphthalene, space group $P2_1/a$. (a). Projection along *a* axis. (b). Projection along *b* axis. (c). Projection along *c* axis. (d). General view.

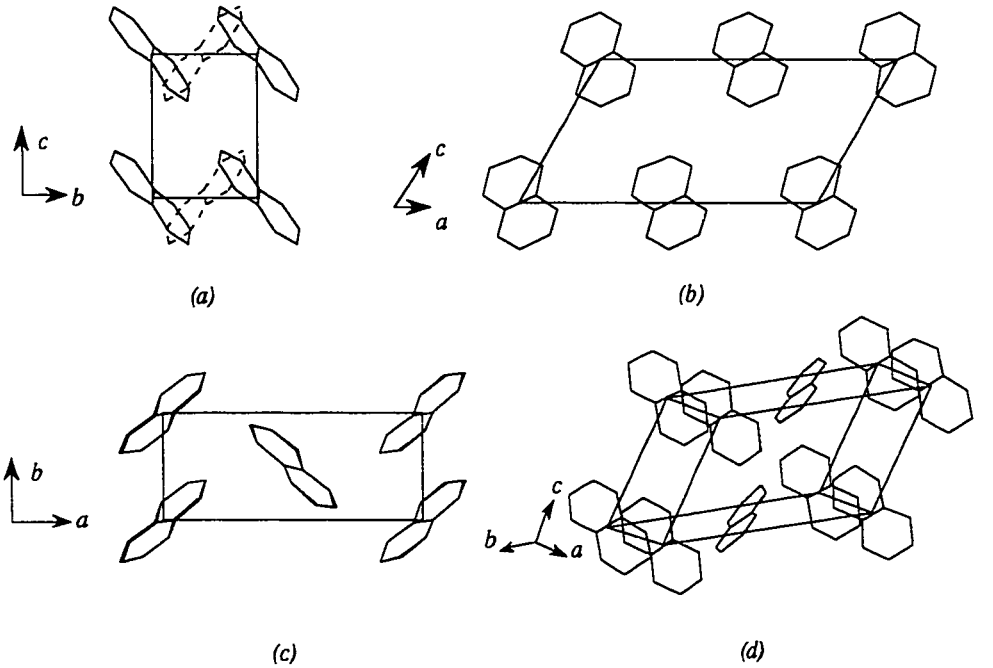

Figure 6.2.2. Lowest energy structure predicted for naphthalene, space group $P2_1/a$. (a). Projection along a axis. Second layer is indicated with dashed lines. (b). Projection along b axis. (c). Projection along c axis. (d). General view.

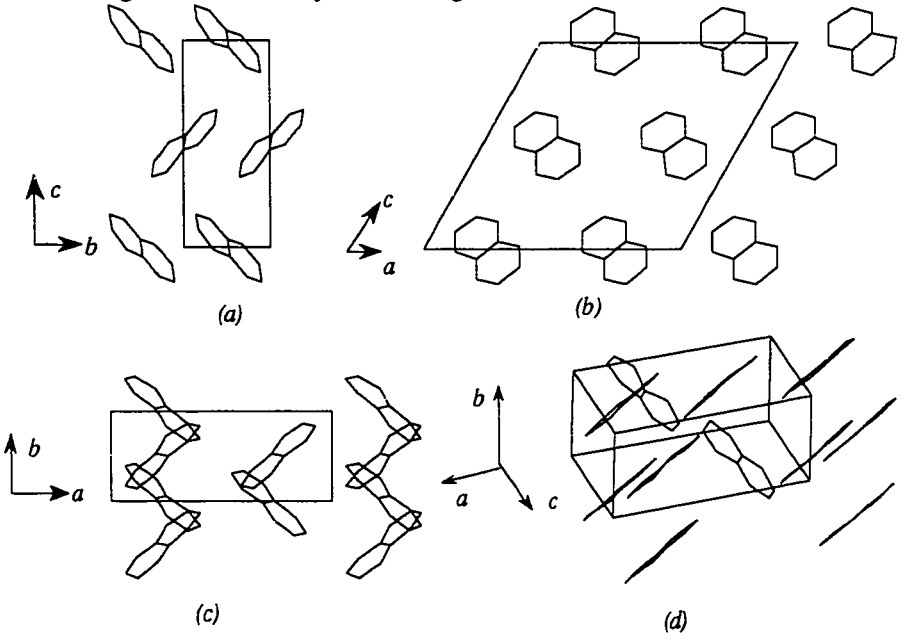

Figure 6.2.3. Second lowest energy space group, $P2_1/c$, predicted for naphthalene. (a). Projection along *a* axis. (b). Projection along *b* axis. Second layer is indicated with dashed lines. (c). Projection along *c* axis. (d). General view.

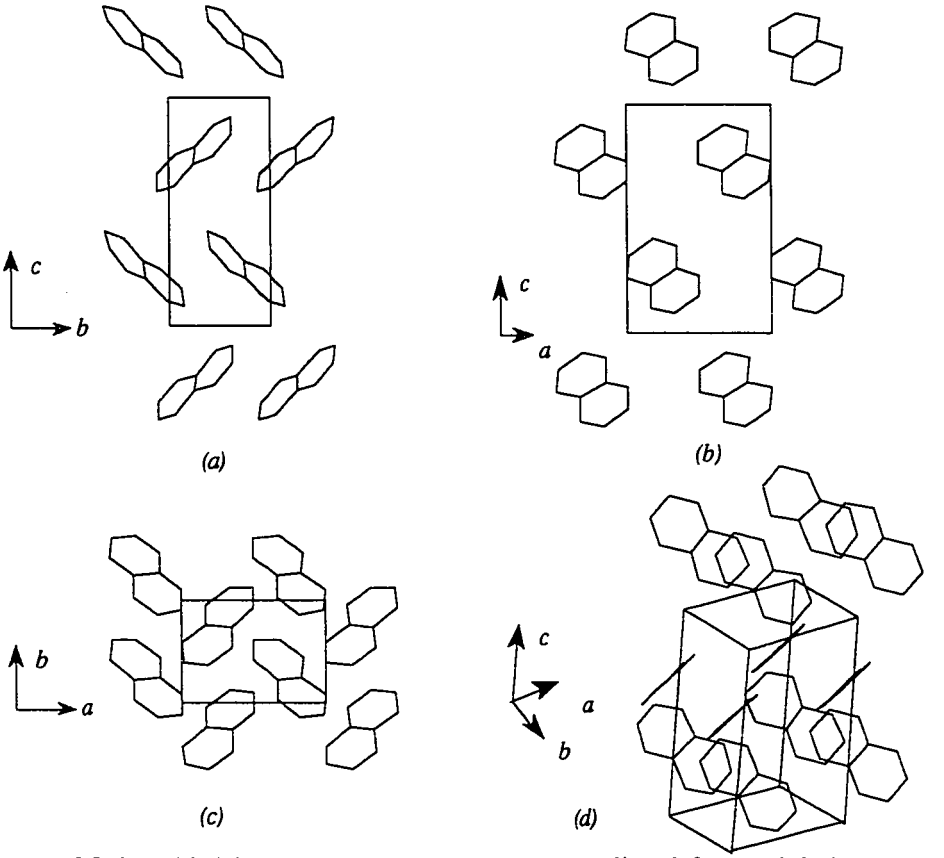

Figure 6.2.4. Third lowest energy space group predicted for naphthalene, space group $P2_1$. (a). Projection along *a* axis. (b). Projection along *b* axis. (c). Projection along *c* axis. (d). General view.

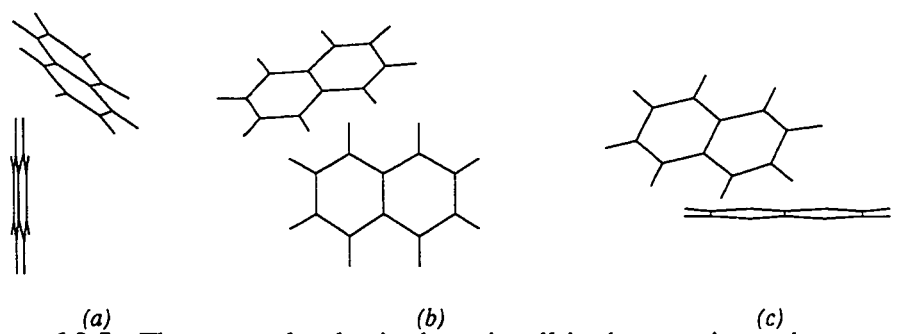

Figure 6.2.5. The two molecules in the unit cell in the experimental structure of naphthalene, as viewed along the principal axes of one of the molecules.

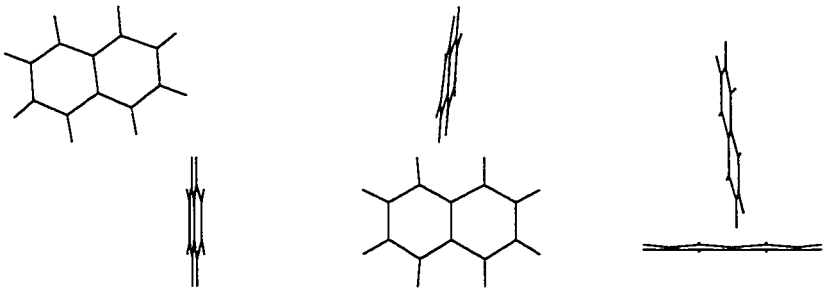

(a) (b) (c)

Figure 6.2.6. The two molecules in the unit cell in the lowest energy space group $P2_1/a$ for naphthalene, as viewed along the principal axes of one of the molecules.

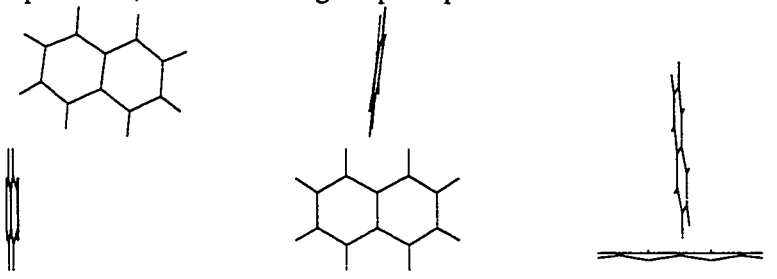

(a) (b) (c)

Figure 6.2.7. The two molecules in the unit cell in the second lowest energy space group $P2_1/c$ for naphthalene, as viewed along the principal axes of one of the molecules.

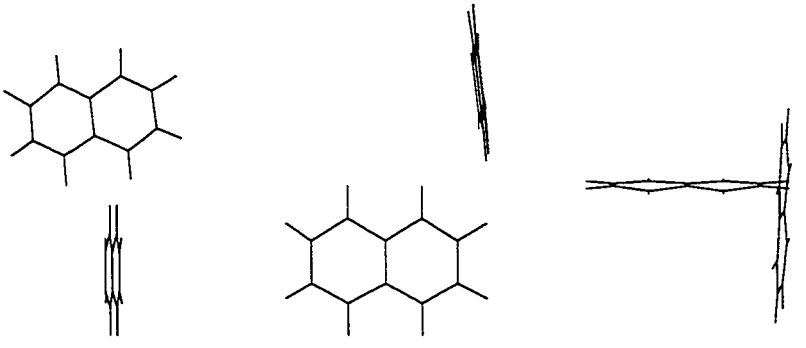

(a) (b) (c)

Figure 6.2.8. The two molecules in the unit cell in the third lowest energy space group $P2_1$ for naphthalene, as viewed along the principal axes of one of the molecules.

6.3. Anthracene

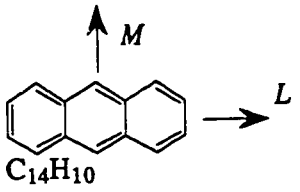

6.3.1 Experimental Data

Heat of sublimation: 21.7-23.9 [128,] 23.6 kcal/mol [129].

Experimental 1 [130]:

Temperature: 95K
Space Group: $P2_1/a$
Molecules per cell: 2

a:	8.443	α:	90°
b:	6.002	β:	125.6°(54.4°)
c:	11.124	γ:	90°

$LOa = 120.78°$	$MOa = 107.67°$	$NOa = 36.51°$
$LOb = 97.53°$	$MOb = 153.76°$	$NOb = 114.97°$
$LOc' = 31.89°$	$MOc' = 108.75°$	$NOc' = 65.22°$

Experimental 2 [131]:

Temperature: 290K
Space Group: $P2_1/a$
Molecules per cell: 2

a:	8.562	α:	90°
b:	6.038	β:	124.7°
c:	11.184	γ:	90°

$LOa = 119.61°$	$MOa = 108.51°$	$NOa = 35.97°$
$LOb = 97.32°$	$MOb = 153.44°$	$NOb = 115.38°$
$LOc' = 30.68°$	$MOc' = 108.35°$	$NOc' = 66.33°$

6.3.2 Results

Input for calculations:

Coordinates: Experiment
Multipole moments: Gaussian 90, 6-31G basis set
Van der Waals Volume: 144.674 Å^3

Table 6.3 Lowest Energy Structures in Each Space Group for Anthracene

Space Group	Z	Total Energy	E_{lj}	E_{coul}	Packing Index
$P\bar{1}$	2	-23.61	-21.83	-1.78	0.6309
$P\bar{1}$	1	-23.55	-21.83	-1.73	0.6314
$P2_1$	2	-23.46	-21.73	-1.74	0.6363
$P2_1/c$	4	-23.43	-21.74	-1.70	0.6325
$P2_1/c$	2	-23.42	-21.60	-1.82	0.6334
$P2_1/a$	2	-23.41	-21.67	-1.74	0.6298
Pna	4	-22.64	-21.06	-1.58	0.6211
$C2/c$	4	-22.49	-22.57	0.84	0.5323
$P2_12_12_1$	4	-22.34	-20.99	-1.35	0.6145
$P2_1/a$	4	-22.25	-21.36	-0.89	0.6277
Pca	4	-22.08	-19.81	-2.27	0.5838
$Pbca$	4	-22.03	-22.55	-1.48	0.6138
$Pnma$	4	-21.64	-21.34	-0.30	0.6267
Pmc	2	-21.40	-19.00	-2.40	0.5643
$C2/c$	4	-21.02	-19.71	-1.31	0.6084
Cmc	4	-20.89	-19.16	-1.73	0.5839
$Pbcn$	4	-19.72	-19.64	-0.88	0.6010

Predicted Structure with Lowest Energy:

Space Group: $P\bar{1}$
Molecules per cell: 2
Packing index: 0.6309

a:	6.863	α:	80.13°	Energy:	-23.61
b:	9.815	β:	71.17°	Lennard-Jones:	-21.83
c:	7.897	γ:	65.77°	Coulombic:	-1.78

Second lowest energy structure in first most probable space group:

Space Group: $P\bar{1}$
Molecules per cell: 1
Packing index: 0.6315

a:	4.219	α:	73.39°	Energy:	-23.58
b:	6.204	β:	73.24°	Lennard-Jones:	-21.87
c:	9.541	γ:	84.10°	Coulombic:	-1.706

Structure with lowest energy in second most probable space group:

Space Group: $P2_1$
Molecules per cell: 2
Packing index: 0.6363

a:	17.79	α:	90.0°	Energy:	-23.46
b:	4.75	β:	77.74°	Lennard-Jones:	-21.73
c:	5.50	γ:	90.0°	Coulombic:	-1.738

Structure with lowest energy in third most probable space group:

Space Group: $P2_1/c$
Molecules per cell: 4
Packing index: 0.6325

a:	9.98	α:	90.0°	Energy:	-23.43
b:	5.17	β:	86.83°	Lennard-Jones:	-21.74
c:	17.76	γ:	90.0°	Coulombic:	-1.70

Predicted Structure Closest to Experiment # 1:

Space Group: $P2_1/a$
Molecules per cell: 2
Packing index: 0.6204

a:	8.428	α:	90°	Energy:	-22.48
b:	5.914	β:	57.26°	Lennard-Jones:	-20.85
c:	11.122	γ:	90°	Coulombic:	-1.63

6.3.3. Discussion of Anthracene Results

The experimental structure of anthracene is a herringbone structure in $P2_1/a$ equivalent to that of naphthalene, with the unit cell expanded along the c vector to accommodate the additional ring (Fig. 6.3.1). ICE9 found a structure corresponding to the experimental configuration very close in energy to the global mninimum, being only 0.18 kcal/mol higher (Fig.6.3.5). This predicted structure has the lowest energy in space group $P2_1/c$, which is equivalent to $P2_1/a$, but with the axes in a different orientation. Hence the molecules in the predicted structure are oriented differently with respect to the axes in $P2_1/c$ than the molecules in the experimental structure are to $P2_1/a$, due to this difference in settings of the space group, but the relationship between the molecules themselves, shown in Fig. 6.3.6 (a)-(c) and 6.3.9, is virtually indistinguishable from the experimental structure.

The lowest energy space group predicted by the program, however, is $P\bar{1}$ in which the molecules exhibit the slipped-stack of pancakes structure (Fig. 6.3.2 and Fig. 6.3.3). In $P\bar{1}$ there are two predominant types of stacking configurations in which the molecules are eclipsed to varying degrees. In both configurations the molecules are stacked so that the hydrogen atoms of one molecule are directly over the carbon atoms in the layer below (Fig. 6.3.7 and 6.3.8). The electrostatic energy calculated for these two structures is the same as that obtained for the experimental structure at -1.70 kcal/mol.

The second and third most probable space groups predicted by the program, $P2_1$ and $P2_1/c$, do exhibit the herringbone, edge-to-face configuration between layers (Fig. 6.3.2 and 6.3.3). The structure in $P2_1/c$ corresponds to the experimental structure, and was discussed previously. The energies of these top three space groups are very close, at -23.61, -23.46, and -23.43 kcal/mol, respectively. Within a layer in $P2_1$, the molecules exhibit the slipped-stacking seen in the lowest energy configuration in $P\bar{1}$ (Fig. 6.3.9(a)-(c)), but across the layers, the molecules are arranged in the edge-to-face configuration very similar to the experimentally observed structure (Fig.6.3.9(d)-(f)).

6.3.4. Graphical Representation of Anthracene Crystal Structures

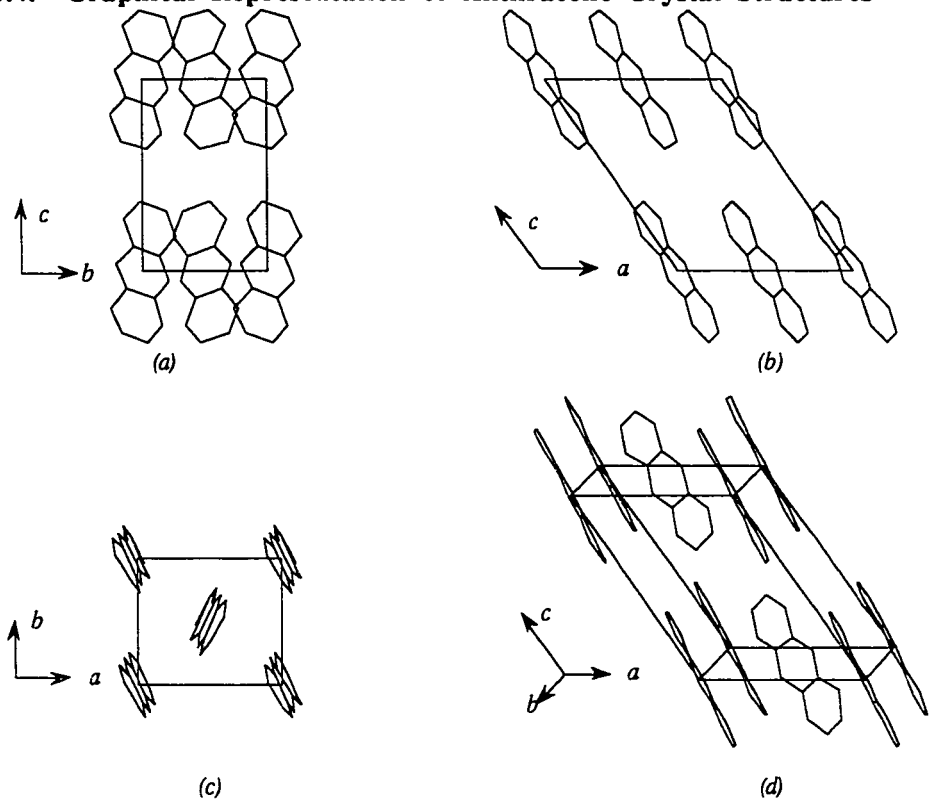

Figure 6.3.1. Experimental structure of anthracene, space group $P2_1/a$. (a). Projection along *a* axis. (b). Projection along *b* axis. (c). Projection along *c* axis. (d). General view.

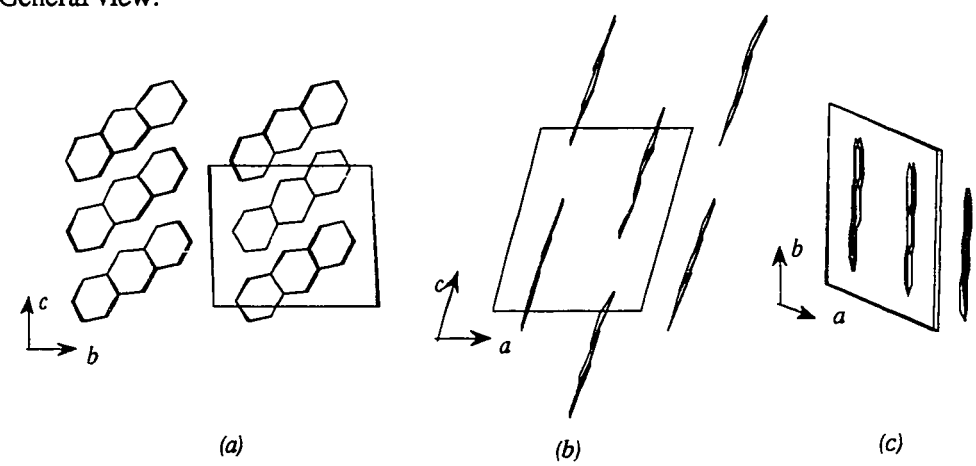

Figure 6.3.2. Most probable structure of anthracene predicted by the program, space group $P\bar{1}$ (a). Projection along *a* axis. (b). Projection along *b* axis. (c). Projection along *c* axis.

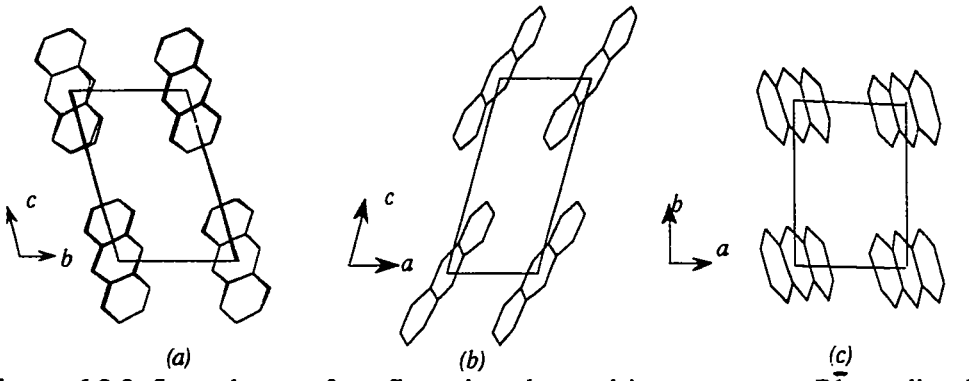

Figure 6.3.3. Second type of configuration observed in space group $P\bar{1}$, predicted by the program for anthracene. (a). Projection along *a* axis. (b). Projection along *b* axis. (c). Projection along *c* axis.

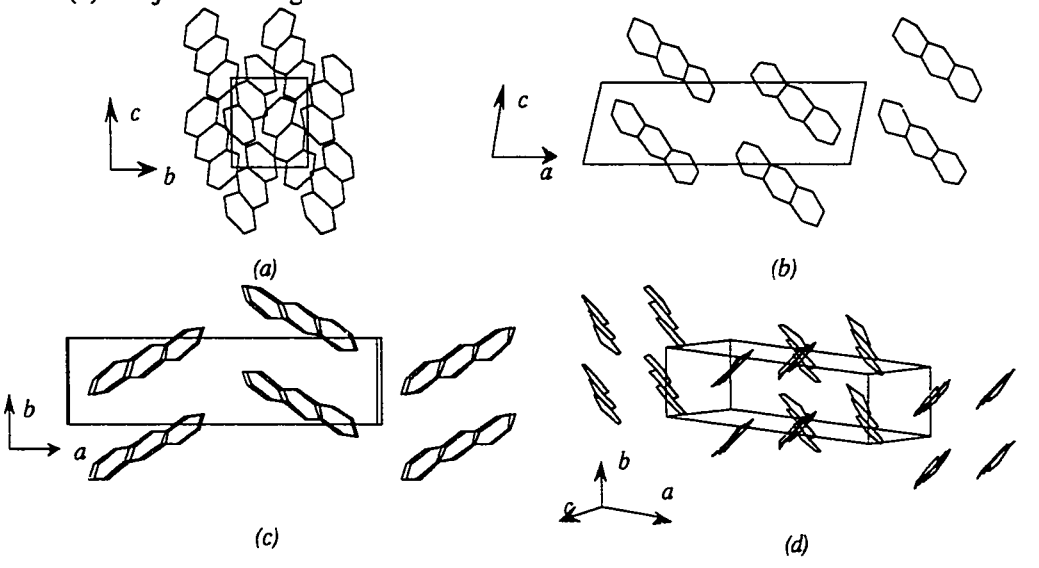

Figure 6.3.4. Second most probable space group $P2_1$, predicted by the program for anthracene (a). Projection along *a* axis. (b). Projection along *b* axis. (c). Projection along *c* axis. (d). General view.

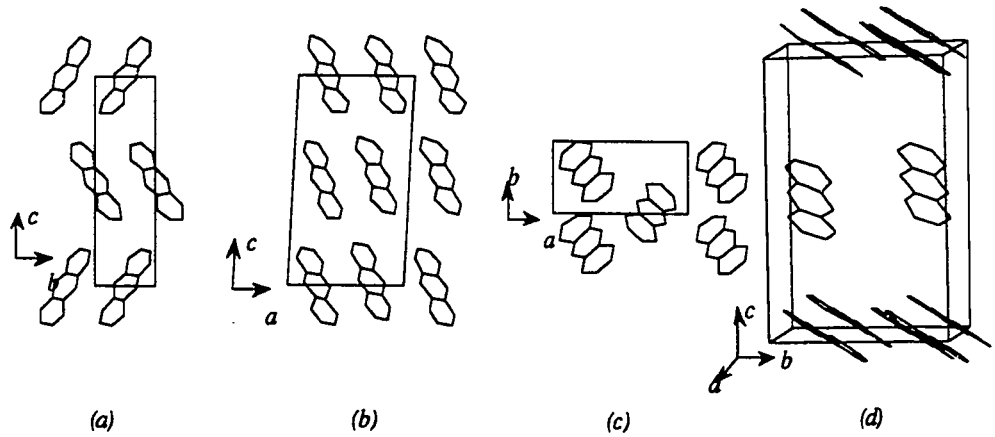

Figure 6.3.5. Third most probable space group $P2_1/c$, predicted by the program for anthracene (a). Projection along *a* axis. (b). Projection along *b* axis. (c). Projection along *c* axis. (d). General view.

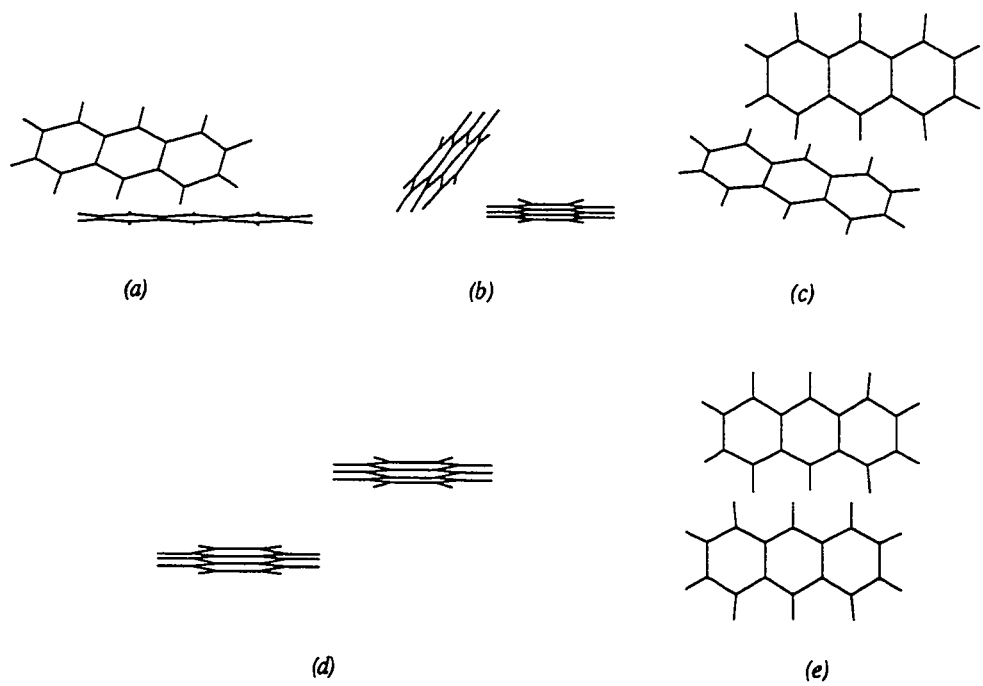

Figure 6.3.6. (a)-(c). The two molecules in the unit cell in the experimental structure of anthracene in space group $P2_1/a$, as viewed along the principal axes of one of the molecules. (d)-(e). Two molecules in adjacent unit cells showing arrangement of parallel molecules.

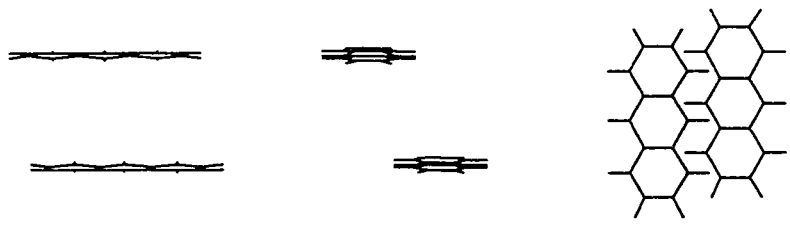

(a) (b) (c)

Figure 6.3.7. Nearest neighbor molecules in adjacent unit cells in the [100] direction, in the most probable structure of anthracene in $P\bar{1}$, as viewed along the principal axes of one of the molecules.

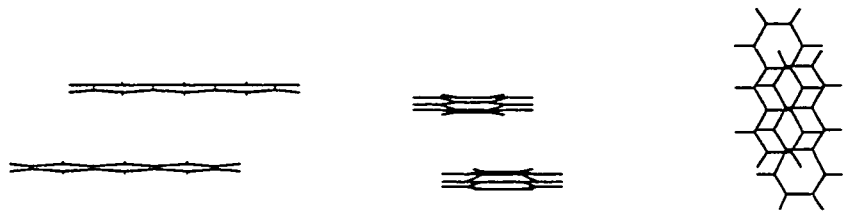

(a) (b) (c)

Figure 6.3.8. The second most probable configuration in space group $P\bar{1}$ for anthracene, as viewed along the principal axes of one of the molecules.

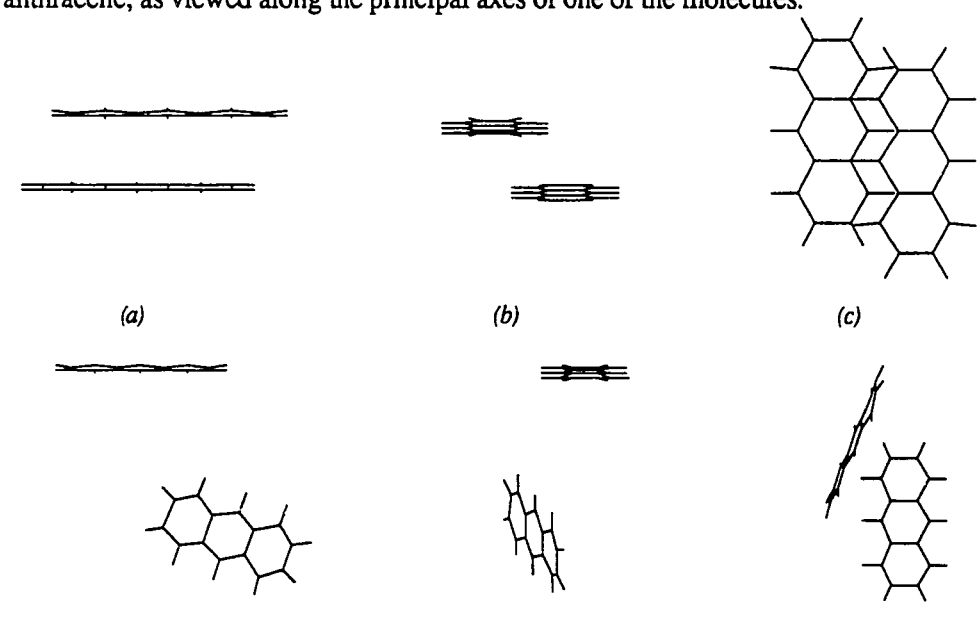

(a) (b) (c)

(d) (e) (f)

Figure 6.3.9. Second most probable space group $P2_1$ for anthracene. (a)-(c). The configuration of molecules in the slipped-stack layer as viewed along the principal axes of one of the molecules. (d)-(f). The edge-to-face configuration exhibited between molecules in different layers as viewed along the principal axes of one of the molecules.

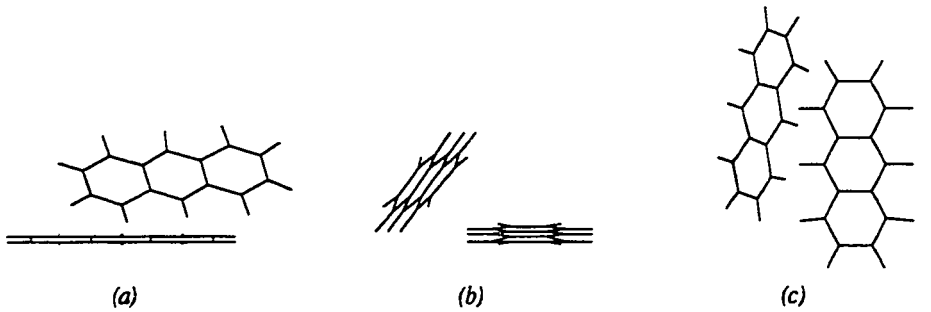

(a) *(b)* *(c)*

Figure 6.3.11. Two molecules within the unit cell in the third most probable space group $P2_1/c$ for anthracene, as viewed along the principal axes of one of the molecules.

6.4. Tetracene

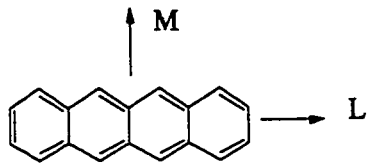

$C_{18}H_{12}$

6.4.1 Experimental Data

Experimental [132]:

Temperature:		RT	
Space Group:		$P\bar{1}$	
Molecules per cell:		1 (Note: asymmetric unit is 2 half-molecules.)	
a:	7.98	α:	101.3°(78.7°)
b:	6.14	β:	113.2°(66.8°)
c:	13.574	γ:	87.5°

6.4.2 Results

Input for calculations:

Coordinates:	Carbon atoms from X-ray diffraction, hydrogens from CHEM-X
Multipole moments:	Gaussian 90, 6-31G basis set
Van der Waals Volume:	181.743 $Å^3$

Table 6.4 Lowest Energy Structures in Each Space Group for Tetracene

Space Group	Z	Total Energy	E_{lj}	E_{coul}	Packing Index
$P2_1/c$	4	-30.58	-27.83	-2.75	0.6506
$P\bar{1}$	1	-30.50	-27.90	-2.60	0.6462
$P2_1/a$	2	-30.42	-27.13	-3.29	0.6450
$P2_1/c$	2	-30.27	-26.37	-3.90	0.6223
$P2_1$	2	-29.94	-26.40	-3.54	0.6244
$P\bar{1}$	2	-29.79	-27.58	-2.21	0.6423
Pca	4	-29.50	-25.78	-3.71	0.6047
Pmc	2	-28.81	-24.86	-3.94	0.5872
$C2/c$	4	-27.87	-27.93	0.06	0.5978
$Pbca$	4	-28.55	-26.36	-2.15	0.6185
Cmc	4	-27.35	-25.99	-1.36	0.6281
$C2/c$	4	-27.71	-26.13	-1.58	0.6105
$Pnma$	4	-25.99	-23.30	-2.68	0.5697
$Pbcn$	4	-25.27	-25.40	0.13	0.6182
Cmc	4	-15.63	-23.08	7.45	0.5462
Cmc	4	-15.63	-23.08	7.45	0.5462

Predicted Structure with Lowest Energy:

Space Group: $P2_1/c$
Molecules per cell: 4
Packing index: 0.6506

a:	11.012	α:	90.0°	Energy:	-30.58
b:	4.663	β:	87.0°	Lennard-Jones:	-27.83
c:	21.779	γ:	90.0°	Coulombic:	-2.75

Structure with lowest energy in second most probable space group:

Space Group: $P\bar{1}$
Molecules per cell: 1
Packing index: 0.6462

a:	7.853	α:	54.02°	Energy:	-30.50
b:	13.899	β:	50.70°	Lennard-Jones:	-27.90
c:	4.244	γ:	58.28°	Coulombic:	-2.606

Structure with lowest energy in third most probable space group:

Space Group: $P2_1/a$
Molecules per cell: 2
Packing index: 0.6223

a:	14.234	α:	90.0°	Energy:	-30.27
b:	6.303	β:	68.68°	Lennard-Jones:	-26.37
c:	6.980	γ:	90.0°	Coulombic:	-3.905

6.4.3. Discussion of Tetracene Results

The asymmetric unit in the experimental structure of tetracene consists of two half-molecules arranged in a herringbone configuration. The herringbone structure of tetracene is similar to that exhibited by naphthalene and anthracene except that the **L** axes of the molecules are parallel to each other (Fig.6.4.1 and 6.4.5). At the present time, ICE9 allows for only one molecule per asymmetric unit, so a local minimum corresponding exactly to the experimental structure is not possible. ICE9, however, did predict an edge-to-face structure in $P2_1/a$, Z=2, very similar to the experimental one (Fig. 6.4.4 and Fig. 6.4.8), and very close in energy to the calculated global minimum, being 0.18 kcal/mol higher. The angles (50°) and distances between molecular planes are the same in both the experimental and the predicted structure in $P2_1/a$. In both structures the hydrogen atoms of one molecule are located over the central aromatic region of its nearest neighbor. The only difference is that in the experimental structure one molecule is displaced $\sim$ 1.7 Å along the **L** molecular axis. The similarities and differences in the relationship between nearest neighbors can be seen clearly in Figures 6.4.5 and 6.4.8. This structure so similar to the experimental structure was the third mnost probable.

The second most probable structure occurred in $P\bar{1}$, with Z=1. The main feature in the packing in the two most probable structures predicted by ICE9 is the slipped-stack of pancakes configuration shown in Fig. 6.4.6 (a)-(c) and Fig. 6.4.7. In both cases the stacks are displaced the same amount along the **L** axis of the molecule, but different amounts parallel to the **M** axis of the molecule, 2.2 Å and 1.5 Å in the first and second structures, respectively. In the first structure in $P\bar{1}$, the layers of slipped stacks are all parallel. In the second structure each layer is related by a screw axis rotation and displacement parallel to the *c*-axis, to give a herringbone relationship between the layers. Both slipped-stack structures exhibited negative electrostatic energies at -2.75 and -2.60 kcal/mol respectively.

The structure closest to experiment in $P2_1/a$ exhibited a much lower electrostatic energy, -3.288, than either of the slipped-stack structures, but had a higher Lennard-Jones energy and lower packing index.

6.4.4. Graphical Representation of Tetracene Results

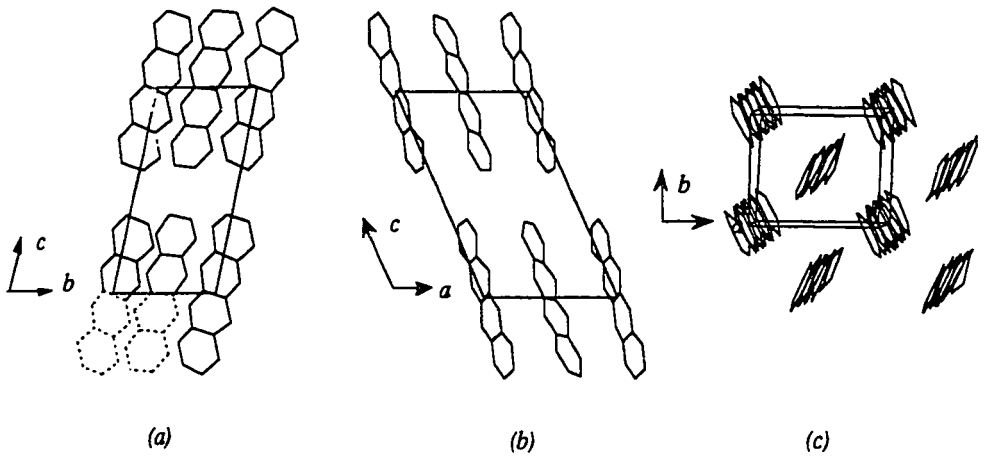

Figure 6.4.1. Experimental structure of tetracene, space group $P\bar{1}$ with two half molecules in the asymmetric unit. (a). Projection along *a* axis, indicating the asymmetric unit with dashed lines. (b) Projection along *b* axis. (c). Projection along *c* axis.

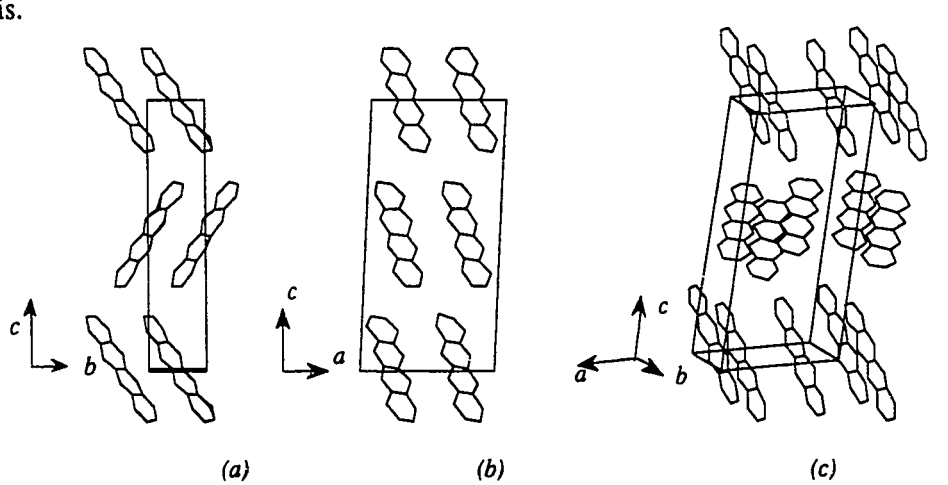

Figure 6.4.2. Most probable structure of tetracene predicted by the program, space group $P2_1/c$. (a). Projection along *a* axis. (b). Projection along *b* axis. (c). General view.

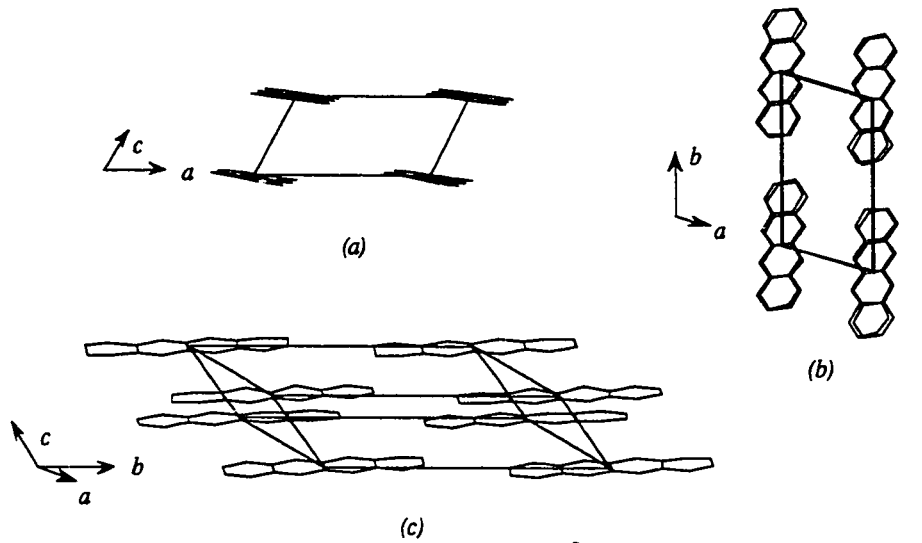

Figure 6.4.3. Second most probable space group $P\bar{1}$, predicted by the program for tetracene. (a). Projection along *b* axis. (b). Projection along *c* axis. (c). General view.

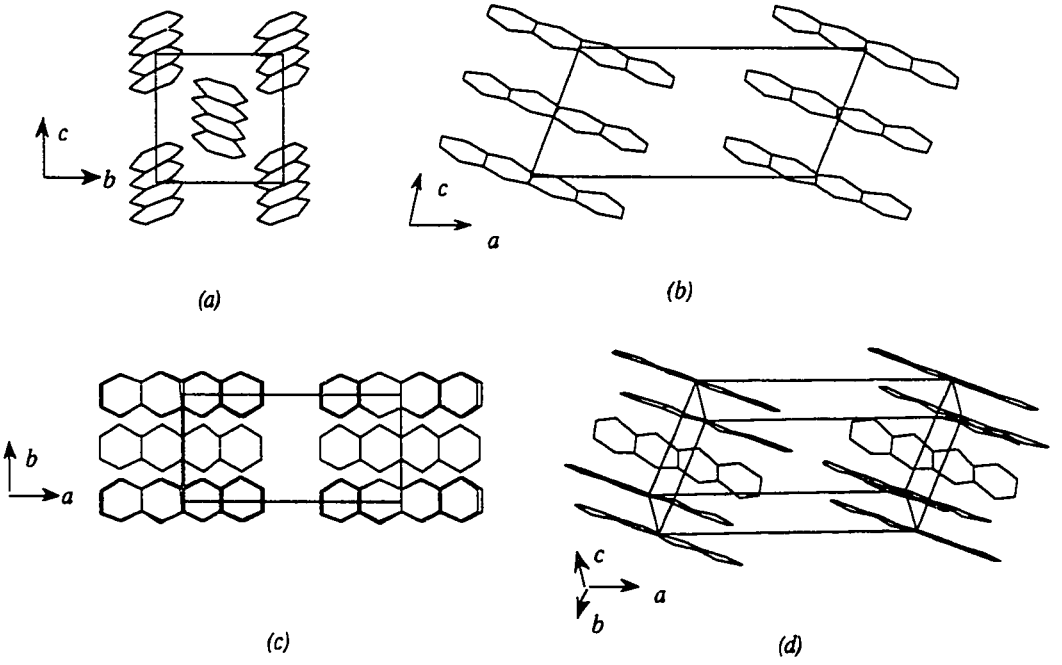

Figure 6.4.4. Third most probable space group $P2_1/a$ orientation, predicted by the program for tetracene (a). Projection along *a* axis. (b). Projection along *b* axis. (c). Projection along *c* axis. (d). General view.

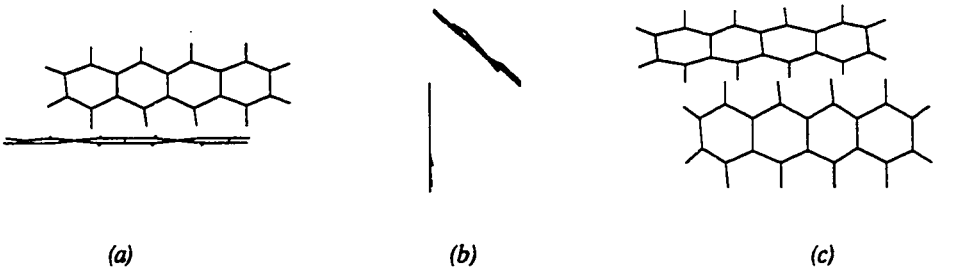

(a) (b) (c)

Figure 6.4.5. The two molecules in the unit cell in the experimental structure of tetracene, as viewed along the principal axes of one of the molecules.

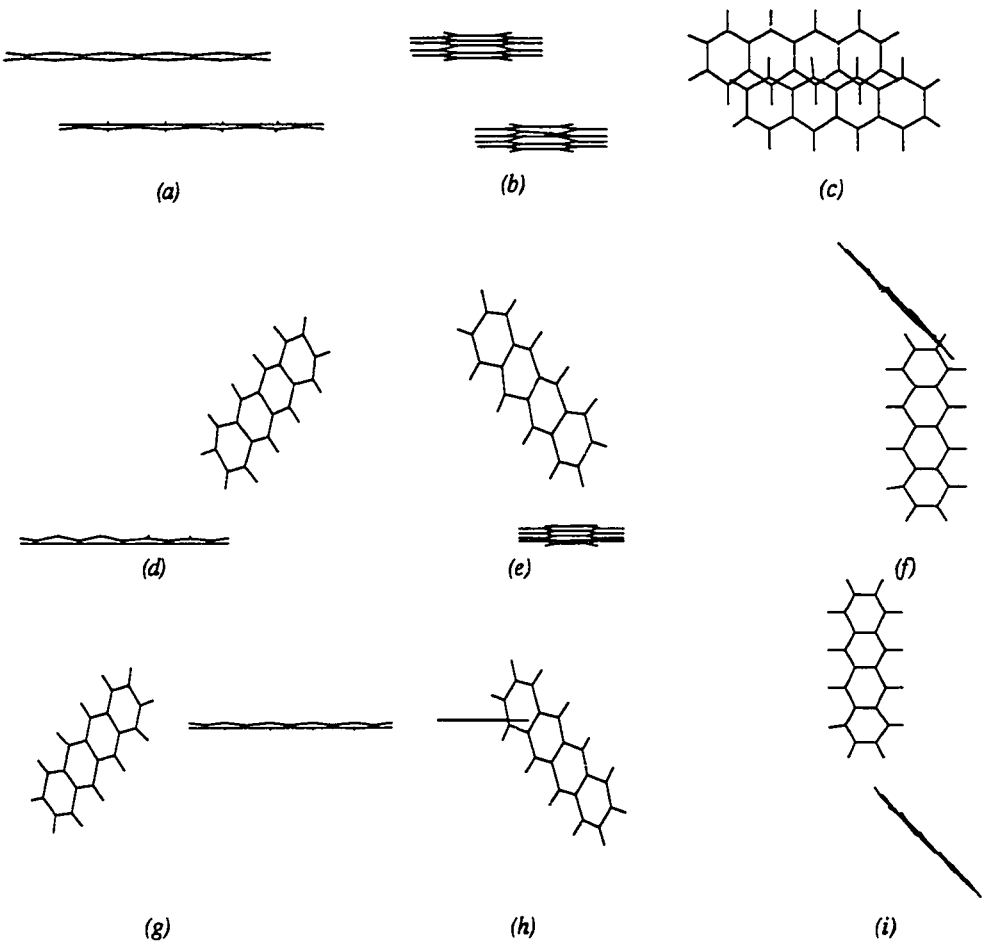

(a) (b) (c)

(d) (e) (f)

(g) (h) (i)

Figure 6.4.6. The four molecules in the unit cell in the most probable structure of tetracene in $P2_1/c$, as viewed along the principal axes of a reference molecule.

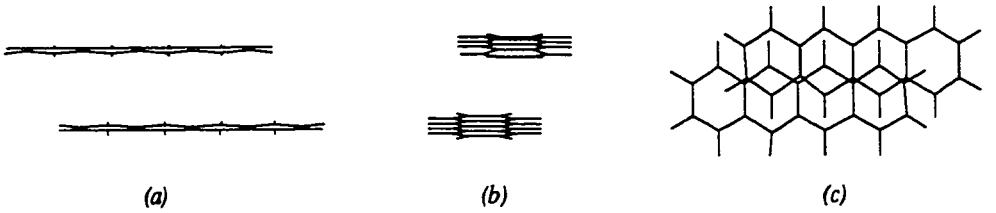

(a) (b) (c)

Figure 6.4.7. Nearest neighbor molecules in adjacent unit cells in the [010] direction in the second most probable space group P$\bar{1}$, for tetracene, as viewed along the principal axes of one of the molecules.

(a) (b) (c)

Figure 6.4.8. The two molecules in the unit cell in the third most probable space group $P2_1/a$ for tetracene, as viewed along the principal axes of one of the molecules.

6.5. Pentacene

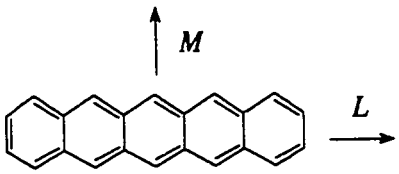

$C_{22}H_{14}$

6.5.1 Experimental Data

Experimental [132]:

Temperature:			RT
Space Group:			$P\bar{1}$
Molecules per cell:			1 (Note: the asymmetric unit is 2 half-molecules)
a:	7.90	α:	101.9 (78.1°)
b:	6.06	β:	112.6°(67.4°)
c:	16.01	γ:	85.8°

6.5.2 Results

Input for calculations:

Coordinates:	Carbon atoms from X-ray diffraction, hydrogens from CHEM-X
Multipole moments:	Gaussian 90, STO-3G basis set * 2.33
Van der Waals Volume:	219.303 $Å^3$

Table 6.5 Lowest Energy Structures in Each Space Group for Pentacene

Space Group	Z	Total Energy	E_{lj}	E_{coul}	Packing Index
$P\bar{1}$	1	-34.83	-34.13	-0.70	0.5668
$P2_1$	2	-34.52	-33.82	-0.70	0.5659
$P2_1/a$	4	-34.39	-33.34	-1.05	0.5597
$P2_1/c$	4	-34.11	-33.54	-0.57	0.5639
$P2_1/a$	2	-33.96	-32.90	-1.07	0.5555
Pca	4	-33.24	-32.74	-0.50	0.5472
$Pbca$	4	-33.23	-32.72	-0.51	0.5481
$P2_1/c$	2	-32.70	-31.63	-0.68	0.5469
Pca	4	-31.99	-31.56	-0.43	0.5493
Pmc	2	-31.80	-30.66	-1.14	0.5213
Pna	4	-31.39	-30.50	-0.89	0.5307
$C2/c$	4	-31.34	-31.37	0.026	0.5451
$C2/c$	4	-31.03	-30.98	-0.05	0.5460
$Pnma$	4	-30.21	-30.48	0.27	0.5443
Cmc	4	-29.88	-29.33	-0.56	0.5254
$Pbcn$	4	-29.26	-29.48	0.22	0.5228
Cmc	4	-24.96	-25.13	0.17	0.4715

Predicted Structure with Lowest Energy:

Space Group: $P\bar{1}$
Molecules per cell: 1
Packing index: 0.5668

a:	4.276	α:	75.13°	Energy:	-34.83
b:	6.115	β:	54.04°	Lennard-Jones:	-34.13
c:	16.337	γ:	83.02°	Coulombic:	-0.6850

Structure with lowest energy in second most probable space group:

Space Group: $P2_1$
Molecules per cell: 2
Packing index: 0.5659

a:	4.320	α:	90.0°	Energy:	-34.52
b:	25.320	β:	83.70°	Lennard-Jones:	-33.82
c:	6.155	γ:	90.0°	Coulombic:	-0.70

Structure with lowest energy in third most probable space group:

Space Group: $P2_1/a$
Molecules per cell: 4
Packing index: 0.5597

a:	30.837	α:	90.0°	Energy:	-34.39
b:	6.911	β:	84.99°	Lennard-Jones:	-33.34
c:	6.373	γ:	90.0°	Coulombic:	-1.05

6.5.3. Discussion of Pentacene Results

The experimental structure of pentacene is analogous to that of tetracene in $P\bar{1}$ (Fig.6.5.1), with the asymmetric unit consisting of two half molecules inclined at an angle of 57°to each other (Fig.6.5.6). The order of the two most probable structures were reversed for tetracene and pentacene. For pentacene, the slipped-stack structure in $P\bar{1}$ equivalent to that predicted for tetracene was found to have the lowest energy by 0.31 kcal/mol (Fig. 6.5.2 and Fig. 6.5.7). The second most probable structure in $P2_1/a$ is similar to the first structure predicted for tetracene in that it consists of layers of parallel slipped-stack molecules identical to those in $P\bar{1}$, but with adjacent layers angled in a herringbone fashion (Fig. 6.5.3 and Fig. 6.5.8).

The third most probable structure, in space group $P2_1/a$, is an edge-to-face configuration which is close to the experimental structure, given that the asymmetric unit is one whole molecule, rather than two half molecules. One of the differences between the experimental and predicted structures, which is a result of the choice of asymmetric unit, is that the molecules must be aligned in $P2_1/a$ and cannot be displaced ~1.7 Å parallel to their long axes (Fig. 6.5.4 and Fig. 6.5.9) as they are in the observed stucture in $P\bar{1}$. The other difference is in the angle

formed by the molecular planes, which is 39° in the predicted structure and 57° in the observed structure. This structure closest to experiment is very close to the global minimum in energy, being only 0.44 kcal/mol higher.

6.5.4. Graphical Representation of Pentacene Results

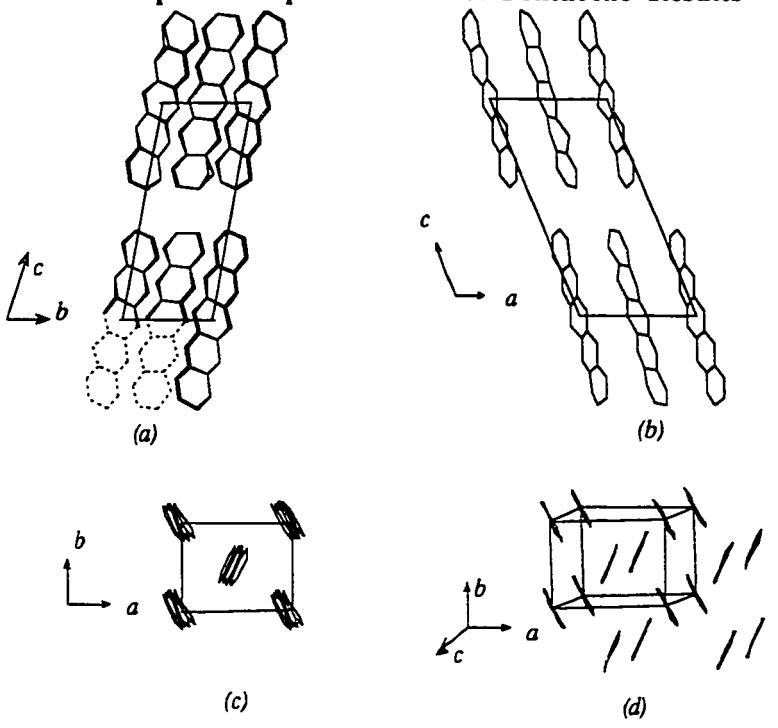

Figure 6.5.1. Experimental structure of pentacene, space group $P\bar{1}$. The asymmetric unit is two half molecules, indicated by dashed lines. (a). Projection along *a* axis. (b). Projection along *b* axis. (c). Projection along *c* axis. (d). Projection along the molecular planes.

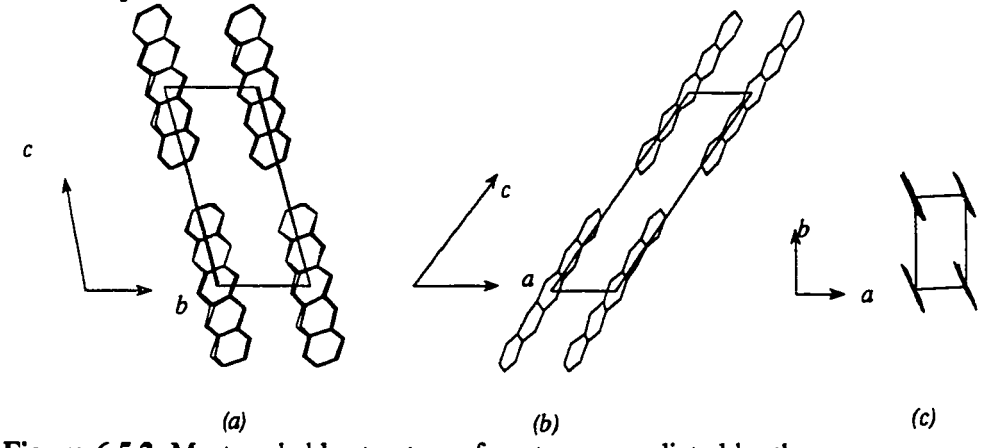

Figure 6.5.2. Most probable structure of pentacene predicted by the program, space group $P\bar{1}$ (a). Projection along *a* axis. (b). Projection along *b* axis. (c). Projection along *c* axis.

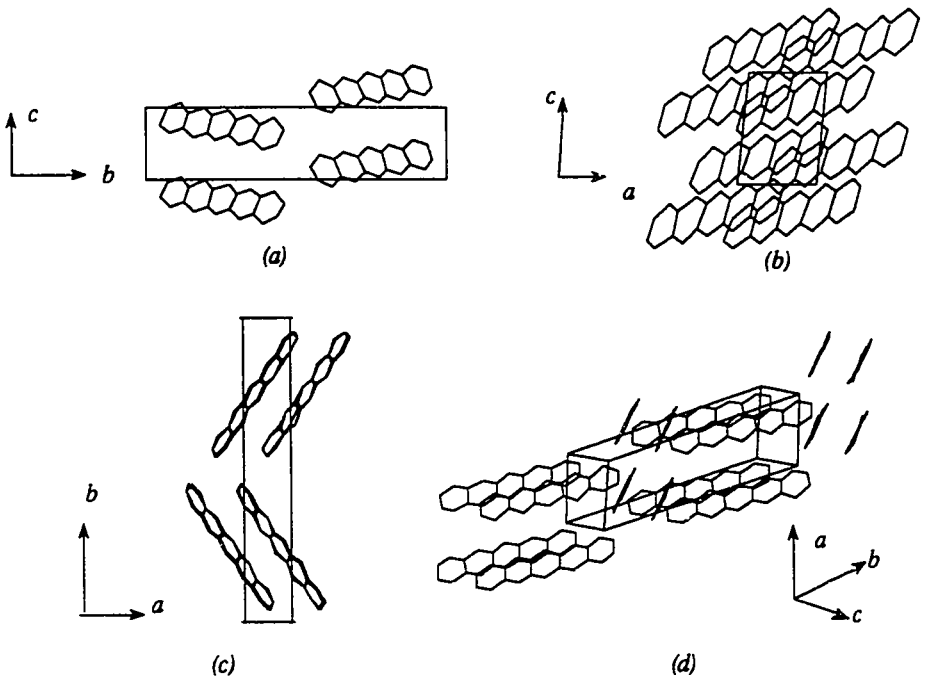

Figure 6.5.4. Second most probable space group $P2_1$, predicted by the program for pentacene. (a). Projection along *a* axis. (b). Projection along *b* axis. (c). Projection along *c* axis. (d). General view.

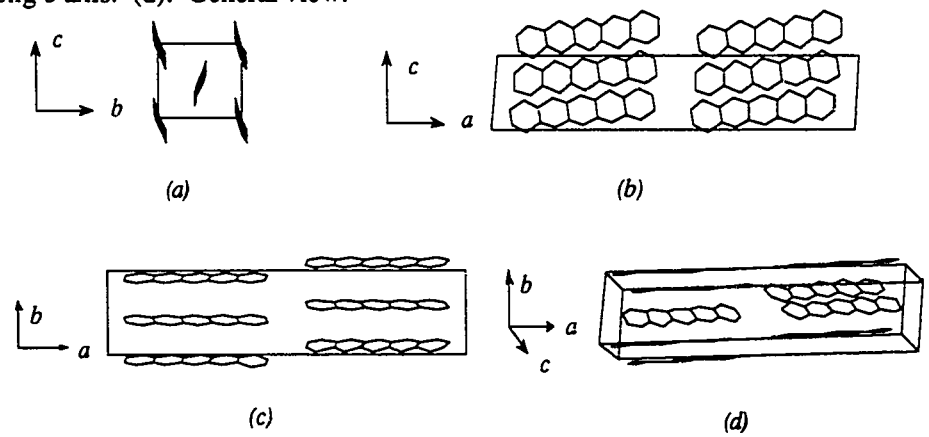

Figure 6.5.5. Third most probable space group $P2_1/a$, predicted by the program for pentacene. (a). Projection along *a* axis. (b). Projection along *b* axis. (c). Projection along *c* axis. (d). General view.

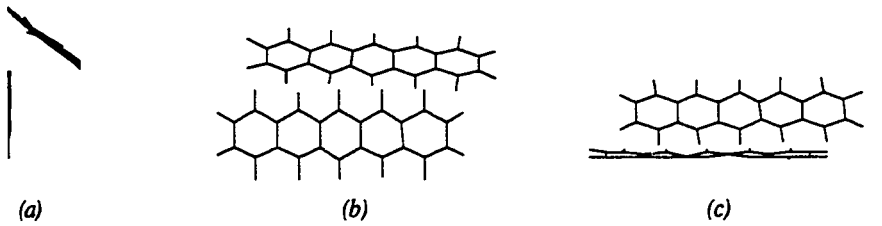

Figure 6.5.6. The two molecules in the unit cell in the experimental structure of pentacene, as viewed along the principal axes of one of the molecules.

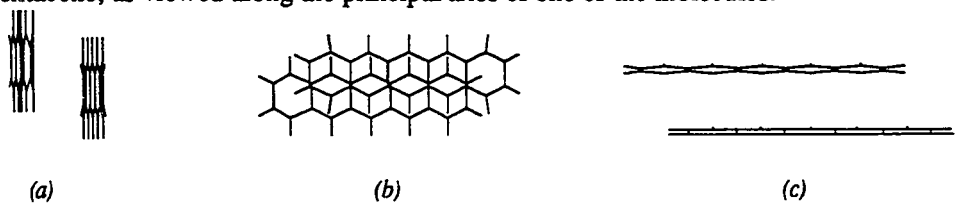

Figure 6.5.7. Nearest neighbor molecules in adjacent unit cells in the [100] direction, as viewed along the principal axes of one of the molecules.

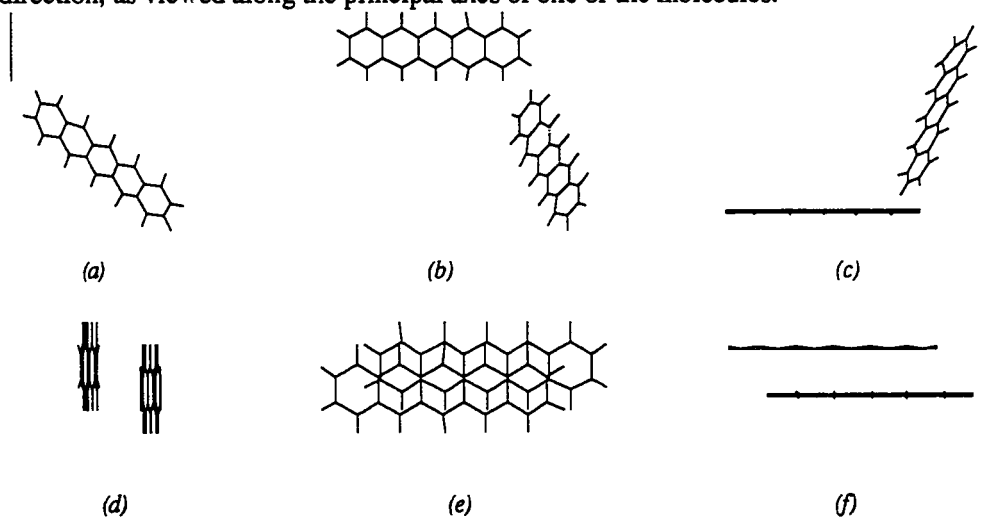

Figure 6.5.8. Second most probable space group $P2_1$ for pentacene, as viewed along the principal axes of one of the molecules. (a)-(c). The two molecules within the unit cell showing the herringbone structure between layers. (d)-(f): Nearest neighbor molecules in adjacent unit cells in the [100] direction showing the slipped stack structure within layers.

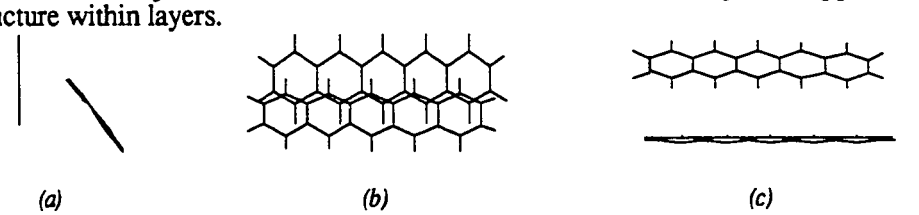

Figure 6.5.9. The two molecules in the unit cell in the third most probable space group for pentacene, $P2_1/a$, as viewed along the principal axes of one of the molecules.

6.6. Phenanthrene

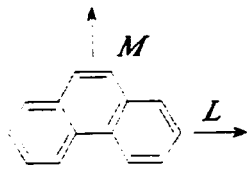

$C_{14}H_{10}$

6.6.1 Experimental Data

Heat of sublimation: 20.7 [36], 21.7 kcal/mol [125].

Experimental 1 [133]:

Temperature:		RT	
Space Group:		$P2_1$	
Molecules per cell:		2	
a:	8.46	α:	90°
b:	6.16	β:	97.7°(82.3°)
c:	9.47	γ:	90°

Experimental 2 [134] (Questionable Refinement):

Temperature:		RT	
Space Group:		$P2_1/a$	
Molecules per cell:		4	
a:	8.66	α:	90.0°
b:	6.11	β:	98.0°
c:	19.24	γ:	90.0°

6.6.2 Results

Input for calculations:

Coordinates:	Carbon atoms from X-ray diffraction, hydrogens from CHEM-X
Multipole moments:	Gaussian 90, 3-21G basis set * 0.858
Van der Waals Volume:	143.603 Å^3

Table 6.6 Lowest Energy Structures in Each Space Group for Phenanthrene

Space Group	Z	Total Energy	E_{lj}	E_{coul}	Packing Index
$P2_1/a$	4	-27.41	-21.76	-5.65	0.6326
$P2_1/c$	4	-26.58	-20.38	-6.21	0.6099
$P2_12_12_1$	4	-26.41	-20.89	-5.52	0.6142
Pca	4	-26.12	-19.97	-6.16	0.6040
$P\bar{1}$	2	-26.37	-20.91	-5.47	0.6154
$P2_1$	2	-25.31	-20.10	-5.21	0.6054
Pna	4	-24.90	-19.28	-5.62	0.5999
$C2/c$	4	-20.16	-14.44	-5.72	0.4684
$Pbcn$	4	-16.95	-16.74	-0.21	0.5356

Predicted Structure with Lowest Energy:

Space Group: $P2_1/a$
Molecules per cell: 4
Packing index: 0.6326

a:	21.13	α:	90.0°	Energy:	-27.41
b:	3.79	β:	59.15°	Lennard-Jones:	-21.76
c:	13.195	γ:	90.0°	Coulombic:	-5.65

Structure with lowest energy in second most probable space group:

Space Group: $P2_1/c$
Molecules per cell: 4
Packing index: 0.6099

a:	7.92	α:	90.0°	Energy:	-26.58
b:	7.93	β:	60.0°	Lennard-Jones:	-20.38
c:	17.32	γ:	90.0°	Coulombic:	-6.21

Structure with lowest energy in third most probable space group:

Space Group: $P2_12_12_1$
Molecules per cell: 4
Packing index: 0.6142

a:	10.17	α:	90.0°	Energy:	-26.41
b:	3.76	β:	90.0°	Lennard-Jones:	-20.89
c:	24.44	γ:	90.0°	Coulombic:	-5.52

Predicted Structure Closest to Experiment:

Space Group: $P2_1$
Molecules per cell: 2
Packing index: 0.5858

a:	8.7673	α:	90°	Energy:	-20.39
b:	5.960	β:	82.83°	Lennard-Jones:	-18.47
c:	9.457	γ:	90°	Coulombic:	-1.92

6.6.3. Discussion of Phenanthrene Results

Phenanthrene crystallizes in only one form, but before advanced refinement techniques were available, it was believed to crystallize in two different structures in space groups $P2_1/a$ and $P2_1$. Then in 1962, 3-dimentional refinement techniques found that phenanthrene crystallized only in space group $P2_1$ (Fig. 6.6.1). The details of the edge-to-face configuration of the experimental structure are shown in Figure 6.6.5. In this structure the molecules are placed in a head-to-head, tail-to-tail configuration. The most probable structure predicted by the program also has a head-to-head, tail-to-tail herringbone configuration (Fig. 6.6.2) in $P2_1/a$, but adjacent layers are displaced half a molecular diameter (Fig. 6.6.6). The experimental and predicted structures are compared directly in Figure 6.6.3. In both cases the hydrogen atoms on one molecule are closer to the hydrogen atoms on the other than to the aromatic center.

The second most probable structure is also a herringbone structure, but differs from both the experimental and lowest energy predicted strucutre in that the **L** axes of the molecules are closer to being perpendicular, rather than parallel. (Fig.6.6.8 (d)-(i)).

The third most probable structure consists of rows of slipped-stack molecules which are in a herringbone configuration with one of the neighboring rows, and anti-parallel to the other.

A local minimum very close to the experimental structure was found, but with a surprisingly high energy (-20.39) compared to the global minimum (-27.41). This difference in energy is primarily due to the much less negative electrostatic energy in the predicted structure. The electrostatic energy in the lowest energy structures is about 20% of the total energy. This is much higher than in the benzene-pentacene series.

6.6.4. Graphical Representation of Phenanthrene Crystal Structures

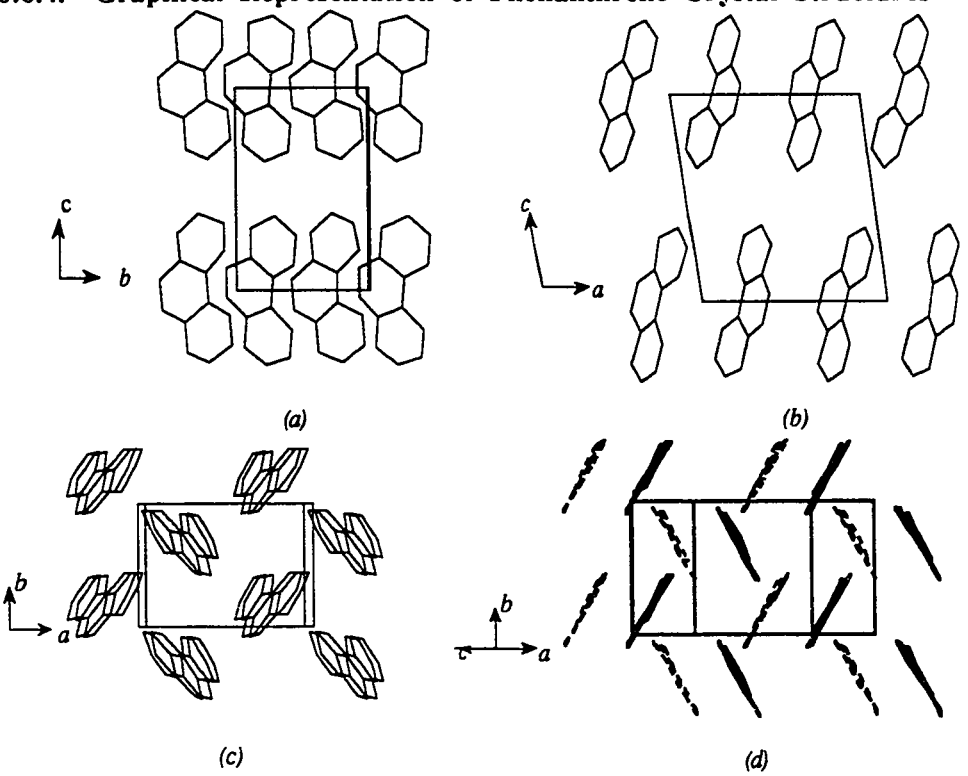

Figure 6.6.1. Experimental structure of phenanthrene, space group $P2_1$ (a). Projection along *a* axis. (b). Projection along *b* axis. (c). Projection along *c* axis. (d). Projection parallel to the molecular planes, with different layers indicated.

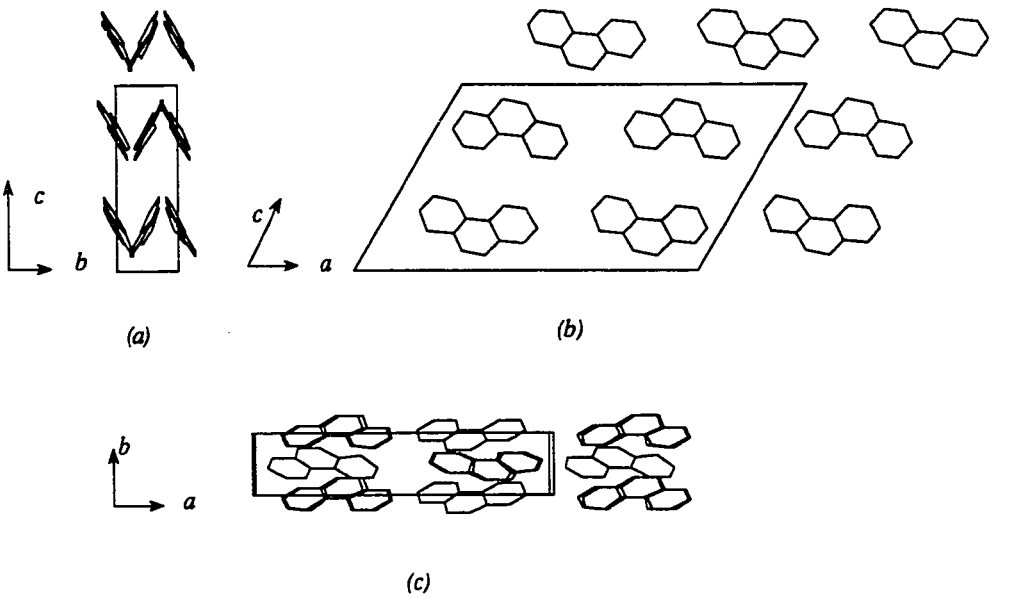

Figure 6.6.2. Most probable structure of phenanthrene predicted by the program, space group $P2_1/a$ (a). Projection along *a* axis. (b). Projection along *b* axis. (c). Projection along *c* axis.

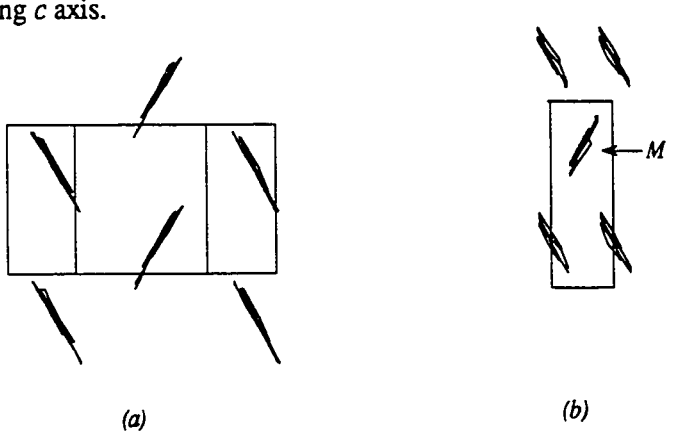

Figure 6.6.3. Comparison of the herringbone structures of the experimental structure (a) and the most probable structure predicted by the program (b). In the experimental structure (a), the molecules are placed head-to-head and tail-to-tail and their centers of mass lie in the same plane. In the most probable structure (b) the molecules are also placed head-to-head and tail-to-tail, but the center of mass of molecule M lies half a molecular diameter behind the plane of the page.

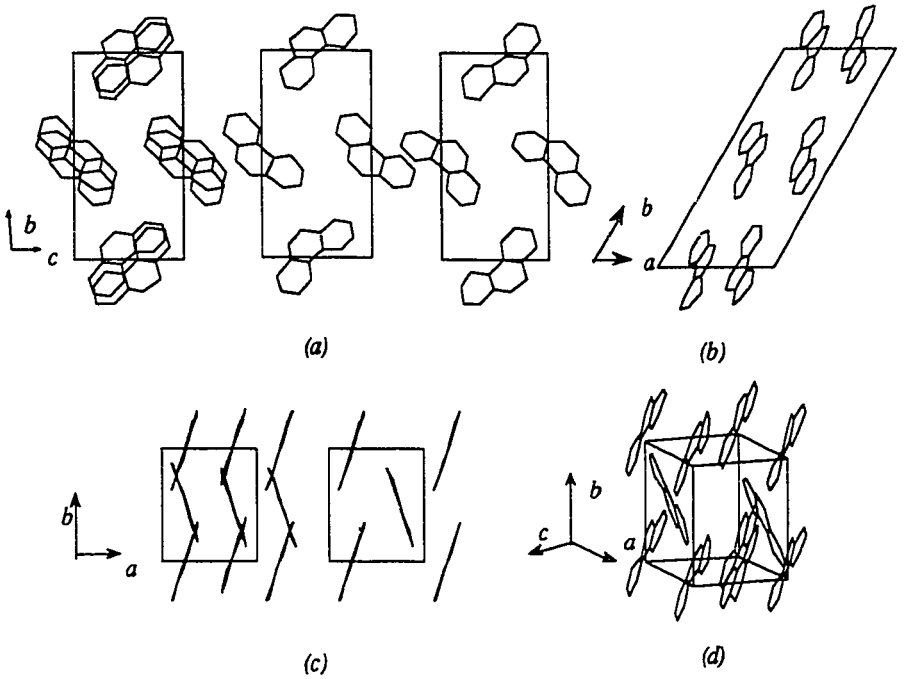

Figure 6.6.4. Second most probable space group P21/*c*, predicted by the program for phenanthrene. (a). Full projection along the *a* axis, as well as showing the structure in two separate layers. (b). Projection along *b* axis. (c). Full projection along *c* the axis, as well as showing an individual layer. (d). General view.

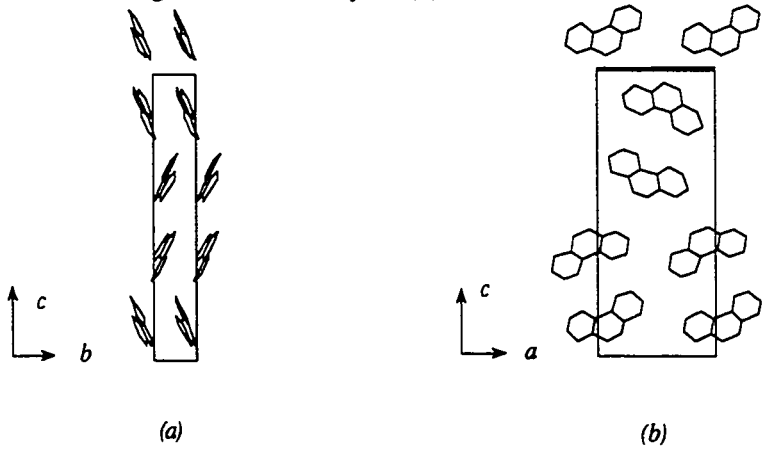

Figure 6.6.5. Third most probable space group $P2_12_12_1$, predicted by the program for phenanthrene. (a). Projection along *a* axis. (b). Projection along *b* axis.

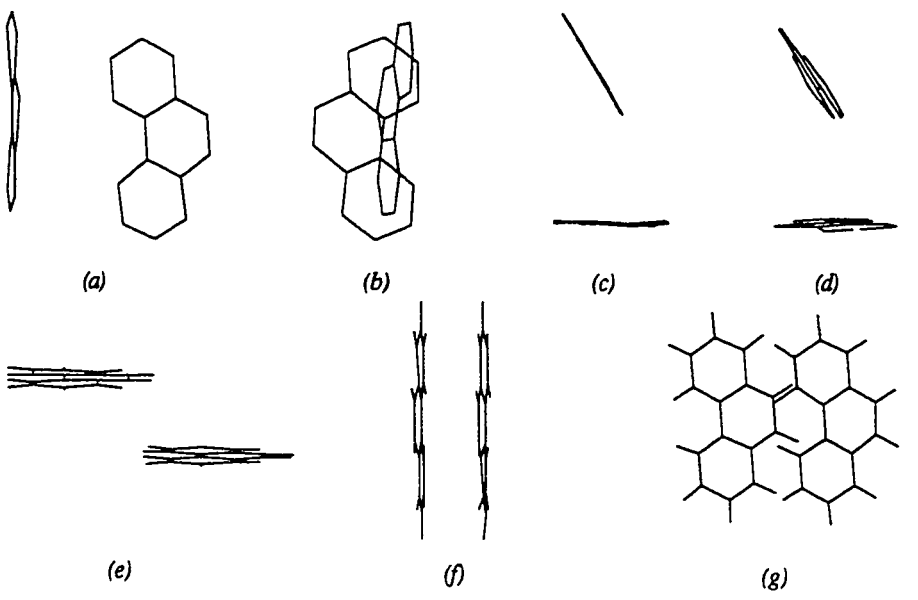

Figure 6.6.6. (a)-(d). The two molecules in the unit cell in the experimental structure of phenanthrene, as viewed along the principal axes of one of the molecules. In (d) the molecules are rotated 5° from the normal. (e)-(g). Nearest neighbor molecules in adjacent unit cells in the [010] direction.

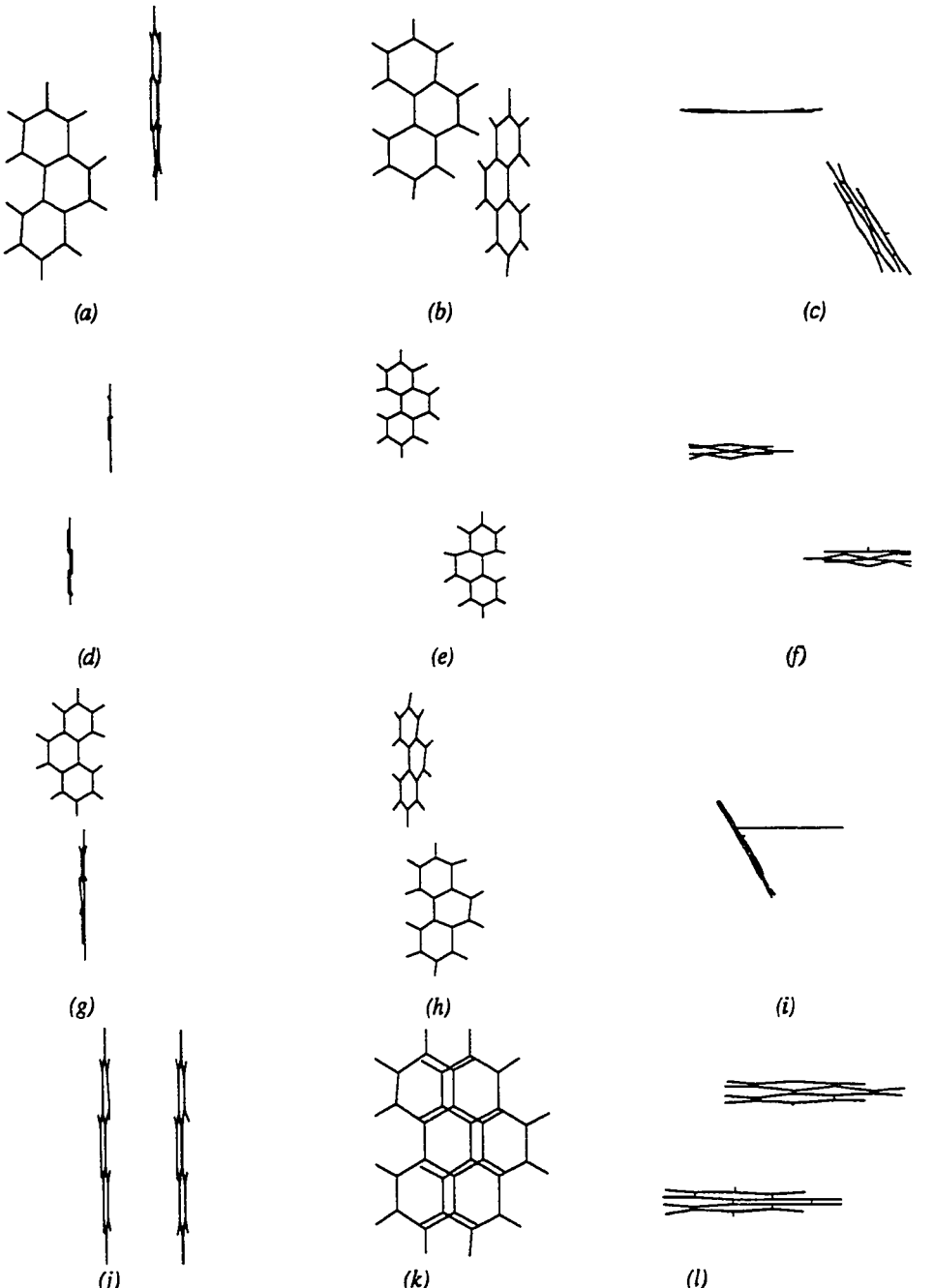

Figure 6.6.7. (a)-(i). The four symmetry positions in the unit cell in $P2_1/a$ in the most probable structure of phenanthrene, as viewed along the principal axes of the reference molecule. (j)-(l). Nearest neighbors in adjacent unit cells in the [010] direction.

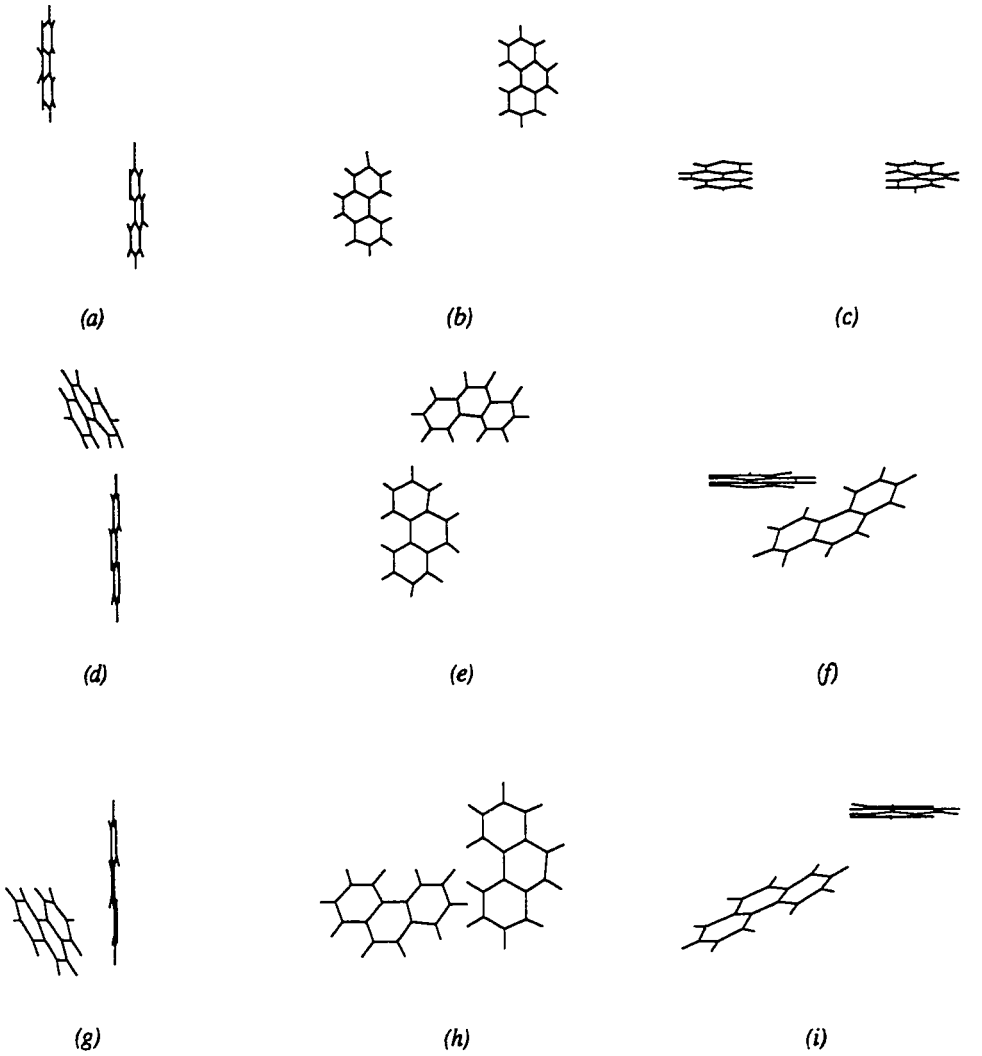

Figure 6.6.8. The four symmetry positions in the unit cell in $P2_1/c$ in the second probable structure of phenanthrene, as viewed along the principal axes of the reference molecule.

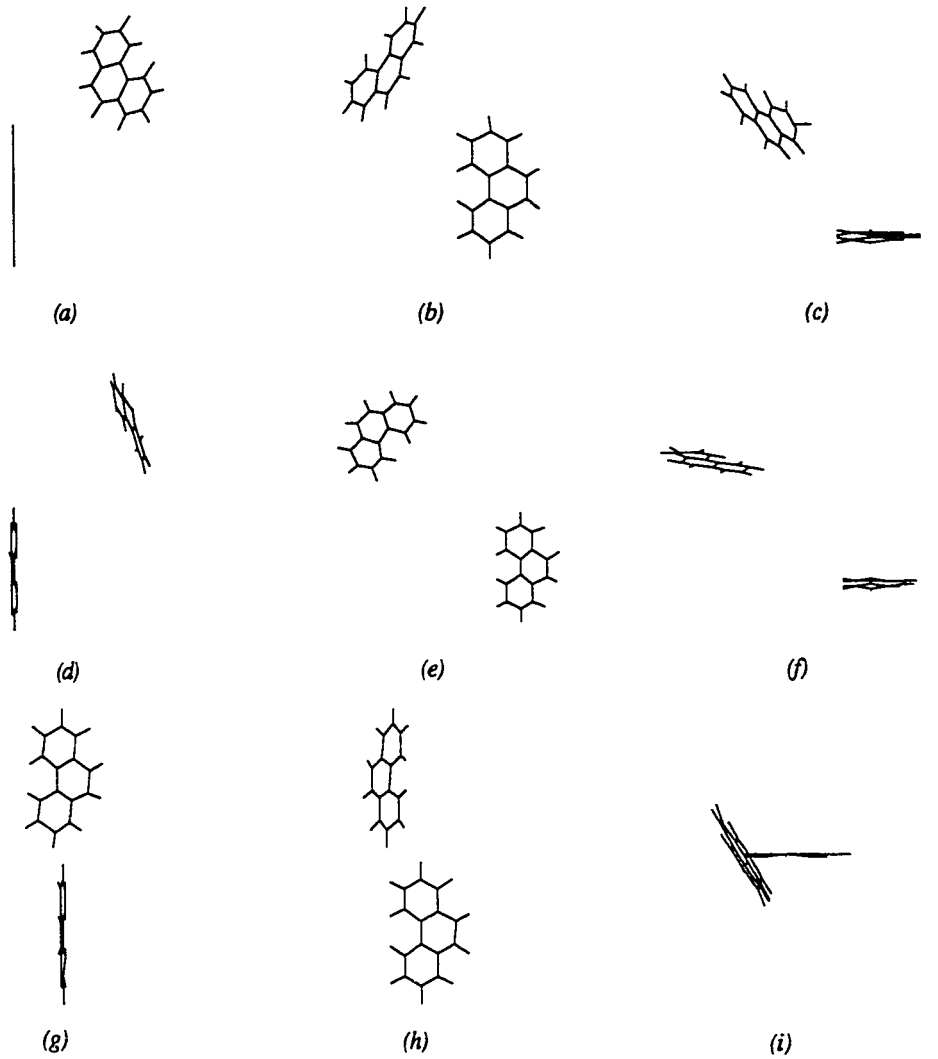

Figure 6.6.9. The four symmetry positions in the unit cell in $P2_12_12_1$ in the third probable structure of phenanthrene, as viewed along the principal axes of the reference molecule

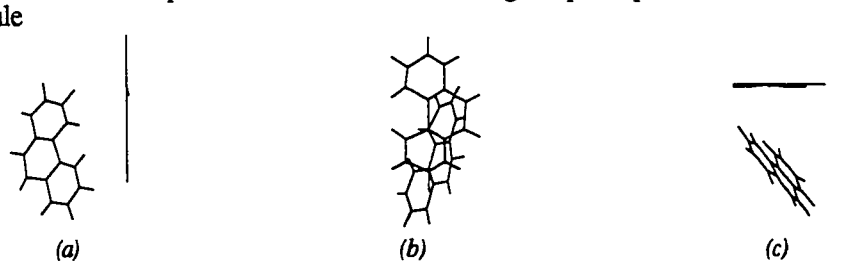

Figure 6.6.10. Local minimum closest to the experimental structure, as viewed along the principal axes of the reference molecule.

6.7. Pyrene

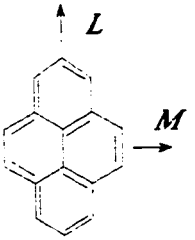

$C_{16}H_{10}$

6.7.1 Experimental Data

Heat of sublimation: 24.8 kcal/mol [135].

Experimental [136]:

Temperature:
Space Group: $P2_1/a$
Molecules per cell: 4

a:	13.60	α:	90°
b:	9.24	β:	100.2°(79.8°)
c:	8.37	γ:	90°

$LOa = 61.1°$	$MOa = 52.2°$	$NOa = 128.7°$
$LOb = 77.7°$	$MOb = 52.4°$	$NOb = 40.2°$
$LOc' = 31.9°$	$MOc' = 120.1°$	$NOc' = 80.5°$

6.7.2 Results

Input for calculations:

Coordinates:	Carbon atoms from X-ray diffraction, H atoms from CHEMX
Multipole moments:	Gaussian 90, STO-3G basis set * 2.33
Van der Waals Volume:	159.293 $Å^3$

Table 6.7 Lowest Energy Structures in Each Space Group for Pyrene

Space Group	Z	Total Energy	E_{lj}	E_{coul}	Packing Index
$P2_1/c$	4	-25.96	-23.70	-2.26	0.6465
$P\bar{1}$	2	-25.78	-23.12	-2.66	0.6363
$P\bar{1}$	1	-25.77	-23.50	-2.77	0.6304
$P2_1/c$	2	-25.74	-23.42	-2.32	0.6439
$P2_1/a$	4	-25.59	-23.21	-2.38	0.6393
$P2_1$	2	-25.02	-22.82	-2.20	0.6360
$P2_12_12_1$	4	-24.60	-22.22	-2.38	0.6293
Pca	4	-24.40	-22.41	-1.99	0.6225
Pna	4	-23.80	-21.70	-2.10	0.6151
$C2/c$	4	-23.02	-21.15	-1.87	0.6123
$Pbca$	4	-22.56	-20.53	-2.125	0.5832
$Pnma$	4	-22.01	-20.82	-1.19	0.5898
Cmc	4	-21.64	-20.39	-1.26	0.5986
$C2/c$	4	-19.82	-19.66	-0.16	0.5919
$Pbcn$	4	-19.44	-19.75	0.31	0.5903
Pmc	2	-17.70	-16.27	-1.43	0.4677
Cmc	4	-16.43	-15.66	-0.77	0.4664
Cmc	4	-16.40	-15.63	-0.77	0.4733

Predicted Structure with Lowest Energy:

Space Group: $P2_1/c$
Molecules per cell: 4
Packing index: 0.6465

a:	7.693	α:	90.0°	Energy:	-25.96
b:	8.228	β:	61.58°	Lennard-Jones:	-23.70
c:	17.704	γ:	90.0°	Coulombic:	-2.256

Structure with lowest energy in second most probable space group:

Space Group:	$P\bar{1}$
Molecules per cell:	2
Packing index:	0.6363

a:	11.040	α:	82.99°	Energy:	-25.78
b:	3.808	β:	84.21°	Lennard-Jones:	-23.12
c:	12.441	γ:	75.28°	Coulombic:	-2.662

Structure with lowest energy in third most probable space group:

Space Group:	$P\bar{1}$
Molecules per cell:	1
Packing index:	0.6304

a:	8.224	α:	65.98°	Energy:	-25.77
b:	3.864	β:	50.50°	Lennard-Jones:	-23.00
c:	12.131	γ:	90.0°	Coulombic:	-2.77

Predicted Structure Closest to Experiment:

Space Group:	$P2_1/a$
Molecules per cell:	4
Packing index:	0.6257

a:	13.478	α:	90°	Energy:	-24.71
b:	9.453	β:	82.06°	Lennard-Jones:	-22.13
c:	8.069	γ:	90°	Coulombic:	-2.571

6.7.3. Discussion of Pyrene Results

The experimental structure of pyrene consists of parallel pairs of molecules arranged in a herringbone configuration in space group $P2_1/a$(Fig. 6.7.1(c)). The relationship between the molecules in each pair is shown in Fig. 6.7.5.

ICE9 found several structures very close in energy near the global minimum. The lowest energy structure was found in space group $P2_1/c$, Z=4, and exhibited a herringbone structure very similar to experiment, but with one molecule occupying each angular position instead of two. (Fig. 6.7.2 & Fig. 6.7.6). Another difference between the experimental and the lowest energy predicted structure is in the angle of the herringbone configuration. In the experimental structure, the planes of the molecules are nearly at 79°, whereas in the lowest energy predicted structure the angle is 43°.

The second most probable structure occurs in $P\bar{1}$, Z=2, and consists of a slipped-stack of parallel molecules. Unlike the experimental structure where the slippage of parallel molecules is approximately 1.5 Å along the **L** axis of the molecule (Fig. 6.7.5), the second most probable structure is slipped 1.5 Å along the **M** axis (Fig. 6.7.6).

The electrostatic energy of the slipped-stack configuration of the second most probable structure is even lower than the herringbone configuration in the global minimum, -2.66 compared to -2.26 kcal/mol, respectively.

6.7.4. Graphical Representation of Pyrene Results

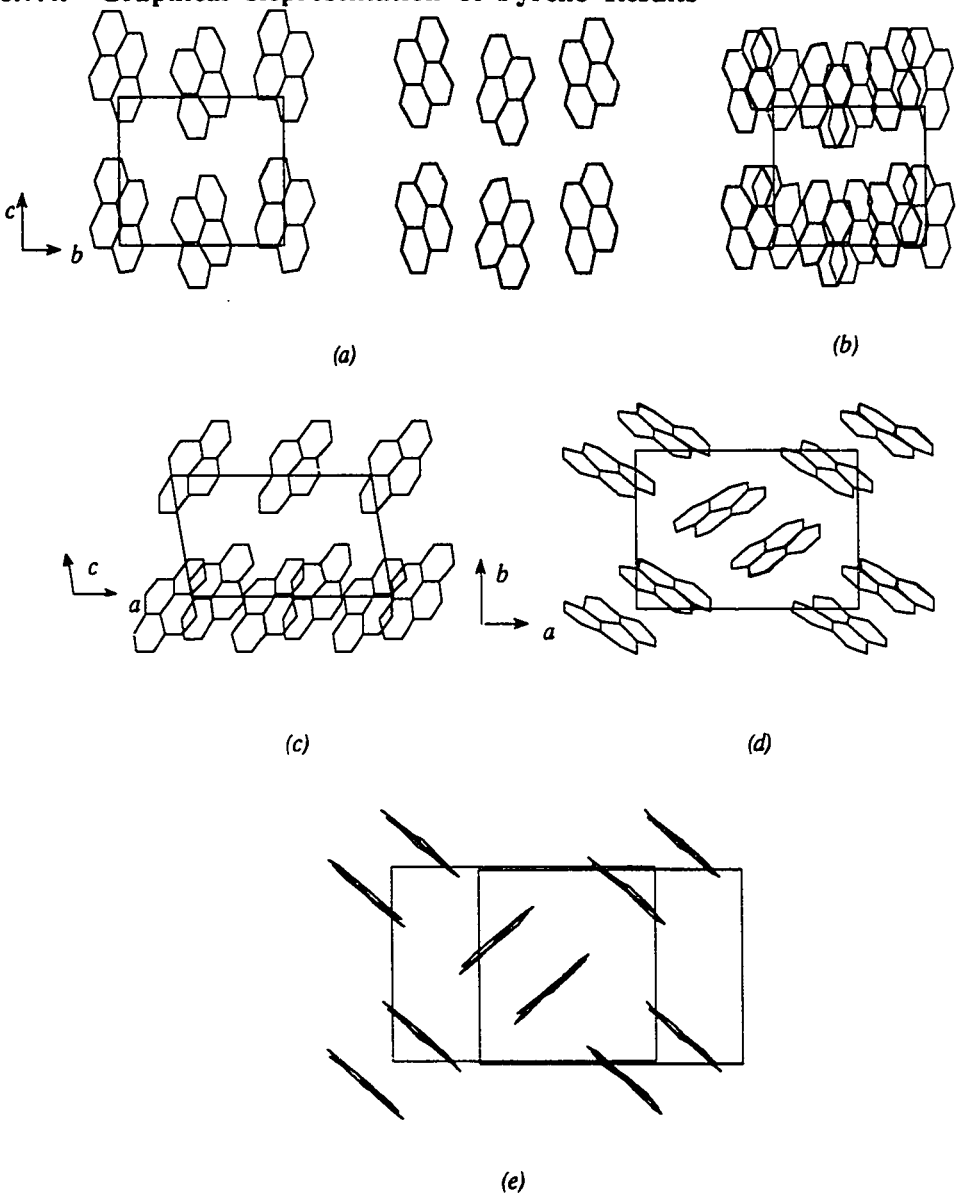

Figure 6.7.1. Experimental structure of pyrene, space group $P2_1/a$ (a). Projection of each layer along *a* axis. (b). Layers superimposed. (c). Projection along *b* axis. (d). Projection along *c* axis. (e). Projection along molecular planes.

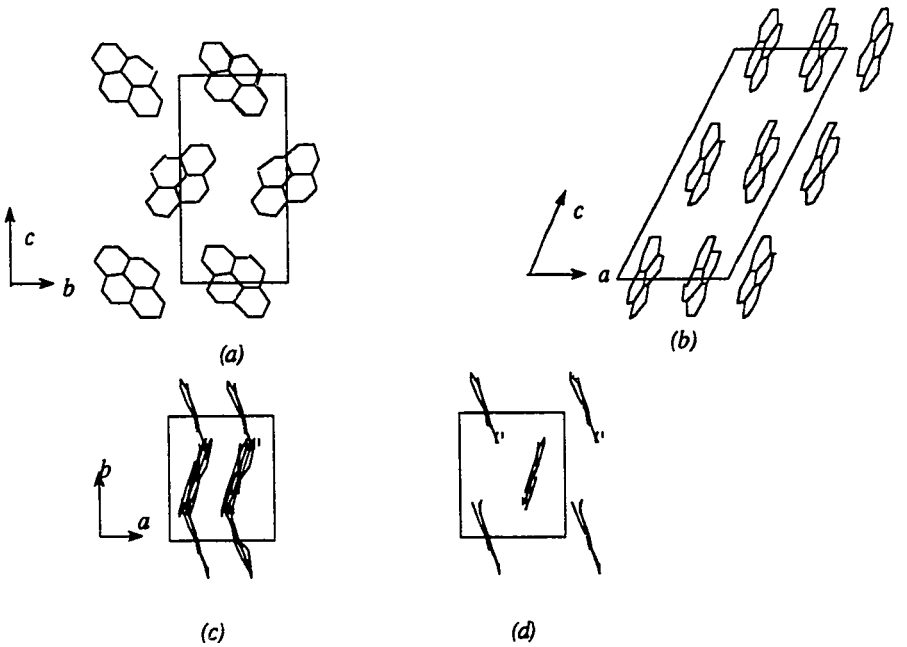

Figure 6.7.2. Most probable structure of pyrene predicted by the program, space group $P2_1/c$ (a). Projection along *a* axis. (b). Projection along *b* axis. (c). Projection of all layers along *c* axis. (d). Projection of one layer along *c* axis.

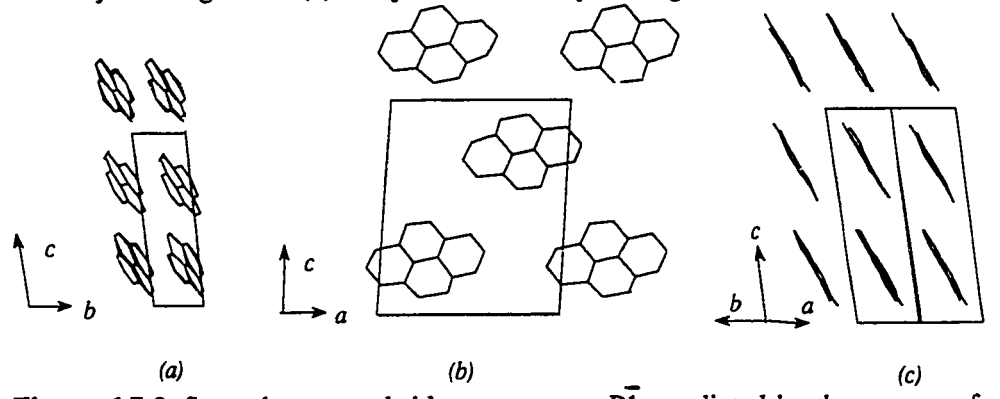

Figure 6.7.3. Second most probable space group $P\bar{1}$, predicted by the program for pyrene (a). Projection along *a* axis. (b). Projection along *b* axis. (c). Projection along *c* axis.

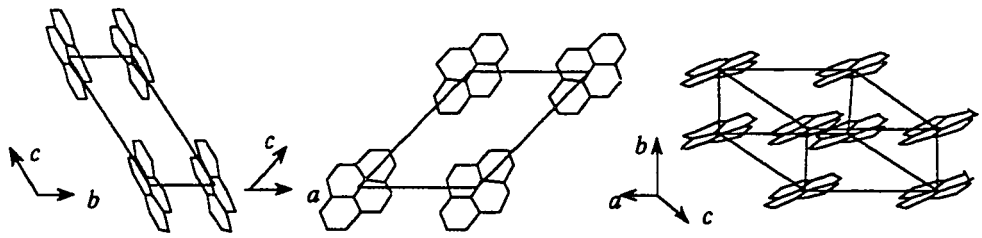

(a) (b) (c)

Figure 6.7.4. Second most probable structure in space group P1, predicted by the program for pyrene. (a). Projection along *a* axis. (b). Projection along *b* axis. (c). General view.

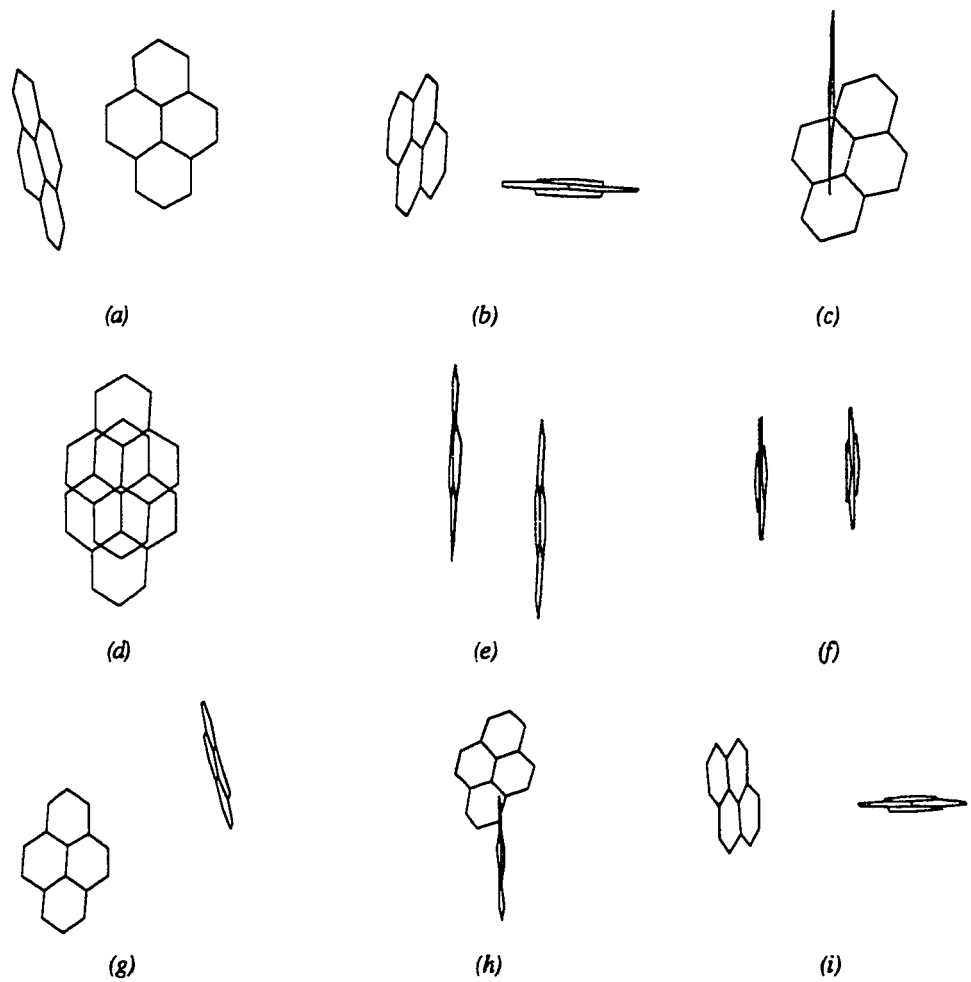

(a) (b) (c)

(d) (e) (f)

(g) (h) (i)

Figure 6.7.5. The two molecules in the unit cell in the experimental structure of pyrene, as viewed along the principal axes of one of the molecules.

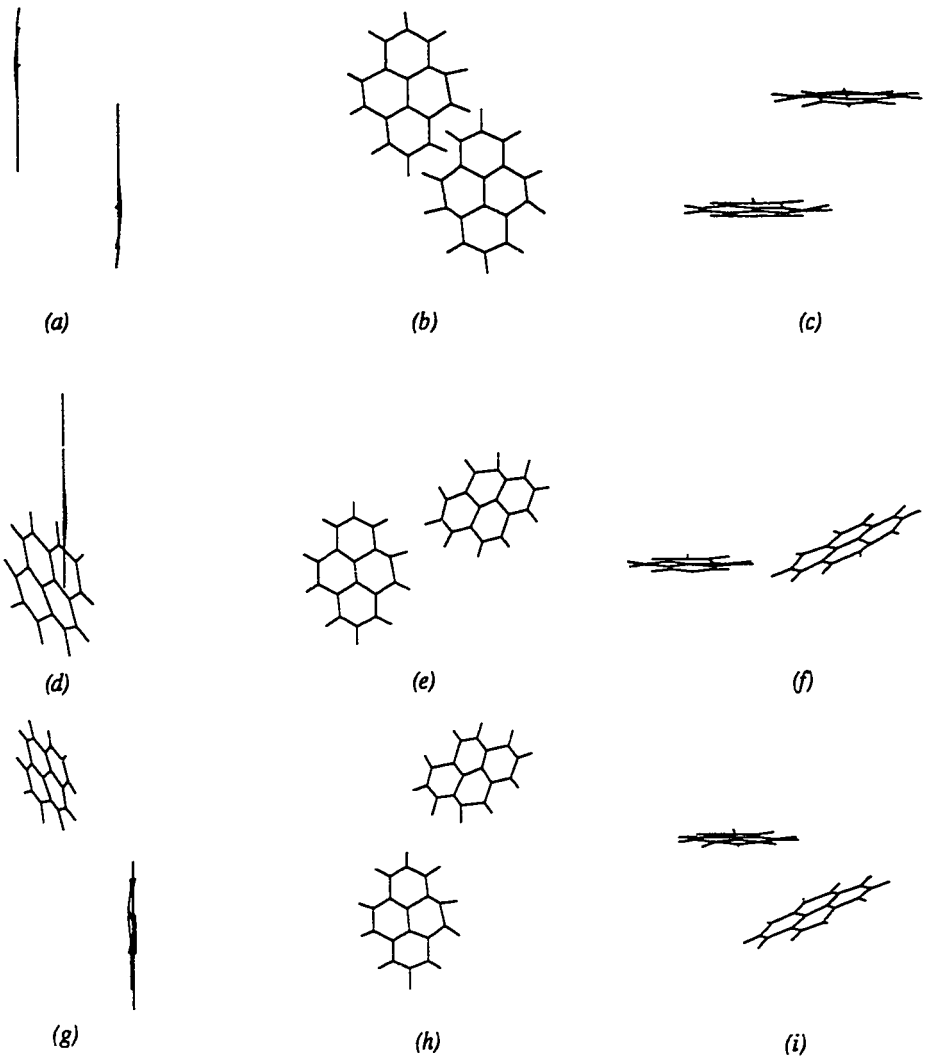

Figure 6.7.6. The four symmetry positions in the unit cell in the most probable structure of pyrene, as viewed along the principal axes of a reference molecule.

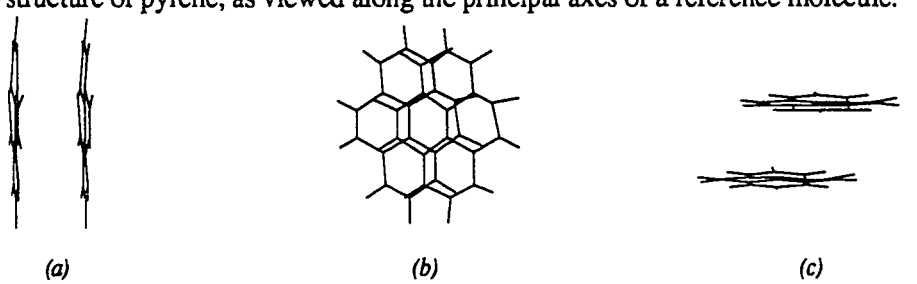

Figure 6.7.7. The two molecules in the unit cell in the second most probable space group for pyrene, as viewed along the principal axes of one of the molecules.

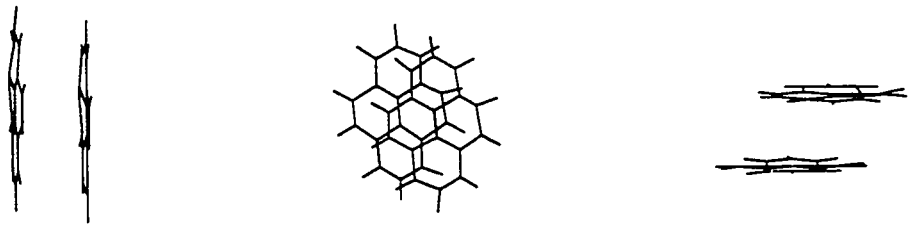

(a) (b) (c)

Figure 6.7.8. The two molecules in adjacent unit cells in the second most probable configuration for pyrene in $P\bar{1}$, as viewed along the principal axes of one of the molecules.

6.8. Triphenylene

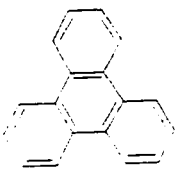

$C_{18}H_{12}$

6.8.1 Experimental Data

Heat of sublimation: 25.6 kcal/mol [36].

Experimental [137]:

Temperature:			RT
Space Group:			$P2_12_12_1$
Molecules per cell:			4
a:	13.17	α:	90°
b:	16.73	β:	90°
c:	5.26	γ:	90°

6.8.2 Results

Input for calculations:

Coordinates:	Carbon atoms from X-ray diffraction, hydrogens from CHEM-X
Multipole moments:	Gaussian 90, STO-3G basis set * 2.33
Van der Waals Volume:	179.831 $Å^3$

Table 6.8 Lowest Energy Structures in Each Space Group for Triphenylene

Space Group	Z	Total Energy	E_{lj}	E_{coul}	Packing Index
$P2_1$	2	-31.20	-26.65	-4.55	0.6393
$P2_12_12_1$	4	-31.14	-26.65	-4.49	0.6393
$P\bar{1}$	2	-30.93	-27.05	-3.88	0.6436
$P2_1/c$	4	-30.74	-25.58	-5.16	0.6309
Pna	4	-30.14	-27.41	-2.73	0.6511
Pca	4	-29.59	-25.68	-3.91	0.6234

Predicted Structure with Lowest Energy:

Space Group: $P2_1$
Molecules per cell: 2
Packing index: 0.6393

a:	4.090	α:	90.0°	Energy:	-31.20
b:	14.123	β:	78.25°	Lennard-Jones:	-26.65
c:	9.948	γ:	90.0°	Coulombic:	-4.551

Structure with lowest energy in second most probable space group:

Space Group: $P2_12_12_1$
Molecules per cell: 4
Packing index: 0.6393

a:	4.090	α:	90°	Energy:	-31.14
b:	14.123	β:	90°	Lennard-Jones:	-26.65
c:	19.479	γ:	90°	Coulombic:	-4.498

Structure with lowest energy in third most probable space group:

Space Group: $P\bar{1}$
Molecules per cell: 2
Packing index: 0.6436

a:	4.1191	α:	85.26°	Energy:	-30.93
b:	10.718	β:	84.80°	Lennard-Jones:	-27.05
c:	12.754	γ:	90.00°	Coulombic:	-3.877

Predicted Structure Closest to Experiment:

Space Group: $P2_12_12_1$
Molecules per cell: 4
Packing index: 0.6482

a:	5.205	α:	90°	Energy:	-28.30
b:	16.578	β:	90°	Lennard-Jones:	-26.94
c:	12.861	γ:	90°	Coulombic:	-1.36

6.8.3. Discussion of Triphenylene Results

Triphenylene crystallizes in $P2_12_12_1$, Z=4, and exhibits a crystal structure in which each molecule is in an edge-to-face orientation with all its nearest neighbors (Fig. 6.8.1). The two most probable space groups predicted by ICE9 are $P2_1$ and $P2_12_12_1$ with structures very similar to experiment. Their energies are also very close, at -31.20 and -31.14 kcal/mol, respectively. The experimental structure and the two most probable structures are built up from the same zig-zag columns. These columns are parallel to the a axis in the experimental structure (Fig 6.8.1(e)) and parallel to the b axis in the two predicted stuctures (Fig. 6.8.2(c),(d) and Fig. 6.8.3(c)). The difference between the experimental and the predicted structures is in the layer perpendicular to these common columns. In the experimental strucure, half of the nearest neighbor molecules in this layer are nearly perpendicular to the reference molecule, and half have parallel molecular planes. In the predicted structures, all of the nearest neighbors in this plane have staggered parallel molecular planes (Fig.6.8.6(d)-(f)). This type of parallel slip-stacking is the predominant mode of packing found in the third most probable space group, $P\bar{1}$, Z=2 (Fig. 6.8.4).

As can be seen in Table 6.8.1, the electrostatic energy is significantly lower in the predicted space groups with at least some edge-to-face packing ($P2_1$, $P2_12_12_1$, $P2_1/c$) than in the totally parallel slipped stack structure ($P\bar{1}$), but the Lennard-Jones energy is higher and the packing index is somewhat lower.

A local minimum fairly close to the experimental structure was observed with an energy of -28.30 kcal/mol, compared to -31.20 kcal/mol for the global minimum. The packing index of this structure is higher than that of the global minimum, 0.6482 compared to 0.6393, indicating it is much more closely packed. The Lennard-Jones energy is lower as well, but the electrostatic energy was much higher, -1.36 kcal/mol compared to -4.551, making it overall a higher energy structure.

6.8.4. Graphical Representation of Triphenylene Results

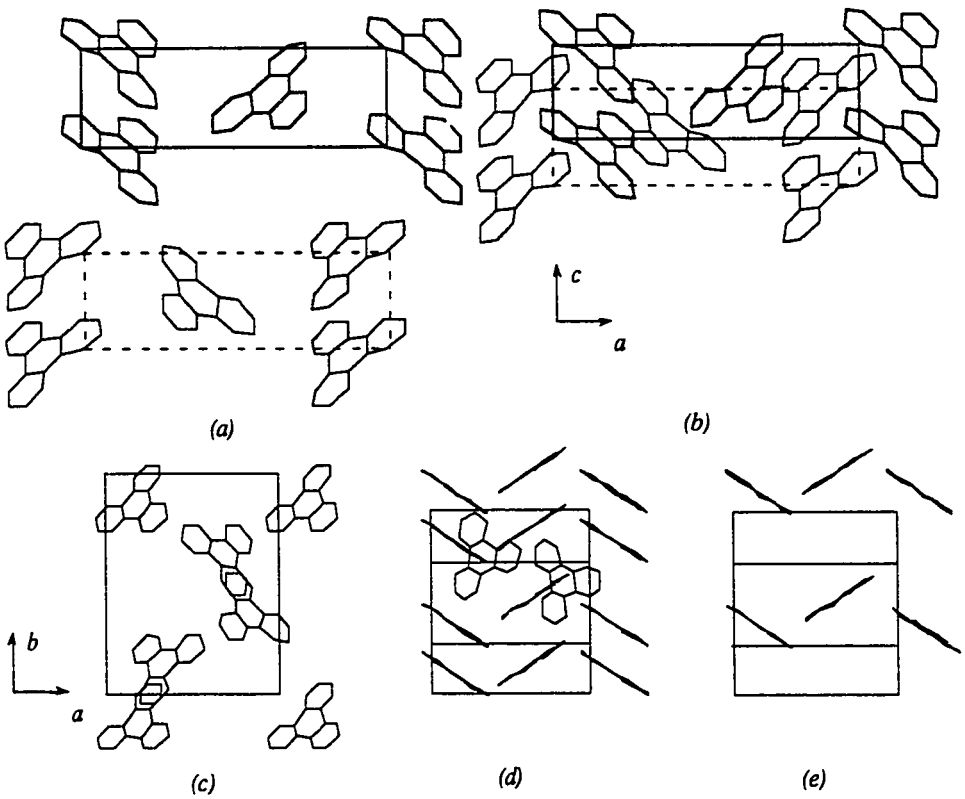

Figure 6.8.1. Experimental structure of triphenylene, space group $P2_12_12_1$. (a). Two different layers viewed along the *b* axis. (b). Projection of both layers in *ac* plane. (c). Projection along *c* axis. (d). General view showing herringbone configuration. (e) Two rows of molecules at the same depth in the projection shown in (d).

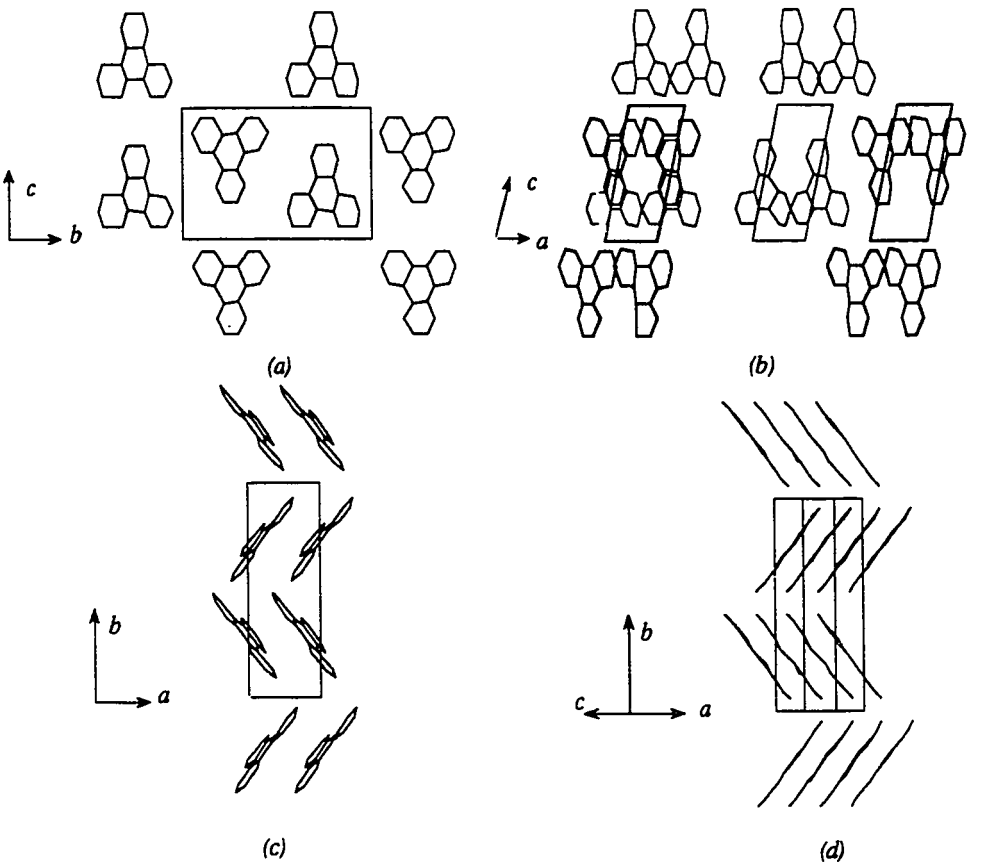

Figure 6.8.2. Most probable structure of triphenylene, predicted by the program, space group $P2_1$. (a). Projection along *a* axis. (b). Projection along *b* axis, showing two layers, together and separately. (c). Projection along *c* axis. (d). Projection along molecular plane, showing all layers.

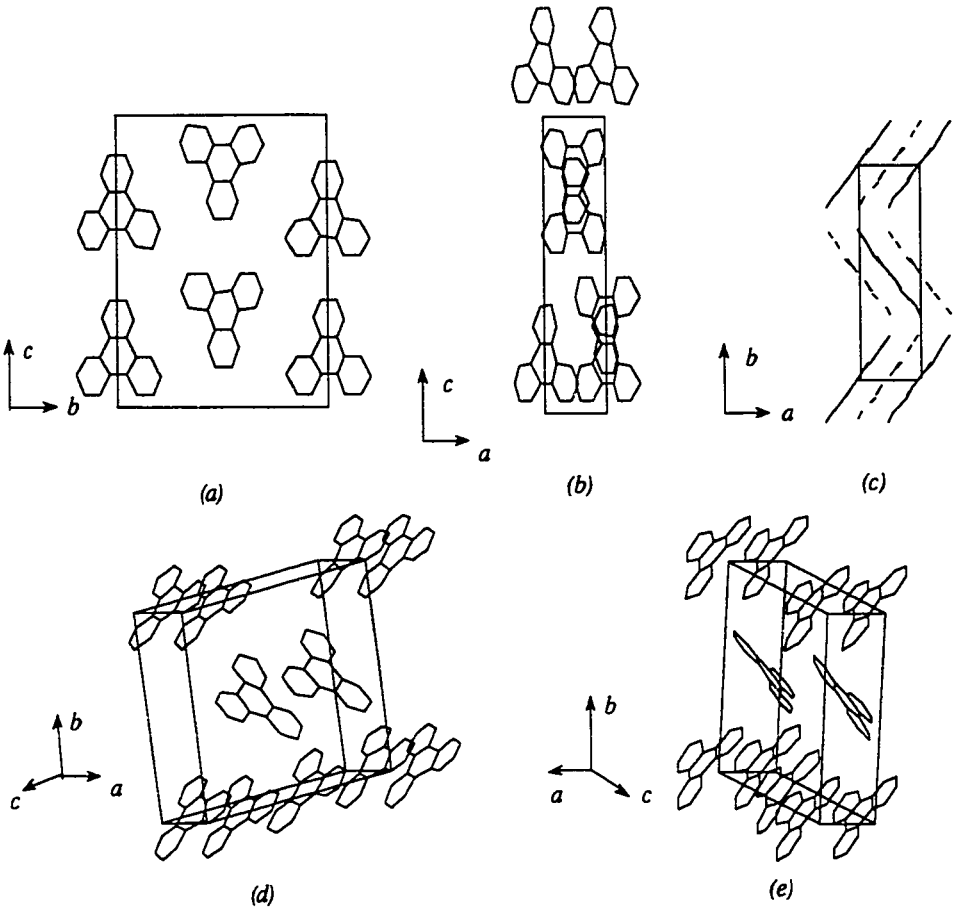

Figure 6.8.3. Second most probable space group, $P2_12_12_1$, predicted by the program for triphenylene. (a). Projection along *a* axis. (b). Projection along *b* axis. (c). Projection along *c* axis, second layer is shown with dashed lines. (d)-(e). General views.

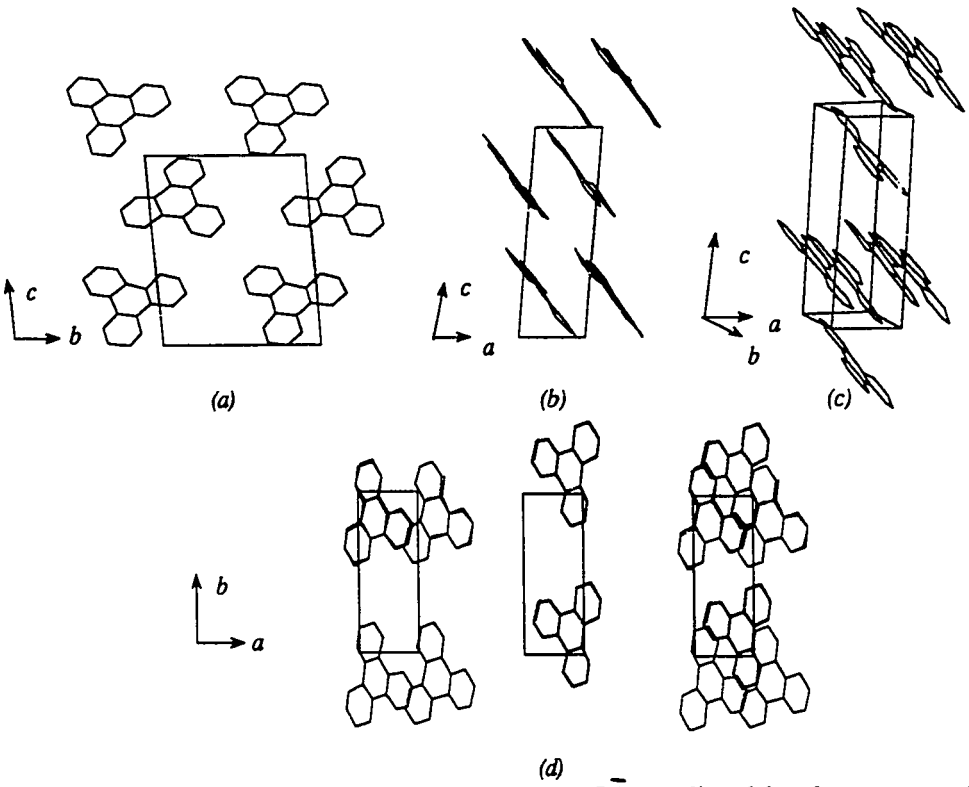

Figure 6.8.4. Third most probable space group $P\bar{1}$, predicted by the program for triphenylene. (a). Projection along *a* axis. (b). Projection along *b* axis. (c). General view. (d). Projection along *c* axis, showing the two layers observed in the full projection on the *ab* plane.

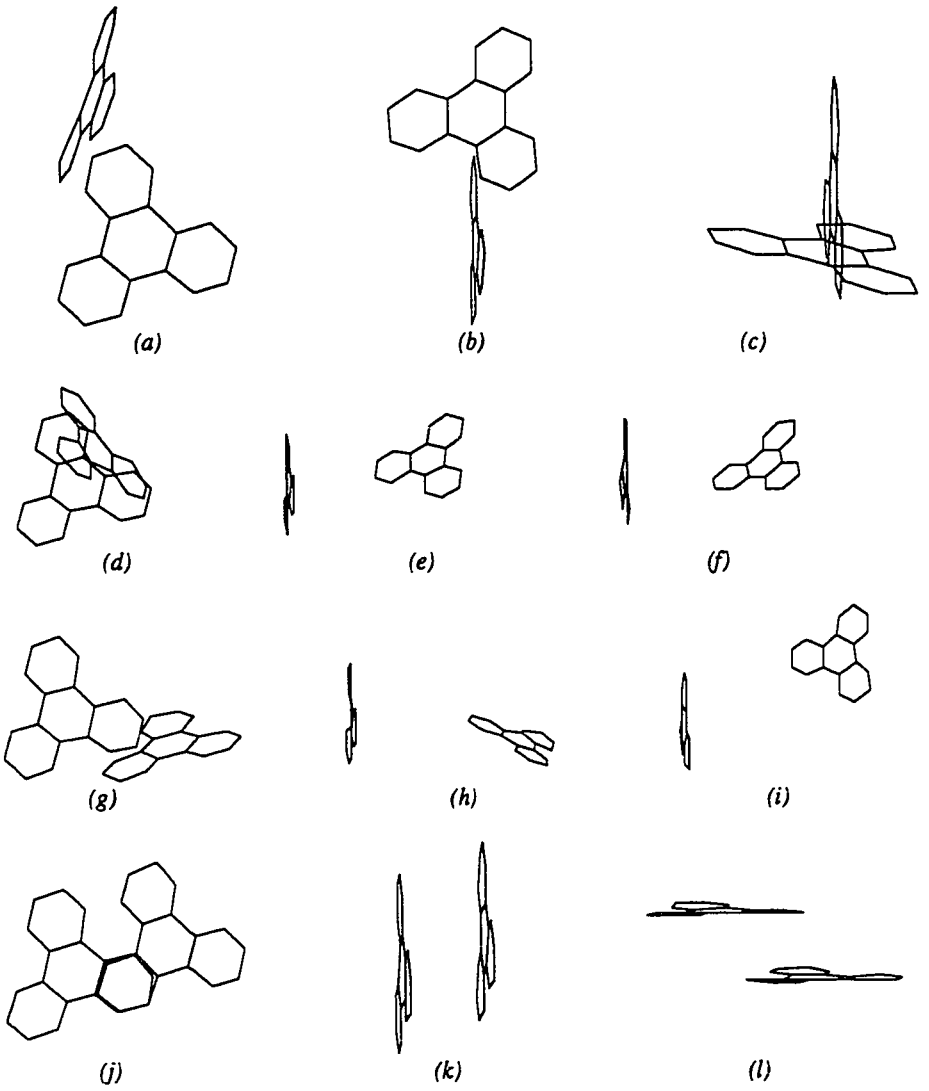

Figure 6.8.5. (a)-(i). The four symmetry positions in the unit cell in the experimental structure of triphenylene, as viewed along the principal axes of one of the molecules. (j)-(l) Nearest neighbors in adjacent unit cells in the [001] direction.

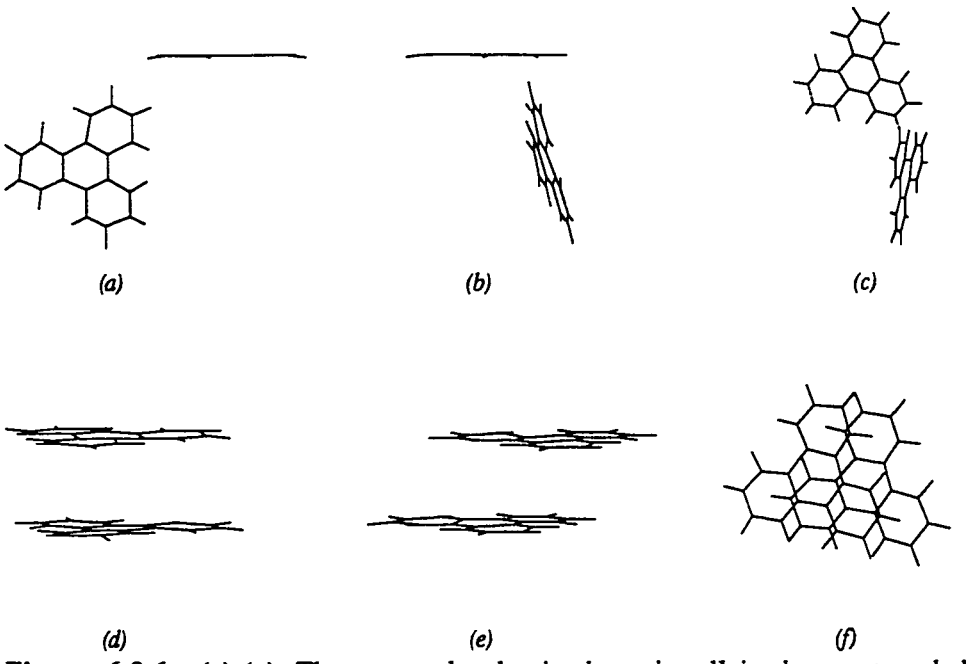

Figure 6.8.6. (a)-(c). The two molecules in the unit cell in the most probable structure of triphenylene in $P2_1$, as viewed along the principal axes of one of the molecules. (d)-(f). Two molecules in adjacent unit cells, showing the slipped-stack configuration within layers.

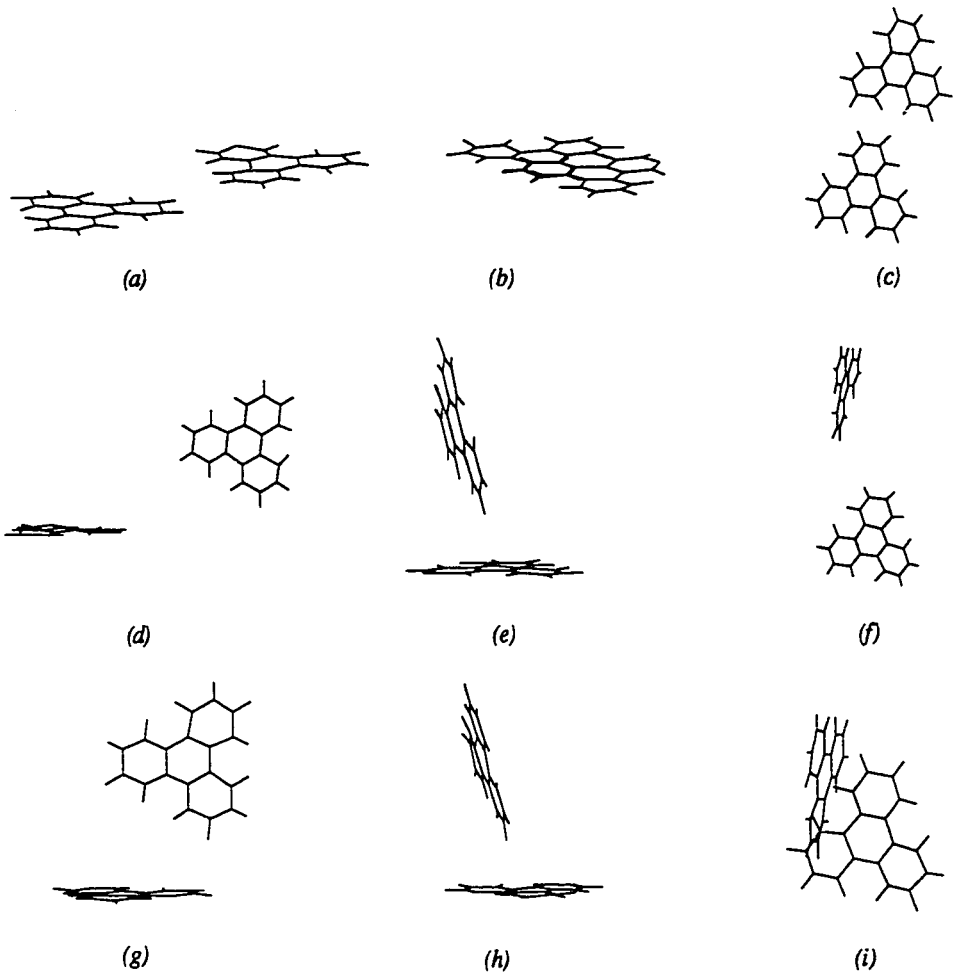

Figure 6.8.7. The four symmetry positions in the unit cell in the second most probable space group, $P2_12_12_1$, for triphenylene, as viewed along the principal axes of one of the molecules.

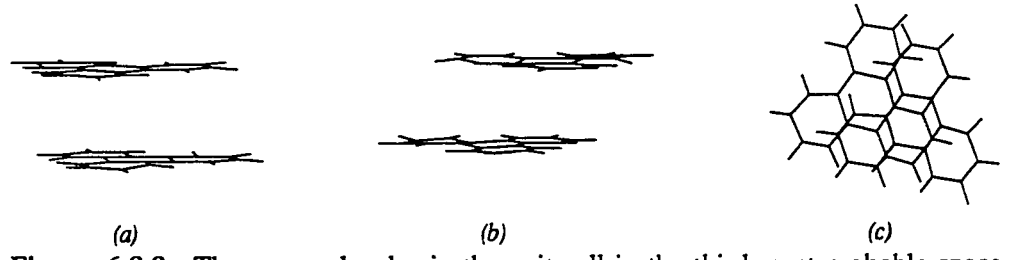

Figure 6.8.8. The two molecules in the unit cell in the third most probable space group for triphenylene, as viewed along the principal axes of one of the molecules.

6.9. 1:2:5:6-Dibenzanthracene

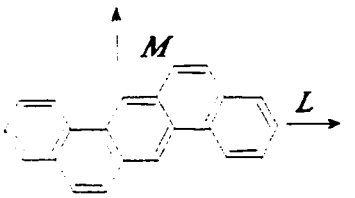

$C_{22}H_{14}$

6.9.1 Experimental Data

Experimental A [138-140]:

Temperature:		RT	
Space Group:		$P2_1$	
Molecules per cell:		2	
a:	6.59	α:	90°
b:	7.84	β:	103.5°(76.5°)
c:	14.17	γ:	90°

Experimental B [141]:

Temperature:		RT	
Space Group:		$Pcab$	
Molecules per cell:		4	
a:	8.22	α:	90.0°
b:	11.39	β:	90.0°
c:	15.14	γ:	90.0°

$LOa = 92.1°$	$MOa = 58.8°$	$NOa = 31.3°$
$LOb = 106.1°$	$MOb = 35.3°$	$NOb = 120.5°$
$LOc' = -16.2°$	$MOc' = 75.2°$	$NOc' = 96.5°$

6.9.2 Results

Input for calculations:

Coordinates:	Carbon atoms from X-ray diffraction, hydrogen atoms from ChemX
Multipole moments:	Gaussian 90, STO-3G basis set * 2.33
Van der Waals Volume:	207.280 Å^3

Table 6.9 Lowest Energy Structures in Each Space Group for 1:2:5:6-Dibenzanthracene

Space Group	Z	Total Energy	E_{lj}	E_{coul}	Packing Index
$P2_1$	2	-37.31	-33.22	-4.09	0.6208
$P\bar{1}$	1	-37.18	-32.81	-4.38	0.6182
$P\bar{1}$	2	-36.48	-33.29	-3.19	0.6193
$P2_1/c$	2	-36.07	-33.42	-2.65	0.6244
$P2_1/c$	4	-35.36	-30.79	-4.60	0.6018
Pca	4	-34.72	-30.96	-3.76	0.5997
Pna	4	-34.32	-29.51	-4.80	0.5851
$C2/c$	4	-34.07	-29.47	-4.60	0.5774
$Pcab$	a	-33.94	-30.66	-3.28	0.5989
$Pbca$	4	-33.90	-30.63	-3.28	0.5988

Predicted Structure with Lowest Energy:

Space Group: $P2_1$
Molecules per cell: 2
Packing index: 0.620847

a:	11.1673	α:	90.00°	Energy:	-37.31
b:	14.6532	β:	76.24°	Lennard-Jones:	-33.22
c:	4.2010	γ:	90.00°	Coulombic:	-4.087

Structure with lowest energy in second most probable space group:

Space Group: $P\bar{1}$
Molecules per cell: 1
Packing index: 0.6182

a:	4.2824	α:	66.87°	Energy:	-37.18
b:	7.8488	β:	83.18°	Lennard-Jones:	-32.81
c:	13.9755	γ:	51.97°	Coulombic:	-4.376

Structure with lowest energy in third most probable space group:

Space Group:	$P\bar{1}$				
Molecules per cell:	2				
Packing index:	0.619260				
a:	4.0242	α:	69.98°	Energy:	-36.48
b:	29.3658	β:	84.54°	Lennard-Jones:	-33.29
c:	6.3526	γ:	71.65°	Coulombic:	-3.194

Predicted Structure Closest to Experiment A:

Space Group:	$P2_1$				
Molecules per cell:	2				
Packing index:	0.6062				
a:	6.399	α:	90°	Energy:	-32.80
b:	7.818	β:	77.63°	Lennard-Jones:	-30.05
c:	13.996	γ:	90°	Coulombic:	-2.752

Predicted Structure Closest to Experiment B:

Space Group:	P*cab*				
Molecules per cell:	2				
Packing index:	0.5803				
a:	8.266	α:	90°	Energy:	-28.82
b:	11.840	β:	90°	Lennard-Jones:	-28.16
c:	14.670	γ:	90°	Coulombic:	-0.652

6.9.3. Discussion of 1:2:5:6-Dibenzanthracene Results

1:2:5:6-Dibenzanthracene crystallizes in two different polymorphs, a monoclinic form in $P2_1$ with Z=2, and an orthorhomibic form in P*cab* (P*bca*) with Z=4. Experimental complications with the monoclinic crystals made it difficult for early researchers to measure intensities accurately and thereby locate atomic positions. Modern researchers with improved techniques, however, have not chosen to further refine the structure, and therefore the atomic coordinates have not yet been determined for the $P2_1$ polymorph. Iball and Robertson [138] were

able to deduce from the diffraction pattern that the orientation of the molecules correspond to those in chrysene if the *a* and *b* axes are interchanged, and if Z=2. The molecular and crystal structures of chrysene are shown in Fig. 6.9.1.

The most probable structure predicted by ICE9 is in one of the experimentally observed space groups, $P2_1$. This structure is shown in Fig. 6.9.3. In this structure the molecular planes are all parallel, in contrast to the supposed edge-to-face configuration in the monoclinic polymorph. The monoclinic angle in both the predicted and observed structures are virtually identical, being 76.24° and 76.5°, respectively. A local minimum was found whose lattice constants and angles match the experimentally observed values.

In the orthorhombic modification, the atomic positions have been determined to a high degree of accuracy, and direct comparison between the experimental and predicted structures is possible. The experimental structure, shown in Fig. 6.9.2, is a herringbone structure built from rows of molecules with their planes parallel. The predicted structure closest to the experimental lattice constants has the L axes of the molecules almost parallel to the *b* axis instead of the *c* axis in the experimental structure.

In the top three predicted structures for dibenzanthracene, all of the molecular planes are parallel, as opposed to the two observed polymorphs in which the molecules exhibit the edge-to-face herringbone configuration. Both lower electrostatic and Lennard-Jones energies were observed for the parallel configurations than for the herringbone structures, as well as higher packing indices.

6.9.4. Graphical Representation of Dibenzanthracene Results

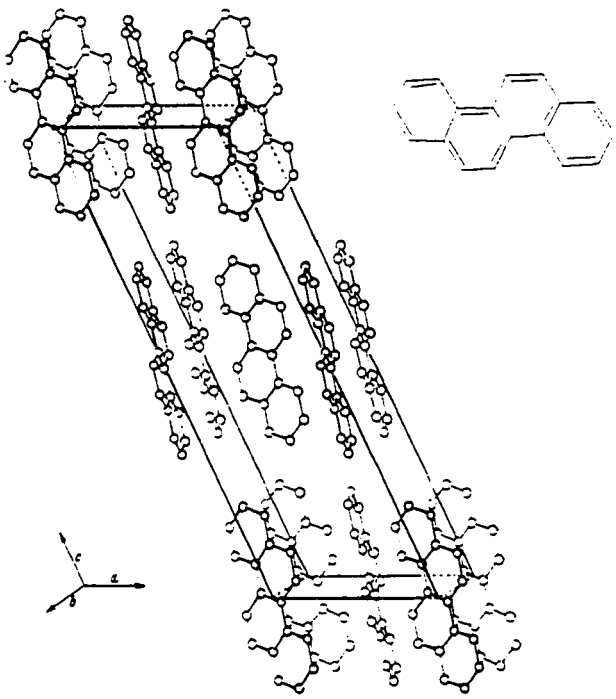

Figure 6.9.1. Crystal structure of chrysene in $P2_1$, Z=4. Iball and Robertson report that this crystal structure is similar to that of the monoclinic form of dibenzanthracene if the *a* and *b* axes are reversed, and Z=2.

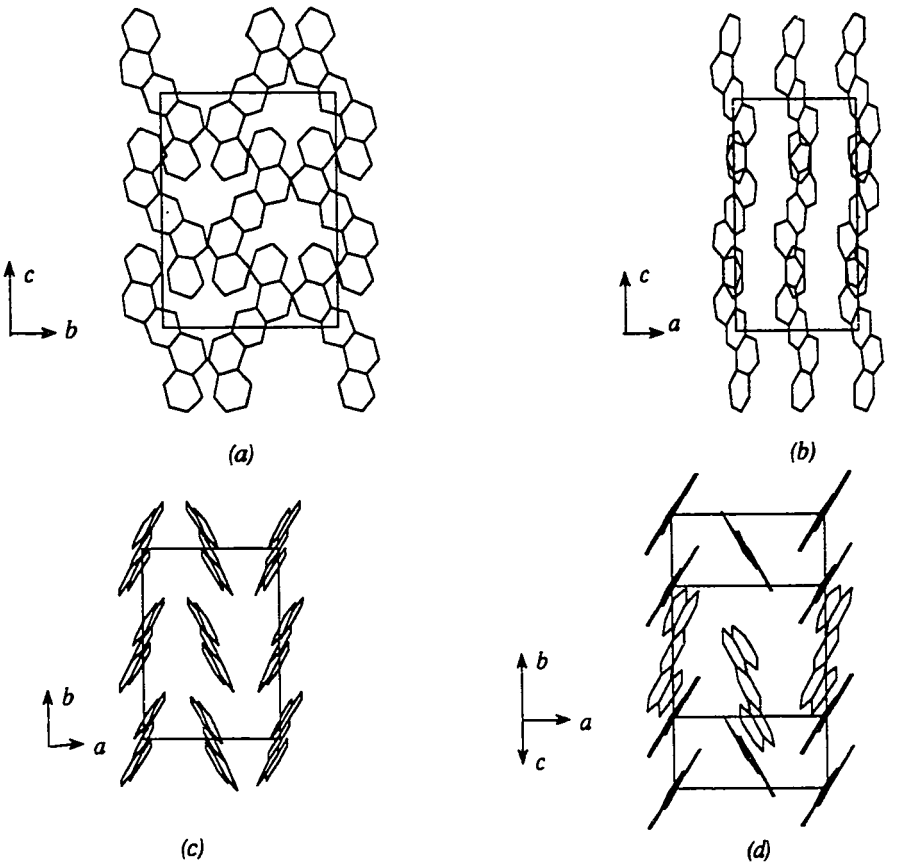

Figure 6.9.2. Experimental structure of dibenzanthracene, space group P*cab* (a). Projection along *a* axis. (b). Projection along *b* axis. (c). Projection along *c* axis. (d). Projection parallel to the molecular plane of molecules in a layer.

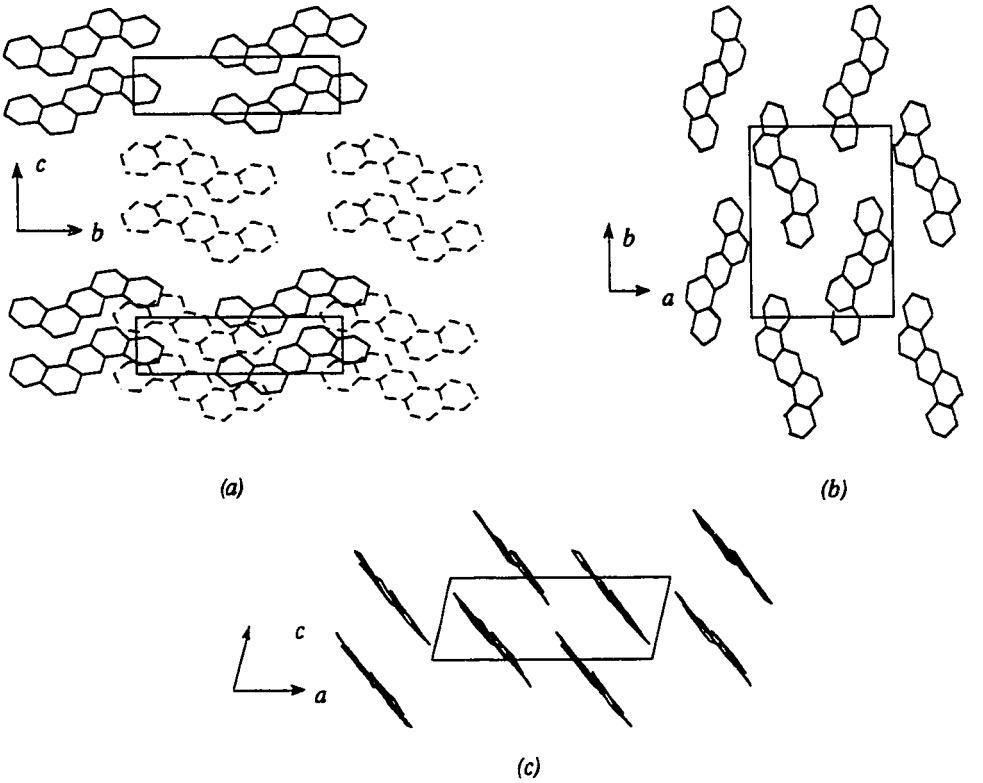

Figure 6.9.3. Most probable structure of dibenzanthracene predicted by the program, space group $P2_1$. (a). Projection along *a* axis of two layers separately and together. (b). Projection along *b* axis. (c). Projection along *c* axis.

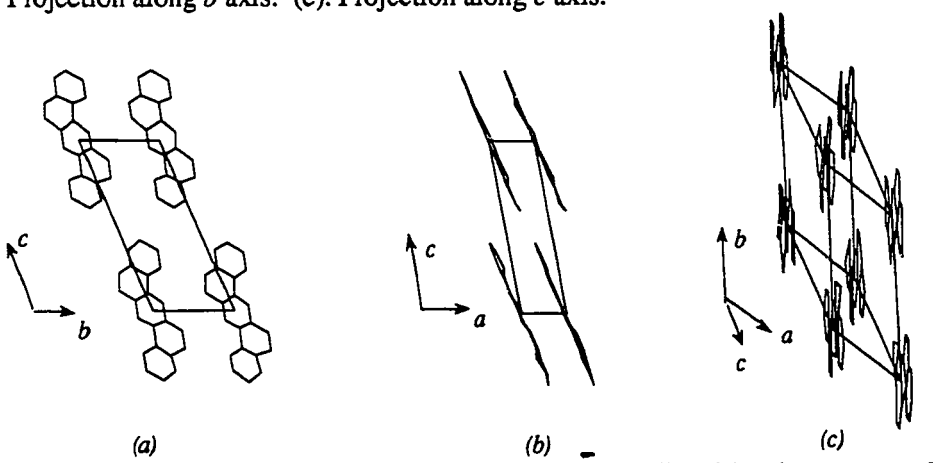

Figure 6.9.4. Second most probable space group, $P\bar{1}$, predicted by the program for dibenzanthracene. (a). Projection along *a* axis. (b). Projection along *b* axis. (c). General view.

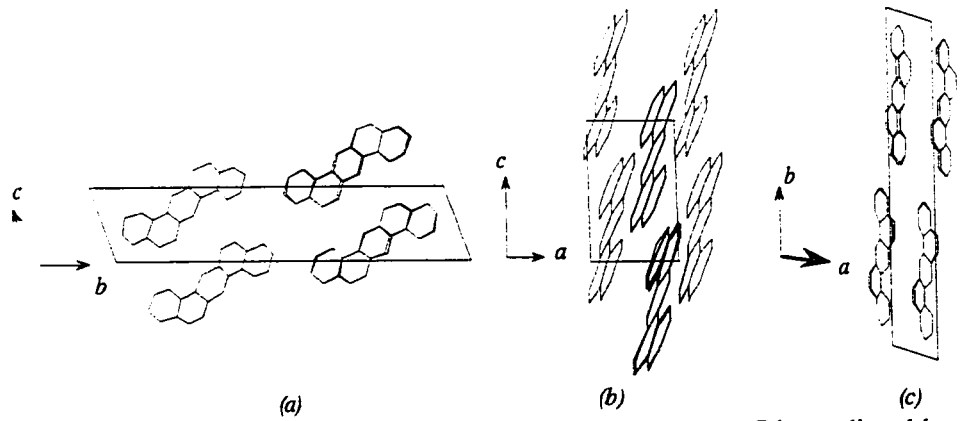

Figure 6.9.5. Second most probable structure in space group P1, predicted by the program for dibenzanthracene. (a). Projection along *a* axis. (b). Projection along *b* axis. (c). Projection along *c* axis.

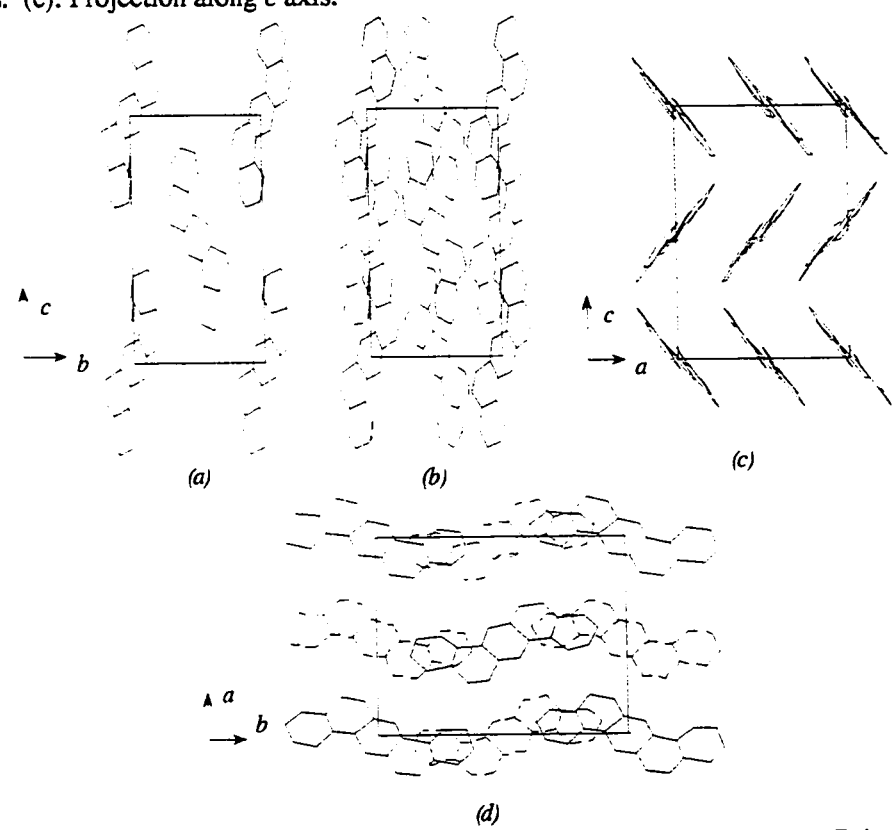

Figure 6.9.6. The predicted structure closest to Experimental Structure B in space group P*cab*. (a). Projection of one layer along the *a* axis. (b). Projection of all layers along the *a* axis. (c) Projection along the *b* axis. (d). Projection along the *c* axis of all layers. Second layer indicated by dashed lines.

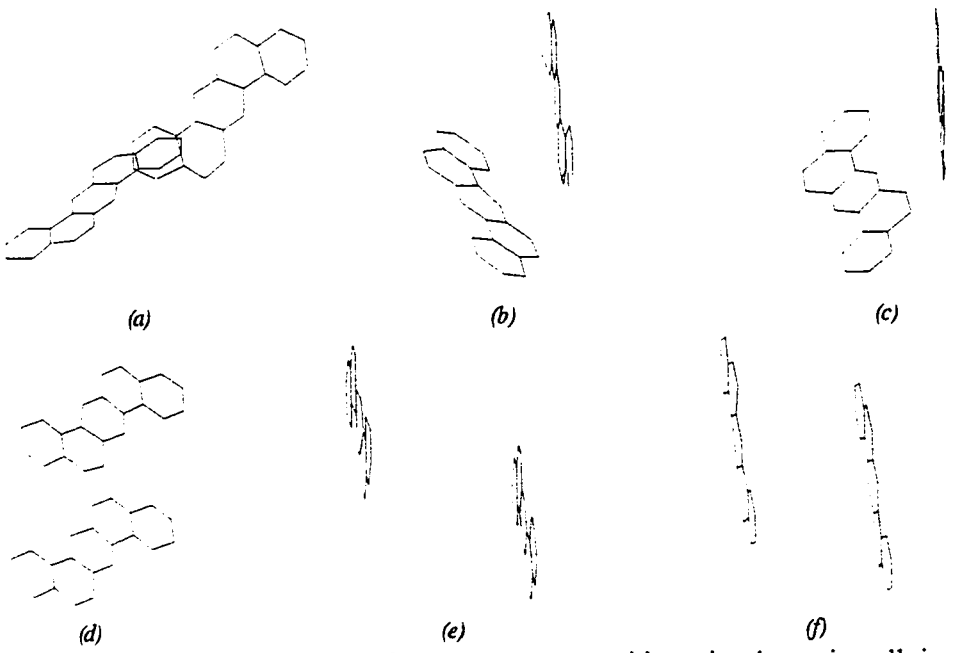

Figure 6.9.7. Three of the four symmetry positions in the unit cell in the experimental structure of dibenzanthracene, as viewed along the principal axes of one of the molecules.

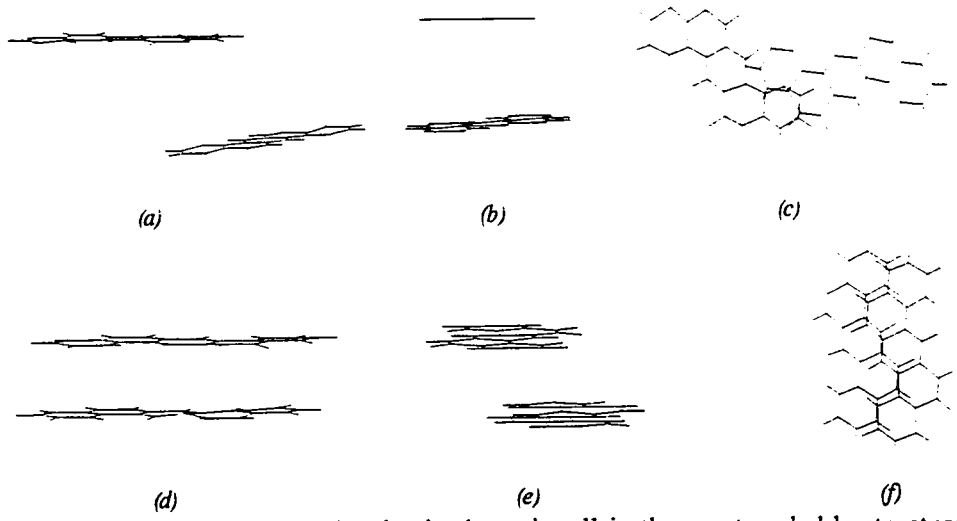

Figure 6.9.8. The two molecules in the unit cell in the most probable structure of dibenzanthracene, as viewed along the principal axes of one of the molecules.

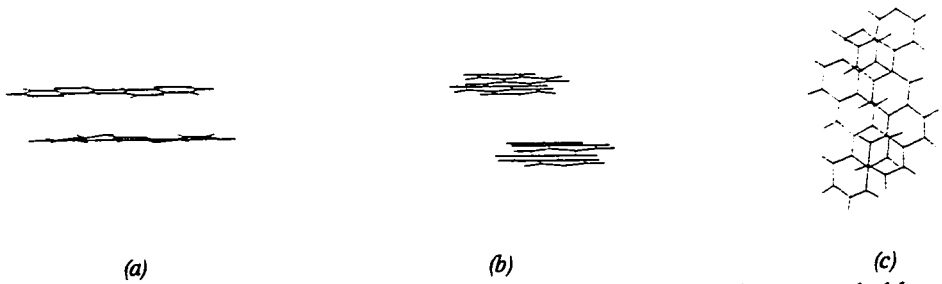

(a) (b) (c)

Figure 6.9.9. The two molecules in the unit cell in the second most probable space group for dibenzanthracene, as viewed along the principal axes of one of the molecules.

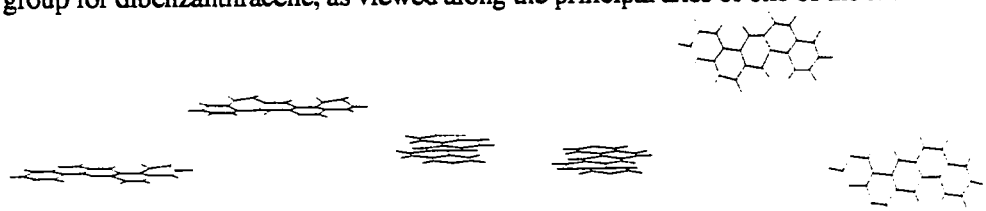

(a) (b) (c)

Figure 6.9.10. The two molecules in the unit cell in the third most probable space group for dibenzanthracene, as viewed along the principal axes of one of the molecules.

6.10. Perylene

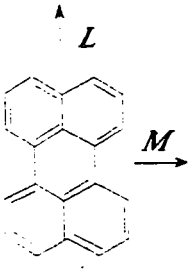

$C_{20}H_{12}$

6.10.1 Experimental Data

Experimental [142]:

Temperature:	RT		
Space Group:	$P2_1/a$		
Molecules per cell:	4		
a:	11.35	α:	90°
b:	10.87	β:	100.8°(79.2°)
c:	10.31	γ:	90°

$LOa = 83.3°$ $MOa = 55.4°$ $NOa = 144.5°$
$LOb = 89.2°$ $MOb = 35.0°$ $NOb = 55.0°$
$LOc' = 6.8°$ $MOc' = 94.5°$ $NOc' = 84.9°$

6.10.2 Results

Input for calculations:

Coordinates:	Carbon atoms from X-ray diffraction, hydrogens from CHEM-X
Multipole moments:	Gaussian 90, STO-3G basis set * 2.33
Van der Waals Volume:	179.831 Å^3

Table 6.10 Lowest Energy Structures in Each Space Group for Perylene

Space Group	Z	Total Energy	E_{lj}	E_{coul}	Packing Index
$P2_1/c$	2	-34.93	-29.84	-5.099	0.6072
$P2_1/c$	4	-34.79	-29.24	-5.56	0.6096
$P\bar{1}$	1	-34.29	-29.29	-4.99	0.6026
$P\bar{1}$	2	-34.25	-29.85	-4.401	0.6056
$P2_1/a$	2	-34.03	-29.69	-4.340	0.6098
$P2_12_12_1$	4	-33.30	-28.74	-4.56	0.5926
Pca	4	-33.14	-28.11	-5.03	0.5811
$P2_1$	2	-32.71	-27.63	-5.076	0.5802
$P2_1/a$	4	-32.38	-27.70	-4.68	0.5847
Pna	4	-32.22	-27.14	-5.074	0.5793
$Pnma$	4	-31.07	-27.03	-4.034	0.5704
$Pbca$	4	-30.31	-28.58	-1.73	0.5818
Pmc	2	-30.25	-25.04	-5.209	0.5285
$C2/c$	4	-28.03	-27.94	-0.087	0.5492
Cmc	4	-27.15	-25.96	-1.196	0.5650
$C2/c$	4	-27.13	-27.53	0.399	0.5703
$Pbcn$	4	-25.90	-25.92	0.025	0.5601
Cmc	4	-21.65	-23.93	2.274	0.5214

Predicted Structure with Lowest Energy:

Space Group: $P2_1/c$
Molecules per cell: 2
Packing index: 0.6072

a:	10.514	α:	90.0°	Energy:	-34.93
b:	4.264	β:	70.44°	Lennard-Jones:	-29.84
c:	14.020	γ:	90.0°	Coulombic:	-5.099

Structure with lowest energy in second most probable space group:

Space Group:	$P2_1/c$
Molecules per cell:	4
Packing index:	0.6096

a:	14.024	α:	90.0°	Energy:	-34.79
b:	4.160	β:	66.42°	Lennard-Jones:	-29.24
c:	22.070	γ:	90.0°	Coulombic:	-5.56

Structure with lowest energy in third most probable space group:

Space Group:	$P\bar{1}$
Molecules per cell:	1
Packing index:	0.6026

a:	4.295	α:	80.75°	Energy:	-34.29
b:	10.016	β:	50.00°	Lennard-Jones:	-29.29
c:	9.178	γ:	83.22°	Coulombic:	-4.994

Structure with lowest energy in fourth most probable space group:

Space Group:	$P2_1/a$
Molecules per cell:	2
Packing index:	0.6098

a:	12.937	α:	90.0°	Energy:	-34.03
b:	4.559	β:	71.98°	Lennard-Jones:	-29.69
c:	10.516	γ:	90.0°	Coulombic:	-4.34

Predicted Structure Closest to Experiment:

Space Group:	$P2_1/a$
Molecules per cell:	4
Packing index:	0.5544

a:	11.640	α:	90°	Energy:	-26.05
b:	10.836	β:	81.20°	Lennard-Jones:	-25.26
c:	10.409	γ:	90°	Coulombic:	-0.784

6.10.3. Discussion of Perylene Results

The experimental structure of perylene is composed of parallel pairs of molecules in the configuration shown in Fig. 6.10.4(d)-(f), in space group $P2_1/a$, Z=4 (Fig. 6.10.1). Within one layer these pairs of molecules are arranged in an edge-to face herringbone manner with surrounding pairs (6.10.1(e)). Across these layers, the pairs are arranged in an extended edge-to-edge stack of parallel molecules as shown in Fig. 6.10.5(d)-(f).

The lowest energy structure found by ICE9 was in space group $P2_1/c$, the same space group but different orientation than the experimental structure (Fig.6.10.2). The relationship between molecules is similar in the predicted structure except that instead of being composed of pairs of parallel molecules, it is composed of extended rows of parallel molecules within the layer, which are angled to form edge-to-face arrangement with the adjacent rows. The differences between the parallel and nearly perpendicular molecules can be seen in Fig. 6.10.6. In the experimental structure the parallel molecules are eclipsed by 1.2 Å more than in the predicted structure. Across the layers, the same type of edge-to-edge arrangement is observed in the predicted structure as in the experimental structure.

The second most probable structure also occurred in space group $P2_1/c$, but with Z=4. The structure within layers is essentially identical to that of the lowest energy structure, but the layers are oriented such that the molecules within adjacent layers are arranged in a herringbone fashion (at an angle of 75°), rather than parallel. The overall energy of these two structures is very close. The second structure has a slightly lower electrostatic energy than the first one (-5.56 compared to -5.10 respectively), but it has a higher Lennard-Jones energy.

The third most probable structure, in space group $P\bar{1}$, Z=1, is constructed entirely of the same type of parallel stacking seen in the first two predicted structures. The electrostatic energy of this entirely parallel structure is only 0.1 kcal/mole higher than the lowest energy structure composed of edge-to-face layers.

A local minimum very close to the experimental structure was found, but with a much higher energy and lower packing index than the global minimum.

6.10.4. Perylene Results

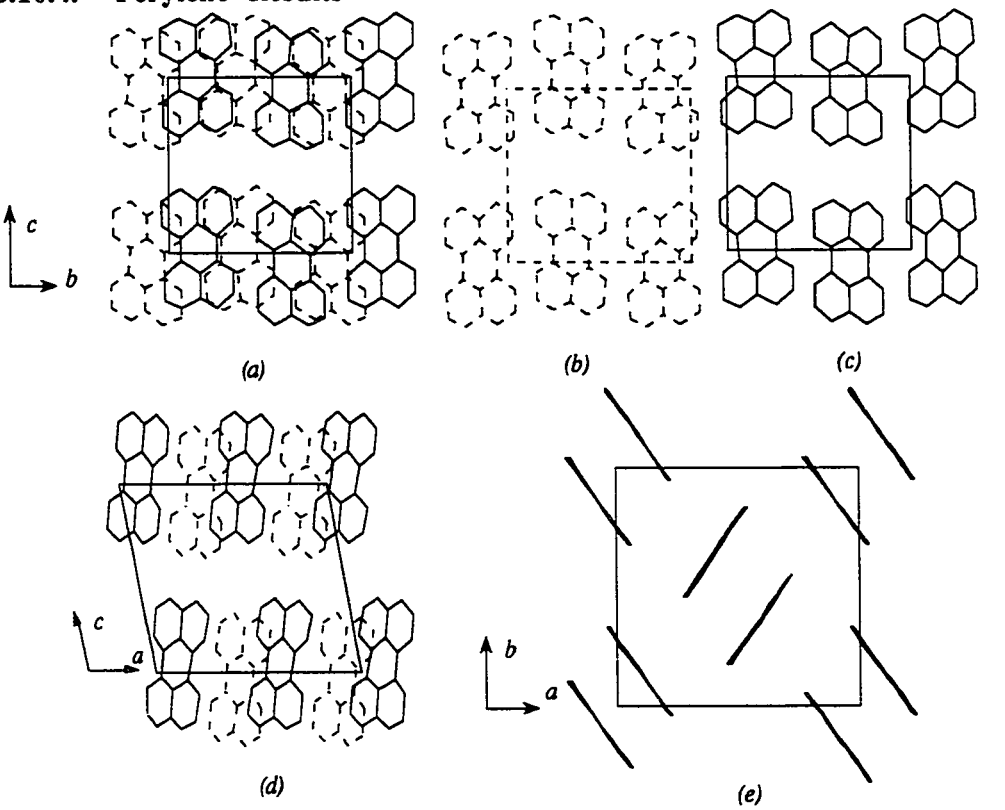

Figure 6.10.1. Experimental structure of perylene, space group $P2_1/a$ (a). Projection of all layers in the *bc* plane. (b). One layer in the *bc* plane. (c). Second layer parallel to *bc* plane. (d). Projection along *b* axis. (e). Projection along *c* axis.

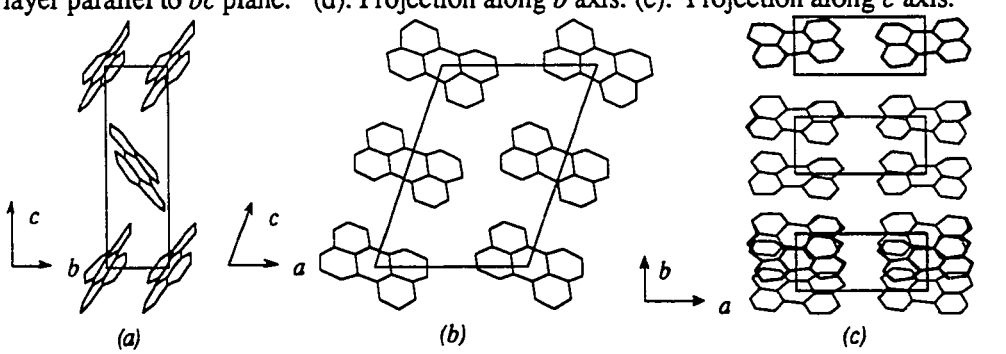

Figure 6.10.2. Most probable structure of perylene predicted by the program, space group $P2_1/c$, Z=2. (a). Projection along *a* axis. (b). Projection along *b* axis. (c). Projection along *c* axis showing two different layers.

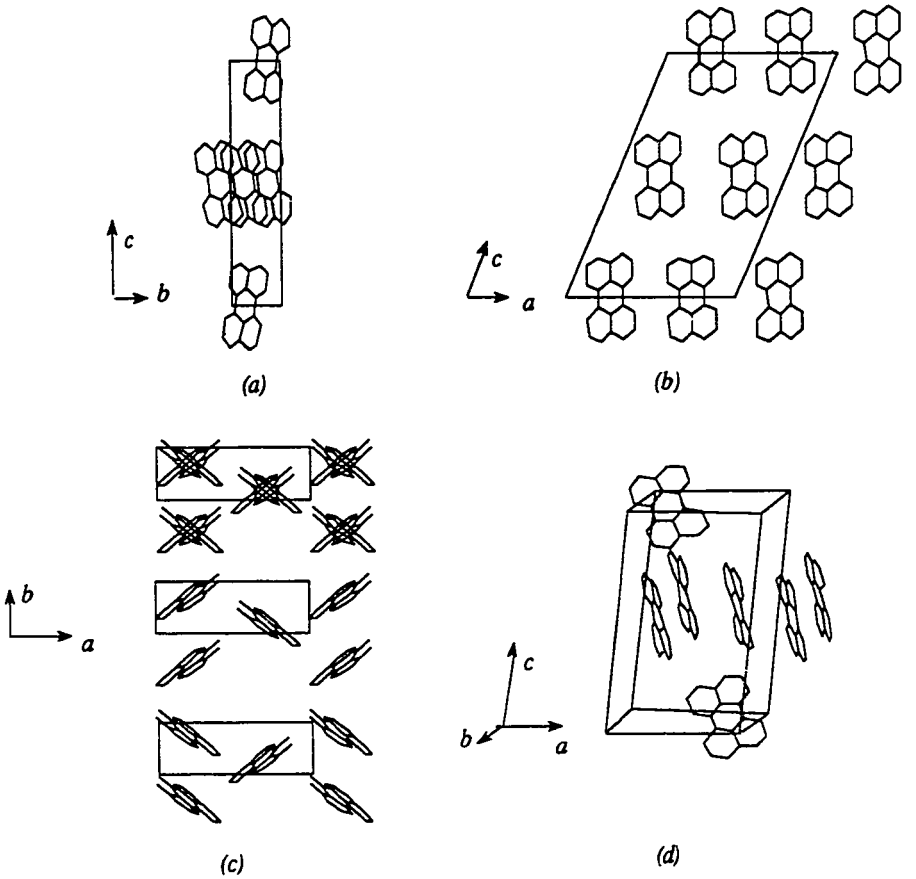

Figure 6.10.3. Second most probable configuration in space group $P2_1/c$, Z=4, predicted by the program for perylene. (a). Projection along *a* axis. (b). Projection along *b* axis. (c). Projection along *c* axis showing projection of layers together and separately. (d). General view.

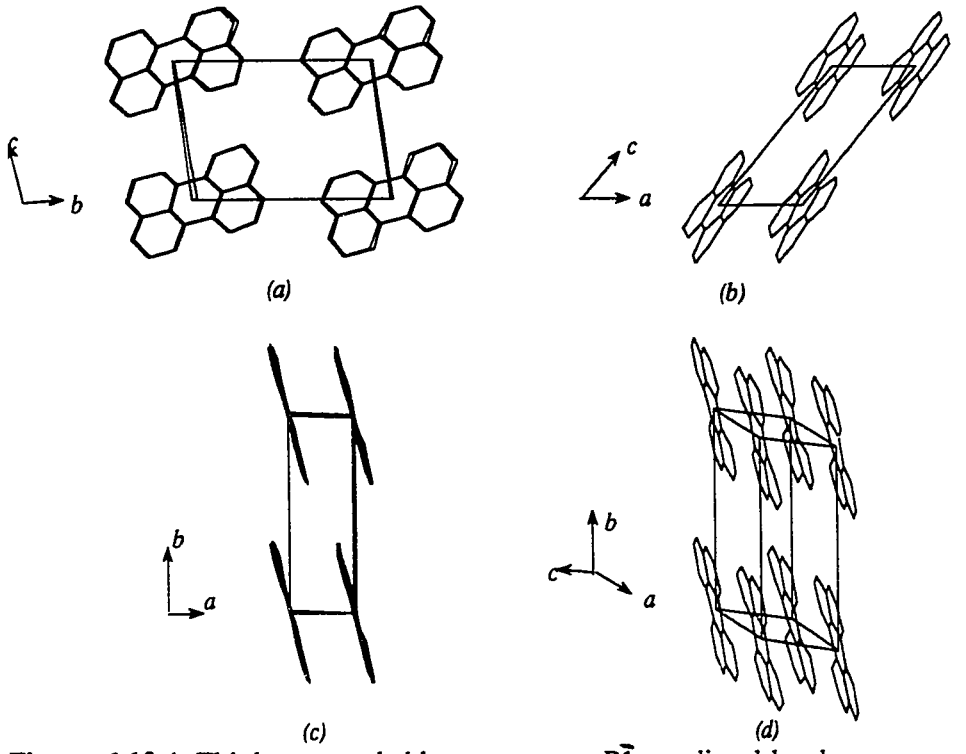

Figure 6.10.4. Third most probable space group $P\bar{1}$, predicted by the program for perylene. (a). Projection along *a* axis. (b). Projection along *b* axis. (c). Projection along *c* axis. (d). General view.

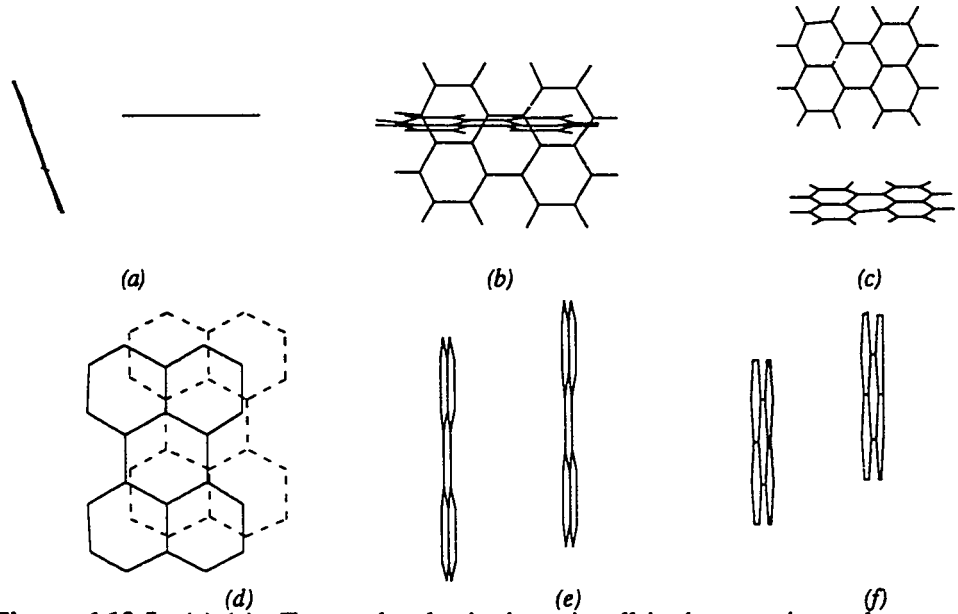

Figure 6.10.5. (a)-(c). Two molecules in the unit cell in the experimental structure of perylene, as viewed along the principal axes of one of the molecules. (d)-(f). Two parallel molecules in the unit cell the principal axes of one of the molecules.

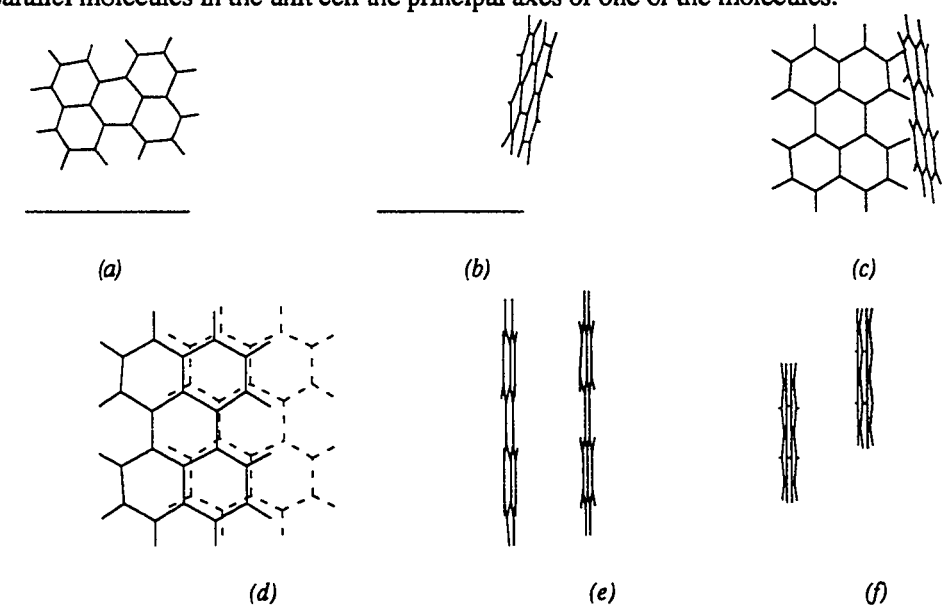

Figure 6.10.6. (a)-(c). The two molecules in the unit cell in the most probable structure of perylene, as viewed along the principal axes of one of the molecules. (d)-(f). Nearest neighbors in the [010] direction.

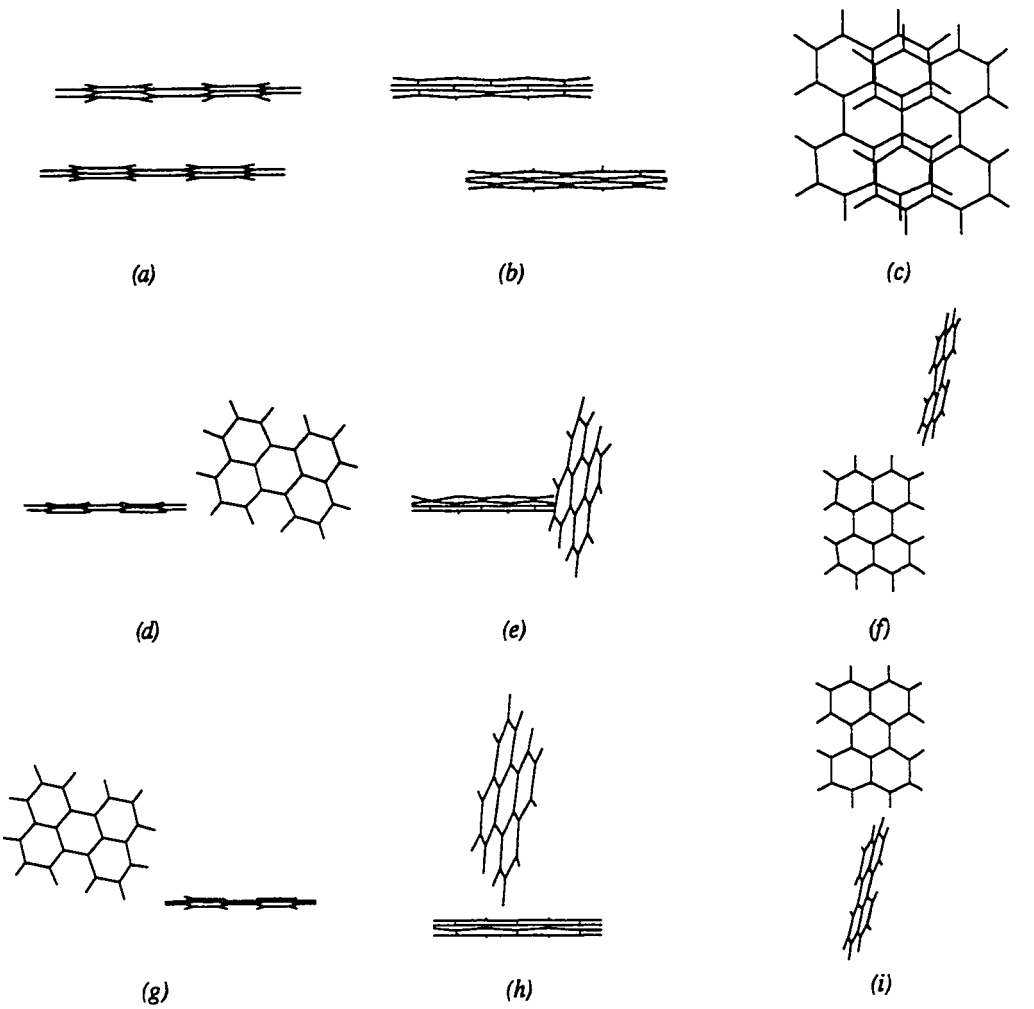

Figure 6.10.7. The four symmetry positions in the unit cell in the second most probable configuration in the space group $P2_1/c$, for perylene, as viewed along the principal axes of one of the molecules.

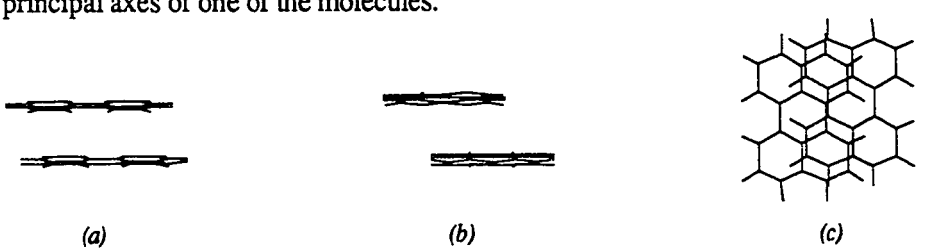

Figure 6.10.8. The two molecules in the unit cell in the third most probable space group for perylene, as viewed along the principal axes of one of the molecules.

6.11. Durene

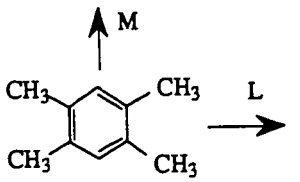

$C_{10}H_{14}$

6.11.1 Experimental Data

Experimental [143]:

Temperature:	RT		
Space Group:	$P2_1/a$		
Molecules per cell:	2		
a:	11.57	α:	90°
b:	5.77	β:	113.3°(66.7°)
c:	7.03	γ:	90°

$LOa = 49.1°$ $MOa = 96.8°$
$LOb = 91.2°$ $MOb = 91.2°$
$LOc' = 84.5°$ $MOc' = 6.9°$

6.11.2 Results

Input for calculations:

Coordinates:	Gaussian 90 3-21G Optimization
Multipole moments:	Gaussian 90, 6-31G basis set
Van der Waals Volume:	115.447 Å^3

Table 6.11 Lowest Energy Structures in Each Space Group for Durene

Space Group	Z	Total Energy	E_{lj}	E_{coul}	Packing Index
$P\bar{1}$	2	-20.41	-20.41	-0.004	0.5653
$P\bar{1}$	1	-20.00	-20.31	0.31	0.5611
Pca	4	-19.90	-20.15	-0.24	0.5593
$P2_12_12_1$	4	-19.78	-19.76	0.03	0.5526
$P2_1/a$	4	-19.64	-19.85	0.21	0.5591
$P2_1/c$	4	-19.51	-19.54	0.03	0.5494
Pna	4	-19.33	-19.63	0.30	0.5501
$P2_1$	2	-19.26	-19.38	0.19	0.5481
$P2_1/a$	2	-19.22	-19.03	-0.19	0.5429
$P2_1/c$	2	-19.05	-19.28	0.23	0.5444
$Pbca$	4	-18.30	-18.60	0.30	0.5349
$C2/c$	4	-18.30	-18.44	0.15	0.5330
$Pnma$	4	-17.78	-17.76	-0.11	0.5248
$C2/c$	4	-17.55	-17.44	-0.11	0.5139
Cmc	4	-16.93	-16.85	-0.08	0.5114
Pmc	2	-16.51	-16.80	0.29	0.5000
$Pbcn$	4	-15.36	-15.35	-0.01	0.4879
Cmc	4	-14.48	-14.46	-0.02	0.4705

Predicted Structure with Lowest Energy:

Space Group: $P\bar{1}$
Molecules per cell: 2
Packing index: 0.5653

a:	7.772	α:	74.83°	Energy:	-20.41
b:	13.539	β:	88.18°	Lennard-Jones:	-20.41
c:	4.137	γ:	76.56°	Coulombic:	-0.0004

Structure with lowest energy in second most probable space group:

Space Group:	$P\bar{1}$				
Molecules per cell:	1				
Packing index:	0.5611				
a:	3.980	α:	74.41°	Energy:	-20.00
b:	6.2804	β:	74.79°	Lennard-Jones:	-20.31
c:	8.855	γ:	86.08°	Coulombic:	0.313

Structure with lowest energy in third most probable space group:

Space Group:	Pca				
Molecules per cell:	4				
Packing index:	0.5593				
a:	12.2055	α:	90.0°	Energy:	-19.90
b:	4.001	β:	90°	Lennard-Jones:	-20.15
c:	16.9054	γ:	90.0°	Coulombic:	0.244

Predicted Structure Closest to Experiment:

Space Group:	$P2_1/a$				
Molecules per cell:	2				
Packing index:	0.5324				
a:	11.157	α:	90°	Energy:	-18.48
b:	6.014	β:	65.91°	Lennard-Jones:	-18.35
c:	7.080	γ:	90°	Coulombic:	-0.131

6.11.3. Discussion of Durene Results

Durene crystallizes in a completely herringbone structure in which each molecule is surrounded by nearly perpendicular nearest neighbors (Fig. 6.11.1). In this way the structure resembles that of benzene, but with a significant difference. In benzene, the molecules are arranged so that the hydrogen atoms on the edge of one molecule are placed at the center of the aromatic face of the other, whereas in the durene structure the methyl groups on different molecules interact with each other, rather than with the center of the aromatic ring (Fig. 6.11.5).

The lowest energy structure found by ICE9 consists entirely of parallel molecules in a slipped stack configuration in $P\bar{1}$, Z=2 (Fig. 6.11.2 and 6.11.6). The stacking structure is such that the methyl groups are staggered along the **L** axes of the molecule. This structure, in which the methyl groups of molecules in one layer are over the aromatic hydrogen atoms in the next layer, minimizes the steric interactions between the bulky methyl groups and allows the molecular planes to approach as close as possible, thus maximizing the Lennard-Jones energy. This structure, therefore, exhibited the highest packing index of all the structures found, as well as the lowest Lennard-Jones energy. The electrostatic energy of this structure was negligible. In the experimental structure, the closest intermolecular contact occurs where the methyl groups are ortho to each other and cannot dovetail effectively to allow closer packing as they can in the proedicted structure. Hence the lower packing index of the experimental structure.

In the second most probable structure, also in $P\bar{1}$ but with Z=1, the molecules are arranged so that the methyl groups are staggered on the ortho side, similar to the experimental structure, but with parallel instead of perpendicular molecular planes. Because of this arrangement of the relatively bulky methyl groups, the molecular faces cannot approach as closely as in the lowest energy structure and the Lennard-Jones energy is higher and the packing index is lower. The electrostatic energy for this structure is positive, but small (0.3 kcal/mol).

In the third most probable structure, in Pca with Z=4, the molecules are arranged in rows of slipped-stacks which interact with adjacent rows at 54°to form a herringbone structure (Fig. 6.11.4). The rows are configured such that the hydrogen atoms are staggered, as can be seen in Fig. 6.11.8(h). This structure has a small negative electrostatic energy at -0.24 kcal/mol.

A local minimum was found which was very close to the experimental structure, but with an overall energy of -18.48 kcal/mol, compared to the global energy minimum at -20.41 kcal/mol. The packing index of this structure was considerably lower than the structure with the lowest calculated energy.

6.11.4. Graphical Representation of Durene Results

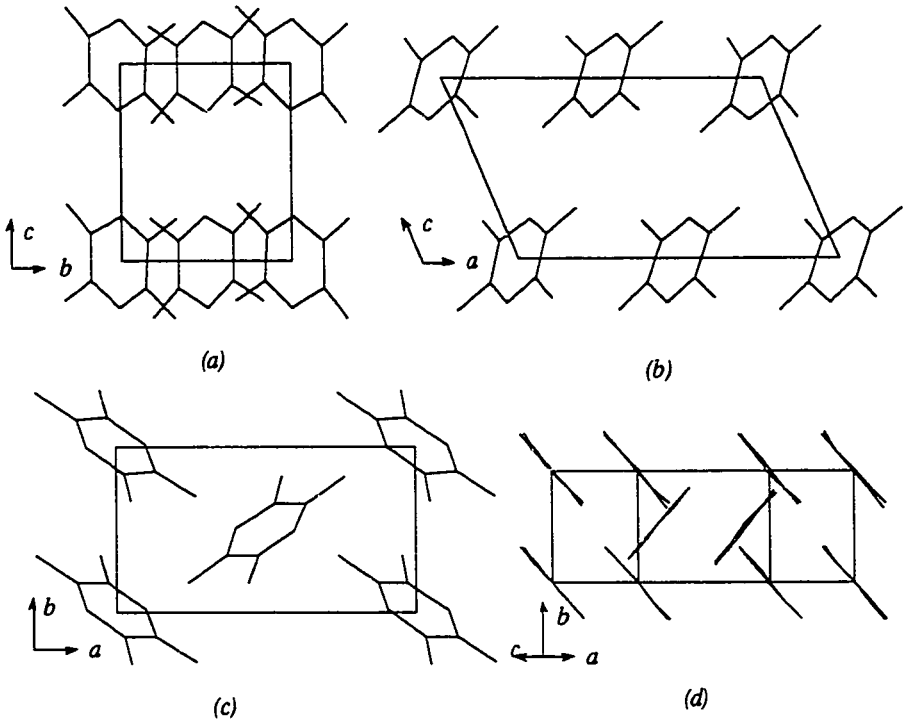

Figure 6.11.1. Experimental structure of durene, space group $P2_1/a$, Z=2. (a). Projection along *a* axis. (b). Projection along *b* axis. (c). Projection along *c* axis. (d). Projection along the molecular plane, showing the projection of two herringbone layers.

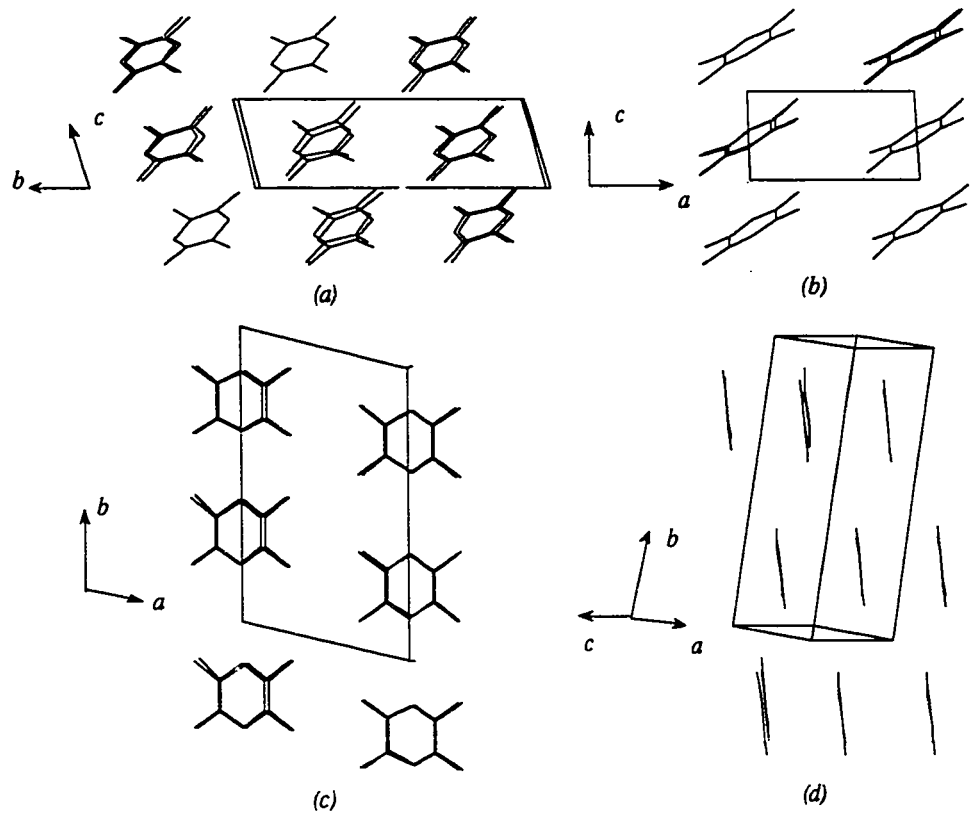

Figure 6.11.2. Most probable structure of durene predicted by the program, space group $P\bar{1}$, Z=2. (a). Projection along *a* axis. (b). Projection along *b* axis. (c). Projection along *c* axis. (d). Projection parallel to the molecular plane.

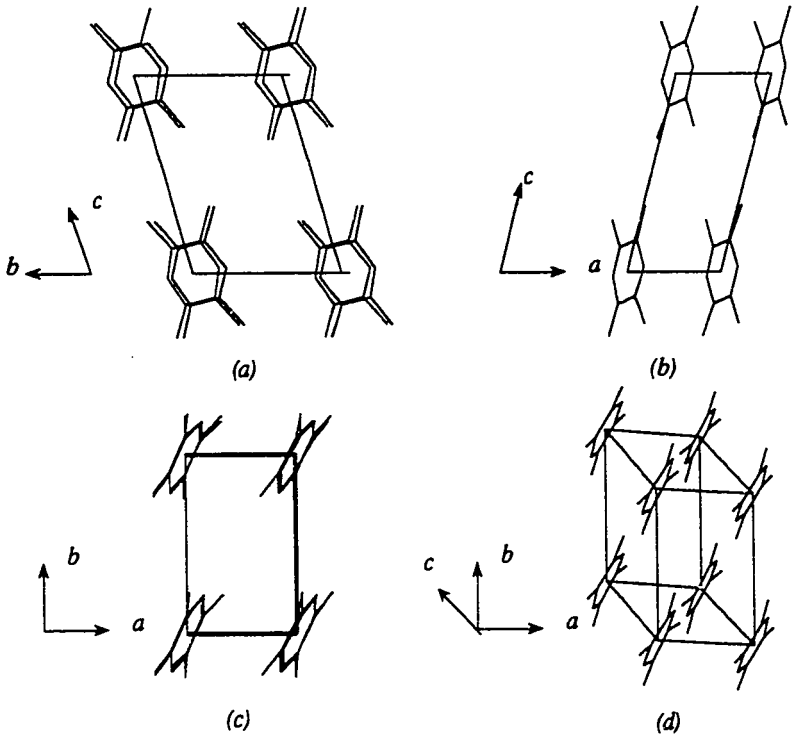

Figure 6.11.3. Second most probable configuration in space group $P\bar{1}$, Z=1, predicted by the program for durene. (a). Projection along *a* axis. (b). Projection along *b* axis. (c). Projection along *c* axis. (d). General view.

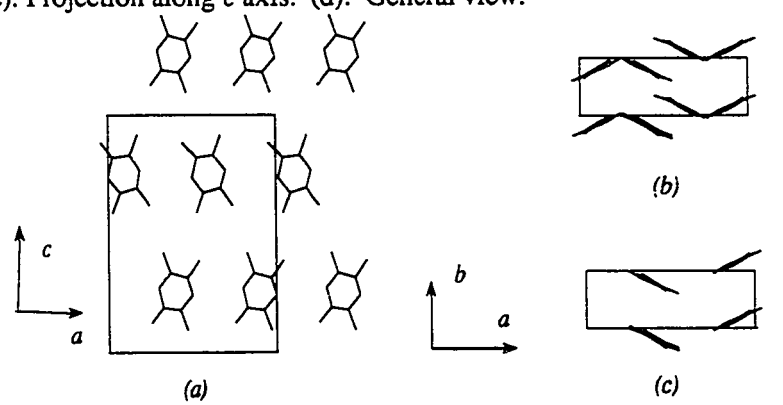

Figure 6.11.4. Third most probable space group P*ca*, predicted by the program for durene. (a). Projection along *b* axis. (b). Projection along *a* axis, showing projection of all layers in *ab* plane. (c). An individual layer parallel to *ab* plane.

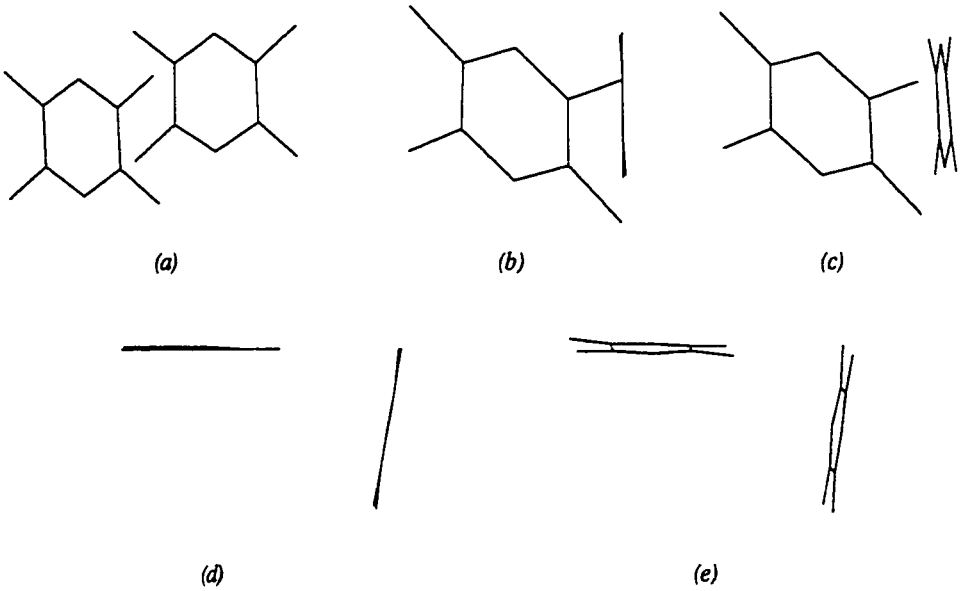

Figure 6.11.5. The two molecules in the unit cell in the experimental structure of durene, as viewed along the principal axes of one of the molecules. (c) and (e) are the same orientations as in (b) and (d), respectively, but rotated 5°.

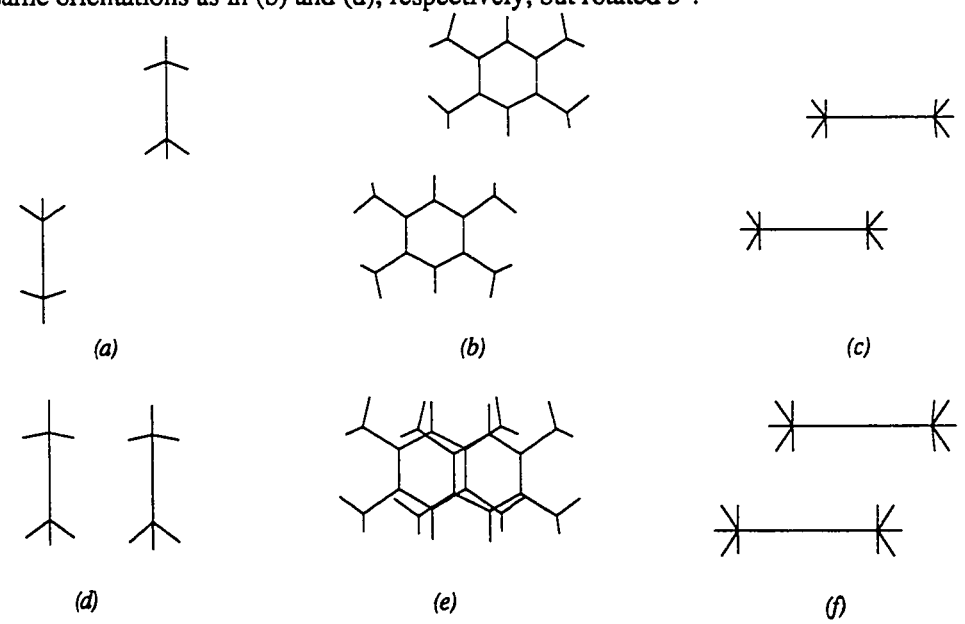

Figure 6.11.6. (a)-(c). The two molecules in the unit cell in the most probable structure of durene, as viewed along the principal axes of one of the molecules. (d)-(f). Nearest neighbors in adjacent unit cells in the [001] direction, showing stacking.

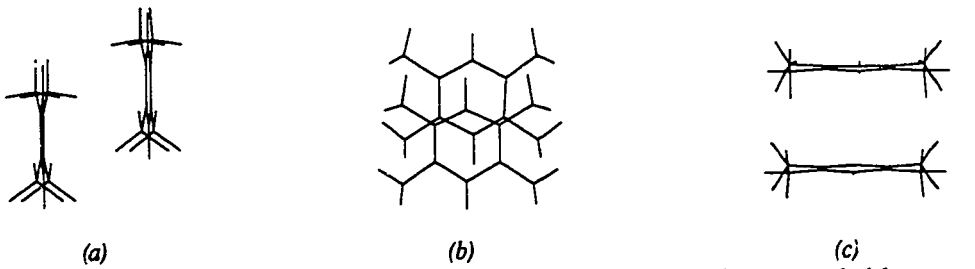

Figure 6.11.7. The two molecules in the unit cell in the second most probable space group for durene, as viewed along the principal axes of one of the molecules.

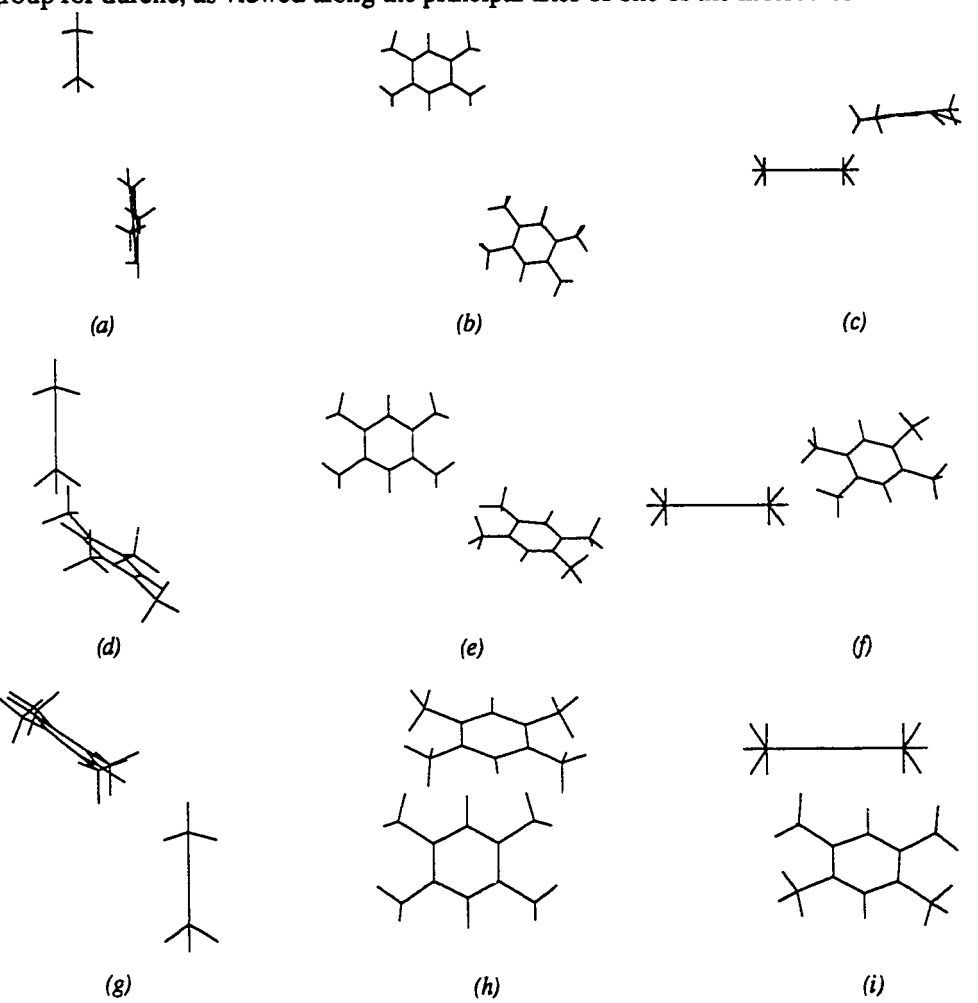

Figure 6.11.8. The four symmetry positions in the unit cell in the third most probable space group, P*ca*, for durene, as viewed along the principal axes of one of the molecules.

6.12. Hexane

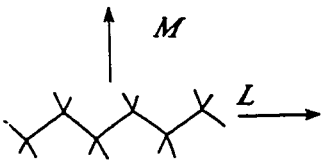

C_6H_{14}

6.12.1 Experimental Data

Experimental [144]:

Temperature:			-115°C
Space Group:			$P\bar{1}$
Molecules per cell:			1
a:	4.17	α:	96.6°(83.4°)
b:	4.70	β:	87.2°
c:	8.57	γ:	105.0°(75.0°)

6.12.2 Results

Input for calculations:

Coordinates:	Carbon atoms from X-ray diffraction, hydrogens from CHEM-X
Multipole moments:	Gaussian 90
Van der Waals Volume:	84.219 $Å^3$

Table 6.12 Lowest Energy Structures in Each Space Group for Hexane

Space Group	Z	Total Energy	E_{lj}	E_{coul}	Packing Index
$P\bar{1}$	2	-18.01	-18.05	0.03	0.5541 A*
$P\bar{1}$	2	-18.01	-18.05	0.03	0.5540 B*
$P\bar{1}$	1	-18.00	-18.03	0.03	0.5540 C*
$P2_1/c$	4	-17.72	-17.69	0.02	0.5494
$P2_1/c$	2	-17.69	-17.67	-0.02	0.5461
$P2_1$	2	-17.60	-17.63	0.03	0.5460
Pna	4	-16.98	-16.97	-0.02	0.5355
Pca	4	-16.85	-16.86	0.01	0.5355
$C2/c$	4	-16.85	-16.84	-0.02	0.5334
$P2_12_12_1$	4	-16.22	-16.28	0.06	0.5245
$Pbca$	4	-15.06	-15.05	-0.01	0.5046

*A, B and C are three global minima with slightly different structures.

Predicted Lowest Energy Structure A:

Space Group: $P\bar{1}$
Molecules per cell: 2
Packing index: 0.5541

a:	9.304	α:	78.78°	Energy:	-18.01
b:	6.622	β:	58.85°	Lennard-Jones:	-18.05
c:	6.464	γ:	63.25°	Coulombic:	0.0339

Predicted Lowest Energy Structure B:

Space Group: $P\bar{1}$
Molecules per cell: 1
Packing index: 0.5540

a:	7.300	α:	88.74°	Energy:	-18.01
b:	13.079	β:	85.82°	Lennard-Jones:	-18.05
c:	4.153	γ:	50.28°	Coulombic:	0.0339

Predicted Lowest Energy Structure C:

Space Group: $P\bar{1}$
Molecules per cell: 1
Packing index: 0.5540

a:	4.154	α:	83.82°	Energy:	-18.00
b:	8.124	β:	89.05°	Lennard-Jones:	-18.03
c:	5.055	γ:	63.75°	Coulombic:	0.035

Structure with lowest energy in second most probable space group:

Space Group: $P2_1/c$
Molecules per cell: 4
Packing index: 0.5494

a:	9.985	α:	90.0°	Energy:	-17.72
b:	4.777	β:	58.64°	Lennard-Jones:	-17.69
c:	15.054	γ:	90.0°	Coulombic:	-0.022

Predicted Structure Closest to Experiment:

Space Group: $P\bar{1}$
Molecules per cell: 1
Packing index: 0.5362

a:	4.16	α:	90.0°	Energy:	-17.15
b:	5.029	β:	61.94°	Lennard-Jones:	-17.18
c:	8.527	γ:	86.58°	Coulombic:	0.03

6.12.3. Discussion of Hexane Results

The experimental structure of hexane consists of parallel molecules aligned so that two rows of hydrogen atoms interlock between two neighboring molecules. The space group is $P\bar{1}$, Z=1 (Fig. 6.12.1). ICE9 found three global minima in space group $P\bar{1}$ with negligible energy differences, labelled A, B, and C in Table 6.12. The structure within layers in the B and C structures (Fig. 6.12.7(a)-(c) and 6.12.8(a)-(c)) is identical to that of the experimental structure (Fig. 6.12.5(a)-(c)). The difference between the experimental and predicted structures is in how the

layers are aligned. In the experimental structure the corresponding carbon atoms in each molecule are in the same plane parallel to the *ab* plane. These planes are nearly perpendicular to the **L** axis of the molecules. In the predicted structures B and C, however, the plane perpendicular to the **L** axis of the molecule passes through the first carbon atom in one layer and the third carbon atom in the layer below. These planes are indicated in ures 6.12.1(a), 6.12.3(c), and 6.12.4(a). Despite the difference in the location of the adjacent layers, the dimensions of the unit cell for global minimum C are very similar to experiment, being 4.15 Å, 5.05 Å, 8.12 Å for structure C, and 4.17 Å, 4.70 Å, and 8.57 Å for the observed structure, reflecting the common structure within layers. The similarities in the relative positions of the molecules within layers can be seen clearly in Fig. 6.12.5 and Fig. 6.12.6.

A local minimum was found by ICE9 in $P\bar{1}$ whose lattice constants were very close to experiment, 4.16 Å, 5.03 Å, and 8.53 Å, but the energy was higher than the global minimum by 0.86 kcal/mol. The packing index was also considerably lower at 0.5101, compared to 0.5541.

In the second most probable space group, $P2_1/c$ with Z=4, the crystal is constructed of layers very similar to the layers in the experimental structure. The screw axis and glide plane of the space group $P2_1/c$, however, creates differences between the layers. In this space group all of the molecules in one layer are rotated 72°about the **L** axis relative to the molecules in the adjacent layers (Fig. 6.12.9(d)-(i)), in contrast to the experimental and most probable predicted structures in which all the molecules are parallel throughout the structure.

Electrostatic interactions were negligible, as expected, and did not influence the ranking of the predicted structures.

6.12.4. Graphical Representation of Hexane Results

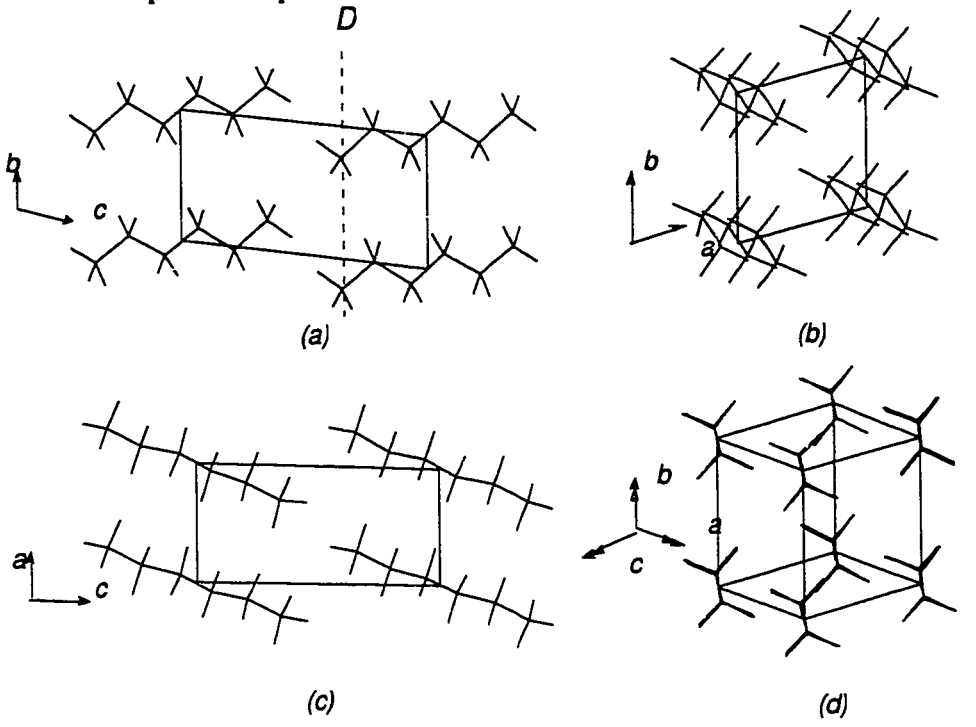

Figure 6.12.1. Experimental structure of hexane, space group $P\bar{1}$ (a). Projection along *a* axis. Dashed line *D* represents the family of planes parallel to the *ab* plane which passes through the first carbon atoms in all of the molecules in the solid. (b). Projection along *b* axis. (c). Projection along *c* axis. (d). General view along the ***L*** axes of the molecules.

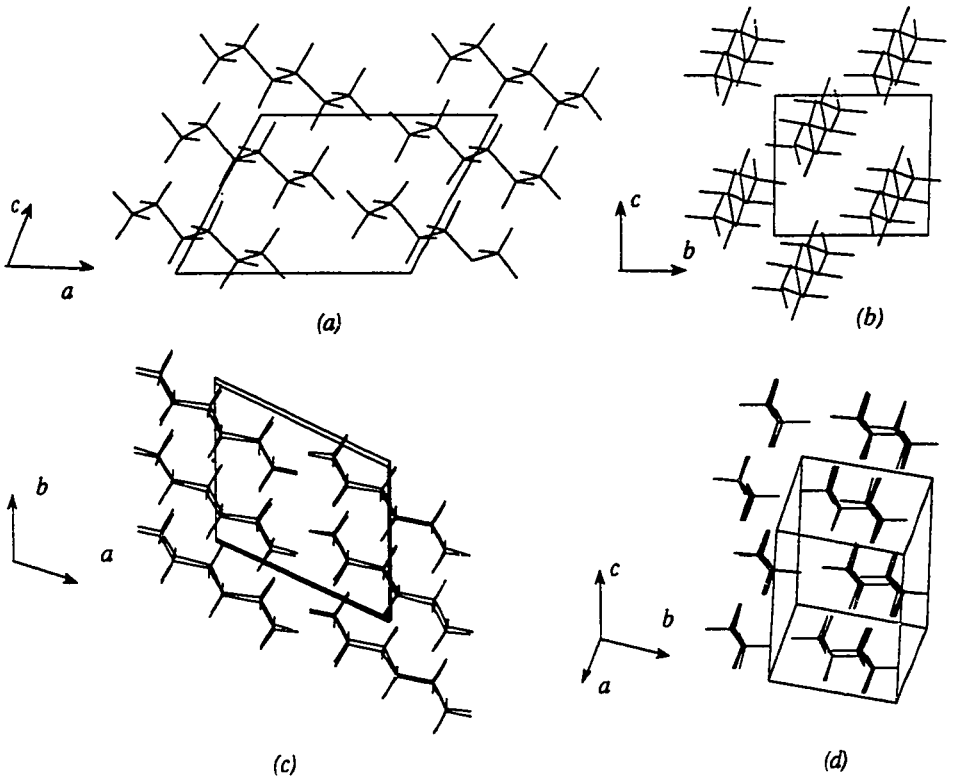

Figure 6.12.2. Most probable structure A of hexane predicted by the program, space group $P\bar{1}$. (a). Projection along *a* axis. (b). Projection along *b* axis. (c). Projection along *c* axis. (d). General view.

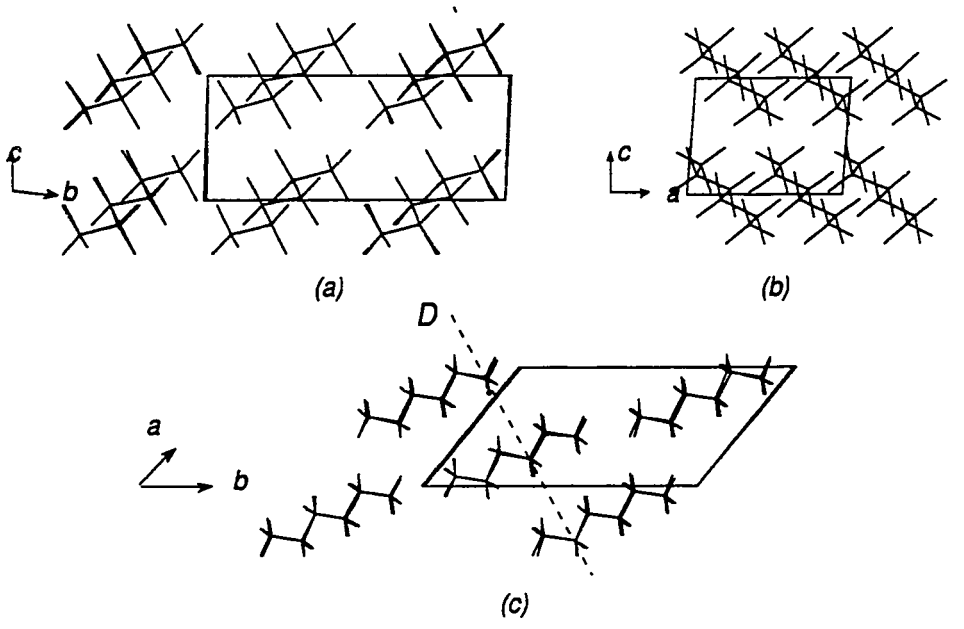

Figure 6.12.3. Most probable structure B in space group $P\bar{1}$, with the same energy as the structure in Fig.6.12.2. (a). Projection along *a* axis. (b). Projection along *b* axis. (c). Projection along *c* axis. Dashed line *D* is perpendicular to the molecular axis **L** and shows the alignment of atoms in molecules directly below them in adjacent layers.

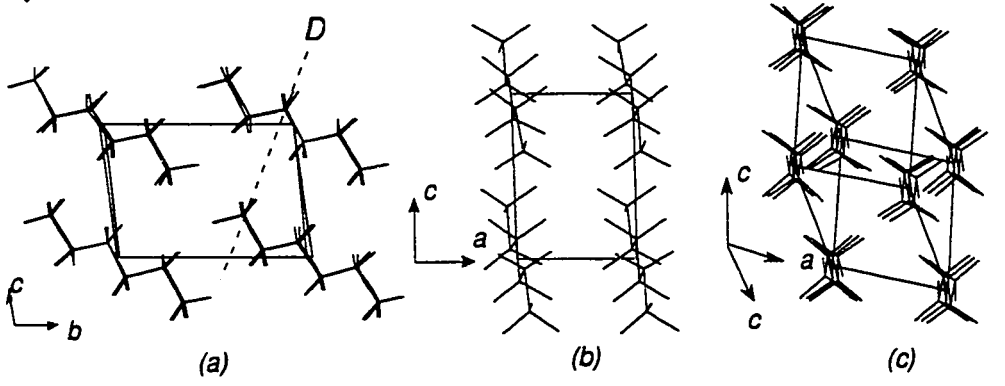

Figure 6.12.4. Most probable structure C in space group $P\bar{1}$, predicted by the program for hexane. (a). Projection along *a* axis. Dashed line *D* is perpendicular to the molecular axis **L** and shows the alignment of atoms in molecules directly below them in adjacent layers. (b). Projection along *b* axis. (c). General view.

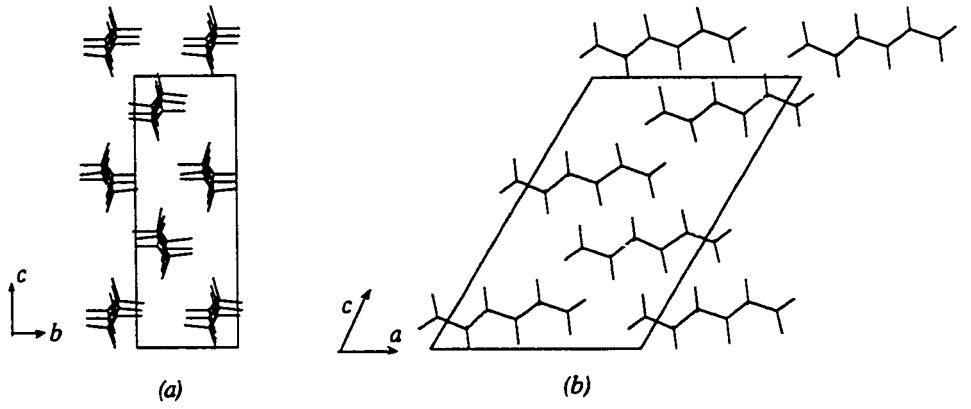

Figure 6.12.5. Second most probable space group P21/*c*, predicted by the program for hexane. (a). Projection along *a* axis. (b). Projection along *b* axis.

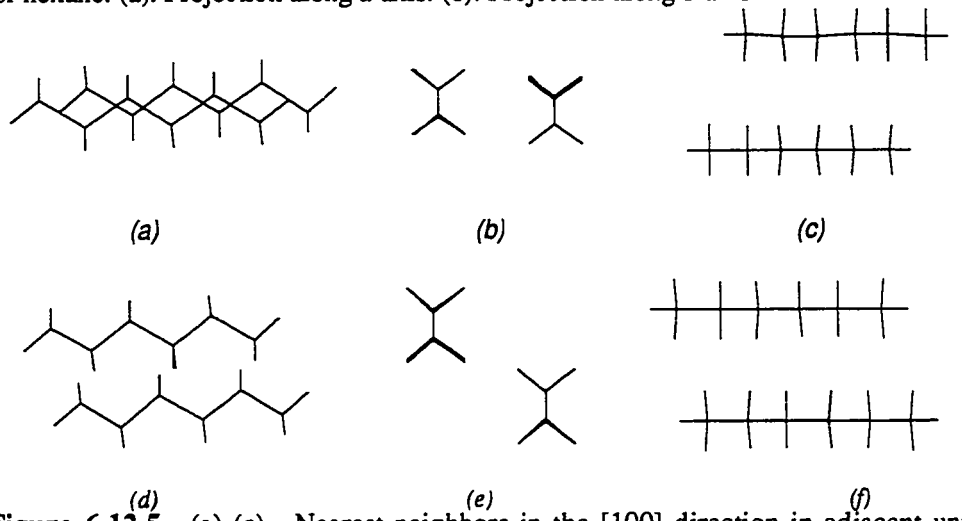

Figure 6.12.5. (a)-(c). Nearest neighbors in the [100] direction in adjacent unit cells in the experimental structure of hexane, as viewed along the principal axes of one of the molecules. (d)-(f). Nearest neighbors in the [010] direction in adjacent unit cells.

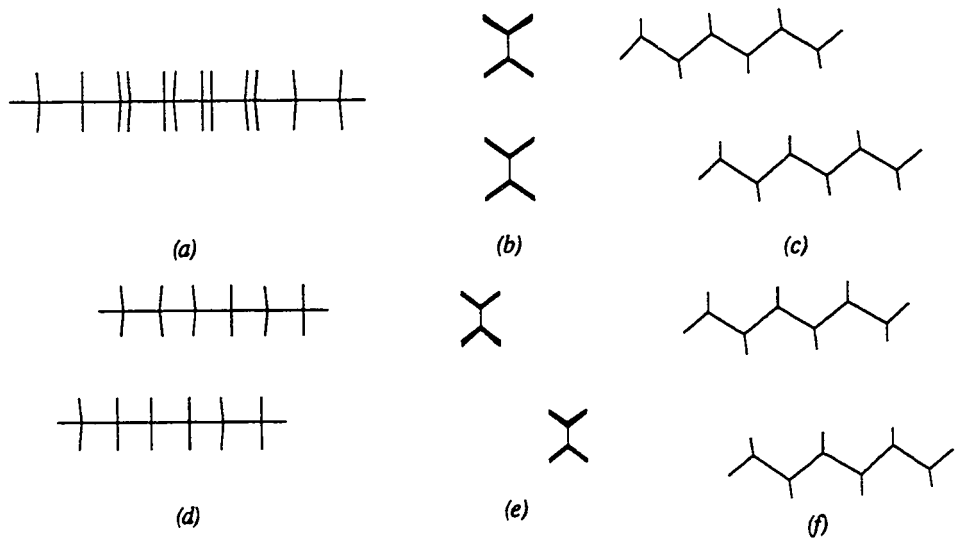

Figure 6.12.6. (a)-(c). The two molecules in the unit cell in the most probable structure A of hexane in $P\bar{1}$, as viewed along the principal axes of one of the molecules. (d)-(f). Nearest neighblors in adjacent unit cells in the [001] direction.

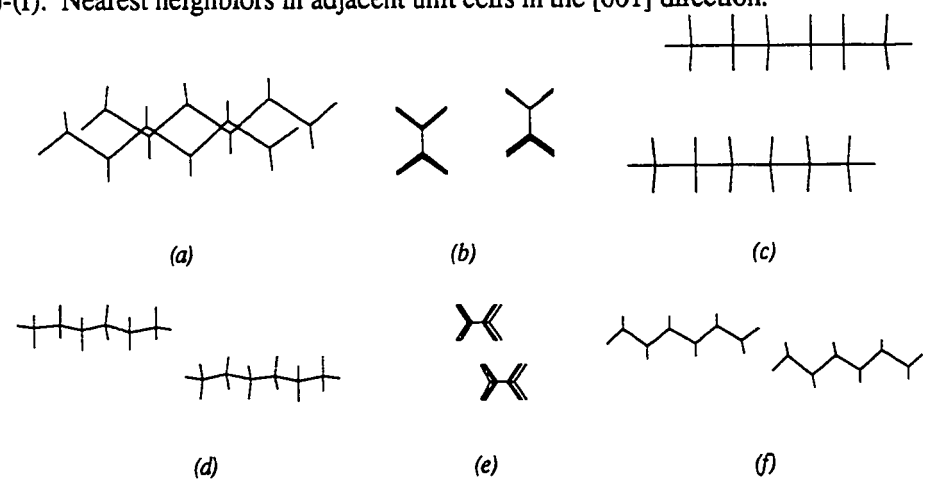

Figure 6.12.7. Most probable structure B. (a)-(c). Nearest neighbors in adjacent unit cells in the [010] direction, viewed along the principal axes of one of the molecules. (d)-(f) The two molecules in the unit cell.

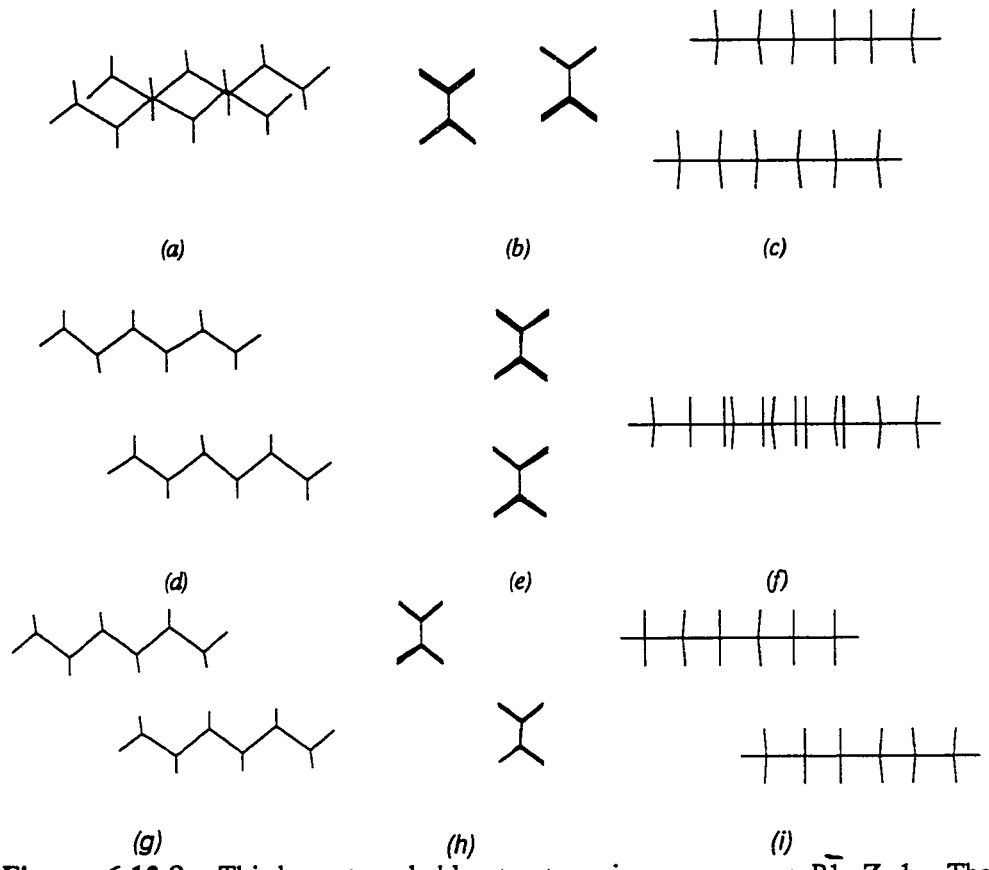

Figure 6.12.8. Third most probable structure, in space group $P\bar{1}$, Z=1. The structure has essentially the same energy as the previous two, being only 0.01 kcal/mol higher. (a)-(c) Nearest neighbor in [100] direction. (d)-(f) Nearest neighbor in [001] direction. (g)-(i). Nearest neighbor in the [110] direction.

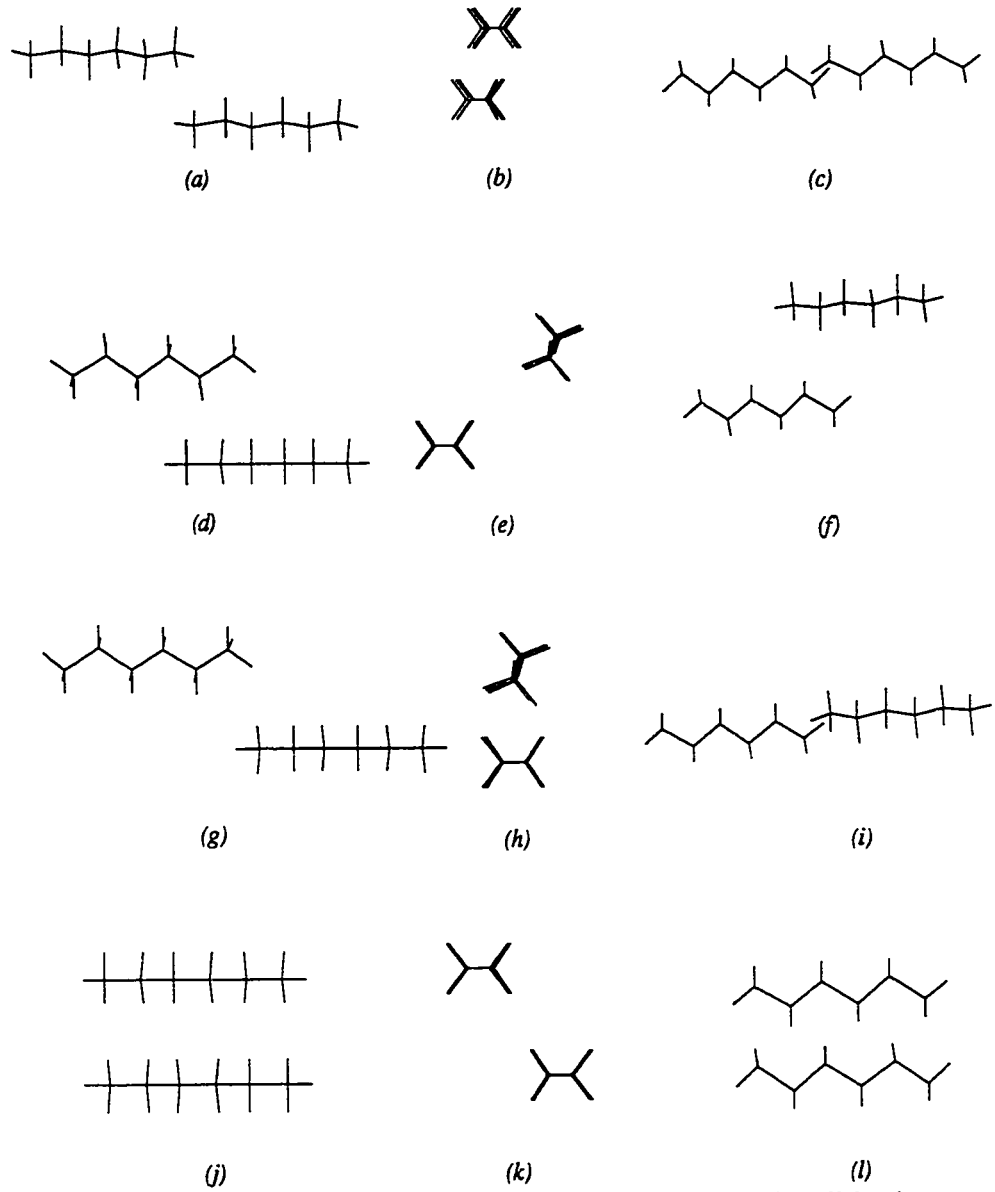

Figure 6.12.9. (a)-(i). The four symmetry positions in the unit cell in the second most probable space group for hexane, $P2_1/c$, as viewed along the principal axes of one of the molecules. (j)-(l). Nearest neighbors in adjacent unit cells in the [010] direction.

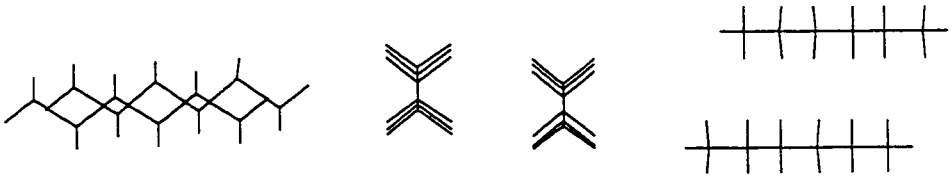

(a) (b) (c)

Figure 6.12.10. Nearest neighbors in the predicted structure closest to experiment.

6.13. Octane

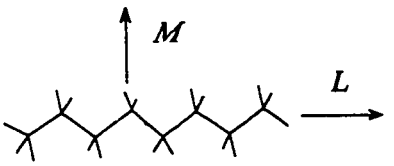

C_8H_{18}

6.13.1 Experimental Data

Experimental [145]:

Temperature: ~-78°C
Space Group: $P\bar{1}$
Molecules per cell: 1

a:	4.16	α:	94.8°(85.2°)
b:	4.75	β:	84.5°
c:	11.00	γ:	105.1°(74.9°)

6.13.2 Results

Input for calculations:

Coordinates: Experiment
Multipole moments: Gaussian 90, 6-31G basis set
Van der Waals Volume: 113.195 Å^3

Table 6.13 Lowest Energy Structures in Each Space Group for Octane

Space Group	Z	Total Energy	E_{lj}	E_{coul}	Packing Index
$P\bar{1}$	1	-23.38	-23.44	-0.06	0.5807
$P2_1/c$	4	-23.04	-23.00	-0.04	0.5744
$P2_1/c$	2	-22.89	-22.87	-0.02	0.5732
$C2/c$	4	-22.36	-22.48	0.13	0.5708
$P2_1$	2	-22.36	-22.43	0.07	0.5675
Pca	4	-22.04	-22.09	0.05	0.5601
Pna	4	-21.99	-22.16	0.17	0.5634
$Pbca$	4	-19.24	-19.20	-0.04	0.5266

Predicted Structure with Lowest Energy:

Space Group:	$P\bar{1}$				
Molecules per cell:	1				
Packing index:	0.5807				
a:	12.494	α:	89.38°	Energy:	-23.38
b:	4.158	β:	55.17°	Lennard-Jones:	-23.44
c:	5.058	γ:	69.05°	Coulombic:	0.062

Structure with lowest energy in second most probable space group:

Space Group:	$P2_1/c$				
Molecules per cell:	4				
Packing index:	0.5744				
a:	8.254	α:	90.0°	Energy:	-23.04
b:	5.049	β:	89.64°	Lennard-Jones:	-23.00
c:	18.915	γ:	90.0°	Coulombic:	-0.037

Predicted Structure Closest to Experiment:

Space Group:	$P\bar{1}$				
Molecules per cell:	1				
Packing index:	0.5568				
a:	4.166	α:	90.00°	Energy:	-21.41
b:	4.755	β:	92.20°	Lennard-Jones:	-21.53
c:	11.105	γ:	76.77°	Coulombic:	0.119

6.13.3. Discussion of Octane Results

Octane crystallizes in the space group $P\bar{1}$, Z=1 (Fig. 6.13.1), in a configuration analogous to that of hexane, with the c dimension increasing from 8.57 Å in hexane to 11.00 Å in octane. ICE9 predicted the correct space group, $P\bar{1}$, and the correct structure within layers as it did with hexane (Fig. 6.13.5(a)-(c), Fig. 6.13.6(a)-(c)). The only difference with the experimental structure is in how these common layers are placed relative to each other in the solid, as in hexane. In the predicted structure the first carbon atom in one molecule is located directly over

the third carbon atom in the molecule in the layer below (Fig. 6.13.6(d)-(f)), whereas in the experimental structure the first carbon atom in one molecule is directly over a hydrogen atom attached to the first carbon atom in the layer below (Fig. 6.13.5(g)-(i)). This placement of adjacent layers in the predicted structure creates bridged axial spacings as in the predicted hexane structures, and as opposed to a relatively continuous spacings from layer to layer as in the experimental hexane and octane structures. In both types of structures, experimental and predicted, the atoms in neighboring molecules are staggered to fill space efficiently. The arrangement of layers in the predicted structure, however, is more efficient and has a packing index of 0.5807 compared to 0.5568 for the local minimum corresponding to the experimental structure, as well as having a Lennard-Jones energy almost 2 kcal/mol lower.

The next most probable space group is $P2_1/c$, with Z=4. The structure consists of layers identical to those in $P\bar{1}$, but adjacent layers are angled at 63° to produce a herringbone structure shown in Fig. 6.13.8. The packing in $P2_1/c$ for octane is quite different from that for obtained for the lowest energy structure for hexane in $P2_1/c$.

Electrostatic interactions in these structures were negligible, as expected.

6.13.4. Graphical representation of Octane Results

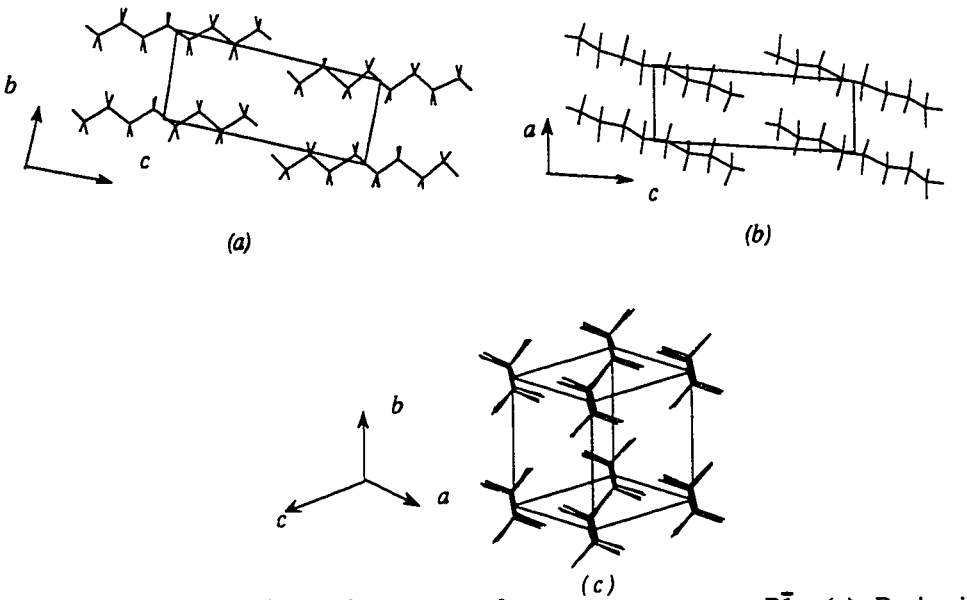

Figure 6.13.1. Experimental structure of octane, space group $P\bar{1}$. (a). Projection along *a* axis. (b). Projection along *b* axis. (c). General view.

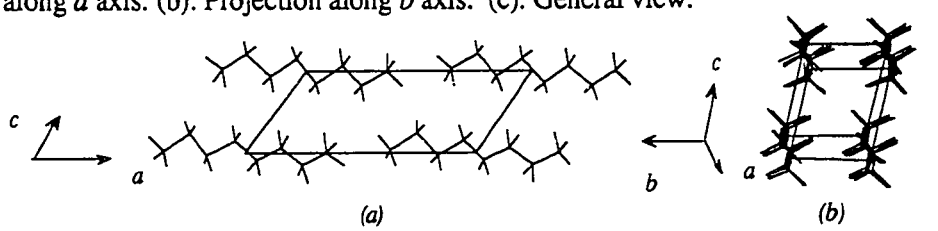

Figure 6.13.2. Most probable structure of octane predicted by the program, space group $P\bar{1}$, Z=1. (a). Projection along *b* axis. (b). General view.

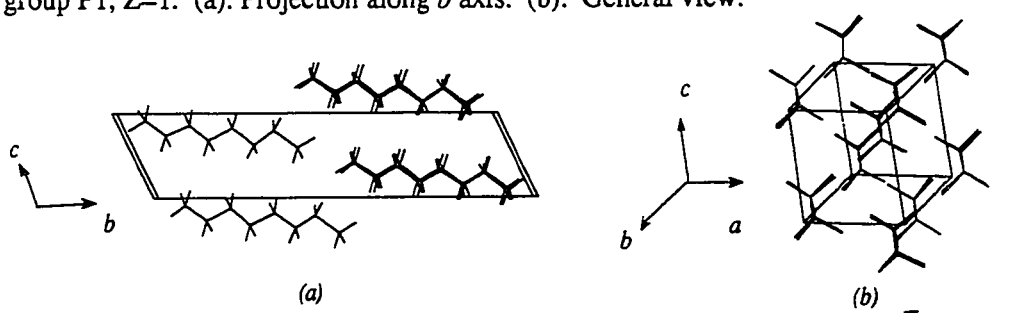

Figure 6.13.3. Second most probable configuration in space group $P\bar{1}$, Z=2, predicted by the program for octane (a). Projection along *a* axis. (b). General view.

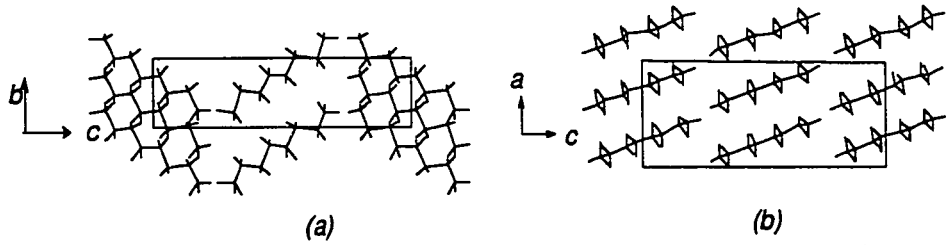

Figure 6.13.4. Second most probable space group $P2_1/c$, predicted by the program for octane (a). Projection along *a* axis. (b). Projection along *b* axis.

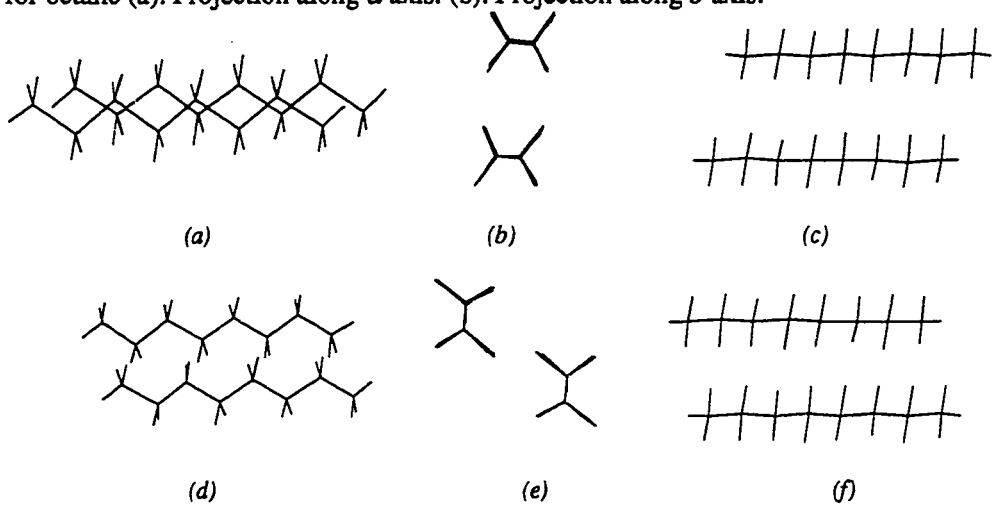

Figure 6.13.5. (a)-(c). Nearest neighbors in the [100] direction in the experimental structure of octane, as viewed along the principal axes of one of the molecules. (d)-(f). Nearest neighbors in the [010] direction. (Note: the angles of the bonds to the hydrogen atoms in this are slightly skewed. These are the estimated coordinates for the hydrogen atoms in octane given in the literature by Norman and Mathisen. [146] The positions of the carbon atoms were determined by X-ray diffraction, and are correct.)

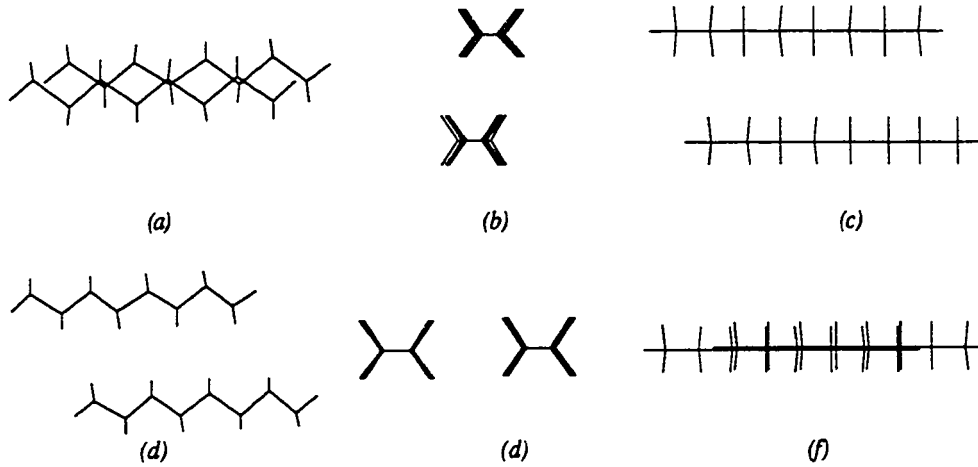

Figure 6.13.6. (a)-(c). Nearest neighbors in the [010] direction in the most probable structure of octane, as viewed along the principal axes of one of the molecules. (d)-(f). Nearest neighbors in the [001] direction.

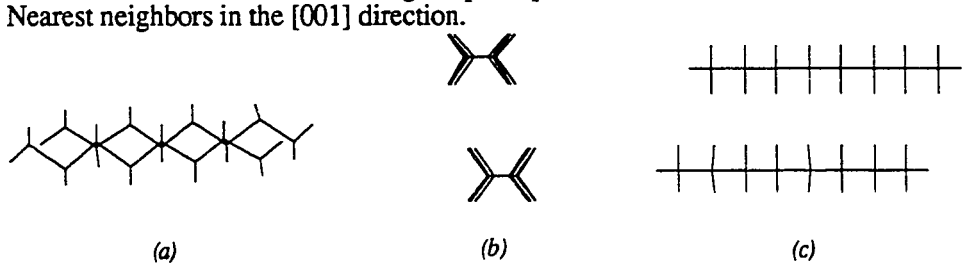

Figure 6.13.7. The two molecules in the unit cell in the second structure in P1, as viewed along the principal axes of one of the molecules.

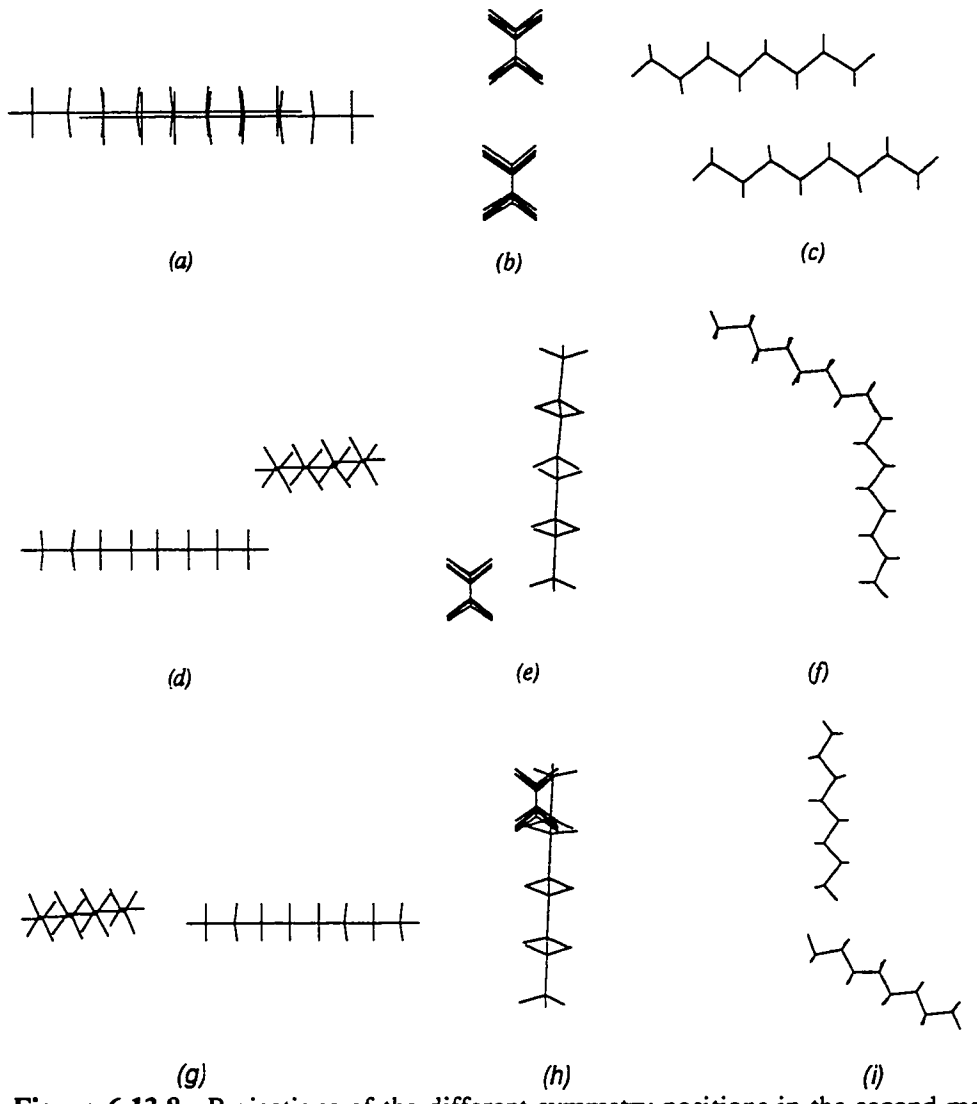

Figure 6.13.8. Projections of the different symmetry positions in the second most probable space group $P2_1/c$, Z=4, with respect to the principal axes of one reference molecule for octane.

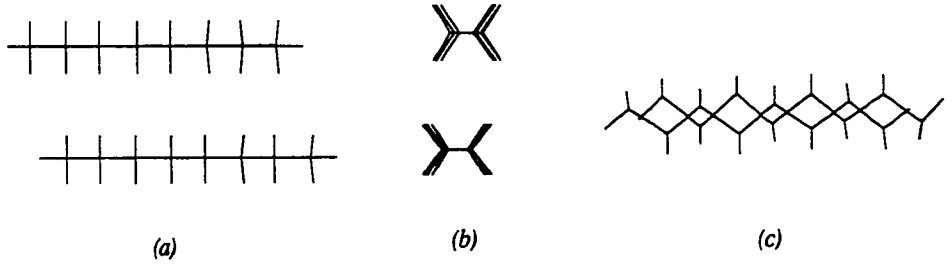

Figure 6.13.9. Second type of configuration in the second most probable space group $P2_1/c$, Z=2, for octane, viewed along the principal axes of one molecule.

6.14. Bicyclohexylidene

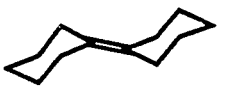

$C_{12}H_{20}$

6.14.1 Experimental Data

Experimental [146]:

Temperature:
Space Group: $P\bar{1}$
Molecules per cell: 1

a:	5.32	α:	107.2°(72.8°)
b:	6.25	β:	79.1°
c:	8.36	γ:	105.6°(74.4°)

6.14.2 Results

Input for calculations:

Coordinates:	MM2 Optimization
Multipole moments:	Gaussian 90, 6-31G basis set
Van der Waals Volume:	151.599 Å^3

Table 6.14 Lowest Energy Structures in Each Space Group for Bicyclohexylidene

Space Group	Z	Total Energy	E_{lj}	E_{coul}	Packing Index
$P\bar{1}$	2	-27.58	-27.57	-0.008	0.6242
$P\bar{1}$	1	-27.54	-27.53	-0.01	0.6232
$C2/c$	4	-25.83	-25.83	-0.003	0.6031
$P2_1/c$	4	-25.45	-25.45	-0.007	0.5984
Pca	4	-24.81	-24.80	-0.01	0.5872
Pna	4	-24.74	-24.73	-0.003	0.5927
$P2_1/c$	2	-24.34	-24.33	-0.009	0.5864
$P2_1$	2	-24.24	-24.23	0.005	0.5857
$P2_12_12_1$	4	-23.74	-23.73	-0.005	0.5839
$Pbca$	4	-20.33	-20.32	-0.005	0.5139

Predicted Structure with Lowest Energy:

Space Group: $P\bar{1}$
Molecules per cell: 2
Packing index: 0.6242

a:	6.86	α:	58.51°	Energy:	-27.58
b:	11.938	β:	83.04°	Lennard-Jones:	-27.57
c:	8.403	γ:	57.97°	Coulombic:	-0.008

Second lowest energy Structure in most probable space group:

Space Group: $P\bar{1}$
Molecules per cell: 1
Packing index: 0.6232

a:	6.142	α:	90.0°	Energy:	-27.54
b:	5.206	β:	66.07°	Lennard-Jones:	-27.53
c:	8.738	γ:	73.81°	Coulombic:	-0.01

Structure with lowest energy in second most probable space group:

Space Group: C2/c
Molecules per cell: 4
Packing index: 0.6031

a:	12.030	α:	90.0°	Energy:	-25.83
b:	5.152	β:	61.82°	Lennard-Jones:	-25.83
c:	17.927	γ:	90.0°	Coulombic:	-0.003

6.14.3. Discussion of Bicyclohexylidene Results

Bicyclohexylidene crystallizes in space group $P\bar{1}$, Z=1, with the structure shown in Fig.6.14.1. ICE9 found two structures in $P\bar{1}$, very close in energy at -27.58 and -27.54 kcal/mol. The second of these structures corresponds to the experimental structure (Fig. 6.14.3). The packing index for this structure is very high, 0.6232, considering the irregular shape of the molecule. The contours of the molecule fit efficiently into each other, with the postions of the hydrogen atoms being staggered to allow closest packing.

The second most probable space group predicted by the program is C2/c (Fig. 6.14.4). Unlike many of the other molecules whose packing was investigated in this study where there are many space groups very close in energy, the gap between the first and second most probable space groups is relatively large, at 1.7 kcal/mol. This is probably due to the irregular shape of bicyclohexylidene which severely limits the possbile ways to achieve close-packing. The configuration within layers in C2/c is very similar to the predicted and experimental structure (6.14.8). Unlike the experimental strucutre, however, alternate layers are inverted, as shown in Figure 6.14.4(a).

6.14.4. Graphic Representations of Bicyclohexylidene Results

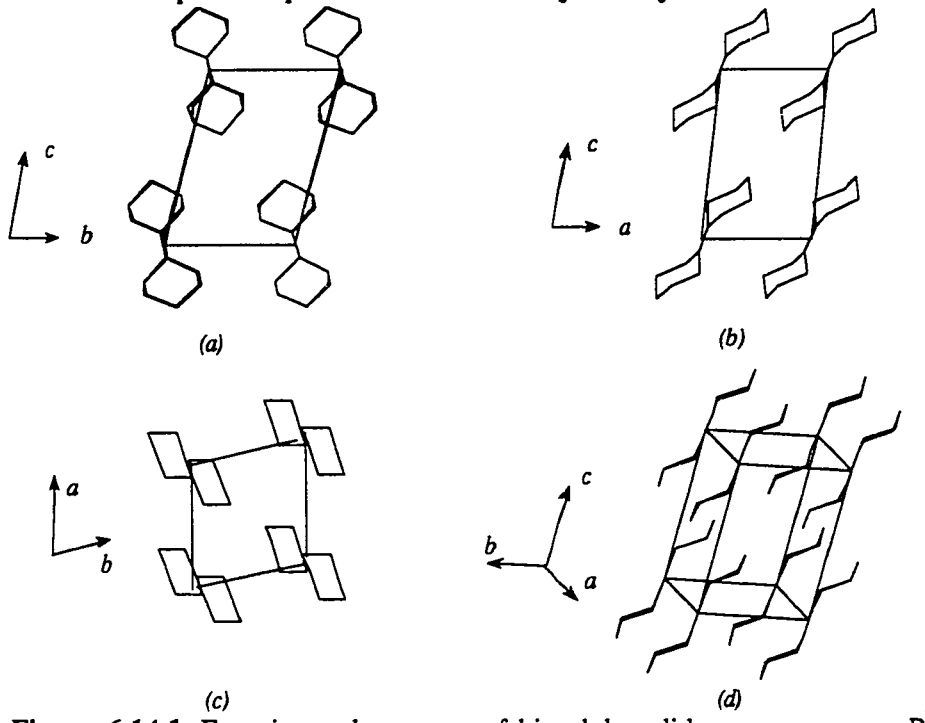

Figure 6.14.1. Experimental structure of bicyclohexylidene, space group $P\bar{1}$ (a). Projection along *a* axis. (b). Projection along *b* axis. (c). Projection along *c* axis. (d). General view.

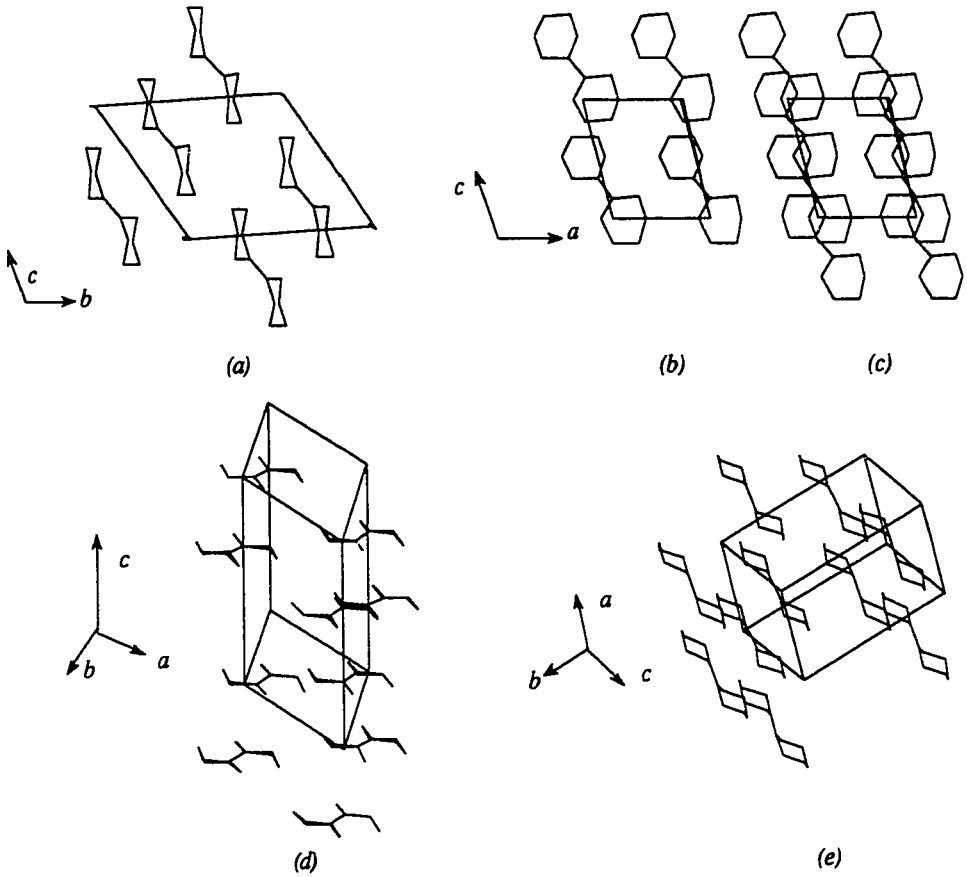

Figure 6.14.2. Most probable structure of bicyclohexylidene predicted by the program, space group $P\bar{1}$ with 2 molecules per unit cell. (a). Projection along *a* axis. (b). Projection along *b* axis. (c). Projection along *c* axis. (d)-(e). General views.

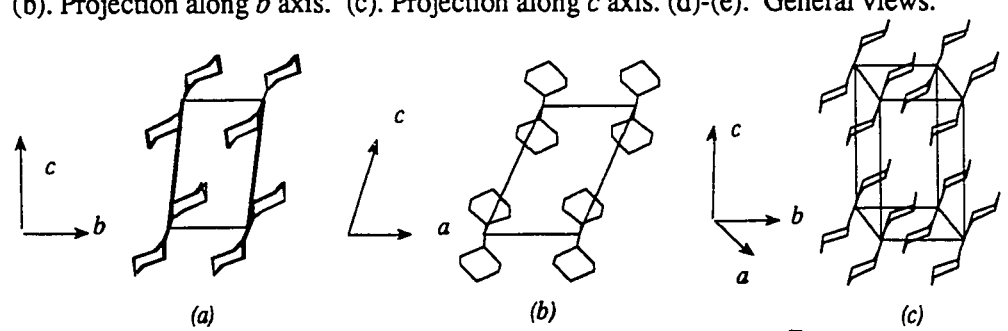

Figure 6.14.3. Second most probable structure in space group $P\bar{1}$ with 1 molecule per unit cell, predicted by the program for bicyclohexylidene. (a). Projection along *a* axis. (b). Projection along *b* axis. (c). Projection along *c* axis.

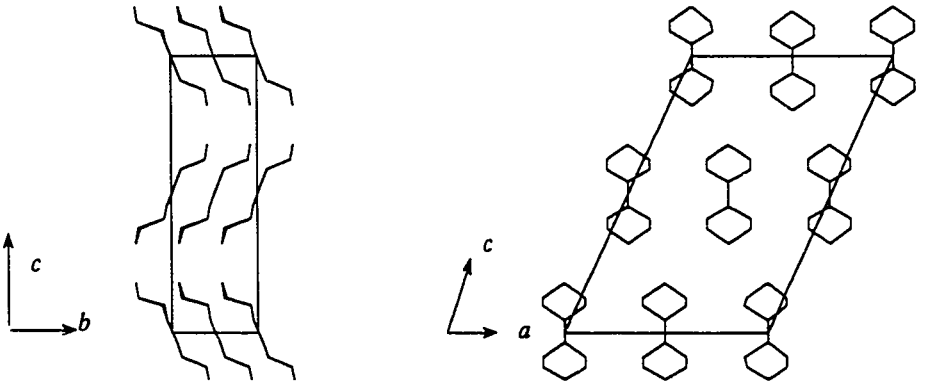

Figure 6.14.4. Third most probable space group C2/*c*, predicted by the program for bicyclohexylidene. (a). Projection along *a* axis. (b). Projection along *b* axis.

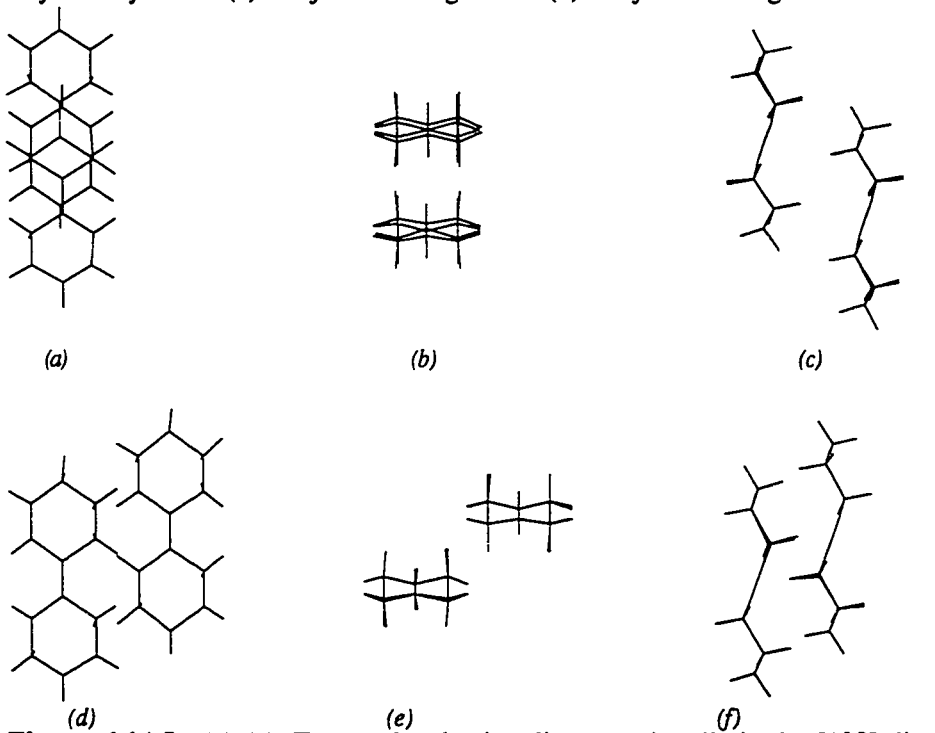

Figure 6.14.5. (a)-(c). Two molecules in adjacent unit cells in the [100] direction, in the experimental structure of bicyclohexylidene, as viewed along the principal axes of one of the molecules. (d)-(f) Nearest neighbors in adjacent unit cells in the [010] direction.

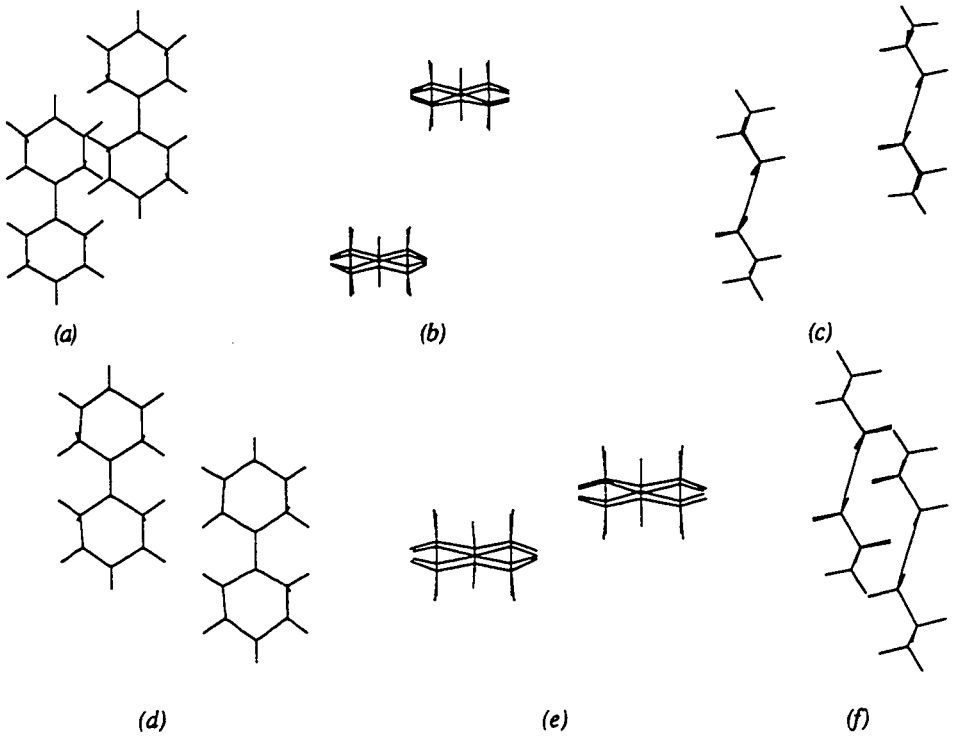

Figure 6.14.6. *(a)-(c).* The two molecules in the unit cell in the most probable structure of bicyclohexylidene, as viewed along the principal axes of one of the molecules. *(d)-(f).* Nearest neighbors in the [100] direction.

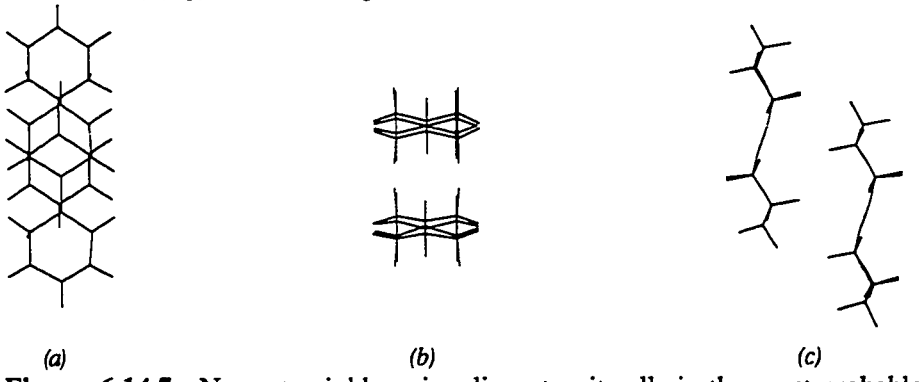

Figure 6.14.7. Nearest neighbors in adjacent unit cells in the most probable space group for bicyclohexylidene, as viewed along the principal axes of one of the molecules. This structure is equivalent to the experimental structure.

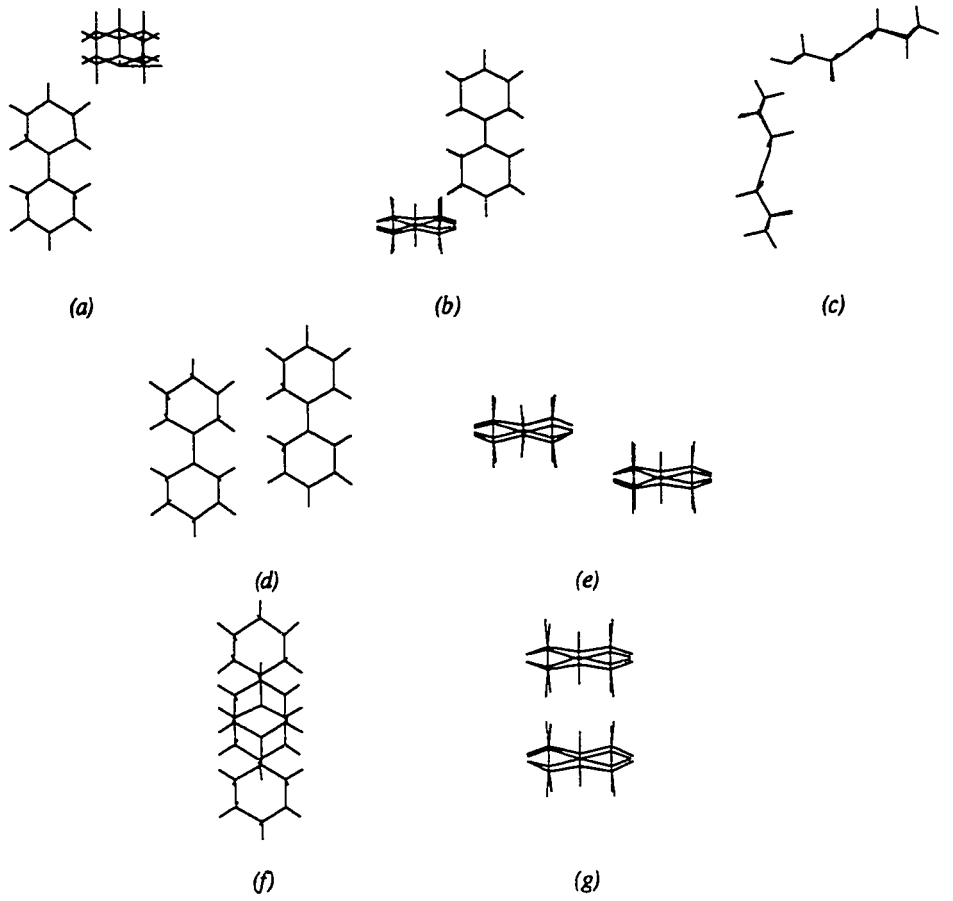

Figure 6.14.8. (a)-(c). Two molecules in the unit cell in the third most probable space group for bicyclohexylidene, as viewed along the principal axes of one of the molecules. (d)-(e). Different symmetry position in the unit cell. (f)-(g). Nearest neighbors in adjacent unit cells in the [010] direction.

6.15. Trindan (tris-Trimethylenebenzene)

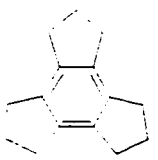

$C_{15}H_{18}$

6.15.1 Experimental Data

Experimental [147]:

Temperature:		RT	
Space Group:		$P2_1/c$	
Molecules per cell:		4	
a:	12.67	α:	90.0°
b:	5.87	β:	111.68°(68.32°)
c:	16.92	γ:	90.0°

6.15.2 Results

Input for calculations:

Coordinates:	Carbon coordinates from experiment, hydrogens from CHEM-X
Multipole moments:	Gaussian 90, STO-3G basis set
Van der Waals Volume:	166.984 Å^3

Table 6.15 Lowest Energy Structures in Each Space Group for Trindan

Space Group	Z	Total Energy	E_{lj}	E_{coul}	Packing Index
$P2_1/c$	4	-27.23	-27.29	0.055	0.4027
$P\bar{1}$	2	-27.17	-27.20	0.029	0.4171
$P2_12_12_1$	4	-26.92	-26.91	-0.158	0.4231
$P2_1/c$	4	-26.48	-26.53	0.051	0.4132
Pna	4	-26.29	-26.34	0.052	0.4128
$P2_1$	2	-25.93	-25.98	0.050	0.4071
Pca	4	-24.99	-24.98	-0.015	0.4056

Predicted Structure with Lowest Energy:

Space Group: $P2_1/c$
Molecules per cell: 4
Packing index: 0.4207

a:	4.136	α:	90.0°	Energy:	-27.23
b:	14.655	β:	73.80°	Lennard-Jones:	-27.29
c:	19.108	γ:	90.0°	Coulombic:	0.056

Structure with lowest energy in second most probable space group:

Space Group: $P\bar{1}$
Molecules per cell: 2
Packing index: 0.4171

a:	7.859	α:	84.96°	Energy:	-27.17
b:	8.699	β:	78.71°	Lennard-Jones:	-27.20
c:	9.252	γ:	64.74°	Coulombic:	0.0297

Structure with lowest energy in third most probable space group:

Space Group: $P2_12_12_1$
Molecules per cell: 4
Packing index: 0.4231

a:	7.722	α:	90.0°	Energy:	-26.92
b:	15.412	β:	90.0°	Lennard-Jones:	-26.91
c:	9.292	γ:	90.0°	Coulombic:	-0.158

Predicted Structure Closest to Experiment:

Space Group: $P2_1/c$
Molecules per cell: 4
Packing index: 0.3595

a:	13.132	α:	90.0°	Energy:	-20.31
b:	6.176	β:	69.29°	Lennard-Jones:	-20.31
c:	17.157	γ:	90.0°	Coulombic:	-0.004

6.15.3. Discussion of Trindan Results

Trindan crystallizes in the space group $P2_1/c$ with Z=4, in a structure formed from columns of slipped-stacked molecules shown in Fig. 6.15.5(j)-(l). Layers are formed by alternating stacks related by an inversion center, perpendicular to the c axis. The molecular planes of these molecules within a layer are all parallel. Adjacent layers perpendicular to c axes are related by a screw axis, producing a herringbone structure with angles between molecular planes close to 90°.

The most probable structure predicted by ICE9 also consists of columns of parallel slipped-stacks of molecules, arranged at angles to other columns to form a herringbone structure (Fig. 6.15.2). The differences between the experimental and predicted structures is in the degree of skewness within the stacks and the angle between stacks. In the experimental structure the aromatic rings at the center of the molecule do not overlap (Fig. 6.15.5(j)), but in the predicted structure they are partially eclipsed (Fig. 6.15.6(l)). The angle formed between the stacks is 33° rather than the observed 90°.

The second most probable space group predicted by the program, $P\bar{1}$, Z=2, is made of stacks of parallel molecules which are skewed as shown in Fig. 6.15.7(d)-(f). Adjacent stacks are related by an inversion center and have parallel molecular planes. The first two structures exhibit a positive, but very small, electrostatic energy.

The third most probable structure, in $P2_12_12_1$, Z=4, has all molecular planes parallel throughout the structure. The layers are built from rows on which the 'nose' of one molecule fits into the hollow of the 'tail' of another. The adjacent rows in the layer are related by a screw axis parallel to the *b* axis in such a way that the lobes of trindan interlock to fill space. Parallel layers are staggered. This structure has a negative electrostatic energy, three to five times larger in magnitude than the two lowest energy structures.

A local minimum was found which corresponds to the experimental structure. This structure has a considerably higher energy (-20.31 compared to -27.23 kcal/mol) and lower packing index (0.3595 compared to 0.4207) than the global minimum.

6.15.4. Graphical representation of Trindan Results

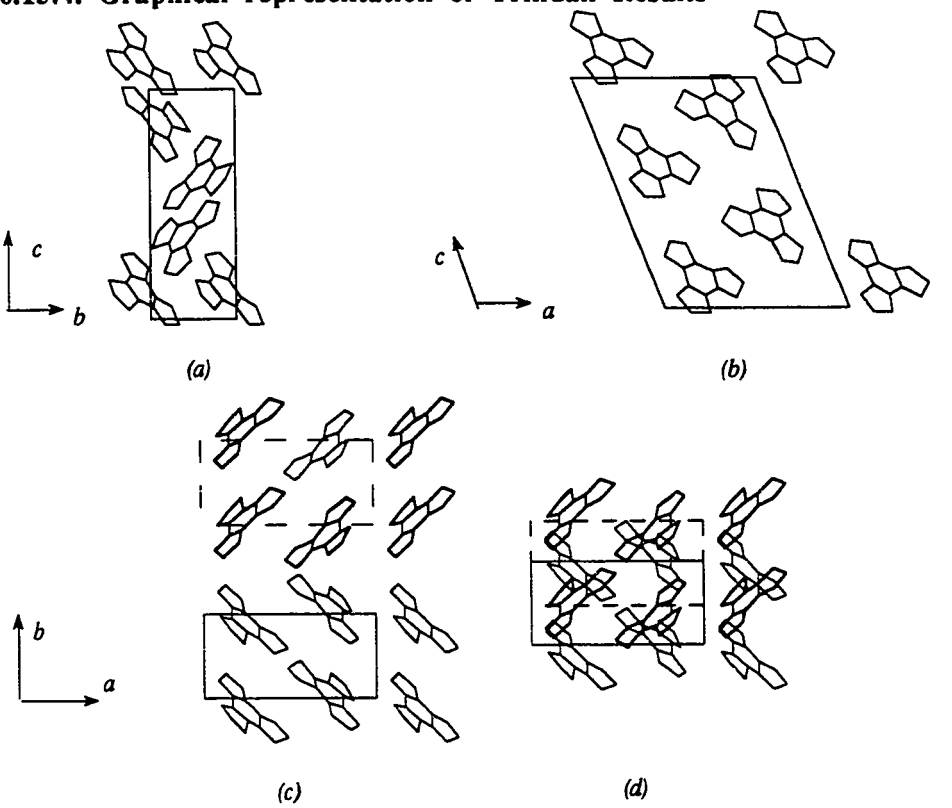

Figure 6.15.1. Experimental structure of trindan, space group $P2_1/c$. (a). Projection along *a* axis. (b). Projection along *b* axis. (c). Projection along *c* axis, layers parallel to *ab* plane shown separately. (d). Projection of all layers in *ab* plane.

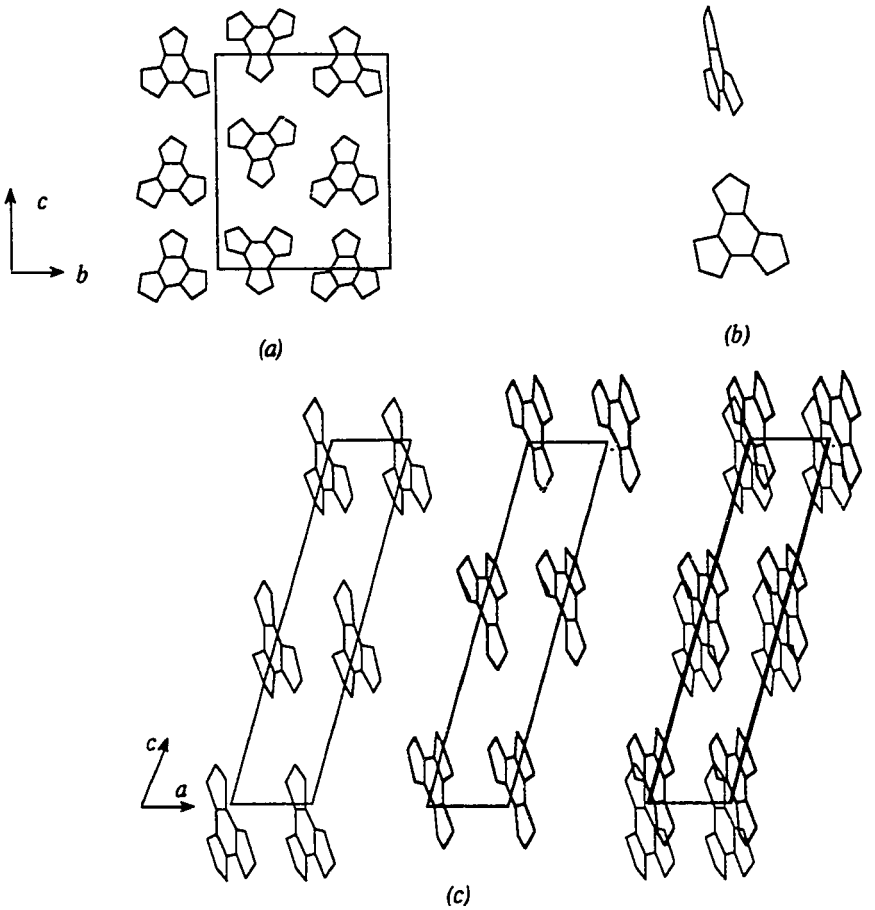

Figure 6.15.2. Most probable structure of trindan predicted by the program, space group $P2_1/c$. (a). Projection along *a* axis. (b). Projection along *b* axis. (c). Projection along *c* axis.

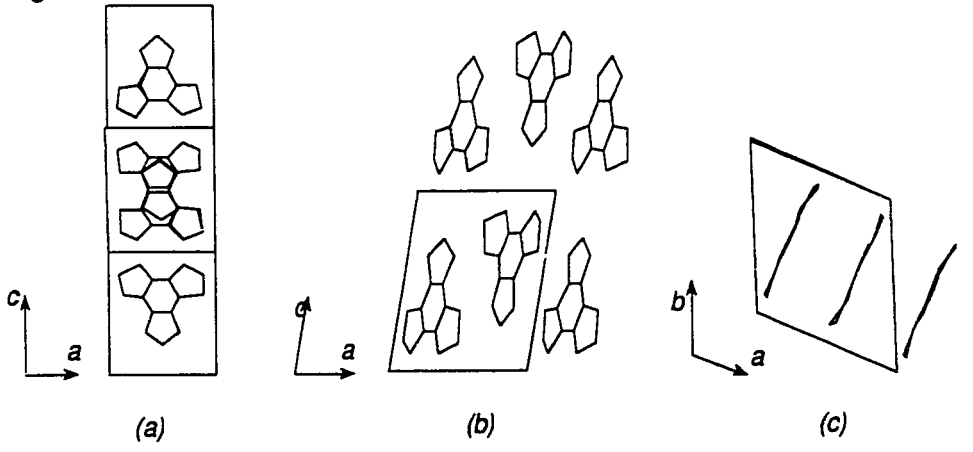

Figure 6.15.3. Second most probable space group P1, predicted by the program for trindan. (a). Projection along *a* axis. (b). Projection along *b* axis. (c). Projection along *c* axis.

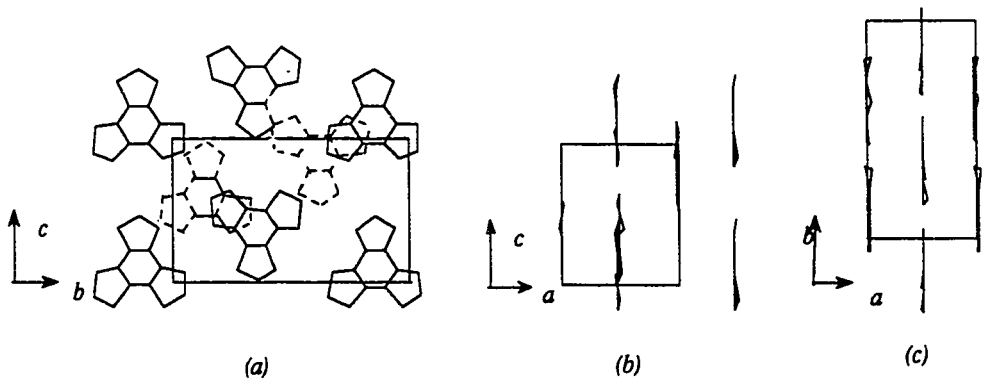

Figure 6.15.4. Third most probable space group $P2_12_12_1$, predicted by the program for trindan (a). Projection along *a* axis. (b). Projection along *b* axis. (c). Projection along *c* axis. (d). General view.

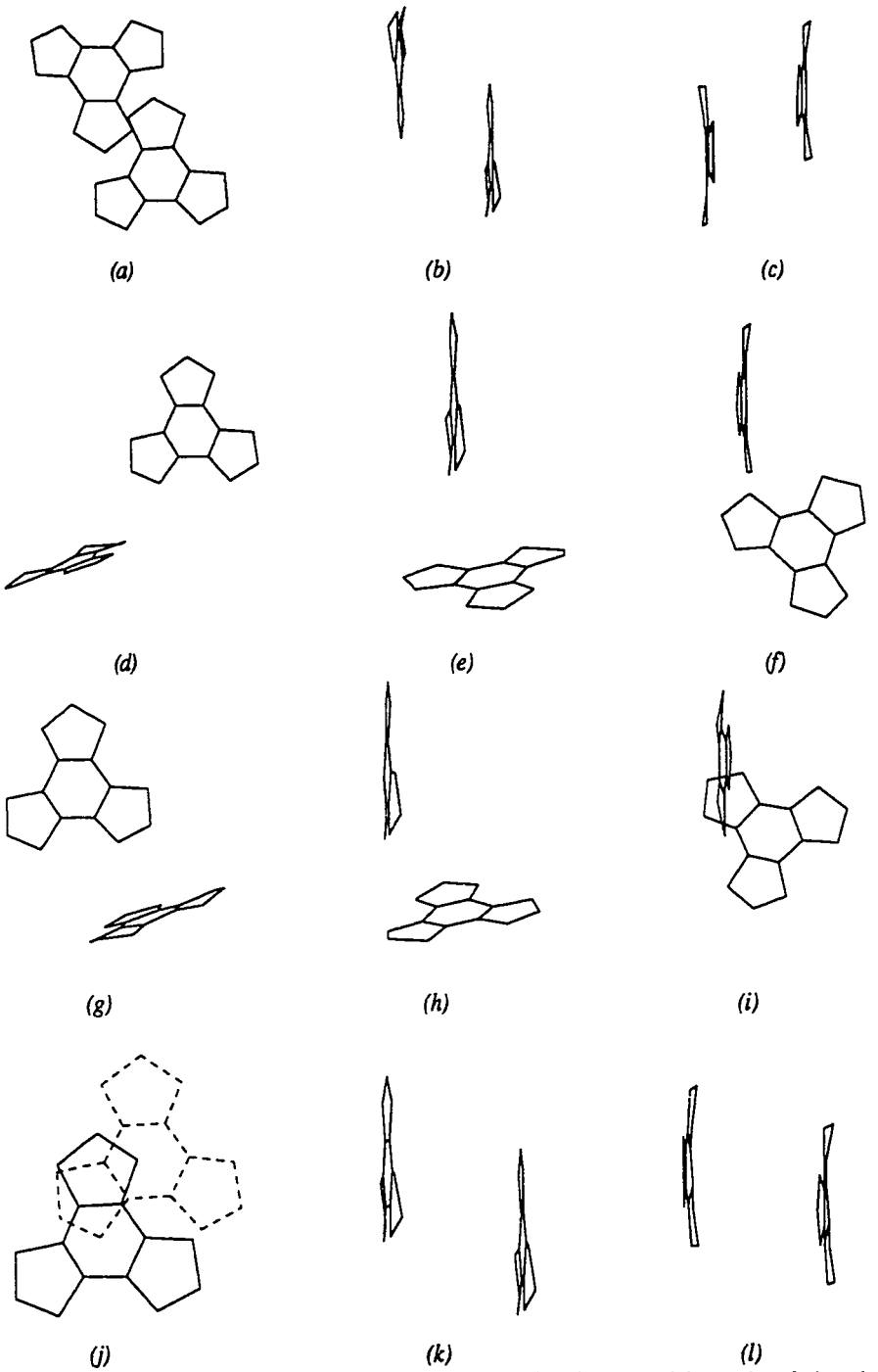

Figure 6.15.5. (a)-(i). A reference molecule shown with each of the three other symmetry positions in the unit cell in the experimental structure of trindan, as viewed along the principal axes of one of the molecules. (j)-(l) Nearest neighbors in adjacent unit cells.

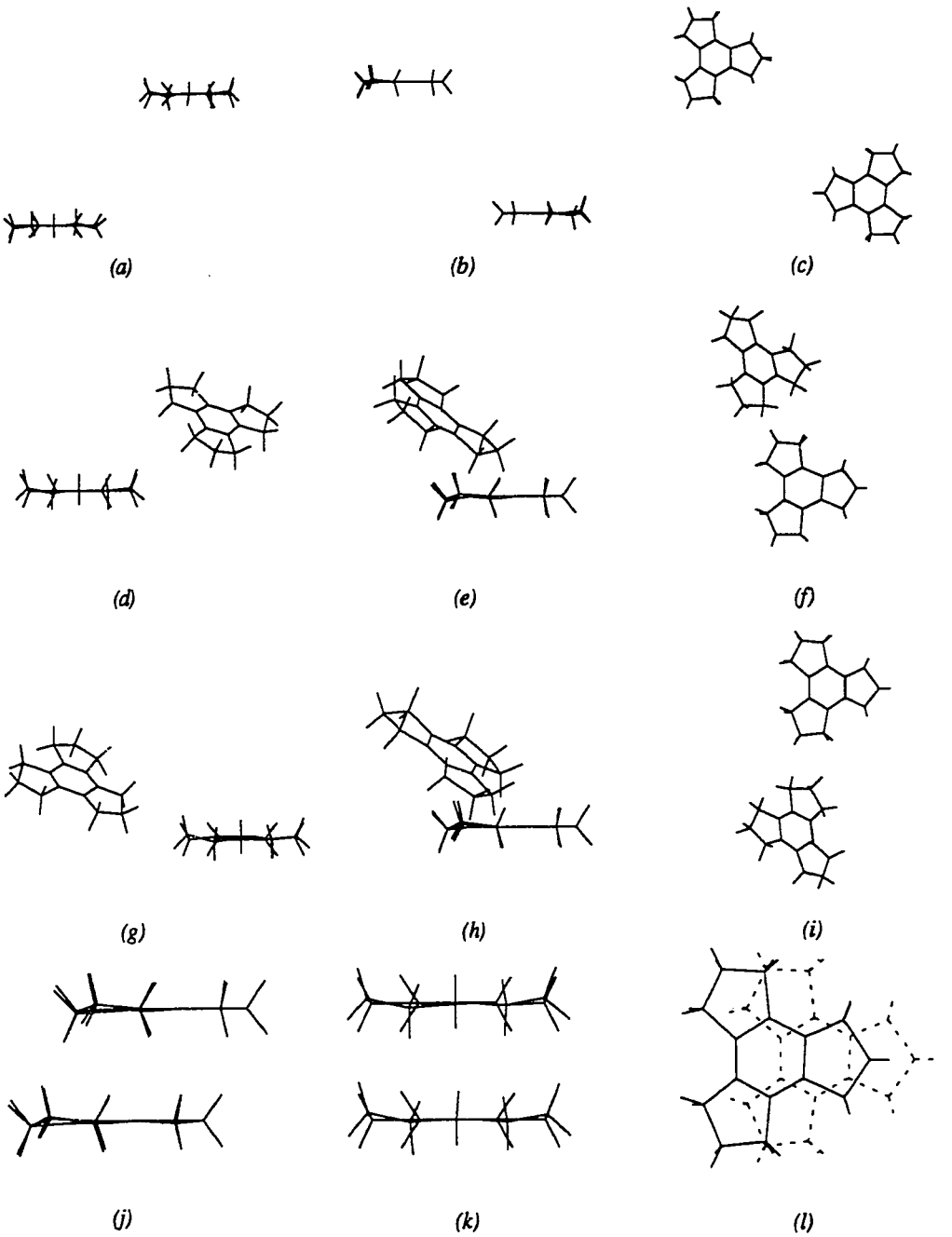

Figure 6.15.6. (a)-(i). The four symmetry positions in the unit cell in the most probable structure of trindan, as viewed along the principal axes of one of the molecules. (j)-(l). Nearest neighbors in adjacent unit cells in the [100] direction.

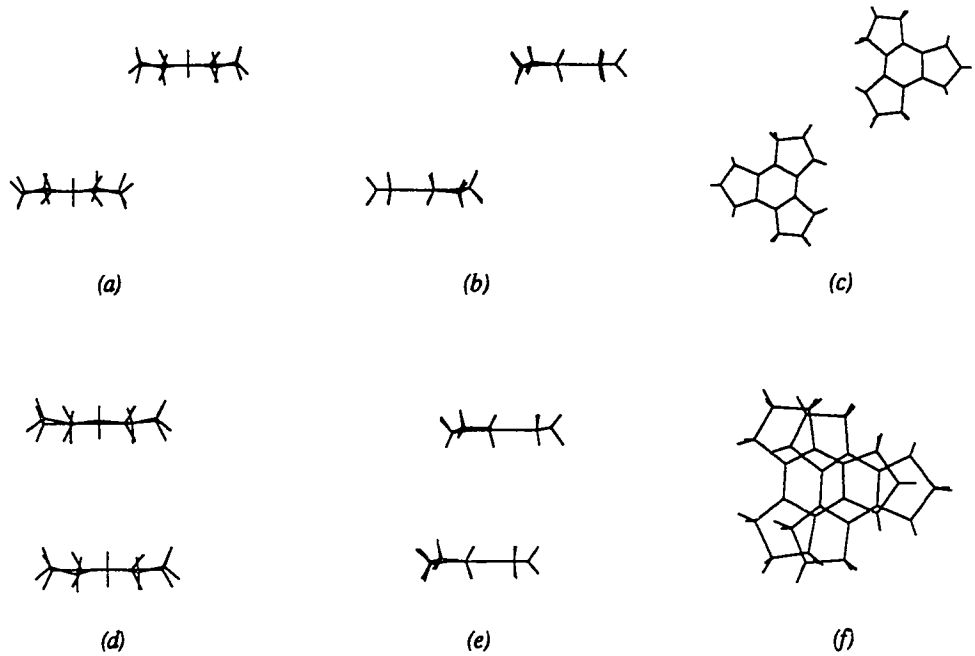

Figure 6.15.7. The two molecules in the unit cell in the second most probable space group for trindan, as viewed along the principal axes of one of the molecules.

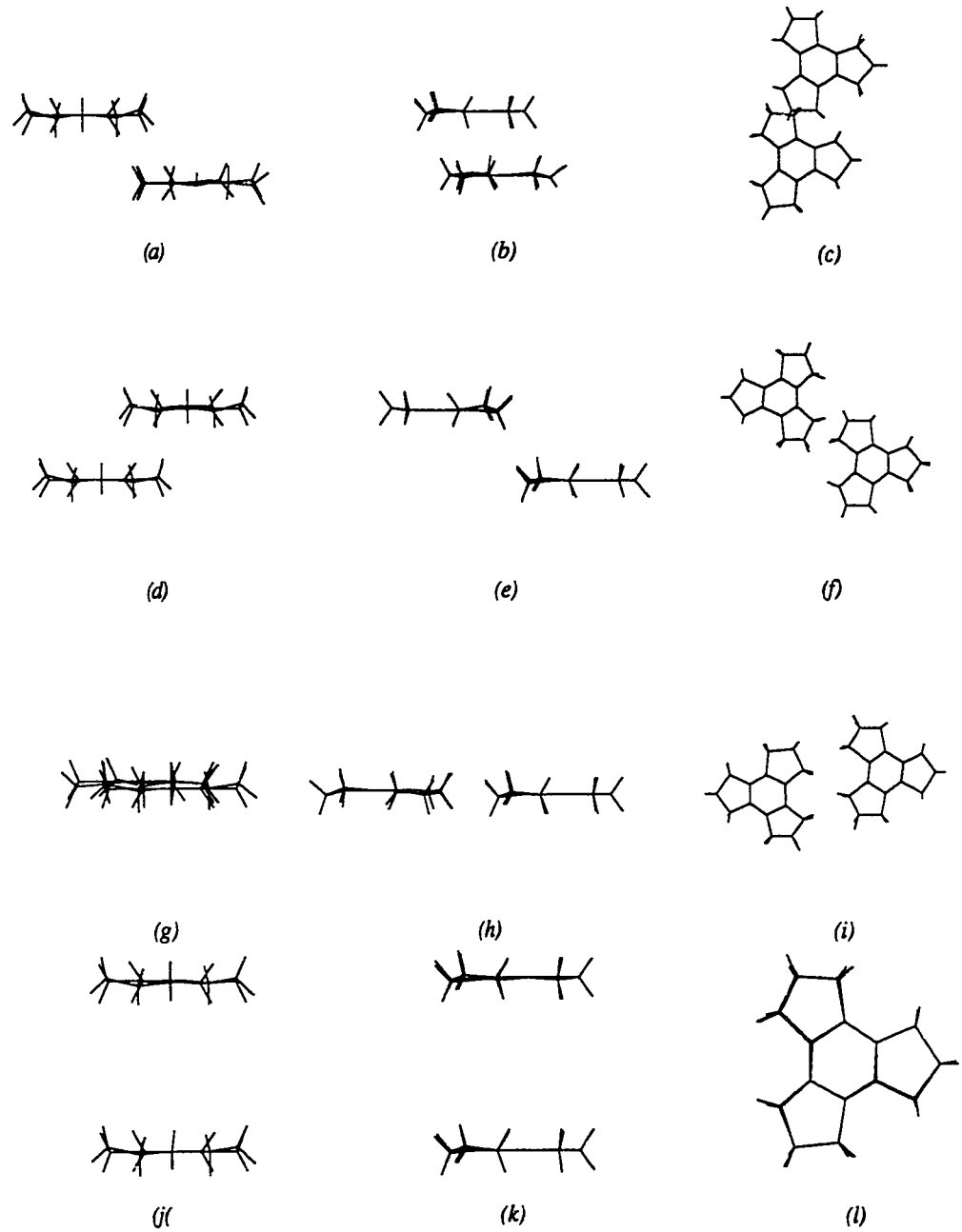

Figure 6.15.8. (a)-(i). The four symmetry positionsin the unit cell of the third most probable space group for trindan, as viewed along the principal axes of one of the molecules. (j)-(l). Nearest neighbors in adjacent unit cells in the [100] direction.

6.16. Summary

The correct space group was predicted to be the most probable for nine of the fifteen molecules studied (sixteen if dibenzanthracene is counted twice), and second most probable for two more of them. These results are summarized in Table 6.16.1. Groups containing mirror planes, such as P*mc* and C*mc*, were found to have the lowest packing indices and the highest energy, and hence the lowest probability of all structures in the cases where they were considered.

ICE9 found an energy minimum corresponding to the experimental structure for ten of the fifteen molecules studied, and one very close to experiment for the other five, indicating that the Lennard-Jones parameters used in this study were valid. Exact comparisons to the monoclinic form of dibenzanthracene could not be made. It should be noted that in searching for structures close to experiment, many structures would usually be found with good lattice constants, but with quite different energies. The data for an example of two such structures for hexane are shown below in Table 6.16.2. Both of these structures are very close to the experimental structure, but slight differences in position are sufficient to produce an energy difference of 1.64 kcal/mol, from displacing just a few atoms towards the high energy, repulsive portion of the Lennard-Jones potential energy curve. In phenanthrene, dibenzanthracene B, pyrene, and trindan, in which the experimental structures were not reproduced exactly despite having lattice constants which were close, the molecular orientations deviated by small changes in the angles of inclination with respect to each other. This small deviation in angles would often result in compression of the separation distances between molecules in order for

the structure to fit within the lattice constants, thereby creating several unfavorable interactions and the higher energies seen in Table 6.16.1 for these structures. The best example of this can be seen in the case of the dibenzanthracene orthorhombic modification (Fig. 6.9.2 and Fig. 6.9.6). It should also be noted that the parameterization was based on structures at 78K, and the experimental data is often taken at much higher temperatures. This variation in temperature can account for some of the energy and structural differences in Table 6.16.1, due to thermal expansion.

In general, the number of possible structures with energy close to the global minimum correlated strongly with the shape of the molecule. The most unequivocal results obtained by ICE9 were for bicyclohexylidene, the correct structure being almost 2 kcal/mol lower in energy than the next best structure in $C2/c$. The packing index was also dramatically higher, indicating that the predicted structure was by far the most closely packed. The irregular shape of bicyclohexylidene severly limits the possible number of low energy, closest-packed structures, and is undoubtedly responsible for the unambiguousness of the results.

For the saturated linear hydrocarbons hexane and octane, the number of reasonable structures obtained was greater than for bicyclohexylidene, but much less than for the aromatic molecules. Dovetailing of the hydrogen atoms along the entire length of the saturated molecule maximizes the dispersion energy and fills space efficiently, and hence was a dominant characteristic in the layers of all of the low energy structures for hexane and octane. The structure within layers was the same for the experimental structures and for the predicted structures in space groups $P\bar{1}$ and $P2_1/c$, and other possible configurations of the molecules within

Table 6.16.1 Summary of Results. ΔE indicates the difference in energy between the structure corresponding to the experiemntal structure and the global minimum.

Molecule	Ranking of correct space group	ΔE (kcal/mol)	Expt. struc. found
Benzene	10	0.52	Yes
Naphthalene	1	0.31	Yes
Anthracene	4	0.18	Yes
Tetracene	2	0.16	Close*
Pentacene	1	0.44	Close*
Phenanthrene	6	7.02	Close
Pyrene	1	1.25	Yes
Triphenylene	2	2.9	Yes
1:2:5:6-Dibenz-anthracene A	1	N.A.	Yes**
1:2:5:6-Dibenz-anthracene B	7	-	Close
Perylene	1	8.88	Close
Durene	5	1.93	Yes
Hexane	1	0.86	Yes
Octane	1	1.97	Yes
Bicyclohexylidene	1	0	Yes
Trindan	1	6.92	Close

*Predicting the exact structure is not possible for tetracene and pentacene, as the experimental asymmetric unit consists of two half molecules, for which ICE9 does not make previsions at this time. The ΔE given for the energy is for structures which come as close as possible to the experimental structures, including intermolecular angles and separation. See Sections 6.4 and 6.5.

**Structure with similar lattice constants were found, but experimental coordinates are not known.

Table 6.16.2. Comparison of Predicted Structures A and B Closest to Experiment for Hexane

Experimental Data [1]:

Temperature:	-115°C		
Space Group:	$P\bar{1}$		
Molecules per cell:	1		
a:	4.17	α:	96.6°(83.4°)
b:	4.70	β:	87.2°
c:	8.57	γ:	105.0°(75.0°)

Predicted Structure Closest to Experiment 1:

Space Group:	$P\bar{1}$				
Molecules per cell:	1				
Packing index:	0.5101				
a:	4.18	α:	84.9°	Energy:	-15.51
b:	4.77	β:	90.0°	Lennard-Jones:	-15.57
c:	8.728	γ:	72.19°	Coulombic:	0.0586

Predicted Structure Closest to Experiment 2 (Better Energy):

Space Group:	$P\bar{1}$				
Molecules per cell:	1				
Packing index:	0.5362				
a:	4.16	α:	90.0°	Energy:	-17.15
b:	5.029	β:	61.94°	Lennard-Jones:	-17.18
c:	8.527	γ:	86.58°	Coulombic:	0.03

layers were clearly eliminated. The principal difference between the experimental and predicted structures is that interlocking layers are displaced two carbon atoms along the **L** axes of the molecules. Between these layers, however, weaker interactions between molecules across the interface were not sufficient to give an overwhelming preference to configurations where the molecules in separate layers were parallel or rotated. Hence the difference in energies for space groups $P\bar{1}$ and $P2_1/c$ for both hexane and octane are small, on the order of 0.3 kcal/mol.

For the planar aromatic hydrocarbons, the possibilities are not as limited as with bicyclohexylidene, hexane, and octane. The lack of protrusions, bumps, and hollows on the aromatic molecules allows for many more degrees of freedom than for the mostly saturated hydrocarbons, and hence many more ways to achieve closest packing and a low Van der Waals energy. The result is a large number of structures in many different space groups with an energy near the global minimum for the aromatic molecules. Within these varied structures, however, many common features were observed. The smaller molecules, such as benzene, naphthalene, anthracene and phenanthrene can achieve close packing and hence a low energy with an edge-to-face herringbone structure, and this type of packing was predicted. The larger molecules, such as pyrene and perylene, could not fill space if they were arranged entirely edge-to-face and hence are observed to be constructed of dimers or rows of parallel molecules which were then angled to neighboring dimers or rows to take advantage of the lower electrostatic energy.

The packing indices for the lowest energy structures were found to lie within a fairly narrow range of 0.5541 to 0.6506, with one exception. Trindan's trifold symmetry and protruding hydrogen atoms contributed to a very low packing index of 0.4207. The packing indices are summarized in Table 6.16.3. The calculated packing indices are below the range of 0.65 to 0.77 reported by Kitaigorodsky. This difference is due to the way in which the molecular volumes are defined, and not due to a difference in the structures.

Table 6.16.3. Comparison of packing indices

Molecule	Packing index
Tetracene	0.6506
Pyrene	0.6465
Triphenylene	0.6396
Phenanthrene	0.6326
Anthracene	0.6309
Bicyclohexyl.	0.6242
Dibenzanth.	0.6208
Naphthalene	0.6174
Perylene	0.6098
Octane	0.5807
Benzene	0.5675
Pentacene	0.5668
Durene	0.5653
Hexane	0.5541
Trindan	0.4207

Chapter 7 Conclusion

Local minima corresponding to experimental structures were found for almost all of the 15 molecules examined in this study, validating the accuracy of the Lennard-Jones parameters, and justifying their utilization as the sole minimization criterion in ICE9. For saturated, or mostly saturated hydrocarbons like the ones investigated in this work, ICE9 appears to give good results without extensive additional refinements in the energy calculations of the predicted lowest energy Van der Waals structures, i.e. in solids where shape plays a strong role and complicated electronic effects are minimal. For the planar aromatic hydrocarbons, however, the empirical parameters and molecular multipole moments are sufficient to give good approximations, and were able to locate minima corresponding to the experimental structures, but are too limited to distinguish the actual structure from a number of possibilities on the basis of energy alone. Further refinement of the energy with more sophisticated methods would be necessary for these materials to arrive at an unequivocal prediction.

Van der Waals interactions are often though of as being very simple to describe, and on a certain level that is true. Yet the inability to clearly distinguish the experimental structure in all cases in this study is a limitation of empirical pair parameters in general, and not due to inadequate parameters or electrostatic model. We need to do more than merely add electrostatic potentials on top of Van der Waals pair potentials to obtain results accurate enough to distinguish the experimental structures from a number of reasonable possibilities on the basis of energy. The assumption of independent, transferable pair potentials ignores the possibility of multibody effects and polarization of intermediate bodies, as well

as differences in the same type of atom from molecule to molecule. In addition, the separation of the energy of molecular solids into dispersion, repulsion, and electrostatic contributions is but an artificial construct for simplicity and expediency. To describe the intermolecular interactions accurately in molecular solids is actually very complicated and requires the most advanced quantum mechanical methods which are available today.

The use of empirical pair potentials to describe Van der Waals interactions is widespread among today's scientific researchers, however, because this simplified model allows us to approach problems which would otherwise be intractible. Yet, there is a danger in putting too much credence in the answers given by empirical pair potentials for Van der Waals interactions. They can do an excellent job of describing molecular shape and packing characteristics, but cannot give accurate values for the energy of molecular solids. At best they can give one a general idea of what to expect, and provide some direction to the synthetic chemist or to the quantum chemist performing more rigorous calculations. They are no substitute for these more intensive calculations. Programs such as ICE9 can be used to eliminate unreasonable starting points, as well as aid in the refinement of crystal structure. ICE9 lets us look at all the possibilities for closest-packed structures, thus providing a good framework in which to study improved empirical models, as well as a way to gauge the importance of weak intermolecular interactions in more complicated systems such as the charge-transfer materials.

Appendix A Crystal Structure and Symmetry: Definitions

An ideal crystal is comprised of an infinite array of identical structural units, called unit cells. These unit cells, when aligned in three dimension, fill space completely without gaps or overlap. The lattice of the crystal is a three-dimensional, effectively infinite array of identical points in space, which may or may not coincide with actual atomic positions. Each lattice point has a set of one or more atoms associated with it, which is known as the asymmetrical unit, or basis, of the crystal structure.

Lattice points are related by simple translations which can be described in terms of three abritrary, independent vectors $\vec{a}, \vec{b}$, and $\vec{c}$, called the primitive translation vectors. All points in the lattice can then be generated by the crystal translation vector $\vec{T}$ as follows:

$$\vec{T} = u_1\vec{a} + u_2\vec{b} + u_3\vec{c} \qquad \text{[Eq. A.1]}$$

where u_i is any integer. The lattice angles, i.e. the interaxial angles between the primitive lattice vectors, are defined in the following manner: α is the angle between $\vec{b}$ and $\vec{c}$, β is the angle between $\vec{a}$ and $\vec{c}$, and γ is the angle between $\vec{a}$ and $\vec{b}$,

The location of an arbitrary point of an atom in the crystal structure can be described in terms of a position vector with components $f_1\vec{a}, f_2\vec{b}$, and $f_3\vec{c}$, or in terms of coordinates x', y', and z' expressed in units of $\vec{a}$, $\vec{b}$, and $\vec{c}$.

For energy calculations to be performed on the crystal structure, it is essential to express the atomic positions in terms of reference cartesian space rather than in fractions of lattice vectors. The convention is to choose cartesian axes X_2 and X_3 coincident with lattice vectors $\vec{b}$ and $\vec{c}*$, where $\vec{c}*$ is the unit cell vector in reciprocal space space corresponding to $\vec{c}$. X_1 is then chosen to lie in the ab plane perpendicular to $bc*$. Unit cell space can then be transformed into cartesian space by the operation $X = DX'$ where D is the transformation matrix in Figure A.1.

$$\begin{pmatrix} a\,sin(\alpha) & 0 & c(cos(\beta) - cos(\alpha)cos(\gamma))/sin(\gamma) \\ a\,cos(\gamma) & b & c\,cos(\gamma) \\ 0 & 0 & V/ab\,sin(\gamma) \end{pmatrix}$$

Figure A.1. Transformation matrix D for unit cells with nonorthogonal axes. a, b, and c are the lattice constants; α is the angle between the b– and c–axes, β between a and c, and γ between a and b; V is the volume of the unit cell and is equal to $abc(1 + 2cos(\alpha)cos(\beta)cos(\gamma) - cos2(\alpha) - cos2(\beta) - cos2(\gamma)]^{1/2}$.

By placing symmetry restrictions on the lattice points, crystals can be divided into seven distinct systems: triclinic, monoclinic, orthorhombic, tetragonal, trigonal, hexagonal, and cubic. There are fourteen types of three-dimensional lattices, called the Bravais lattices, which are distributed amoung the seven crystal systems.

Point groups are sets of symmetry operations which are applied to a finite body about a point, and leave the body unchanged. These symmetry operations may be any of the following: identity, proper rotation, reflection, improper rotation (rotation-reflection). Point groups are used to describe the symmetry of individual molecules. Space groups, on the other hand, are sets of symmetry operations which leave the structure of an infinite crystal unchanged. Hence, space groups include the translation operations, i.e., glide planes and screw axes, in

addition to the point group symmetry operations listed above. Combining these elements with the fourteen Bravais lattices results in a total of 230 space groups.

The asymmetric unit may consist of a single atom, part of a molecule, or possibly even several molecules. For example, in a space group containing a mirror plane, if a molecule lies on that plane, then only half that molecule is necessary and sufficient to generate the entire crystal structure. (Fig. A.2). For some crystals, such as tetracene and pentacene, the asymmetric unit consists of two separate half-molecules.

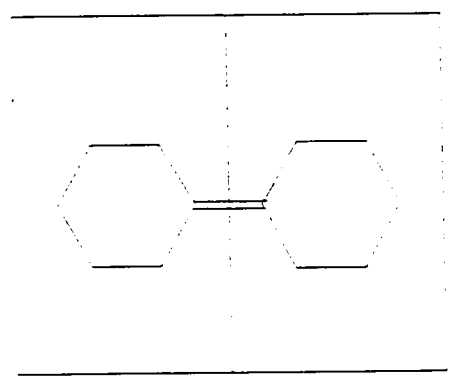

Figure A.2. Molecule located on a mirror plane. The asymmetric unit for this structure would consist of half the molecule.

Symmetry equivalent positions within the unit cell of a space group are related to the reference position x, y, z by algebraic expressions such as -x, -y, and -z for an inversion center and -x, $1/2 + y$, -z for a 2-fold screw axis. Within a given space group, the molecules can be oriented such that the symmetry of the molecule is coincident with that of the crystal lattice. These are the so-called special positions

and are shown in Table 1.3 under the headings -1, 2, and m for inversion center, 2-fold rotation axis, and mirror plane, respectively. Positions which are not located on special symmetry sites are called 'general' positions, and are listed in the first column in Table 1.3. Crystal structures can be formed in which both special and general positions are occupied.

Appendix B Quantum Mechanical Methods

The Hamiltonian for a molecule is as follows:

$$H = \frac{-\hbar^2}{2m_e}\nabla_r^2 + V_{nn} + V_{ne} + V_{ee} \qquad \text{[Eq. B.1]}$$

where ∇_r^2 is the kinetic energy of the electron, V_{nn} is the internuclear repulsion $\sum \frac{Z_A Z_B}{R_{AB}}$, V_{ne} is the nuclear-electron attraction $\frac{eZ_n}{r_{ne}}$, and V_{ee} is the potential energy due to the electron-electron interaction.

Ψ cannot be calculated exactly for systems more complicated than a one-electron atom, and hence approximations to the molecular wave function must be used. The most convenient approach is to construct the molecular orbitals (MO) from a linear combination of atomic orbitals (LCAO), with the proper symmetry, and adjust the coefficients from each AO to give the lowest energy in a self-consistent field (SCF) calculation. The electron repulsion integrals

$$J_{\mu\nu} = \langle \mu\mu | \frac{1}{r_{12}} | \nu\nu \rangle \qquad \text{[Eq. B.2]}$$

consume a considerable amount of time and memory to evaluate on even the most advanced computers.

B.1 Semi-Empirical Methods

For large molecules several semi-empirical methods have been developed to approximate the electron repulsion by neglecting differential overlap [3] to varying degrees. That is, all two-electron integrals, such as $\langle \mu\nu | \lambda\sigma \rangle$ which depend on the overlapping of different orthonormal basis orbitals, are ignored unless $\mu = \nu$ and $\lambda = \sigma$.

The Complete Neglect of Differential Overlap (CNDO) is the simplest approximation, in which atomic orbitals are assumed to be spherically symmetric in calculating the one-center repulsion integrals. The electron repulsion integrals for all atomic orbitals μ on atom A and λ on atom B are assumed to have the same constant value, i.e. $\langle\mu\mu|\lambda\lambda\rangle = \gamma_{AB}$, where γ_{AB} is a constant for atoms A and B. CNDO was parameterized to reproduce electronic properties, such as the dipole moment, rather than molecular geometries or heats of formation.

MINDO/3 uses parameters to approximate the energy of the one-center electron repulsion integrals, rather than evaluating them analytically. Directionality, although included in the 1 electron resonance integrals

$$K_{\mu\nu} = \langle\mu(1)\nu(2)|\frac{1}{r_{12}}|\mu(2)\nu(1)\rangle \qquad \text{[Eq. B.3]}$$

is not included in the repulsion integrals.

Directionality is considered in the repulsion integrals in MNDO, one of the methods which neglects diatomic differential overlap (NDDO). MNDO is parameterized to reproduce experimental heats of formation. AM1, the most recently developed semi-empirical method, is based on MNDO but with improved parameterization.

B.2 Ab initio Methods

For smaller molecules it is possible to perform a more rigorous *ab initio* MO calculation. In general, the only assumptions made in these calculations are the Born-Oppenheimer approximation and a single-determinental wave function. In most commercial programs Gaussian-type orbitals of the form

$$\phi = e^{-\alpha r^2} \qquad \text{[Eq. B.4]}$$

are used to approximate the Slater-Type Orbitals (STO) because they are several orders of magnitude faster to calculate. The unnormalized radial term for an STO is as follows:

$$r^{n-1}e^{-\zeta r} \qquad \text{[Eq. B.5]}$$

For the STO-3G basis set, 3 Gaussian-type orbials are used to approximate each STO. The exponents are fixed for each type of atom, and are not sensitive to the molecular environment. Some flexibility is necessary, however, to adequately describe the molecular environment. In *split-valence* or *double zeta* basis sets, such as 3-21G, the atomic valence orbitals are split into an inner, compact orbital, and an outer, more diffuse one.

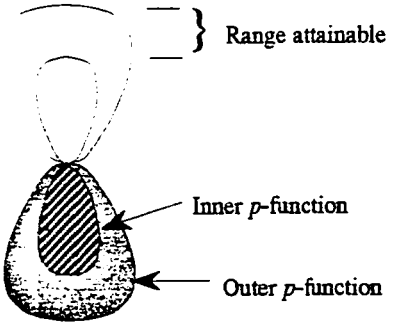

Figure B.1 Schematic representation of the effect of *split-valence* orbitals. [148]

The nomenclature 3-21G indicates that in this basis set the core orbitals are each constructed from 3 Gaussian wavefunctions, and the valence orbitals consist of 2 and 1 Gaussian functions for the inner and outer orbitals, respectively. Calculations using the 3-21G basis set are very fast, and the accuracy is sufficient to make 3-21G the most commonly used basis set for initial geometry optimization.

The addition of *d*-orbitals provides for polarization of *p*-orbitals in organic molecules, and is indicated by an asterisk, as in 6-31G*. P-orbitals can be used to polarize the *s*-orbitals on hydrogen by adding a second asterisk, as in 6-31G**.

The 6-31G** basis set was required to reproduce the polarization across the C-H bond which Williams uses in PCK83. This degree of polarization produces a quadrupole moment much greater than the experimental value.

For molecules or anions with nonbonding electron pairs, a set of very diffuse orbitals are available in the Gaussian programs to be used in addition to those mentioned previously, and are indicated by a '+', as in 6-31+G*. Marvin Fritsch, of Gaussian, Inc., recommends 6-31+G* for benzene. Unfortunately, for larger molecules such as pentacene studied in this work, the 6-31+G* basis set requires too much memory to be feasible, even on a Cray Y-MP 864. When comparing results in different molecules, it is essential to use a consistent basis set with the largest possible number of basis functions.

Appendix C Example of an Input File

```
Naphthalene -631G
 18  104.32100
C01  -1.24689  -1.41038   0.00000    6   0   -0.16086
C02  -2.43765  -0.71195   0.00000    6   0   -0.19966
C03  -0.00002  -0.70890   0.00000    6   0   -0.07224
H04  -1.25635  -2.46033   0.00000    1   0    0.20299
C05  -2.43768   0.71187   0.00000    6   0   -0.19960
C06   1.24686  -1.41035   0.00000    6   0   -0.16039
C07   0.00000   0.70910   0.00000    6   0   -0.07215
H08  -3.34877  -1.23384   0.00000    1   0    0.19348
C09  -1.24697   1.41041   0.00000    6   0   -0.16099
C10   1.24699   1.41037   0.00000    6   0   -0.16025
C11   2.43765  -0.71196   0.00000    6   0   -0.19986
H12  -3.34883   1.23369   0.00000    1   0    0.19348
H13   1.25631  -2.46030   0.00001    1   0    0.20301
C14   2.43771   0.71184   0.00000    6   0   -0.19987
H15  -1.25655   2.46036   0.00001    1   0    0.20297
H16   1.25657   2.46032  -0.00001    1   0    0.20301
H17   3.34875  -1.23386   0.00000    1   0    0.19346
H18   3.34887   1.23366   0.00000    1   0    0.19346
 DIPOLE MOMENTS.
   X  = 0.15265903E-03 Y  =-0.18420876E-03 Z  =-0.12464436E-05
 SECOND MOMENTS.
   XX =-0.51052102E+02 YY =-0.50940389E+02 ZZ =-0.64941884E+02
   XY = 0.24375262E-03  XZ =-0.74695960E-05 YZ =-0.77800048E-05
 THIRD MOMENTS.
   XXX= 0.12556236E-02 YYY =-0.17484826E-02 ZZZ =-0.27623666E-05
   XYY= 0.13567592E-02 XXY =-0.18913039E-03 XXZ= 0.32076762E-04
   XZZ= 0.82656505E-04  YZZ =-0.24131326E-03 YYZ= 0.39717850E-04
   XYZ =-0.29904309E-04
 FOURTH MOMENTS.
   XXXX=-0.10752017E+04 YYYY=-0.46804336E+03 ZZZZ=-0.70594194E+02
   XXXY= 0.17697556E-02 XXXZ=-0.13998329E-04 YYYX= 0.13383427E-02
   YYYZ=-0.99167564E-04 ZZZX=-0.87368267E-05 ZZZY=-0.15108696E-04
   XXYY=-0.26172282E+03 XXZZ=-0.23883798E+03 YYZZ=-0.10984371E+03
   XXYZ= 0.12790866E-03 YYXZ=-0.78265970E-04 ZZXY= 0.52444421E-04
```

Appendix D Example of an Output File

The calculations on each molecule are broken down into several separate runs to minimize loss of data in case there is a problem with the execution of the program. This is an example of the output file for one of the naphthalene runs in which the monoclinic and orthorhobic space groups with molecules generally positioned were searched. Included is the timing information for this run. In addition to this file below in which the best results in each space group are presented, a list file is produced which contains the results for each local minimum obtained.

OUTPUT FILE:

```
DATE: 08/09/91
TIME: 19:46
+ hpm -g 0 a.out
calling main subroutine
initializing common blocks
Interaction radius cutoff is 10.000 angstroms.
*****INPUT CHECK:
Naphthalene -631G
 18  104.32100
C01  -1.24689 -1.41038  0.00000    6   0   -0.160
C02  -2.43765 -0.71195  0.00000    6   0   -0.199
C03  -0.00002 -0.70890  0.00000    6   0   -0.072
H04  -1.25635 -2.46033  0.00000    1   0    0.202
C05  -2.43768  0.71187  0.00000    6   0   -0.199
C06   1.24686 -1.41035  0.00000    6   0   -0.160
C07   0.00000  0.70910  0.00000    6   0   -0.072
H08  -3.34877 -1.23384  0.00000    1   0    0.193
C09  -1.24697  1.41041  0.00000    6   0   -0.160
C10   1.24699  1.41037  0.00000    6   0   -0.160
C11   2.43765 -0.71196  0.00000    6   0   -0.199
H12  -3.34883  1.23369  0.00000    1   0    0.193
H13   1.25631 -2.46030  0.00001    1   0    0.203
C14   2.43771  0.71184  0.00000    6   0   -0.199
H15  -1.25655  2.46036  0.00001    1   0    0.202
H16   1.25657  2.46032 -0.00001    1   0    0.203
H17   3.34875 -1.23386  0.00000    1   0    0.193
H18   3.34887  1.23366  0.00000    1   0    0.193
 DIPOLE MOMENT
 1.5265903E-4, -1.8420877E-4, -1.2464436E-6
 QUADRUPOLE MOMENT
```

```
 4.593     0.2438E-03 -0.7470E-05
 0.2438E-03  4.704    -0.7780E-05
-0.7470E-05 -0.7780E-05  -9.297

OCTUPOLE TENSOR ELEMENTS
3.2076761E-5, 3.9717848E-5, -2.7623666E-6
1.3567592E-3, -1.8913038E-4, 3.2076761E-5
8.2656508E-5, -2.4131326E-4, 3.9717848E-5
-2.9904309E-5
CENTER OF MASS: 0.2887E-14 0.2344E-05 0.7813E-07
SPACE GROUP SYMMETRY FILE
IFAIL =  0


EIGENVECTORS:
    1.000000     0.0000000E+00 0.0000000E+00
   0.3057692E-07 0.1517064E-06  1.000000
  -0.2211929E-07 -1.000000     0.1517064E-06

XSYM:  2 YSYM:  2 ZSYM:  2
**ALIGN AXIS OF HIGHEST SYMMETRY ALONG Z
axis of highest symmetry is:  3 with symmetry:  2
CENTER OF MASS: -0.4441E-14 -0.1588E-20  0.4441E-14
 MOLECULE HAS AN INVERSION CENTER. MOLSYM(1)=1
 MOLECULE HAS 222 SYMMETRY.  MOLSYM(2)=1.
 MOLECULE HAS mmm SYMMETRY. MOLSYM(3)=1
 FULLY ALIGNED COORDINATES XYZ0:
   6     -1.2469     0.0000    -1.4104
   6     -2.4377     0.0000    -0.7120
   6      0.0000     0.0000    -0.7089
   1     -1.2564     0.0000    -2.4603
   6     -2.4377     0.0000     0.7119
   6      1.2469     0.0000    -1.4104
   6      0.0000     0.0000     0.7091
   1     -3.3488     0.0000    -1.2338
   6     -1.2470     0.0000     1.4104
   6      1.2470     0.0000     1.4104
   6      2.4376     0.0000    -0.7120
   1     -3.3488     0.0000     1.2337
   1      1.2563     0.0000    -2.4603
   6      2.4377     0.0000     0.7118
   1     -1.2565     0.0000     2.4604
   1      1.2566     0.0000     2.4603
   1      3.3487     0.0000    -1.2339
   1      3.3489     0.0000     1.2337
 check after rotPOLES in getsym
 Dipole:  0.000  0.000  0.000
 QuadruPOLES:
     4.593  0.000  0.000
     0.000 -9.297  0.000
     0.000  0.000  4.704
```

```
MOLECULAR DIAMETER (DIAMOL):  7.138
SUBROUTINE GETJONES
EPSCC: 0.1232374 EPSHH: 0.1207778
SIGMAC: 1.694 SIGMAH: 1.272
molsym:  1   1   1
SUBROUTINE GENERAL MONOCLINIC
NROT:    1 EPACK:-12.05    ELJ:-12.21    ecoul -.2445    calls  552
NROT:    2 EPACK:-14.17    ELJ:-14.38    ecoul -.3478    calls  643
NROT:    3 EPACK:-14.68    ELJ:-14.88    ecoul -.5987    calls  699
NROT:    4 EPACK:-14.41    ELJ:-14.37    ecoul -1.005    calls  684
.
.
.
.
Total function calls for this job:    2647583
Number of starting positions:    3710

**************************************************
**********FINAL RESULTS**********
**************************************************


 P2(1)   Wyck a  E: -17.28   PI:  0.613644     169
ELJ:  -16.80    ECOUL: -0.4809    NAXIS:     1
A:  10.2548   ALPHA:  90.00   ROTX:  -1.05   TRANSX:  0.25
B:   5.3189   BETA:   82.36   ROTY:  38.56   TRANSY:  0.24
C:   6.2895   GAMMA:  90.00   ROTZ:  52.50   TRANSZ:  0.25


 P2(1)   Wyck a  E: -17.28   PI:  0.608832     128
ELJ:  -16.57    ECOUL: -0.7072    NAXIS:     1
A:   6.8026   ALPHA:  90.00   ROTX:   9.92   TRANSX:  0.25
B:   4.7357   BETA:   90.00   ROTY:  55.88   TRANSY:  0.00
C:  10.6377   GAMMA:  90.00   ROTZ:  37.50   TRANSZ:  0.25


 P2(1)   Wyck a  E: -17.25   PI:  0.605816     127
ELJ:  -16.51    ECOUL: -0.7427    NAXIS:     1
A:   6.8332   ALPHA:  90.00   ROTX:   7.50   TRANSX:  0.25
B:   4.6161   BETA:   90.00   ROTY:  55.71   TRANSY:  0.25
C:  10.9183   GAMMA:  90.00   ROTZ:  37.50   TRANSZ:  0.25


 P2(1)   Wyck a  E: -17.05   PI:  0.604117     223
ELJ:  -16.07    ECOUL: -0.9792    NAXIS:     1
A:   4.7683   ALPHA:  90.00   ROTX:  78.99   TRANSX:  0.24
B:   5.3189   BETA:   76.88   ROTY:  45.40   TRANSY:  0.25
C:  13.9821   GAMMA:  90.00   ROTZ:  67.50   TRANSZ:  0.25
```

P2(1)/c Wyck e E: -17.40 PI: 0.607843 177
ELJ: -16.65 ECOUL: -0.7521 NAXIS: 1
A: 13.6410 ALPHA: 90.00 ROTX: 7.50 TRANSX: 0.25
B: 4.6097 BETA: 60.00 ROTY: 54.02 TRANSY: 0.50
C: 12.6063 GAMMA: 90.00 ROTZ: 37.50 TRANSZ: 0.00

P2(1)/c Wyck e E: -17.31 PI: 0.605762 307
ELJ: -16.15 ECOUL: -1.160 NAXIS: 1
A: 6.6260 ALPHA: 90.00 ROTX: 75.91 TRANSX: 0.25
B: 6.6431 BETA: 64.83 ROTY: 12.92 TRANSY: 0.24
C: 17.2917 GAMMA: 90.00 ROTZ: 97.50 TRANSZ: 0.25

P2(1)2(1)2(1) Wa E: -17.10 PI: 0.604960 326
ELJ: -16.24 ECOUL: -0.8590 NAXIS: 1
A: 12.5729 ALPHA: 90.00 ROTX: 21.06 TRANSX: 0.27
B: 4.2192 BETA: 90.00 ROTY: 41.86 TRANSY: 0.19
C: 13.0028 GAMMA: 90.00 ROTZ: 22.50 TRANSZ: 0.13

P2(1) Wyck a E: -17.04 PI: 0.606273 318
ELJ: -16.00 ECOUL: -1.037 NAXIS: 1
A: 4.0063 ALPHA: 90.00 ROTX: 28.80 TRANSX: 0.00
B: 7.7543 BETA: 90.00 ROTY: 37.50 TRANSY: 0.24
C: 11.0774 GAMMA: 90.00 ROTZ: 92.11 TRANSZ: 0.25

P2(1) Wyck a E: -17.37 PI: 0.609843 177
ELJ: -16.69 ECOUL: -0.6803 NAXIS: 1
A: 6.7431 ALPHA: 90.00 ROTX: 7.50 TRANSX: 0.25
B: 4.7872 BETA: 90.00 ROTY: 55.98 TRANSY: 0.25
C: 10.5984 GAMMA: 90.00 ROTZ: 40.08 TRANSZ: 0.25

P2(1) Wyck a E: -17.35 PI: 0.615676 176
ELJ: -16.91 ECOUL: -0.4423 NAXIS: 1
A: 6.0933 ALPHA: 90.00 ROTX: 1.78 TRANSX: 0.25
B: 5.5944 BETA: 80.08 ROTY: 59.54 TRANSY: 0.25
C: 10.0920 GAMMA: 90.00 ROTZ: 52.50 TRANSZ: 0.25
****
**********TOP STRUCTURES IN EACH GROUP**********
****

P2(1) Wyck a E: -17.28 PI: 0.613644 169
ELJ: -16.80 ECOUL: -0.4809 NAXIS: 1
A: 10.2548 ALPHA: 90.00 ROTX: -1.05 TRANSX: 0.25
B: 5.3189 BETA: 82.36 ROTY: 38.56 TRANSY: 0.24
C: 6.2895 GAMMA: 90.00 ROTZ: 52.50 TRANSZ: 0.25

P2(1) Wyck a E: -17.35 PI: 0.615676 176
ELJ: -16.91 ECOUL: -0.4423 NAXIS: 1
A: 6.0933 ALPHA: 90.00 ROTX: 1.78 TRANSX: 0.25
B: 5.5944 BETA: 80.08 ROTY: 59.54 TRANSY: 0.25
C: 10.0920 GAMMA: 90.00 ROTZ: 52.50 TRANSZ: 0.25

P2(1) Wyck a E: -17.37 PI: 0.609843 177
ELJ: -16.69 ECOUL: -0.6803 NAXIS: 1
A: 6.7431 ALPHA: 90.00 ROTX: 7.50 TRANSX: 0.25
B: 4.7872 BETA: 90.00 ROTY: 55.98 TRANSY: 0.25
C: 10.5984 GAMMA: 90.00 ROTZ: 40.08 TRANSZ: 0.25

P2(1)/c Wyck e E: -17.31 PI: 0.605762 307
ELJ: -16.15 ECOUL: -1.160 NAXIS: 1
A: 6.6260 ALPHA: 90.00 ROTX: 75.91 TRANSX: 0.25
B: 6.6431 BETA: 64.83 ROTY: 12.92 TRANSY: 0.24
C: 17.2917 GAMMA: 90.00 ROTZ: 97.50 TRANSZ: 0.25

P2(1)/c Wyck e E: -17.40 PI: 0.607843 177
ELJ: -16.65 ECOUL: -0.7521 NAXIS: 1
A: 13.6410 ALPHA: 90.00 ROTX: 7.50 TRANSX: 0.25
B: 4.6097 BETA: 60.00 ROTY: 54.02 TRANSY: 0.50
C: 12.6063 GAMMA: 90.00 ROTZ: 37.50 TRANSZ: 0.00

P2(1)/c Wyck e E: -16.82 PI: 0.600164 95
ELJ: -16.08 ECOUL: -0.7462 NAXIS: 1
A: 11.8572 ALPHA: 90.00 ROTX: 37.50 TRANSX: 0.25
B: 4.6375 BETA: 81.53 ROTY: 96.35 TRANSY: 0.49
C: 12.7839 GAMMA: 90.00 ROTZ: 7.50 TRANSZ: 0.12

Pca Wyck a E: -16.47 PI: 0.584546 102
ELJ: -15.60 ECOUL: -0.8749 NAXIS: 1
A: 13.2858 ALPHA: 90.00 ROTX: 76.73 TRANSX: 0.15
B: 7.7598 BETA: 90.00 ROTY: 114.62 TRANSY: 0.26
C: 6.9242 GAMMA: 90.00 ROTZ: -7.50 TRANSZ: 0.25

Pca Wyck a E: -16.86 PI: 0.600411 247
ELJ: -16.04 ECOUL: -0.8150 NAXIS: 1
A: 13.0867 ALPHA: 90.00 ROTX: 92.98 TRANSX: 0.14
B: 7.4046 BETA: 90.00 ROTY: 120.53 TRANSY: 0.25
C: 7.1722 GAMMA: 90.00 ROTZ: 19.52 TRANSZ: 0.26

Pca Wyck a E: -16.79 PI: 0.599418 391

ELJ: -16.01 ECOUL: -0.7771 NAXIS: 1
A: 12.9379 ALPHA: 90.00 ROTX: 90.79 TRANSX: 0.14
B: 7.3267 BETA: 90.00 ROTY: 121.84 TRANSY: 0.25
C: 7.3440 GAMMA: 90.00 ROTZ: 22.50 TRANSZ: 0.25

Pna Wyck a E: -16.67 PI: 0.597730 899
ELJ: -16.00 ECOUL: -0.6710 NAXIS: 1
A: 7.8753 ALPHA: 90.00 ROTX: 157.50 TRANSX: 0.25
B: 16.6663 BETA: 90.00 ROTY: 32.38 TRANSY: 0.13
C: 5.3189 GAMMA: 90.00 ROTZ: 97.50 TRANSZ: 0.20

Pna Wyck a E: -16.52 PI: 0.602602 577
ELJ: -16.11 ECOUL: -0.4089 NAXIS: 1
A: 10.6377 ALPHA: 90.00 ROTX: 0.04 TRANSX: 0.37
B: 5.6187 BETA: 90.00 ROTY: -0.04 TRANSY: 0.00
C: 11.5854 GAMMA: 90.00 ROTZ: 54.90 TRANSZ: 0.17

Pna Wyck a E: -16.63 PI: 0.581988 1002
ELJ: -15.45 ECOUL: -1.174 NAXIS: 1
A: 6.7506 ALPHA: 90.00 ROTX: 77.53 TRANSX: 0.33
B: 6.4902 BETA: 90.00 ROTY: 164.31 TRANSY: 0.01
C: 16.3649 GAMMA: 90.00 ROTZ: 92.28 TRANSZ: 0.25

P2(1)2(1)2(1) Wa E: -16.93 PI: 0.605803 774
ELJ: -16.29 ECOUL: -0.6401 NAXIS: 1
A: 11.1624 ALPHA: 90.00 ROTX: 74.14 TRANSX: 0.27
B: 4.0034 BETA: 90.00 ROTY: 67.50 TRANSY: 0.26
C: 15.4139 GAMMA: 90.00 ROTZ: 78.84 TRANSZ: 0.36

P2(1)2(1)2(1) Wa E: -16.93 PI: 0.597010 900
ELJ: -16.16 ECOUL: -0.7638 NAXIS: 1
A: 13.0546 ALPHA: 90.00 ROTX: 170.94 TRANSX: 0.13
B: 8.7197 BETA: 90.00 ROTY: 22.50 TRANSY: 0.13
C: 6.1402 GAMMA: 90.00 ROTZ: 83.98 TRANSZ: 0.32

P2(1)2(1)2(1) Wa E: -17.10 PI: 0.604960 326
ELJ: -16.24 ECOUL: -0.8590 NAXIS: 1
A: 12.5729 ALPHA: 90.00 ROTX: 21.06 TRANSX: 0.27
B: 4.2192 BETA: 90.00 ROTY: 41.86 TRANSY: 0.19
C: 13.0028 GAMMA: 90.00 ROTZ: 22.50 TRANSZ: 0.13
STOP (called by ICE9)
CP: 2974.353s, Wallclock: 3266.198s, 11.4% of 8-CPU Machine
HWM mem: 615023, HWM stack: 167396, Stack overflows: 0
Group 0: CPU seconds : 2974.35 CP executing : 495725628918

Million inst/sec (MIPS) : 17.34 Instructions : 51577017377
Avg. clock periods/inst : 9.61
% CP holding issue : 84.36 CP holding issue : 418172475945
Inst.buffer fetches/sec : 0.05M Inst.buf. fetches: 138037461
Floating adds/sec : 66.35M F.P. adds : 197340694434
Floating multiplies/sec : 90.78M F.P. multiplies : 269998011803
Floating reciprocal/sec : 7.27M F.P. reciprocals : 21629444532
I/O mem. references/sec : 0.39M I/O references : 1160793580
CPU mem. references/sec : 62.96M CPU references : 187261918977

Floating ops/CPU second : 164.39M

Job Accounting - Command Report
==========

Command Name	Started At	Elapsed Seconds	User CPU Seconds	Sys CPU Seconds	I/O Wait Sec Lck	I/O Wait Sec Unlck	CPU Mem Avg Mwds Avg
ja	19:46:51	0.0115	0.0031	0.0076	0.0007	0.0000	0.0525 0.0865
cft77	19:46:51	0.3795	0.2864	0.0472	0.0091	0.0231	0.7128 0.4752
cp	19:46:52	0.0104	0.0030	0.0071	0.0002	0.0000	0.0291 0.0713
pwd	19:46:52	0.0131	0.0029	0.0087	0.0000	0.0000	0.0265 0.0000
sh	19:46:52	0.0255	0.0053	0.0066	0.0000	0.0000	0.0507 0.0000
fetch	19:46:52	2.6395	0.0041	0.0211	0.0004	0.0000	0.0425 0.0594
rm	19:46:55	0.0080	0.0030	0.0047	0.0000	0.0002	0.0295 0.0000
segldr	19:46:55	3.1090	0.9991	1.2865	0.0363	0.7378	0.2670 0.1848
date	19:46:58	0.0072	0.0032	0.0037	0.0002	0.0000	0.0296 0.0715
a.out	19:46:58	3266.2220	2974.3991	41.9970	0.0009	14.8636	0.5903
hpm	19:46:58	3266.3226	0.0054	0.0193	0.0002	0.0000	0.0315
pwd	20:41:24	0.0183	0.0030	0.0137	0.0000	0.0000	0.0264 0.0000
sh	20:41:24	0.0355	0.0053	0.0114	0.0000	0.0000	0.0509 0.0000
dispose	20:41:24	112.0257	0.0041	0.0303	0.0004	0.0000	0.0426

References

[1.] ROBERTS, G.G., Sensors and Actuators, **4**, 131-145 (1983).

[2.] SUGI, M., J. Mol. Electron. **1**, 3-17 (1985).

[3.] HOFFMAN, B.M., MARINSEN, J., PACE, L.J., and IBERS, J.A. Extended Linear Chain Compounds, **3**, 459-549, Miller, J.S., (ed.), Plenum Press, New York (1983).

[4.] MILLER, J.S., EPSTEIN, A., REIFF, W.M., Acc. Chem. Res., **21**, 114-120 (1988).

[5.] WILLIAMS, David J. Agnew. Chem. Int. Ed. Engl., **23**, 690-703 (1984).

[6.] CHEMLA, D.S., ZYSS,J., (Eds.) Nonlinear Optical Properties of Organic Molecules and Crystals, Academic Press, New York (1987).

[7.] FRANKEN, P.A., HILL, A.E., PETERS, C.W., WEINRICH,G., Phys. Rev. Lett., **7**, 118 (1961).

[8.] ZYSS, J., OUDAR, J.L., Phys. Rev. **A26**, 2028 (1982).

[9.] TENG, C.C., GARITO, A., Phys. Rev. Lett., **50**, 350 (1983).

[10.] MITCHELL, A.D., RODGERS, J.R. (1980). Acta Cryst., **A36**, 321-326.

[11.] HARRISON, W.A., Solid State Theory, Dover Publications, Inc., New York (1979).

[12.] BAKER, S., ROBERTS, G.G., PETTY, M.C., and TWIGG, M.V., Thin Solid Films, **99**, 71 (1983).

[13.] FERRARA, J.D., TESSIER-YOUNGS, and YOUNGS, W.J.,J. Am. Chem. Soc., **105**, 6719 (1985).

[14.] JEROME, D., MAZAUD, A., RIBAULT, M., BECHGAARD, K., J. Phys. Lett. **41**, L85 (1980).

[15.] McCONNELL, H.M., HOFFMAN, B.M., METZGER, R.M.,Proc. Nat. Acad. Sci. USA, **53**, 46 (1965).

[16.] KRUGLER, J.I.,MONTGOMERY, C.G., MCCONNELL, H.M., J. Chem. Phys., **41**, 2421, (1964).

[17.] SILVERMAN, B.D., J. Chem. Phys., **20**, 1614 (1979).

[18.] KLOPMAN, G.C., EVANS, R.C., "The Neglect of Differential Overlap Methods of Molecular Orbital Theory", in Semiempirical Methods of Electronic Structure Calculation, Part A: Techniques, ed. by G.A. Segal, Plenum Press, New York, 1977.

[19.] CHESNUT, D.B., MOSELEY, R.W., Theor. Chim. Acta , **13**, 230 (1969).

[20.] BERLINSKY, A.J., CAROLAN, J.F., WEILER, L., Solid State Comm., **19**, 1165 (1976).

[21.] COX, E.G., CRUICKSHANK, D.W.J., and SMITH, J.A.S., Proc. R. Soc. **A247**,1 (1958).

[22.] BONDI, A., Molec. Crystals, **3**, 479 (1968).

[23.] BODEN, N., DAVIS, P.P., STAM, C.H., and WESSELINK, G.A., Molec. Phys., **25**, 81 (1973).

[24.] FEDOROV, E.S., SCHOENFLIES, A., and BARLOW, W., Nature, **29**, 186, 205, 404.

[25.] VON LAUE, M., Sitzber. Math. Physik. KI. Bayer. Akad. Wiss., Muenchen, **303** (1912).

[26.] COPPENS, P., J. Chem. Ed., **61(9)**, 761-765 (1984).

[27.] MADELUNG, E., Physik. Z., **19**, 524 (1918).

[28.] BORN, M, and HUANG, K., Dynamical Theory of Crystal Lattices, Oxford (1954).

[29.] BORN, M., OPPENHEIMER, J.R., Ann. Phys. **84**, 457 (1927).

[30.] LOWDIN, P.O., Phil. Mag. Suppl., **5**, 1 (1956).

[31.] GOLDSCHMIDT, V.M., Berichte, **60**, 1263 (1927).

[32.] PAULING, L., The Nature of the Chemical Bond, Cornell University Press, Ithaca.,1940.

[33.] LAVES, F., pp. 124-198 in Theory of Alloy Phases, American Society for Metals, Cleveland, Ohio (1955).

[34.] MOOSER, E., and PEARSON, W.B., Acta Cryst., **12**, 1015 (1959).

[35.] VAN VECHTEN,J.A., and PHILIPS, J.C., Phys. Rev. B, **2**, 2147, 2160, (1970).

[36.] KITAIGORODSKY,A.I Molecular Crystals and Molecules, Academic Press NeW York (1973).

[37.] KITAIGORODSKY, A.I. (1961). Organic Chemistry Crystallography, Consultants Bureau, New York.

[38.] ZORKY, and PORAJ-KOSHITS, Modern Problems of Physical Chemistry, **1**, State University Publishing House, Moscow (1968).

[39.] LONDON, F., Z. Phys. Chem. Abt. **B11**, 222, 236 (1930).

[40.] LONDON, F., Z. Phys. **63**, 245 (1930).

[41.] SLATER, J., and KIRKWOOD, J., Phys. Rev., **37**, 682 (1931).

[42.] AXILROD, B.M., and TELLER, E., J. Chem. Phys. **11**, 299 (1943).

[43.] WOJTALA, V.J., Acta Physica. Pol. **25**, 27 (1964).

[44.] LENNARD-JONES, J.E., Proc. Phys. Soc. London **43**, 461 (1931).

[45.] BUCKINGHAM, R.A., Proc. Roy. Soc. Ser. **A168**, 254 (1938).

[46.] WILLIAMS, D.E., Science, **147**, 605 (1965).

[47.] KITAIGORODSKY, A.I., Acta Cryst., **18**, 585 (1965).

[48.] CRAIG, D.P., MASON, R., PAULING, P.,and SANTRY, D., Proc. Roy. Soc. London **A286**, 98 (1965).

[49.] WILLIAMS, D.E., Acta Cryst., **A25**, 464 (1968).

[50.] LII, J.H., ALLINGER, N.L., J. Am. Chem. Soc., **111**, 8576 (1989).

[51.] WILLIAMS, D.E., Acta Cryst. **A30**, 71-77 (1974).

[52.] BATES, J.B., and BUSING, W.R., J. Chem. Phys., **60**, 2414 (1974).

[53.] WILLIAMS, D.E., and STARR, T.L., Computers and Chemistry, **1**, 173-177 Pergamon Press, Gr. Britain (1977).

[54.] ALLINGER, N.L., J. Am. Chem. Soc. **99**, 8127 (1977).

[55.] COX, S.R., HSU, L.Y., and WILLIAMS, D.E., Acta Cryst. **A37**, 293-301 (1981).

[56.] WILLIAMS, D.E., and COX, S.R., Acta Cryst. **B40**, 404-417 (1984).

[57.] PROFETA, S. and ALLINGER, N.L., J. Am. Chem. Soc. **107**, 1907-1918 (1985).

[58.] WILLIAMS, D.E., and HOUPT, D. J. (1986). Acta Cryst., **B42**, 286-295.

[59.] PRICE, S.L., Acta Cryst., **B42**, 388-401 (1986).

[60.] PRICE, S.L., and STONE, A.J., Molecular Physics, **40**, 805-822 (1980).

[61.] PRICE, S.L., and STONE, A.J., Molecular Physics, **47**, 1457-1470 (1982).

[62.] PRICE, S.L., Molecular Physics, **62(1)**, 45-63 (1987).

[63.] MATSUOKA, O., CLEMENTI, E., YOSHIMINE, M., J. Chem. Phys., **64**, 1351 (1976).

[64.] KARLSTROM, G., LINSE, P., WALLQVIST, A., JO:NSSON, B., J. Am. Chem. Soc., **105**, 3777 (1983).

[65.] FRAGA, S., J. Comput. Chem. **3**, 329-324 (1982).

[66.] McWEENY,R., Methods of Molecular Quantum Mechanics 2nd Ed (1989), AP.

[67.] STONE, A.J., Chemical Physics Letters, **83**, No. 2, 233 (1981).

[68.] BUCKINGHAM, A.D., and FOWLER, P.W., J. Chem. Phys., **79**, 6426 (1983).

[69.] BUCKINGHAM, A.D., and FOWLER, P.W., Can. J. Chem., **63**, 2018 (1985).

[70.] CRIPPEN, G., Distance Geometry and Conformational Calculations, Research Studies Press, Wiley, New York (1981).

[71.] Gaussian 90, Revision H, FRISCH,M. J., HEAD-GORDON,M., TRUCKS,G. W., FORESMAN, J. B., SCHLEGEL, H. B., RAGHAVACHARI, K., ROBB, M., BINKLEY, J. S., GONZALES, C., DEFREES, D. J., FOX, D. J., WHITESIDE, R. A., SEEGER, R., MELIUS, C. F., BAKER, J., MARTIN, R. L., KAHN, L. R., STEWART, J. J. P., TOPIOL, S., and POPLE, J. A., Gaussian, Inc., Pittsburgh, PA, 1990.

[72.] DUPUIS, M., RYS, J., and KING, H.F., QCPE #13, 403 (1981).

[73.] STEWART, J. J. P., QCPE Bulletin, 3:24 (1983).

[74.] CHARMm, Polygen Corporation, 200 Fifth Avenue, Waltham, MA 02254.

[75.] Tripos Associates, Inc., a subsidiary of Evans & Sutherland, 1699 S. Hanley Rd., Suite 303, St. Louis, MO 63144.

[76.] WILLIAMS, D.E., Acta Cryst. **A25**, 464-470 (1969).

[77.] WILLIAMS, D.E. (1983). Quantum Chemistry Program Exchange, #41.

[78.] GAVEZZOTTI, A., and DESIRAJU, G. R. (1988). Acta Cryst., **B44**, 427-434.

[79.] MIRSKY, K. (1976). Acta Cryst., **A32**, 199-207.

[80.] WILLIAMS, D.E., Acta Cryst. **A36**, 715-723 (1980).

[81.] VAN DE WAAL, B. W., Acta Cryst. **A37**, 762-764 (1981).

[82.] OIKAWA, S., TSUDA, M., KATO, H., URABE, T., Acta Cryst. **B41**, 437-445 (1985).

[83.] MIGHELL, A.D., HIMES, V.L., RODGERS, J.R., Acta Cryst. **A39**, 737 (1983).

[84.] MOMANY, F. A., VANDERKOOI, G., SCHERAGA, H. A., Proc. Nat. Acad. Sci. **61**, 429 (1968).

[85.] BUSING, W.R., Oak Ridge National Laboratory Report #5747 (1981).

[86.] HIRSHFELTER, A., Molecular Theory of Gases and Liquid

[87.] LOWDIN, P. O., J. Chem. Phys., **21**, 374 (1953).

[88.] MULLIKEN, R. S., J. Chem. Phys., **23**, 1833 (1955).

[89.] STOUT, E.W, Jr., and POLITZER, P., Theor. Chim. Acta, **4**, 1 (1966).

[90.] DAVIDSON, E.R. J. Chem. Phys., **46**, 3320 (1967).

[91.] POPLE, J.A., and GORDON, M.S., J. Am. Chem. Soc., **89**, 4253 (1967).

[92.] COULSON, C.A., and DOGGETT, G., Int. J. Quantum Chem., **2**, 825 (1968).

[93.] HEHRE, W.J. and POPLE, J.A., J. Am. Chem. Soc., **92**, 2191 (1970).

[94.] POLITZER,P. and HARRIS, R.R., J. Am. Chem. Soc., **92**, 6451 (1970).

[95.] CHRISTOFFERSEN, R.E., and BAKER, K.A., Chem. Phys. Lett., **8**, 4 (1971).

[96.] BADER, R.F.W., BEDDALL, P.M., and CADE, P.E., J. Am. Chem. Soc., **93**, 3095 (1971).

[97.] POLITZER, P., and REGGIO, P.H., J. Am. Chem. Soc., **94**, 8308 (1972).

[98.] JUG, K., Theor. Chim. Acta (Berlin), **31**, 63 (1973).

[99.] MAATSUOKA, O., CLEMENTI, E., and YOSHIME, M., J. Chem. Phys., **64**, 1351 (1976).

[100.] MOMANY, F.A., J. Phys. Chem., **82**, 592 (1978).

[101.] HIRSHFELD, F.L., and MIRSKY, K., Acta Cryst, **A35**, 366-370 (1979).

[102.] WILLIAMS, D.E., and HOUPT, D.J., Acta Cryst., **B42**, 286-295 (1986).

[103.] WEINSTEIN, H., APFELTER, B., and Berg, R.A., Photochem. Photobio. **18**, 175 (1973).

[104.] PULLMAN, A., Chem. Phys. Letters **20**, 29 (1972).

[106.] EVANS, D.J., and WATTS, R.O., Molecular Physics, 1, **31**, 83-96 (1976).

[107.] EWALD, P.P., Ann. Phys. **64**, 253 (1921).

[108.] BERTAUT, F., J. Phys. Radium, **13**, 499 (1952).

[109.] NIJBOER, B.R.A., and DEWETTE, F.W., Physica, **23**, 39 (1957).

[110.] GLASSER, M.L., and ZUCKER, I.J., Theoretical Chemistry: Advances and Perspectives, Volume 5, 67-139, Academic Press, new York and London, 1980.

[111.] WILLIAMS, D.E., Acta Cryst. **A28**, (1972).

[112.] HOPFINGER, A.J., Conformational Properties of Macromolecules, Academic Press, New York and London (1973).

[113.] TRIPATHY, S.K., HOPFINGER, A.J., TAYLOR, P.L.

[114.] AL-JISHI, R., and TAYLOR, P.L., J. Appl. Phys., **57**, 897 (1985).

[115.] HIRSHFELD, F.L., and MIRSKY, K., Acta Cryst., **A35**, 366-370 (1979).

[116.] HIRSHFELD, F.L., Theor. Chim. Acta, **44**, 129-138 (1977).

[117.] JACKSON, J.D., Classical Electrodynamics, John Wiley & Sons, New York (1962).

[118.] BUCKINGHAM, A.D., Personal communication.

[119.] CHEMX, Chemical Design, Ltd., Oxford, England. Copywrite 1990.

[120.] SPIEGEL, M.R.,Theoretical Mechanics, 254, McGraw-Hill Book Company, New York 1967.

[121.] KITTEL, C., Introduction to Solid State Physics, 6th edition, John Wiley & Sons, Inc., New York (1986).

[122.] Bondi, A., J. Chem. Eng. Data **8**, 371-381 (1963).

[123.] BACON, G¿ E¿, CURRY, N. A., WILSON, S. A., Proc. R. Soc. London Ser. A, **279**, 98-110 (1964).

[125.] MORAWTZ, E., J. Chem. Thermodyn. **4**, 455-460 (1972).

[126.] KOZIN, V.M., KITAIGORODSKY, A.I., Z. Fiz. Khim. SSSR, **27**, 534-541 (1953).

[127.] ABRAHAMS, S.C., ROBERTSON, J.M., White, J.G., Acta. Cryst. **2**, 238 (1949).

[128.] BONDI, A., J. Chem. Eng. Data **8**, 371-381 (1963).

[129.] DYGDALA, R.S., and STEFANSKI, K., Chem. Phys. **53**, 51-62 (1980).

[130.] MASON, R., Acta Cryst. **17**, 547 (1964). Anth 95

[131.] MATHIESON, A. McL., ROBERTSON, J.M., and SINCLAIR, V.C., Acta Cryst. **3**, 245 (1950).

[132.] CAMPBELL, R.B., ROBERTSON, J.M., Acta Cryst. **15**, 289 (1962).

[133.] TROTTER, J., Acta Cryst. **16**, 605 (1962). Phen p21

[134.] BERNAL, J.D., CROWFOOT, D., J. Chem. Soc., **93**, (1935). Phen p21/c

[135.] SMOTH, N.K. STUART, R.C., OSBORN, A.G., WISCOTT, D., J. Chem. Thermodyn. **12**, 919-926 (1980).

[136.] ROBERTSON, J. M., and WHITE, J. G., J. Chem. Soc. 358-368 (1947).

[137.] AHMED, F. R., and TROTTER, J., Acta Cryst. **16**, 503 (1963).

[138.] IBALL, J., and ROBERTSON, J. M., Nature **132**, 750 (1933).

[139.] KRISHNAN, K. S., and BANERJEE, K., Z. Krist. **91**, 170-173 (1935).

[140.] IBALL, J., Nature **137**, 361 (1936).

[141.] ROBERTSON, J. M., and WHITE, J. G., J. Chem. Soc. 1001-1010 (1947).

[142.] DONALDSON, D. M., ROBERTSON, J. M., and WHITE, J. G., Proc. Roy. Soc. **A220**, 311-321 (1953).

[143.] ROBERTSON, J.M., Proc. Roy. Soc., **A141**, 594 (1933).

[144.] NORMAN, N., and MATHISEN, H., Acta Chemica Scandinavica **15**, 1755-1760 (1961).

[145.] NORMAN, N., and MATHISEN, H., Acta Chemica Scandinavica **15**, 1747 (1961).

[146.] SASVARI, K., and LOW, M., Acta Cryst. **19**, 840 (1965).

[147.] BOYKO, E. R., and VAUGHAN, P. A., Acta Cryst. **17**, 152 (1964).

[148.] CLARK, T., A Handbook of Computational Chemistry, John Wiley and Sons, New York (1985).